

# **Development of 3D Bioprinting Techniques Based on Supportive Media**

**Ian MacKenzie**

Submitted for the degree of Doctor of Philosophy

Heriot-Watt University

Institute of Mechanical, Process, and Energy Engineering,

School of Engineering and Physical Sciences

June 2020

The copyright in this thesis is owned by the author. Any quotation from the thesis or use of any of the information contained in it must acknowledge this thesis as the source of the quotation or information.

## **Abstract**

The production of anatomically complex tissues and organs with high biological function requires bioinks to have contradictory material properties. Properties that enable bioinks to be mechanically self-sufficient and accurate in terms of geometric fidelity may not be inherently compatible for cell viability and vice versa. Such is the practical dilemma of bioprinting, leading to the development of bioinks with balanced mechanical and biological properties that do not excel in either respect.

In this thesis, the development of a customised, modular, extrusion-based 3D bioprinter and two novel supportive bath strategies is described. This custom bioprinter is able to extrude low-concentration, low-viscosity bioinks deep into the developed support baths and suspend the extruded bioink in 3D space. Printing structures in this manner reduces the demand for mechanically strong bioinks during the fabrication process as the structure's weight is supported by the bath in all dimensions. These supportive strategies enable the production of larger and geometrically more complex anatomical structures whilst using a low-concentration, low-viscosity alginate hydrogel bioink. Therefore the material's mechanical needs for bioprinting are addressed in such a way that encourages the use of bioinks with qualities that can be biologically more favourable.

The support baths detailed in this thesis includes a quiescently gelled gelatine-based approach and a fluidised-agar fluid gel approach. The gelatine baths are prepared in a very simple, reliable, and repeatable two-step manner, and printed structures embedded within the gel are removed gently and easily by utilising gelatine's physiologically relevant melting temperature to liquefy the support. Blood vessel-like structures and noses were fabricated in this manner. Agar fluid gel support baths are also simple to produce and only require a gelled puck of agar be blended prior to its application as a supportive material. Agar fluid gel baths have been used successfully to support the fabrication of geometrically challenging structures such as bucky balls and Eiffel towers as well as replicate anatomical models such as ears, noses, brains, and hearts, which are easily separated from their supports by washing away the residual fluid gel.

## **Acknowledgements**

I would like to thank my supervisors Professor Will Shu and Dr. Xianwen Kong for their continued support and encouragement throughout the duration of my PhD. Professor Shu's tenacity, positive work ethic, and his can-do attitude make him a fantastic driver of research, allowing me to conduct my research to the best of my ability. Dr. Kong has continually offered his helpful advice and research considerations throughout my PhD and guaranteed I had access to the space and facilities I needed during hard times.

I would like to thank my research colleagues, many whom I consider my close friends. This research journey of mine would have been far more arduous if not for the advice and support that they offered, and for all the good jokes, games, and lunch.

I want to express my deepest thanks to my family, my fiancée, and my closest friends – thank you all for putting up with me. Thank you all for your unending support through all those difficult days and celebrating with me in my successes.

I would lastly like to thank the Engineering and Physical Sciences Research Council (EPSRC) for funding this research and granting me with this opportunity to further explore the fascinating world of 3D printing.

## Research Thesis Submission



Please note this form should be bound into the submitted thesis.

Name:	Ian MacKenzie		
School:	School of Engineering and Physical Sciences		
Version: <i>(i.e. First, Resubmission, Final)</i>	Final	Degree Sought:	PhD Mechanical Engineering

### Declaration

In accordance with the appropriate regulations I hereby submit my thesis and I declare that:

1. The thesis embodies the results of my own work and has been composed by myself
2. Where appropriate, I have made acknowledgement of the work of others
3. The thesis is the correct version for submission and is the same version as any electronic versions submitted\*.
4. My thesis for the award referred to, deposited in the Heriot-Watt University Library, should be made available for loan or photocopying and be available via the Institutional Repository, subject to such conditions as the Librarian may require
5. I understand that as a student of the University I am required to abide by the Regulations of the University and to conform to its discipline.
6. I confirm that the thesis has been verified against plagiarism via an approved plagiarism detection application e.g. Turnitin.

\* Please note that it is the responsibility of the candidate to ensure that the correct version of the thesis is submitted.

Signature of Candidate:	Ian MacKenzie	Date:	04/06/2020
-------------------------	---------------	-------	------------

### Submission

Submitted By <i>(name in capitals)</i> :	IAN MACKENZIE
Signature of Individual Submitting:	Ian MacKenzie
Date Submitted:	04/06/2020

### For Completion in the Student Service Centre (SSC)

Limited Access	Requested	Yes	No	Approved	Yes	No
<i>E-Thesis Submitted (mandatory for final thesis)</i>						
Received in the SSC by <i>(name in capitals)</i> :				Date:		



## Table of Contents

List of Tables.....	vi
List of Figures .....	vii
Nomenclature .....	xvii
List of Publications .....	xx
Chapter 1 – Introduction .....	1
Chapter 2 – Literature Review .....	4
2.1 Introduction .....	4
2.2 Development of 3D Printers.....	4
2.2.1 A brief history of 3D printing .....	4
2.2.2 Extrusion-based bioprinting .....	7
2.2.3 Inkjet-based bioprinting .....	9
2.2.4 Valve-based bioprinting .....	11
2.2.5 Light-based bioprinting .....	12
2.3 Development of Supportive Fabrication Strategies .....	15
2.4 Materials for Biofabrication .....	24
2.4.1 Alginate .....	24
2.4.2 Collagen .....	26
2.4.3 Gelatine .....	28
2.4.4 Agar-agar/agarose .....	30
2.4.5 Fluid gels .....	32
2.5 Summary .....	34
2.6 Aims and Objectives .....	37
2.7 Structure of Thesis .....	38
Chapter 3 –Materials and Methods .....	39
3.1 Introduction .....	39

3.2 Equipment and Machinery .....	39
3.2.1 Laser cutter .....	39
3.2.2 3D printer .....	40
3.2.3 Centrifuge.....	41
3.2.4 Cellmixer unit .....	42
3.2.5 Magnetic stirrer and hotplate .....	43
3.2.6 Immersion blender .....	44
3.2.7 Cell imaging microscope .....	44
3.2.8 Incubator .....	45
3.3 Materials.....	46
3.3.1 Preparation of partially crosslinked alginate-based bioink.....	46
3.3.2 Preparation of quiescently gelled gelatine support baths.....	47
3.3.3 Preparation of agar fluid gel support baths .....	48
3.4 Biological Methods .....	48
3.4.1 Cell culture .....	48
3.4.2 Preparation of cell-laden bioinks .....	49
3.4.3 Cell viability assessment.....	50
3.5 Operational Methods.....	50
3.5.1 Modelling .....	50
3.5.2 Slicing and g-code generation.....	51
3.5.3 Printing.....	51
3.5.4 Systematic strategy for optimising print quality .....	52
3.5.5 Releasing printed structures from gelatine support baths .....	53
3.5.6 Releasing printed structures from agar fluid gel support baths.....	54
Chapter 4 – Development of a Modular Extrusion Based 3D Bioprinting Platform.....	55
4.1 Introduction .....	55
4.2 Hardware .....	56
4.2.1 Bioprinter frame – creating the X/Y/Z axes.....	56

4.2.2 Extrusion system .....	64
4.2.3 Miscellaneous hardware .....	67
4.3 Electronics .....	67
4.3.1 RAMPS 1.4 microcontroller .....	67
4.3.2 Power supply unit .....	71
4.3.3 Motors .....	72
4.3.4 Mechanical Endstops .....	74
4.4 Firmware .....	77
4.5 Theoretical Resolution .....	79
4.5.1 Positional resolution of belted X- and Y-axes .....	79
4.5.2 Positional resolution of leadscrew Z-axis .....	79
4.5.3 Depositional resolution of threaded rod E-axis .....	80
4.6 Summary .....	81
Chapter 5 – A Quiescently Gelled Gelatine Supportive Medium to Facilitate 3D Soft Tissue Biofabrication .....	85
5.1 Introduction .....	85
5.2 The Influence of Gelatine Concentration on Bath Properties .....	87
5.3 Extrudate Flow Behaviour within Support Baths .....	91
5.3.1 Manual extrusion of partially crosslinked alginate into gelatine baths .....	91
5.3.2 Manual extrusion of red dye solution into gelatine baths .....	93
5.4 Printability Study of Support Baths .....	95
5.5 Release Study of Support Baths .....	98
5.6 3D Printing of Dense Anatomical Structures .....	100
5.7 3D Bioprinting Live Cells into Gelatine Support Bath .....	102
5.8 Viscosity Modification of Gelatine Support Baths .....	105
5.8.1 Influence of viscosity modifiers on gelatine behaviour .....	105
5.8.2 Printing into guar gum/gelatine support bath gels .....	108
5.9 Coaxial Nozzle Printing into Quiescently Gelled Gelatine Support Baths .....	109

5.9.1 Manufacture of a custom DIY coaxial nozzle.....	109
5.9.2 G-code generation for coaxial printing .....	111
5.9.3 Coaxial extrusion into calcium solution.....	112
5.9.4 Coaxial extrusion into gelatine baths .....	114
5.10 Summary .....	121
Chapter 6 – Supported Fabrication of 3D Structures within an Agar-Agar Fluid Gel Medium .....	124
6.1 Introduction .....	124
6.2 Systematic Evaluation of Agar and Calcium Concentration on Supportive and Print Qualities .....	126
6.3 Supported Fabrication of Macroporous 3D Structures .....	136
6.3.1 Fabrication of large, thick macroporous grids .....	137
6.3.2 Fabrication of honeycomb grids with variable macroporosity .....	140
6.4 Supported Fabrication of High Resolution and Highly Complex 3D Structures	142
6.4.1 Agar fluid gel support bath – nose printing .....	143
6.4.2 Agar fluid gel support bath – ear printing.....	145
6.4.3 Agar fluid gel support bath – bucky ball printing.....	147
6.4.4 Agar fluid gel support bath – Eiffel tower printing.....	150
6.5 Summary .....	151
Chapter 7 – Agar Fluid Gels with Enhanced Tuneability for Further Engineering Control .....	155
7.1 Introduction.....	155
7.2 Influence of the Continuous-Phase on Support Bath Qualities.....	156
7.2.1 Assessment of fluid gel and diluent constituents prior to mixing.....	156
7.2.2 Clarity assessment of fluid gel/diluent mixtures.....	159
7.2.3 Printability assessment of fluid gel/diluent mixtures .....	162
7.2.4 Invertibility assessment of fluid gel/diluent mixtures.....	166
7.2.5 Scoring of fluid gel/diluent mixtures with respect to assessment criteria....	168
7.2.6 Nozzle assessment of optimised fluid gel/diluent mixture support bath.....	170

7.3 Influence of Calcium Concentration and Distribution within the Gel-Phase/Continuous-Phase on Support Bath Qualities .....	172
7.3.1 Printability assessment into fluid gel 3:1 mixtures with respect to calcium distribution and concentration in the gel- and continuous-phases .....	173
7.3.2 Impact of mixing ratio on printability with respect to calcium concentration and distribution .....	176
7.4 Capability of Agar Fluid Gel/Water Mixtures to Facilitate Complex Structure Fabrication.....	182
7.5 Summary .....	187
Chapter 8 – Conclusions and Future Perspectives .....	190
8.1 Conclusions .....	190
8.2 Future Perspectives .....	195
Appendix A – Mixing Material with the Cellink Cellmixer Unit.....	198
Appendix B – Using Excel for Spiralling Structure G-code Generation.....	200
B.1 Generating positional data for the x- and y-axis .....	200
B.2 Generating positional data for the z-axis.....	202
B.3 Generating start and end scripts .....	203
B.4 Compiling generated x, y, and z values into g-code.....	205
Appendix C – Miscellaneous Hardware .....	207
Appendix D – Firmware Configuration .....	211
D.1 Basic settings.....	211
D.2 Thermal settings .....	214
D.3 Mechanical settings .....	215
D.4 Additional settings .....	218
References .....	219

## List of Tables

<b>Table 4.1</b> – Pin configurations for various microstepping modes.....	69
<b>Table 4.2</b> - Comparison of the developed 3D bioprinter’s cost and functionality with commercially available options .....	84
<b>Table 5.1</b> - Invertibility assessment results of 0.6% w/v gelatine mixtures with sugar, GG, and CMC at concentrations of 0.1%, 0.25%, and 0.5% w/v .....	106
<b>Table 7.1</b> - Decision matrix to score the relative strengths and weaknesses of each agar fluid gel and viscosity modifier mixture at various mixing ratios .....	169
<b>Table 7.2</b> - Surmised decision matrix to show the relative score for each of the assessed agar fluid gel and viscosity modifier mixtures at the various mixing ratios.....	169
<b>Table 8.1</b> – Comparison of developed gelatine and agar support bath characteristics.	195

## List of Figures

<b>Figure 1.1</b> - The number of organ donors, number of patients on the transplant list, and the number of transplantations over the course of a decade between 2008 and 2018 [12] .....	2
<b>Figure 2.1</b> – Schematic of the first 3D printer, developed by Charles Hull in 1983 and subsequently patented in 1984 [27] .....	5
<b>Figure 2.2</b> – The first printer customised for the purpose of printing cells, i.e. a ‘bioprinter’, developed by Thomas Boland in 2003 [39].....	7
<b>Figure 2.3</b> - schematic diagram of (a) pneumatic, (b) piston, (c) and screw-driven extrusion bioprinting, adapted from [54] .....	8
<b>Figure 2.4</b> - Schematic diagram of two inkjet-based bioprinting methods - (a) piezo-electric and (b) thermal, adapted from [71] .....	10
<b>Figure 2.5</b> - Schematic diagram of valve-based bioprinting, adapted from [71] .....	12
<b>Figure 2.6</b> - Schematic diagram of two SLA-based bioprinting method - (a) laser scanning and (b) projection, adapted from [101].....	14
<b>Figure 2.7</b> - Schematic diagram of the LIFT bioprinting method, adapted from [109].	15
<b>Figure 2.8</b> - Schematic of the substrate ‘stacking’ process, adapted from [112] - (a) substrate pre-coated with crosslinker, (b) printing of biopolymer layer, (c) printing of cell layer, (d) printing of new crosslinking layer. Steps (b), (c), and (d) are repeated to create stacked cellular structures.....	17
<b>Figure 2.9</b> – Schematic diagram showing the fabrication of perfusable and vascularised tissue, adapted from [121] - (a) fugitive Pluronic-F127 and cells printed inside a chip, (b) cell-laden ECM material cast over the chip, (c) fugitive Pluronic-F127 ink removed via cooling and evacuation, (d) hollow internal network perfused to provide nutrition to cells in thick tissue .....	19
<b>Figure 2.10</b> – Schematic diagram of supported fabrication by means of printing into a crosslinking solution, adapted from [55] – (a) bioink extruded onto a porous platform is lowered into a bath of crosslinking solution, (b) lower layers become rigid enough to support upper layers due to crosslinking, (c) printing is conducted close to the crosslinking bath’s surface for quick crosslinking to maximise shape fidelity .....	20
<b>Figure 2.11</b> – Schematic diagram for structures fabricated with a microparticulate support bath, adapted from FRESH [134] – (a) microparticle baths support bioinks in	

3D space during (b) and after printing, (c) structures fall out of suspension by melting the supportive microparticles (d) and can then be safely retrieved.....23

**Figure 2.12** – The chemical structure of sodium alginate [156] consists of (a) (1,4)-linked- $\alpha$ -L-guluronic acid and (1,4)-linked- $\beta$ -D-mannuronic acid residue called G and M respectively, (b) residues of G and M are arranged in ‘blocks’ throughout the polysaccharide chain, (c) alginate chains form crosslinks with other chains when exposed to divalent cations and forms an ‘egg-box’ structure [157][158][159].....25

**Figure 2.13** – The chemical structure of a collagen consists primarily of three amino acids (a) glycine, (b) proline, (c) and hydroxyproline, (d) joined by peptide bonds. Repeating glycine-proline-hydroxyproline units form polypeptide  $\alpha$ -chains (e) which are hydrogen bonded with other  $\alpha$ -chains which forms the triple-helical molecular structure characteristic of collagens [174][175][176][177] .....27

**Figure 2.14** – Gelatine’s chemical structure (a) contains a large proportion of glycine, proline, and hydroxyproline amino acids like collagen, (b) denatured collagen produces gelatine molecules, (c) renaturation of molecules into collagen-like triple helices (d) and aggregate into a 3D gelled network when cooled [183][191][192][193][194].....29

**Figure 2.15** – Chemical structure of agar’s gelling constituent, agarose, comprises of (a)  $\beta$  -D-galactopyranose and (b)  $\alpha$ -L-galactopyranose, (c) which form glycosidic bonds and makes up agarose’s repeating structural unit [208]: (1,3)-linked- $\beta$ -D-galactopyranose and (1,4)-linked- $\alpha$ -L-3,6-anhydro-galactopyranose. (d) Random coils of agarose molecules, (e) conformation change into double helices upon cooling, (f) aggregation into agar’s 3D gelled network [209][210].....31

**Figure 2.16** – Illustration of fluid gel’s supportive mechanism in a bioprinting context based on hairy particle analogy – (a) network at rest maintains solid-like characteristics due to hair entanglement with neighbouring particles, (b) particles local to the stressor become untangled and exhibit fluid-like characteristics; particles far from the stressor remain entangled, (c) removal of stressor allows untangled particles to become entangled again to exhibit solid-like behaviour [225][226].....34

**Figure 3.1** –The Trotec Speedy 300 Laser Engraver [235].....39

**Figure 3.2** – The MakerBot Replicator 2X 3D Printer [236] .....41

**Figure 3.3** – Schematic of the Cellink Cellmixing unit and its components [237] .....42

**Figure 3.4** – The Nikon Eclipse TE300 inverted fluorescent microscope [238].....45

**Figure 4.1** – The 3D bioprinter’s frame consists of 12 beams fastened together with 8 corner cubes. The empty space within the frame has a volume of  $300 \times 300 \times 300 \text{ mm}^3$  .....56



<b>Figure 4.2</b> – (a) the Z-axis motor mounting assembly consists of a NEMA 17 motor affixed to a mounting bracket which are bolted onto beams below, which are affixed to the frame with corner brackets, ‘L’ brackets, (b) and ‘T’ brackets.....	57
<b>Figure 4.3</b> – (a) Y-axis stepper motor attached to the frame using two ‘T’ brackets and two 45 mm beams (b) to affix the motor’s mounting bracket to the frame .....	58
<b>Figure 4.4</b> – (a) View of the left Y-axis linear rod for guiding the Y-axis carriage – (b) the rod runs slightly beneath the motor’s pin, (c) at the printer’s right side, an assembly of beams and brackets allows for locating of an idler pulley’s shaft and (d) fixing of the linear rod .....	59
<b>Figure 4.5</b> – (a) The Y-axis coupling rod at the front of the frame is supported by two pedestal bearings positioned above the shaft clamps behind the vertical beams, (b) a close up view showing a GT2 pulley and belt aligned parallel with the linear rod .....	60
<b>Figure 4.6</b> – (a) The primary Y-axis carriage (b) with space for a NEMA17 stepper motor to drive the X-axis, (c) the complete carriage assembly showing the positions of all carriages including the X-axis carriage.....	61
<b>Figure 4.7</b> – (a) View of the primary Y-axis carriage from the perspective of the X-axis carriage showing the belt tensioning spring and affixed GT2 belt, (b) the X-axis carriage showing the GT2 belt held in position with a push fit clamp .....	62
<b>Figure 4.8</b> – (a) The Z-axis platform is that of the original Makerbot Replicator 3D printer, (b) the Z-axis leadscrew is joined to the platform between the two back panels with a tr8*8 (p2) nut, (c) the platform is attached to the frame from underneath by aligning the bearings and nut with the leadscrew and linear rods respectively .....	63
<b>Figure 4.9</b> – Laser cut components for the extruder housing assembly, (a) the components for housing the extrusion system, (b) the components for affixing the extruder housing to the printer’s X-axis carriage.....	65
<b>Figure 4.10</b> – (a) Front view of the assembled screw-plunger extruder based on the Fab@Home system, (b) side view of the extrusion system .....	66
<b>Figure 4.11</b> – RAMPS 1.4 pre-soldered shield .....	68
<b>Figure 4.12</b> – Jumpers are inserted into their respective pins to enable microstepping.	69
<b>Figure 4.13</b> – The A4988 stepper driver inserted into its respective pins on the board.	70
<b>Figure 4.14</b> – Schematic showing the connection between power supply unit and the RAMPS 1.4 board.....	72
<b>Figure 4.15</b> – Schematic showing the wiring for correct operation of NEMA 17 stepper motors.....	74
<b>Figure 4.16</b> – (a) Endstop position on the Y-axis endstop, (b) X-axis, (c) and Z-axis ..	75

<b>Figure 4.17</b> – Diagram showing which RAMPS 1.4 pins correspond with minimum and maximum axis position, signal (S), ground (-), and VCC (+) .....	76
<b>Figure 5.1</b> - (a) Schematic representing the crossover between fluidic and elastic dominance with increasing gelatine concentration, (b) different gelatine concentrations are inverted to check for fluidic dominance, (c) or elastic dominance .....	88
<b>Figure 5.2</b> - (a) Ten 15 ml tubes arranged left to right with 0.1% to 1% gelatine concentration prior to inversion, (b) tubes in the same order after inversion. The dotted line corresponds with the fluid/gel level .....	89
<b>Figure 5.3</b> – The storage modulus ( $G'$ ) and loss modulus ( $G''$ ) of 1% gelatine at a temperature of 14° Celsius, adapted from [259] .....	90
<b>Figure 5.4</b> – Frequency sweep of 0.5% to 2% gelatine solutions showing the storage modulus $G'$ and loss modulus $G''$ at a temperature of 10° Celsius, adapted from [260] .	91
<b>Figure 5.5</b> – Partially crosslinked alginate hydrogel manually extruded into gelatine baths of concentration (a-e) 0.1% to 0.5% w/v and (f-j) 0.6% w/v to 1% w/v .....	92
<b>Figure 5.6</b> – Red dye solution manually extruded into gelatine concentrations of (a-e) 0.1% to 0.5% w/v and (f-j) 0.6% to 1% w/v .....	93
<b>Figure 5.7</b> - Systematic study of grid printability at various gelatine and $\text{CaCl}_2$ concentrations .....	97
<b>Figure 5.8</b> - Systematic study of grid release-ability at various gelatine and $\text{CaCl}_2$ concentrations .....	98
<b>Figure 5.9</b> – (a) Photograph of a nose during fabrication within a gelatine support bath, (b) side view (c) and top view of the printed nose after successful release, (d) a self-standing branching arterial-like model (e) with a clear internal network, (f) a thin, single-walled tube held up by an 18 gauge nozzle.....	102
<b>Figure 5.10</b> – Viability of HepaRG cell- and aggregate-laden partially crosslinked alginate printed into 0.8% gelatine 8 mM $\text{CaCl}_2$ support bath at day 0, day 2, and day 7. Scale bars: 200 $\mu\text{m}$ . Green: live cells. Red: dead cells .....	104
<b>Figure 5.11</b> – Turbidity of 0.6% w/v gelatine mixtures with sugar, GG, and CMC at concentrations of 0.1%, 0.25%, and 0.5% w/v .....	106
<b>Figure 5.12</b> – Schematic depicting the complex coacervation process exhibited by gelatine/CMC mixtures .....	107
<b>Figure 5.13</b> – (a) 0.6% w/v gelatine bath without viscosity modification and (b) with 0.1% GG modification. Tubes on the left were printed at 15 mm/s speeds; tubes on the right were printed at 60 mm/s speeds.....	109

<b>Figure 5.14</b> – (a) Schematic diagram showing the core and shell assembly of a coaxial nozzle, (b) the assembled DIY coaxial nozzle .....	110
<b>Figure 5.15</b> – Coaxial extrusion into calcium solution shows some evidence of internal channel formation.....	113
<b>Figure 5.16</b> – Cut section of coaxially extruded filament is perfused with red dye solution to show successful internal channel formation .....	114
<b>Figure 5.17</b> – Coaxial nozzle extrusion into a 0.8% w/v gelatine bath using g-code derived from the developed Excel spreadsheet; the calcium solution core (dyed green) above the structure indicates unsuccessful internal channel formation .....	115
<b>Figure 5.18</b> – Coaxially extruded structure released from 0.8% w/v gelatine support bath.....	116
<b>Figure 5.19</b> – Coaxial extrusion into support baths with gelatine concentrations of (a) 0.3% to (e) 0.7% w/v.....	118
<b>Figure 5.20</b> – Comparison of coaxially printed structures into baths with (a) 0.4% and (b) 0.6% w/v gelatine; extrusion into 0.4% w/v gelatine baths shows some evidence of internal channel formation at a loss of printability .....	118
<b>Figure 5.21</b> – Assessment of print repeatability of coaxial extrusion into 0.4% w/v gelatine baths.....	119
<b>Figure 5.22</b> - Rising filament phenomenon when coaxially extruded filament is printed into various gelatine baths (a) 0.4% to (e) 0.8% w/v. The difference in vertical displacement between (f) 0.4% and (g) 0.8% w/v is measured relative to the nozzle size and is shown to be significantly greater at lower gelatine concentrations.....	120
<b>Figure 5.23</b> – Comparison of 3D structures printed from (a) the developed quiescently gelled gelatine support bath, (b) a Carbopol-based granular gel support bath [128], and (c) the gelatine-based FRESH method [134] .....	122
<b>Figure 6.1</b> - (a) comparison of the relative clarities of fluid gels at concentrations from 0.2% to 1% w/v, (b) and the gel's ability to support printed simple tubular structures at those concentrations.....	126
<b>Figure 6.2</b> – Results of tabletop rheological assessment of five agar fluid gel concentrations from 0.2% to 1% w/v, left to right. All concentrations were successfully inverted except for the weakest 0.2% agar condition .....	127
<b>Figure 6.3</b> - Branching blood vessel-like structures printed into 0.2% agar fluid gel baths with various calcium concentrations (a) 0 mM (control), (b) 2 mM, (c) 4 mM, (d) 6 mM, (e) 8 mM, (f) and 10 mM CaCl <sub>2</sub> .....	128

<b>Figure 6.4</b> – Relative print and structural qualities of branching blood vessel-like structures printed into 1% agar fluid gel baths with calcium concentrations of (a, d) 10 mM, (b, e) 20 mM, and (c, f) 40 mM CaCl <sub>2</sub> .....	131
<b>Figure 6.5</b> – Nozzle deflection observed whilst moving within a 1% agar bath, (a) thicker 25g nozzles resist deflection whereas (b) thinner 30g nozzles readily bend due to viscous forces acting on the nozzle as they through the medium .....	133
<b>Figure 6.6</b> – (a) 30g nozzles retain their straightness in 0.8% w/v agar baths, (b) but fail to print successfully at 20 mM CaCl <sub>2</sub> levels in a manner symptomatic of excessive crosslinking, (c) unlike 25g nozzles which print successfully at these conditions .....	134
<b>Figure 6.7</b> – (a) successful print of blood vessel-like structure with a 30g nozzle within a 0.8% w/v agar 10 mM CaCl <sub>2</sub> bath, (b) successful release of the aforementioned structure, shown to be self-standing.....	135
<b>Figure 6.8</b> – (a) Macroporous grid structures printed into 0.5% w/v agar 4 mM CaCl <sub>2</sub> baths, (b) released grid structures with residual fluid gel trapped within pores .....	138
<b>Figure 6.9</b> – Comparison of nozzle diameter on line thickness and pore size, (a) grid printed with 30g nozzle, (b) grid printed with 25g nozzle.....	140
<b>Figure 6.10</b> – Macroporous grids printed with honeycomb infill patterns, printed with infill densities from 10% to 30% in 5% increments .....	141
<b>Figure 6.11</b> – Honeycomb infill patterned grids printed with 30g nozzle and an infill density of 30% to create tiny pores with trapped agar fluid gel.....	142
<b>Figure 6.12</b> – Noses printed using the developed agar support bath; prints were conducted in a vertical orientation and produced noses with a high print quality.....	144
<b>Figure 6.13</b> – Agar fluid gel bath-printed macroporous nose structure (a) immersed within water to show pores, (b) out of water to show structure.....	145
<b>Figure 6.14</b> – Agar support bath-printed ear (a) encapsulated within supportive medium, (b) post-release.....	146
<b>Figure 6.15</b> – Agar support bath-printed ear (a) immersed within water to show pores, (b) out of water to show structure .....	147
<b>Figure 6.16</b> – Agar support bath-printed bucky-ball (a) during printing, (b) post-printing, (c) post-release immersed in water, (d) self-standing out of water .....	149
<b>Figure 6.17</b> – Support bath-printed simplified Eiffel tower model (a) in an inverted orientation within the medium post-print, (b) self-standing post-release .....	151
<b>Figure 6.18</b> – Print quality comparison of a nose printed using (a, c) the quiescently gelled gelatine support bath and (b, d) the agar fluid gel support bath.....	152

<b>Figure 6.19</b> – An Eiffel tower structure (a) encapsulated within the developed agar fluid gel support bath before (b) and after release, compared with a helical structure (c) encapsulated within an agarose sheared gel before (d) and after release [133] .....	154
<b>Figure 7.1</b> – Clarity assessment of constituents on their own: (top row) viscosity modifiers (a) water, (b) 2% w/v GG, (c) 2% w/v CMC, (bottom row) agar fluid gel at concentrations (d) 0.5%, (e) 1%, (f) and 2% w/v.....	157
<b>Figure 7.2</b> – Printability assessment into each constituent on its own: (top row) viscosity modifiers (a) water, (b) 2% w/v GG, (c) 2% w/v CMC, (bottom row) agar fluid gel at concentrations (d) 0.5%, (e) 1%, (f) and 2% w/v .....	158
<b>Figure 7.3</b> - Printability assessment into each constituent on its own: (top row) viscosity modifiers (a) water, (b) 2% w/v GG, (c) 2% w/v CMC, (bottom row) agar fluid gel at concentrations (d) 0.5%, (e) 1%, (f) and 2% w/v.....	159
<b>Figure 7.4</b> – Clarity assessment of various mixtures of 0.5% w/v agar fluid gel with water, GG, and CMC .....	160
<b>Figure 7.5</b> - Clarity assessment of various mixtures of 1% w/v agar fluid gel with water, GG, and CMC .....	160
<b>Figure 7.6</b> - Clarity assessment of various mixtures of 2% w/v agar fluid gel with water, GG, and CMC .....	161
<b>Figure 7.7</b> – Printability assessment of various mixtures of 0.5% w/v agar fluid gel with water, GG, and CMC .....	163
<b>Figure 7.8</b> - Printability assessment of various mixtures of 1% w/v agar fluid gel with water, GG, and CMC .....	163
<b>Figure 7.9</b> - Printability assessment of various mixtures of 2% w/v agar fluid gel with water, GG, and CMC .....	164
<b>Figure 7.10</b> - Invertibility assessment of various mixtures of 0.5% w/v agar fluid gel with water, GG, and CMC .....	167
<b>Figure 7.11</b> - Invertibility assessment of various mixtures of 1% w/v agar fluid gel with water, GG, and CMC .....	167
<b>Figure 7.12</b> - Invertibility assessment of various mixtures of 2% w/v agar fluid gel with water, GG, and CMC .....	168
<b>Figure 7.13</b> – Nozzle deflection assessment of 25g nozzles moving through 0.5%, 1%, and 2% agar fluid gel baths compared to optimised 3:1 ratio agar/water support bath	171
<b>Figure 7.14</b> – Nozzle deflection assessment of 27g nozzles moving through 0.5%, 1%, and 2% agar fluid gel baths compared to optimised 3:1 ratio agar/water support bath	171

<b>Figure 7.15</b> – Nozzle deflection assessment of 30g nozzles moving through 0.5%, 1%, and 2% agar fluid gel baths compared to optimised 3:1 ratio agar/water support bath	172
<b>Figure 7.16</b> – Impact of CaCl <sub>2</sub> concentration and distribution between continuous/gel-phase in developed 3:1 agar fluid gel/water support baths with 25g nozzles post-print	174
<b>Figure 7.17</b> - Impact of CaCl <sub>2</sub> concentration and distribution between continuous/gel-phase of developed 3:1 agar fluid gel/water support baths with 25g nozzles post-release	174
<b>Figure 7.18</b> - Impact of CaCl <sub>2</sub> concentration and distribution between continuous/gel-phase of developed 3:1 agar fluid gel/water support baths with 30g nozzles post-print	175
<b>Figure 7.19</b> - Impact of CaCl <sub>2</sub> concentration and distribution between continuous/gel-phase of developed 3:1 agar fluid gel/water support baths with 30g nozzles post-release	175
<b>Figure 7.20</b> – Impact of 0 mM CaCl <sub>2</sub> agar fluid gels mixed with 10 mM and 20 mM CaCl <sub>2</sub> at various mixing ratios on macroporous cylindrical structures post-print	177
<b>Figure 7.21</b> - Impact of 0 mM CaCl <sub>2</sub> agar fluid gels mixed with 10 mM and 20 mM CaCl <sub>2</sub> at various mixing ratios on macroporous cylindrical structures post-release	178
<b>Figure 7.22</b> - Impact of 10 mM CaCl <sub>2</sub> agar fluid gels mixed with 10 mM and 20 mM CaCl <sub>2</sub> at various mixing ratios on macroporous cylindrical structures post-print	178
<b>Figure 7.23</b> - Impact of 10 mM CaCl <sub>2</sub> agar fluid gels mixed with 10 mM and 20 mM CaCl <sub>2</sub> at various mixing ratios on macroporous cylindrical structures post-release	179
<b>Figure 7.24</b> - Impact of 20 mM CaCl <sub>2</sub> agar fluid gels mixed with 10 mM and 20 mM CaCl <sub>2</sub> at various mixing ratios on macroporous cylindrical structures post-print	179
<b>Figure 7.25</b> - Impact of 20 mM CaCl <sub>2</sub> agar fluid gels mixed with 10 mM and 20 mM CaCl <sub>2</sub> at various mixing ratios on macroporous cylindrical structures post-release	180
<b>Figure 7.26</b> – Macroporous sphere printed into the developed agar fluid gel/water support bath at 3:1 mixing ratio, shown (a) suspended within the support bath, (b) top-down view showing with visible pores, (c) structure after release	183
<b>Figure 7.27</b> – Cylindrical structure post-release from the developed agar fluid gel/water support baths at 3:1 mixing ratio, shown (a) self-supporting with residual fluid gel trapped inside, (b) held under a light to makes pores visible	184
<b>Figure 7.28</b> – Stacked pyramid structure shown (a) printed in an inverted orientation, (b) top-down view post-print, (c) isometric view of released structure, (d) front view of released structure	184

<b>Figure 7.29</b> – Human brain model printed within developed agar fluid gel/water support bath at 3:1 mixing ratio; red dye is added to highlight the brain’s morphology.....	185
<b>Figure 7.30</b> – Human heart model printed within the developed agar fluid gel/water support baths at 3:1 mixing ratio, shown (a) the large support bath, (b) top-down view of the heart post-print in a horizontal orientation showing its internal honeycomb infill structure, (c) heart successfully released from its support, (d) heart immersed in water .....	186
<b>Figure 7.31</b> – Comparison of a brain printed into (a) the developed agar fluid gel and (b) FRESH V1.0 [134], (c) and a heart printed into the developed agar fluid gel and (d) FRESH V2.0 [136].....	189
<b>Figure 8.1</b> – Photograph of the developed RepRap-inspired 3D bioprinting platform	191
<b>Figure 8.2</b> – Overview of gelatine bath process: (a) gelatine solution is poured into a container and stored in a fridge, (b) once gelled, 0.8% w/v gelatine baths will be invertible and exhibit elastic-dominant behaviour, (c) printing into such baths can produce (d) thin tubes, (e) branched blood vessel-like structures, (f) and noses.....	192
<b>Figure 8.3</b> – Overview of agar fluid gel support bath process: (a) gelled puck of agar is blended (b) until smooth and may be mixed with a secondary solution or used as is and (c) poured into a container for printing structures like (d) Eiffel towers, (e) human brains, (f) and human hearts.....	194
<b>Figure A.1</b> – Process of effective hydrogel mixing with Cellmixer unit: (a) hydrogel is dispensed to force air out of unit, (b) one channel is blocked to allow hydrogel flow into other channel, (c) other channel is blocked to allow hydrogel flow into primary channel, (d) cell-laden syringe (green dye solution in figure) is fitted onto unit and filled with hydrogel, (e) material passed througuh unit multiple times (f) for homogeneous mixing .....	198
<b>Figure B.1</b> – Generation of X and Y positional data using the g-code generating Excel spreadsheet.....	202
<b>Figure B.2</b> – Generation of Z-axis positional data using the g-code generating Excel spreadsheet.....	203
<b>Figure B.3</b> – Start and end scripts generated using the g-code generating Excel spreadsheet.....	204
<b>Figure B.4</b> – Compiling custom g-code with generated X/Y/Z data using the g-code generating Excel spreadsheet (excerpt taken after start script).....	205

<b>Figure C.1</b> – (a) RAMPS 1.4 microcontroller board is installed onto the frame on the left-hand side of the printer, (b) using 3D printed mounts which matches the beam’s and microcontroller’s profiles.....	207
<b>Figure C.2</b> – (a) Front view of LCD2004 screen, (b) mounted to the front of the frame with rotatable 3D printed fittings which matches the beam’s and screen’s profiles.....	208
<b>Figure C.3</b> – 3D printed endstop mounts which clamps around linear rods along the (a) Y-axis, (b) and Z-axis .....	209
<b>Figure C.4</b> – 3D printed mounts for affixing stabilising feet onto the bioprinter’s frame; (a) there are two ‘corner’ pieces (b) and a single ‘flat’ piece to triangularly align the feet positions .....	210
<b>Figure D.1</b> – Configured basic settings in Marlin firmware .....	212
<b>Figure D.2</b> – Configured pin definitions within the Marlin firmware .....	213
<b>Figure D.3</b> – Configured thermal settings within Marlin firmware .....	215
<b>Figure D.4</b> – Configured positional/directional settings within Marlin firmware .....	216
<b>Figure D.5</b> - Configured axis steps per mm within the Marlin firmware.....	218
<b>Figure D.6</b> – Configured LCD2004 settings within Marlin firmware .....	218



## Nomenclature

<b>µm</b>	Micrometre (measure of distance)
<b>2D</b>	Two-Dimensions/Two-Dimensional
<b>3D</b>	Three-Dimensions/Three-Dimensional
<b>ABS</b>	Acrylonitrile Butadiene Styrene
<b>BaCl<sub>2</sub></b>	Barium Chloride
<b>CaCl<sub>2</sub></b>	Calcium Chloride
<b>CAD</b>	Computer Aided Drawing
<b>cc</b>	Cubic Centimetres (measure of volume)
<b>CKD</b>	Chronic Kidney Disease
<b>CLIP</b>	Continuous Liquid Interface Production
<b>CMC</b>	Carboxymethylcellulose
<b>CNC</b>	Computer Numerically Controlled
<b>CO<sub>2</sub></b>	Carbon Dioxide
<b>CT</b>	Computerised Tomography
<b>DC</b>	Direct Current
<b>dECM</b>	Decellularised Extracellular Matrix
<b>DIY</b>	‘Do-It-Yourself’
<b>DNA</b>	Deoxyribonucleic Acid
<b>DXF</b>	Drawing Exchange Format (file format)
<b>ECM</b>	Extracellular Matrix
<b>EDTA</b>	Ethylenediaminetetraacetic Acid
<b>FBS</b>	Foetal Bovine Serum
<b>FDA</b>	Fluorescent Diacetate
<b>FDM</b>	Fused Deposition Modelling
<b>FFF</b>	Fused Filament Fabrication
<b>FRESH</b>	Freeform Reversible Embedding of Suspended Hydrogels
<b>GeIMA</b>	Gelatine Methacrylate
<b>GG</b>	Guar Gum
<b>HeLa</b>	Cervical Cancer Cells

<b>HepaRG</b>	Human Bipotent Progenitor Cell Line
<b>hESCs</b>	Human Embryonic Stem Cells
<b>hiPSCs</b>	Human Induced Pluripotent Stem Cells
<b>HLCs</b>	Hepatic Liver Cells
<b>hMSCs</b>	Human Mesenchymal Stem Cells
<b>hMVECs</b>	Human Microvascular Endothelial Cells
<b>IDE</b>	Integrated Development Environment
<b>IR</b>	Infrared
<b>LCD</b>	Liquid Crystal Display
<b>LCST</b>	Lower Critical Solution Temperature
<b>LEV</b>	Local Exhaust Ventilation
<b>LIFT</b>	Laser Induced Forward Transfer
<b>ml</b>	Millilitre (measure of volume)
<b>mm</b>	Millimetre (measure of distance)
<b>mM</b>	MilliMolar (measure of concentration)
<b>mm/s</b>	Millimetres per second (measure of speed)
<b>NaHCO<sub>3</sub></b>	Sodium Bicarbonate
<b>NEMA</b>	National Electrical Manufacturers Association)
<b>PBS</b>	Phosphate Buffered Saline
<b>PCL</b>	Polycaprolactone
<b>PDMS</b>	Polydimethylsiloxane
<b>PEG</b>	Polyethylene-Glycol
<b>PI</b>	Propidium Iodide
<b>PLA</b>	Polylactic Acid
<b>PMMA</b>	Polymethyl Methacrylate
<b>PSU</b>	Power Supply Unit
<b>PVA</b>	Polyvinyl Alcohol
<b>RAMPS</b>	RepRap Arduino Mega Polulu Shield
<b>RPM</b>	Revolutions Per Minute (measure of angular velocity)
<b>RRT</b>	Renal Replacement Therapy
<b>SD</b>	Secure Digital
<b>SLA</b>	Stereolithography (printing)
<b>SLS</b>	Selective Laser Sintering
<b>SMD</b>	Surface Mount Device

<b>STL</b>	Stereolithography (file format)
<b>UCST</b>	Upper Critical Solution Temperature
<b>UK</b>	United Kingdom
<b>USB</b>	Universal Serial Bus
<b>UV</b>	Ultraviolet
<b>VREF</b>	Voltage Reference
<b>w/v</b>	Ratio of Solute Weight to Solvent Volume (measure of concentration)

## List of Publications

1. **I. MacKenzie**, G. Skeldon, X. Kong, W. Shu. A Quiescently Gelled Gelatine Supportive Medium to Facilitate 3D Biofabrication, *International Conference on Biofabrication*, Germany (2018), Oct 28<sup>th</sup> – Oct 31<sup>st</sup> (oral presentation)
2. **I. MacKenzie**, G. Skeldon, X. Kong, W. Shu. A Quiescently Gelled Gelatine Supportive Medium to Facilitate 3D Soft Tissue Biofabrication, (paper in preparation)
3. **I. MacKenzie**, G. Skeldon, X. Kong, W. Shu. Simple Agar Fluid Gels to Support Fabrication of Complex Structures, (paper in preparation)

## Chapter 1 – Introduction

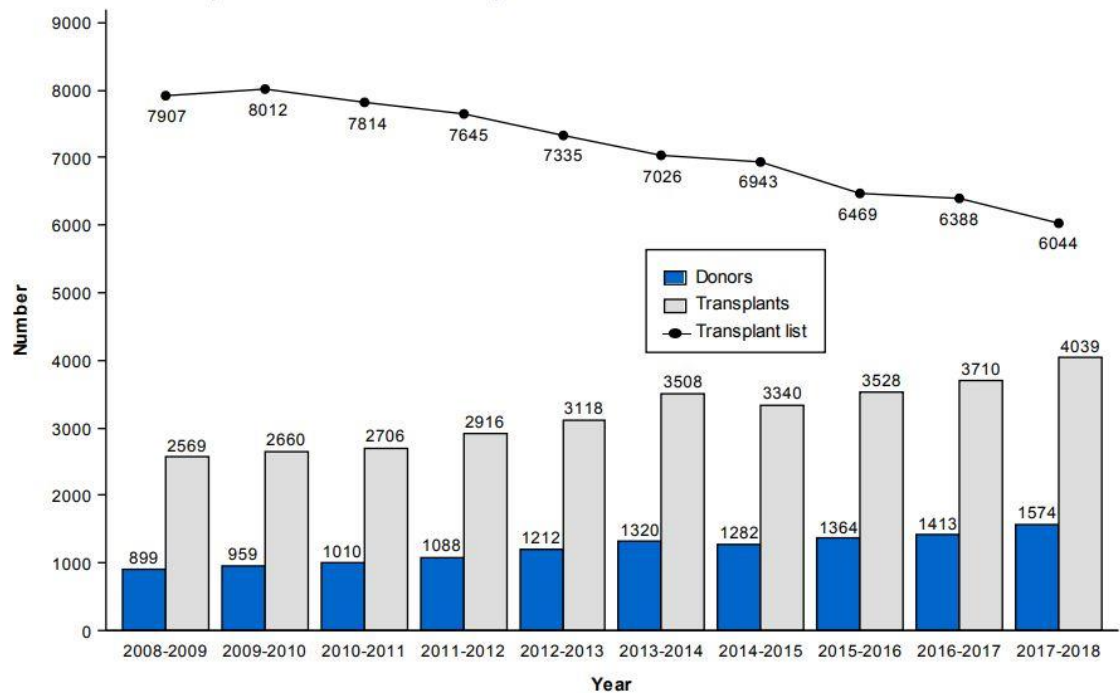
One of the most prevalent issues facing modern society is the deterioration of health. An aging society wherein its citizens are living longer will inevitably be met with health complications pertaining to old age. Type-1 diabetes for example, a disease characterised by the inability of the pancreas to produce the correct amount of insulin to control the level of glucose present in the blood; without appropriate care, the afflicted can become subject to a myriad of debilitating conditions such as blindness (diabetic retinopathy) [1], stroke, and even death as a result of kidney failure (nephropathy) [2]. In the latter case, an organ transplant may be the only solution available to save the life of such patients. This is just a single case; there are many who are currently suffering from life-threatening illnesses and are depending on organ transplantation to save their life.

Medical resources are heavily strained in the face of challenges imposed by an aging population; the cost of healthcare is strongly related to an increased patient age [3]. Individuals of better health do not incur the same level of expense as individuals of poorer health or terminal decline [4]. An example of such would be elderly patients afflicted by chronic kidney disease (CKD) which is attributed to by various precursory risk factors such as hypertension and cardiovascular disease [5]. To treat chronic kidney disease, renal replacement therapy (RRT) may be used; however RRT only accounted for 2% of the patient population afflicted by CKD in the England during the 2009-2010 period, yet it occupied more than half of the estimated £1.23 billion spending on CKD care [6].

With reference to figure 1.1 the discrepancy between the transplant waiting list, the number of donors, and the number of transplant operations in the UK is gradually being addressed and hence the supply of organs suitable for transplantation is converging towards their demand. This positive trend could possibly be attributed to the various initiatives set up to encourage more people to consider organ donation, such as the Organ Donation Task Force in 2006 whose objective was to identify and find solutions to the barriers faced by organ donation in response of the fact that, at the time, the UK had one of the lowest rates of organ donation in the developed world [7]. Despite this, there still remains a deficit and thus a greater demand than supply of available organs. Some identified barriers which prevent a donor from donating their organs include refusal from the bereaved irrespective of the deceased donor's wishes, religious or

cultural beliefs, the perception of loved ones being ‘cut up’ and their organs ‘harvested’, a lack of faith with healthcare systems, and a lack of knowledge about organ donation [8][9]. Whilst the trend over the past decade would suggest that these barriers are slowly being overcome and are likely to continue doing so, there remains the possibility that the discrepancy between organ donor and patient could increase again. Another problem faced by an aging population is the diminishing suitability of organs donated from donors which themselves are older on average [10]. Additionally, the suitability of organs is also impacted by an increase in the donor’s weight [10], whereby approximately a quarter of the UK’s adult population is obese, and 61.7% are either overweight or obese [11], and therefore is statistically likely to affect a significant proportion of the aforementioned donors which are of an average older age.

**Figure 2.1** Number of deceased donors and transplants in the UK, 1 April 2008 - 31 March 2018, and patients on the active transplant list at 31 March



**Figure 1.1** - The number of organ donors, number of patients on the transplant list, and the number of transplantations over the course of a decade between 2008 and 2018 [12]

A potential solution to address these issues lies within the field of biofabrication, or 3D bioprinting. Should the fabrication of human scale and functional organs be realised, then the demand for organs could be alleviated. This would impart a number of benefits such as theoretically eliminating the reliance on a suitable donor becoming available as the organ(s) could be fabricated on a ‘make-to-order’ basis. The suitability of bioprinted organs could also be better as they could be fabricated using the patient’s

own cells and thus overcomes the risk of inducing immunological rejection of a donor's organ [13] – whilst this is speculative, it is reasonable as the patient's own cells may be less likely to be considered foreign by the body's immune system.

Creating fully functional organs that are suitable for transplantation may well be considered the ultimate goal of biofabrication and tissue engineering research, but there remain a number of key technological challenges (such as the fabrication of vascular networks [14]) before such a goal may be realised. A more realistic shorter-term goal of the technology would be to fabricate personalised 3D tissue models, derived from a patient's own cells, to test the efficacy of new drugs and check for any adverse biological response before assessing if such treatment is appropriate for the patient. Modern studies testing the efficacy of new drugs are often based on 2D models which have been shown to translate poorly into 3D [15], and is one reason why new drugs look promising on paper but fail to make it through to into medical practice.

3D printing has shown its viability in the medical field in a plethora of aspects ranging from plastic and reconstructive surgery [16], creating patient specific anatomical models for surgeons to plan how best to conduct an operation as well as for medical training [17], and for creating low-cost medical prostheses [18]. However the distinction that bioprinting makes over more traditional medical 3D printing practices is the production of anatomical models which not only look like organs, but also performs the same biological functions as the organ being replicated.

## Chapter 2 – Literature Review

### 2.1 Introduction

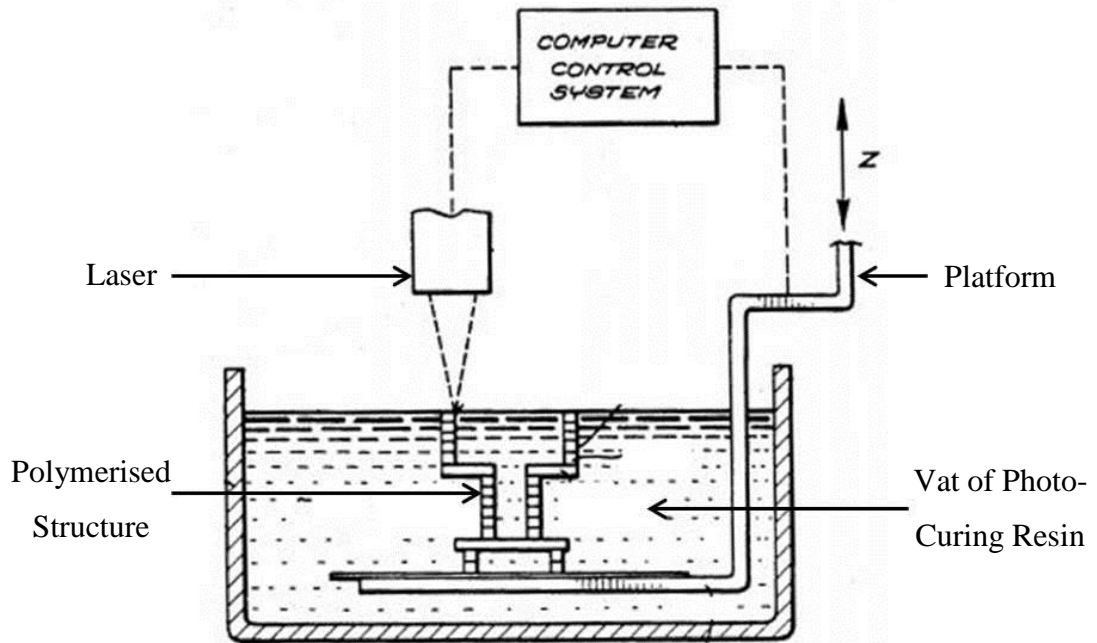
To further expand upon bioprinting as an emerging engineering discipline, a literature review is conducted to describe the key technologies involved in the fabrication of biological structures. The literature review will also discuss various supportive methods to bring into context the range of techniques which may be employed to fabricate soft tissue-like structures with soft materials which are otherwise mechanically insufficient to replicate complex anatomical models at human-relevant scales. Lastly, some suitable biomaterials commonly used in bioprinting practice will also be discussed.

### 2.2 Development of 3D Printers

#### 2.2.1 *A brief history of 3D printing*

In the 1980s it was realised that the traditional, subtractive approach to manufacturing whereby raw material in the form of a block may be reduced via cutting, drilling, milling, etc., to fabricate components [19], was not the only fabrication strategy available to industry; the inverse process, additive manufacturing, is the creation of objects through the strategic and repeated layering or addition of material to create 3D objects [20]. The earliest patent for a 3D printing system, developed by Charles Hull, was a light-based (stereolithography or STL) machine (figure 2.1) which fabricated objects from photo-curable resins which were solidified, or polymerised, via exposure to ultraviolet light [21][22]. Amongst the light-based approach, patents for other fabrication strategies began to emerge in the following years such as selective laser sintering (SLS) [23], fused deposition modelling (FDM) [24], and laminate object manufacturing (LOM) [25] in 1988, 1989, and 1994 respectively, further expanding upon the range of additive manufacturing techniques which fall under the umbrella term ‘3D printing’. However, the price of additive manufacturing machines as well as their perceived value was very high due to the technology being so new at the time [26].





*Figure 2.1 – Schematic of the first 3D printer, developed by Charles Hull in 1983 and subsequently patented in 1984 [27]*

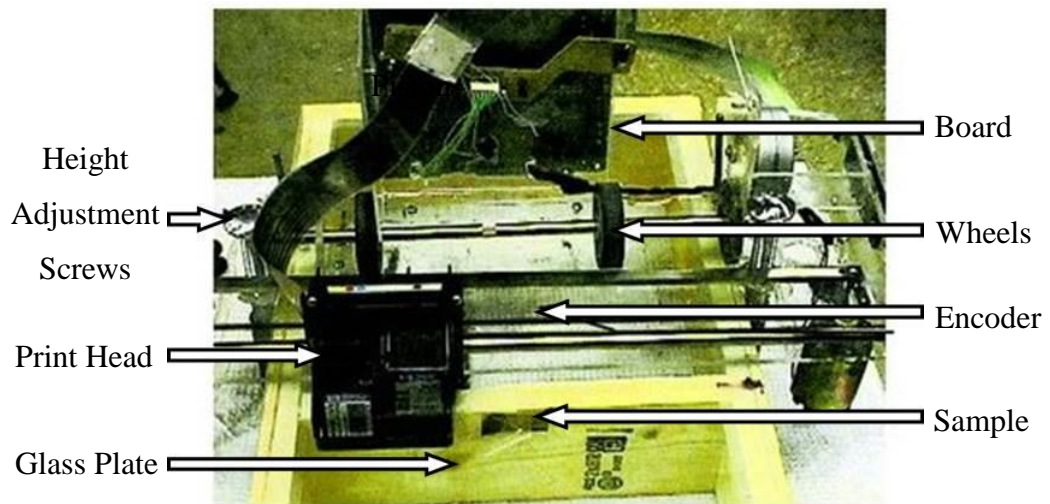
Whilst the world of 3D printing was expanding and the technology continued to develop over the years since, it did so quietly - that was until the dawn of the RepRap project in 2005 [28]. The RepRap project played a key role in bringing 3D printing technology to the masses through the documentation of an “open-source self-replicating rapid prototyping machine” [29] i.e. the development of a 3D printer which can print 3D printers, which can then print more 3D printers and so forth. The designs of developed RepRap machines were made publicly available through the project’s blog [30] which, in conjunction with the open-source license, allowed the everyday enthusiast to create their own RepRap machine at home. It could be argued that that the RepRap project’s approach to increasing accessibility was twofold: accessibility was granted via the distribution of the designs freely worldwide through the internet, as discussed, but further accessibility was achieved by minimising the cost of the machine to help further bring the technology to the consumer level. Aside from the 3D printed components, the designs of the machines were generally based around easily acquirable and cheap standardised components such as the fastenings and linear rods thus the cost of the machine could be minimised. After Crump’s FDM patent expired in 2009 [24], vendors began to sell 3D printers and 3D printer kits based on the various RepRap designs [31]. Even with third party vendors selling RepRap kits or pre-built machines, the cost of RepRap-based FDM 3D printers ranged from \$699 to \$2000 (£565 to £1617) between

the years 2009 and 2011, depending on the model and vendor, whereas other machines around the same time cost up to \$200,000 (£161,780) depending on the specific fabrication method; however other similar FDM-based options were available for between \$1749 to \$3000 (£1414 to £2426) [31]. Whilst the trend was that FDM-based machines were generally the cheaper modality, RepRap-based FDM machines could be produced at the lowest cost despite being sold from a vendor which would include their own mark-up in the sale price for profit.

Aside from the typically low cost of RepRap-based 3D printers, RepRaps can be considered as highly customisable machines which can be tailored to suit a particular aspect of 3D printing. Again, the development of RepRap machines was largely facilitated by the global RepRap community sharing their inputs to optimise the performance of such machines. Whilst traditional RepRap machines such as the Mendel print thermoplastic-based structures using the FDM approach, RepRaps themselves are not necessarily limited by this so long as new innovations can be made compatible with the rest of the machine - the open-source nature of RepRaps has encouraged 3D printing enthusiasts to create a multitude of 'out of the box' solutions to various low-cost fabrication challenges. Solely changing the extruder of a RepRap-based machine can facilitate the extrusion of materials with vastly different material properties to thermoplastics, including wax [32], dough [33], chocolate [34], caulk [35], silica gel [36], and metal [37]. However the extruder is but a single component of a functional 3D printer – the rest of the printer is open to modification too. The RepRap methodology can be applied to create functional 3D printers using Lego as the construction material [38], highlighting the overall modularity of the RepRap approach.

The first record of a customised machine to facilitate the deposition of cells occurred in 2003 – a commercial inkjet printer, instead of being loaded with colourful inks for printing images onto sheets of paper, was instead loaded with living cells and printed (figure 2.2) [39]. This very experiment is often considered the first example of what is now the field of 'bioprinting', that is the spatial deposition of living cells and biological material in a controllable manner. Whilst this bioprinter existed before the RepRap project was formed, it highlights just how a machine may be modified to achieve a specific research objective; the same concept may be applied to RepRap-based 3D printers. Such machines have been readily modified over the years to print with a wide range of different materials as discussed earlier, including a multitude of biomaterials and cell types to bioprint various tissues. Extrusion-based bioprinting approaches are

commonly adopted by RepRap-based 3D printers [40][41][42][43]; the method's popularity is possibly related to the fact that the method requires relatively few modifications to the original FDM-based design and can be done so at a low cost. Other printing methods have been successfully integrated into RepRap-based 3D printers such as inkjet [44] and valve [45] but are far less common than extrusion-based approaches.



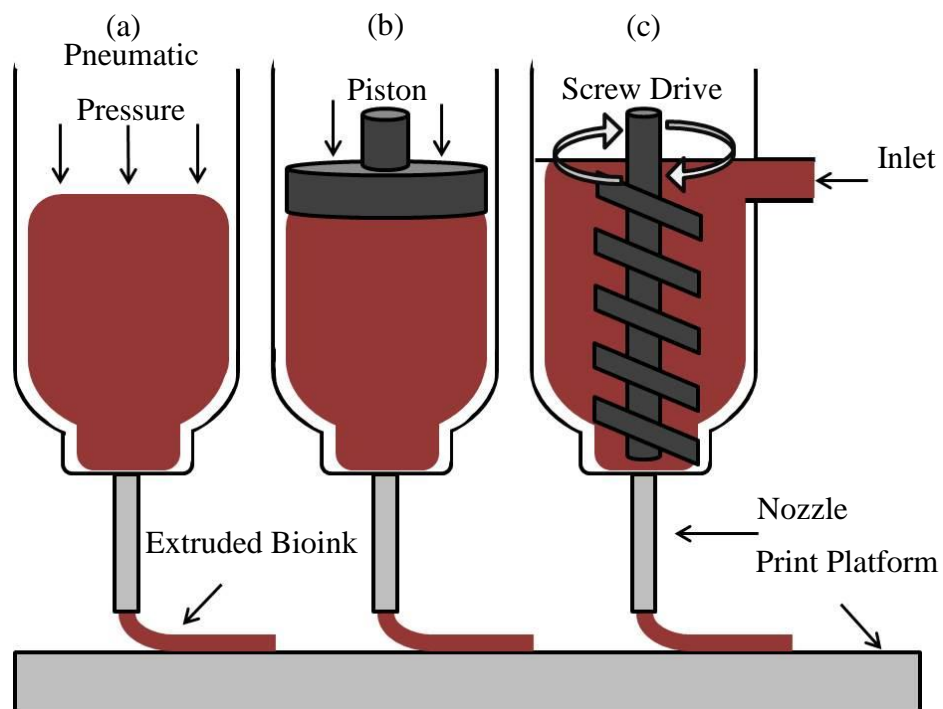
**Figure 2.2** – *The first printer customised for the purpose of printing cells, i.e. a ‘bioprinter’, developed by Thomas Boland in 2003 [39]*

Regardless of whether a 3D bioprinter is derived from the RepRap project or not, there exists a plethora of developed printing methods to accommodate the printing of live cells to create cellular constructs. Each method has desirable merits for bioprinting; any one method is not specifically better than another and therefore the suitability of a particular method depends on its context. Extrusion-based bioprinting as well as inkjet, valve, and light-based approaches will now be discussed further.

### **2.2.2 Extrusion-based bioprinting**

Extrusion-based bioprinters operate by forcing material through a nozzle using a syringe-pump to displace a piston [46], screw [47][48], pneumatic pressure [49][50] (figure 2.3), or combinations thereof for multi-nozzle systems [51], onto the printer's platform. The machines typically have three moving axes (X, Y, and Z) to control the relative position of the nozzle and the platform which enables the fabrication of various 3D cell-laden structures or scaffolds for cell-seeding approaches with various geometries. Each of the aforementioned extrusion methods is capable of handling materials with varying rheological qualities and precision. The pneumatic method can be subject to depositional delay due to the nature of the compressed air behind the

material [52] which takes time to depressurise post-extrusion, but are generally well suited for printing viscous molten thermoplastic material such as polycaprolactone (PCL) and polyethylene glycol (PEG), which have been used as primary and sacrificial materials respectively to create a cell-supporting porous scaffold [53]. Piston- and, for even more viscous materials, screw-driven approaches can cater to a range of material viscosities without the aforementioned depositional delay of pneumatic systems which may otherwise promote inconsistent and less accurate deposition of cellular material, particularly if the print is complex and requires many stop/start operations whereby material oozes out from the nozzle. Furthermore, certain piston- and screw-driven systems can offer better depositional control as the drive direction can be reversed to pull back material, alleviating the build-up of pressure and prevents oozing.



**Figure 2.3** - schematic diagram of (a) pneumatic, (b) piston, (c) and screw-driven extrusion bioprinting, adapted from [54]

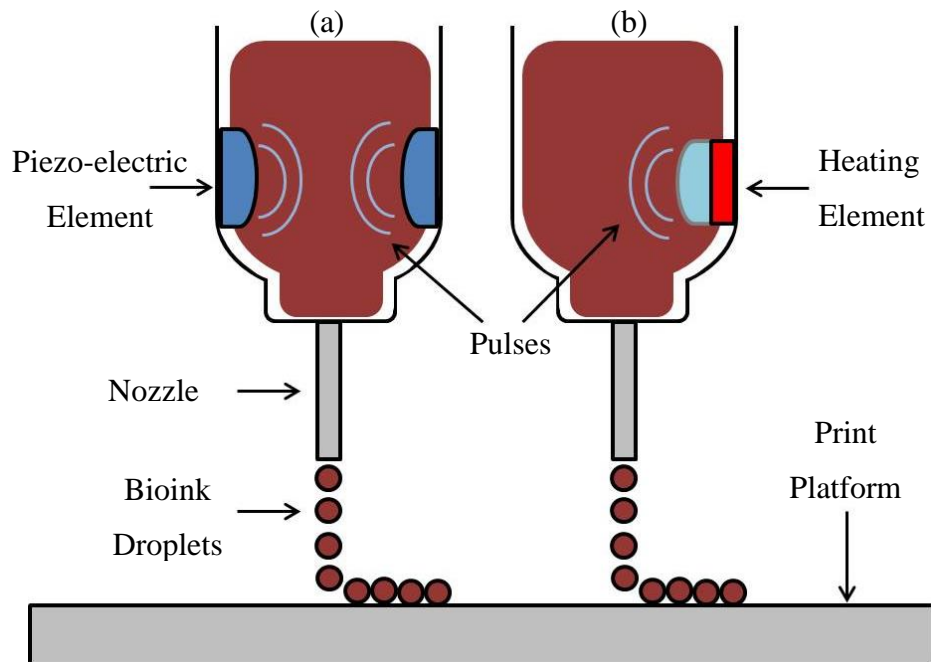
Extrusion-based bioprinting technologies are commonly regarded as a promising method for fabricating biostructures at the necessary scales at a reasonably fast fabrication speed. The justification can be made based on the method's ability to extrude a range of semi-rigid hydrogels and composites which are self-supported post-deposition, enabling the subsequent and quick layering of cell-laden inks [50][55][56]. The technology is also able to extrude high cell density inks and cell aggregates [57][58] - the fabrication of structures with physiologically similar cell densities is one

of multiple key challenges in producing functional organs [59]. The print resolution can be controlled significantly by changing the size of the printing nozzle; the diameter of extruded hydrogel filament is related to the internal diameter of the nozzle used thus a smaller nozzle results in the deposition of finer lines of extrudate. Typical commercially available nozzles are based on the Birmingham gauge wire system may range from 14 to 33 gauge in size which corresponds to an internal diameter 1.6 millimetres and 110 micrometres respectively [60], although nozzles with non-standard sizes and geometries can be custom-made to suit the application. However as the demand increases for higher resolution printing with high cell density inks, it becomes more difficult to extrude materials of such viscosity and induces large shear stresses which is harmful to cells [61]. This is in part responsible for restricting the resolution of extrusion-based technologies. Opting for a less viscous bioink in order to extrude through a finer nozzle is also problematic as the gel becomes more susceptible to lateral spreading which leads to the production of weaker structures with poorer shape fidelity [62] – for such reasons, extrusion-based bioprinting may be considered less resolute than other available methods of biofabrication.

### ***2.2.3 Inkjet-based bioprinting***

Inkjet-based bioprinting, whether achieved thermally [63] or piezo-electrically [64] (figure 2.4), involves the generation of a pulse to eject very small volumes of material precisely through a nozzle onto a substrate to create biostructures in a drop-by-drop manner. Thermal-based inkjet printing employs heat to rapidly vaporise ink near to the heating element inside the printhead, creating a pressure bubble which ejects material out from the nozzle [65]; piezo-electric inkjet systems produce the pulses mechanically to send shock waves through the ink for ejection to occur [54]. One concern between the two methods is related to the viability of cells during the pulse generation. Some researchers were concerned that the heat of thermal-based inkjet printers could be an unwanted stressor to cells [66] but this was later shown to not affect cell viability in a significant manner [67] when the frequency was kept low. This is not to say that piezo-electric printers are necessarily better for cell viability – the sonic pulses generated from the rapid actuation of the piezo-electric element is akin to sonication (ultrasonic disintegration), which at high enough frequencies can disrupt cells and cause them harm [68], encouraging the use of lower frequencies hence slower droplet generation rates and power to ensure that cell viability is maintained [63]. However, thermal inkjet printers have an additional material constraint when compared to piezo-electric printers:

on top of having a sufficiently low viscosity and surface tension [69], the material also needs to have a compatible nucleation temperature in order for pulse generation to succeed [70].



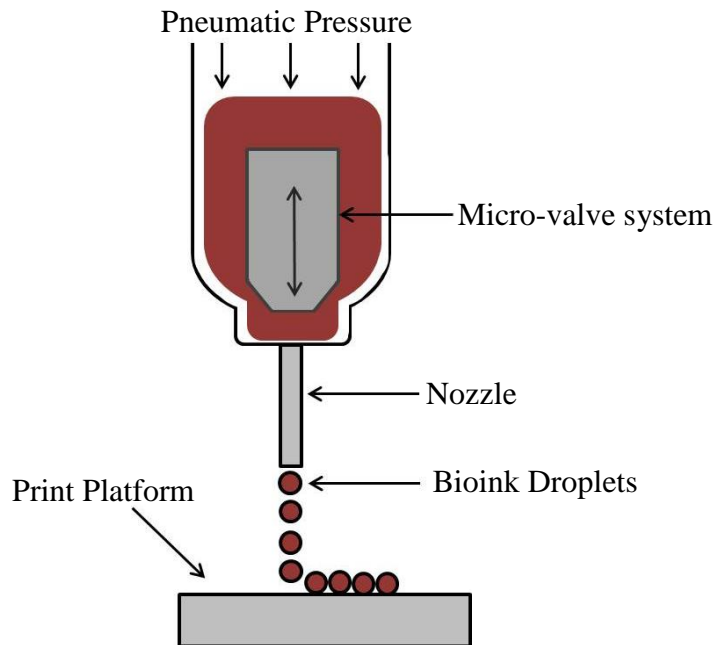
**Figure 2.4** - Schematic diagram of two inkjet-based bioprinting methods - (a) piezoelectric and (b) thermal, adapted from [71]

Inkjet machines are renowned for being the earliest bioprinting technology and their ability to print at a high resolution due to the small size of the ejected droplets. Inkjet printers can generate droplets up to a rate of 30kHz with droplet volumes and diameters generally in the range of 1 to 100 picolitres and 10 to 60 micrometres [72], although as previously discussed lower deposition frequencies, such as 1 kHz [73], are typically used to maintain cell viability. The caveat of using this method for high resolution printing is that the fabrication speed may be too slow to produce cellular structures within a cell-tolerable timescale. The fabrication of larger and stronger structures is commonly considered a key challenge faced by inkjet bioprinting and is primarily a consequence of the technology's inability to process stronger materials - crosslinking of the bioinks needs to occur post-deposition to avoid nozzle blockage [72]. This issue is further compounded when cell settlement occurs; the ink's low viscosity, a functional requirement of the technology as well as an inability to accommodate ink gelation prior to deposition, means that cells will sink to the bottom of the ink cartridge in a short time and accumulate at the nozzle and can lead to inconsistencies in the number of cells per droplet or nozzle blockage due to the settlement and aggregation of too many cells at

the outlet [74][75][76]. Furthermore, whilst this method's printing process is capable of maintaining a high cell viability, the cell density of inkjet bioinks is comparatively lower than other methods with cell densities in the order of  $10^6$  cells per millilitre [77][78].

#### ***2.2.4 Valve-based bioprinting***

Valve-based bioprinters are similar to inkjet-based technologies in that they are both drop-on-demand methods of fabrication; the main difference between the two methods is the employed mechanism for depositing material. In valve-based bioprinting systems droplets are generated electro-mechanically by opening and closing a microvalve, which are then ejected out from a nozzle with pneumatic pressure (figure 2.5) [71]. As a different mode of droplet generation is employed, valve-based bioprinting technologies circumvents the concerns over cell viability compared to both thermal and piezo-electric inkjet technologies in which their droplet generation methods could be detrimental to cells on account for the previously discussed heating or sonicating effects respectively. Valve-based bioprinting technologies may be considered to be a relatively gentle method when bioprinting cells [79], leading to its use when handling mechanically highly sensitive cell lines such as human embryonic stem cells (hESCs) in their pluripotent state [80] and human induced pluripotent stem cells (hiPSCs) which were later differentiated into hepatic liver cells (HLCs) without adversely affecting their viability [81]. To ensure that the cell viability is maximised by minimising the shear stress to cells, valve-based bioprinting approaches use low pneumatic pressures in conjunction with wider nozzles to those commonly used in inkjet machines, thus comparatively the valve-based method is usually slightly less resolute than thermal or piezo-electric inkjet bioprinting due to generating larger droplet sizes on average [82][83]. Additionally, the cell density of bioinks in valve-based technologies is in the relatively low range of  $10^6$  cells per millilitre [84] like inkjet-based approaches.



**Figure 2.5** - Schematic diagram of valve-based bioprinting, adapted from [71]

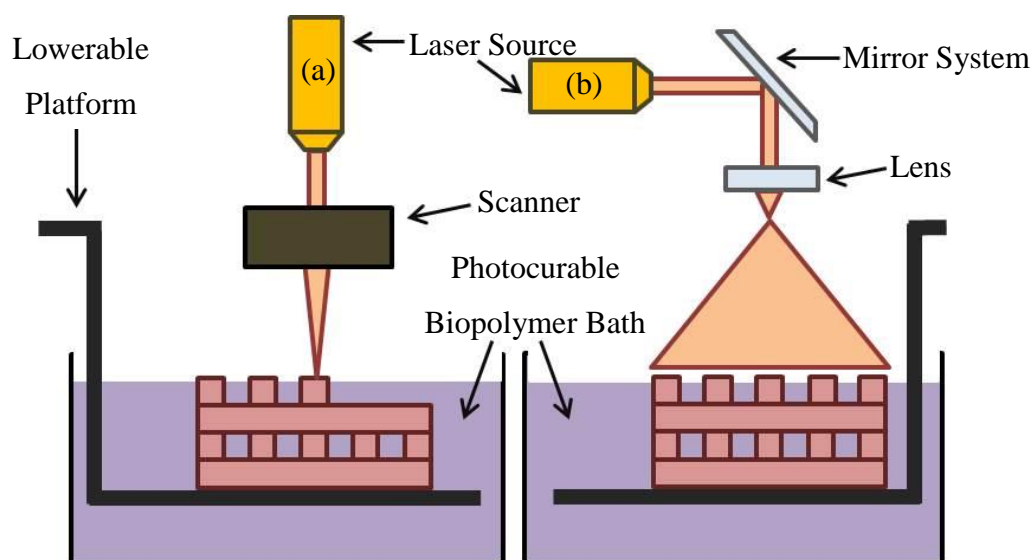
### 2.2.5 Light-based bioprinting

Light-based approaches also exist for the biofabrication of cellular structures. The particular application of lasers in light-based bioprinting depends on the method employed; light may be used to induce photopolymerisation such as in stereolithographic (SLA) bioprinting, or be used directly as a method to transfer droplets with cells onto a substrate such as in laser-induced forward transfer (LIFT) [85]. In both aforementioned light-based techniques, nozzles are not used as fabrication is achieved through the use of the laser itself and thus the technology avoids nozzle-related issues such as viscosity limitations, nozzle-induced shear stress on cells, and nozzle blockages [86].

In SLA bioprinting, cells are mixed with a photocurable biopolymer which is stored in a vat with a movable platform whilst either a projector or a laser crosslinks the bioink into the desired pattern (figure 2.6); subsequent layers are printed by lowering the platform further into the vat which allows bioink to flow over the top of the structure for crosslinking. Projection-based SLA systems can create structures quickly; each layer's cross-section is projected onto the bioink and crosslinks an entire layer at once, thus the fabrication speed is the same for every layer regardless of complexity. Therefore each layer can be fabricated quickly and the total print time is mostly dependent on the structure's thickness/total number of printed layers [87]. Accounting for this speed advantage, SLA technologies has great potential to print large biostructures of relevant



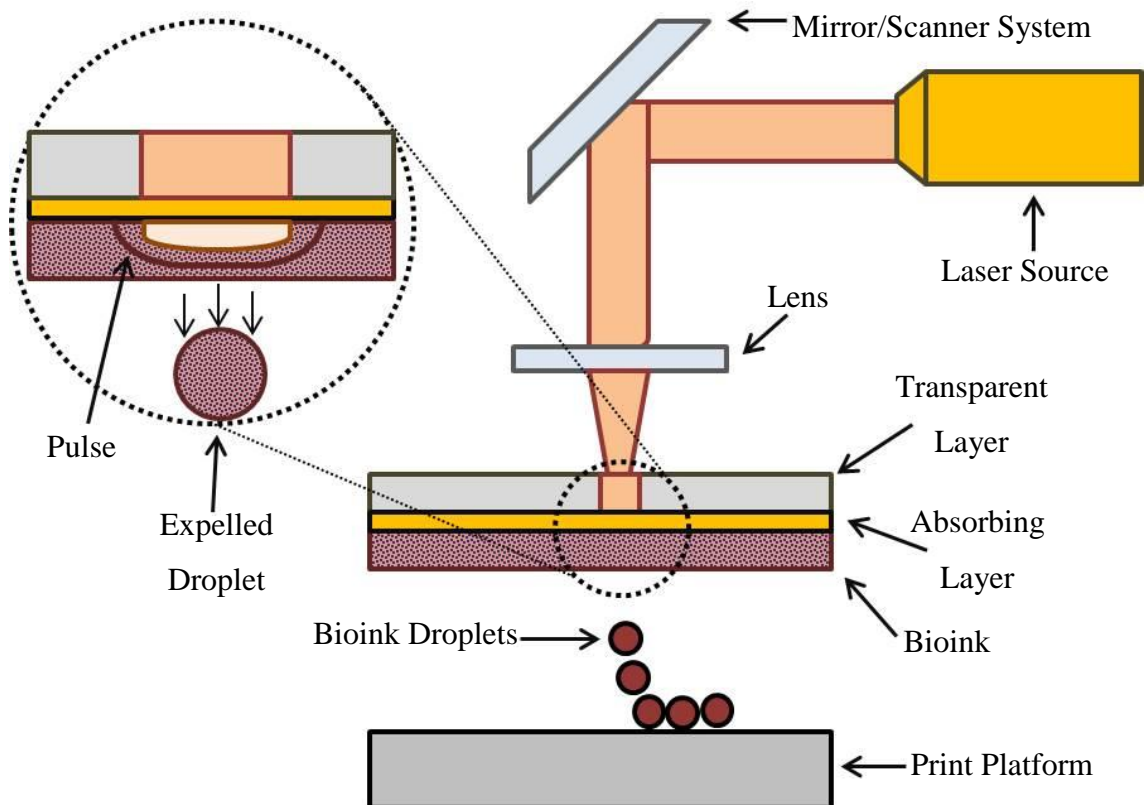
scales within a cell tolerable timeframe. A scanning laser-based SLA technology called ‘continuous liquid interface production’ (CLIP) has also shown very fast fabrication speeds with high resolution, printing structures with feature details less than 100  $\mu\text{m}$  in size [88] but this specific technology has not yet been integrated with cell work. With specific regards to SLA printing with cells, the strength of fabricated structures can be improved by incorporating photoinitiators [85] but many of these are not water soluble and thus require the use of unfavourably toxic organic solvents for their integration [89]. Additionally the range of photocrosslinkable materials which are also cell-compatible materials is limited, the technology is expensive to setup [90], and, aside from the use of potentially cytotoxic materials, the light itself such as ultraviolet (UV), visible blue light (or near UV light), and infrared (IR) can also impart cellular stress and damage [87][91][92][93], making the SLA method a less cell-friendly approach. Whilst the technology was eventually optimised to work with more cell-appropriate materials to bioprint cell-laden structures [94][89], the difficulty in maintaining cell viability may encourage the use of cell-seeding strategies [95][96][97] to circumvent problems such as the exposure of cells to cytotoxic environments and the laser itself. However adopting a cell-seeding biofabrication approach could also be considered disadvantageous biologically speaking; controlling cellular interactions, vascularisation, loss of less adherent cell types during perfusion, low seeding efficiencies, poor distribution of cells, difficulties controlling the positioning of various types of cells within the scaffold, and scaling up of the strategy are significant challenges faced by cell-seeding biofabrication approaches [98][99][100].



**Figure 2.6** - Schematic diagram of two SLA-based bioprinting method - (a) laser scanning and (b) projection, adapted from [101]

LIFT technology involves quite a different application of light compared to the SLA approach. LIFT uses the laser to generate gas pressure to propel droplets of cells from a ‘cell ribbon’ onto a substrate instead of being used directly to photocrosslink photopolymers (figure 2.7) [102]. The technology is perhaps more comparable to inkjet and valve-based printing methods in that LIFT is also a drop on demand technique, but differs specifically in the mechanism of droplet formation and ejects the droplets without nozzles. As discussed earlier, cells exposed directly to various types of light can be harmful; LIFT systems typically have a layer of laser energy absorbing material between a laser-transparent supportive layer and a cell-laden biomaterial layer [103] – these three layers make up the cell printing ribbon. The transparent and absorbing layers are positioned before the cells in order to protect them from light damage as well as provide the mechanism for producing the ejecting gas pressure. Despite the use of the absorbing layer, the viability of LIFT-printed cellular structures can be quite varied. Some literature state the use of lasers as primary detriment to cell viability via laser induced heat generation or exposure to the laser light [104] which perhaps may be a generalised statement of laser-based technologies as a whole; other literature has reported very high cell survival rates with LIFT specifically incorporating various types of cells, such as skin cells (fibroblasts/keratinocytes), human mesenchymal stem cells (hMSCs), and hiPSCs with 98%, 90% [105], and 94% [106] cell survival respectively. The print resolution of LIFT is very high and can achieve single-cell-per-droplet resolution using bioinks with cell densities in the order of  $10^8$  cells per millilitre [107].

However, like other laser-based methods, LIFT technology is expensive to set up. Furthermore the ribbon preparation process can be time consuming and even more-so if multiple ribbons are required for printing larger structures [86] in spite of the method's capability to fabricate at a relatively fast pace [108]. Unlike SLA bioprinting, LIFT is not restricted solely to the use of photopolymeric biomaterials; however LIFT can only process materials with a suitably low viscosity, therefore the technology may struggle to fabricate biostructures at a larger-scale [54].



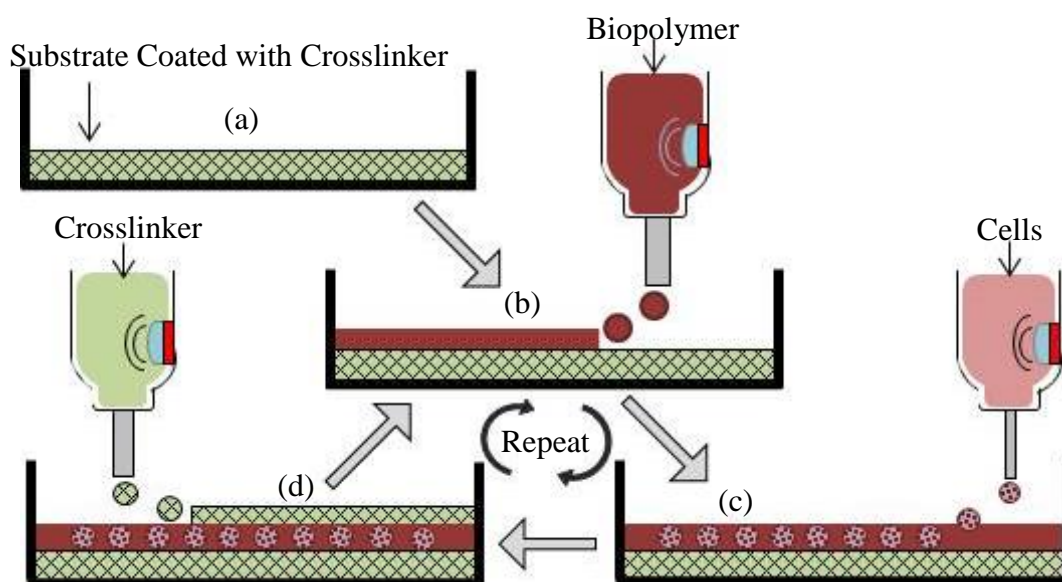
*Figure 2.7 - Schematic diagram of the LIFT bioprinting method, adapted from [109]*

### 2.3 Development of Supportive Fabrication Strategies

The origins and development of various 3D bioprinting modalities has been discussed. However, more recent developmental trends in the field of bioprinting tend to revolve around the convergence of multiple ideas and fabrication strategies. One such idea is the integration of supportive techniques to assist the fabrication of more geometrically complex structures with soft, low viscosity and low strength biomaterials which otherwise cannot retain their shape fidelity and limits their scalability.

Creating a method to crosslink extrudate during the fabrication process is an attractive development in bioprinting technologies, particularly for drop-on-demand techniques

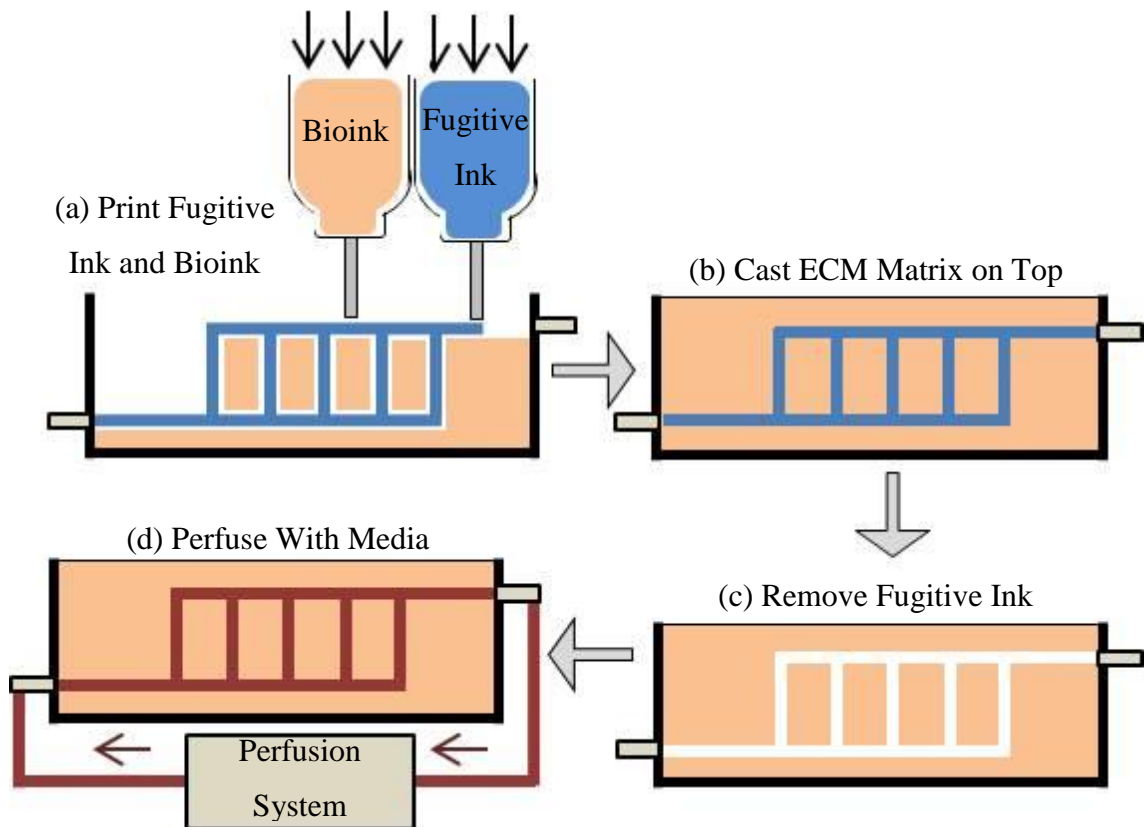
like inkjet and valve which can only process low viscosity inks with limited mechanical properties; incorporating a means of rapidly enhancing the mechanical properties of dispensed droplets could potentially translate to printing larger structures. One approach involves the deposition of bioinks onto substrates prepared with the crosslinker; when compatible bioinks are deposited onto the substrate, the bioink is immediately exposed to the crosslinker and the bioink undergoes gelation. Inkjet-bioprinting of human microvascular endothelial cells (HMVECs) in a thrombin/calcium chloride solution was capable of forming microvasculature by depositing the droplets onto a fibrinogen 'bio-paper' substrate and incubated thereafter to crosslink the fibrinogen [110]. A similar methodology has also been used in extrusion-based bioprinting - solutions of alginate have been extruded onto calcium substrates to fabricate 3D porous, fibroblast-laden matrices [111]. However these approaches are heavily restricted in fabrication capability – the more layers that are printed, the further away the crosslinking substrate is from newly deposited layers, meaning that the mechanical strength and shape fidelity of tall structures progressively deteriorates. Scaling this approach from single to multi-layered fabrication was achieved by using printed hydrogel layers as a substrate for subsequent layering. Collagen and skin cells were printed with a valve-based printer onto a sodium bicarbonate ( $\text{NaHCO}_3$ ) substrate; collagen is gelled via a change in pH and becomes rigid enough to support a new layer of  $\text{NaHCO}_3$ , which supports the next collagen/cell layer and so forth (figure 2.8) [112]. In the literature this method was shown to create structures with a thickness of 10 layers. However this technique is considerably more complex than the single-layered approach, involving the use of multiple nozzles in an alternating manner which lowers the fabrication speed; printing one layer requires the collagen, cells, and  $\text{NaHCO}_3$  to be dispensed one at a time. Furthermore the technique can only offer mechanical support whilst printing on top of previously crosslinked layers and cannot support more complex geometries like overhanging details.



**Figure 2.8** - Schematic of the substrate ‘stacking’ process, adapted from [112] - (a) substrate pre-coated with crosslinker, (b) printing of biopolymer layer, (c) printing of cell layer, (d) printing of new crosslinking layer. Steps (b), (c), and (d) are repeated to create stacked cellular structures

Another method developed to support biofabrication involved the use of a secondary ink material. In some works the secondary ink is designed to coexist with the primary ink to provide long-term mechanical support; in other works the secondary ink is considered to be ‘sacrificial’ or temporary with the intention being removed at a later time and therefore offers short-term support. The rationale behind this approach is identical as its application in traditional thermoplastic 3D printing technologies – printing a secondary support material increases the range of geometries printable with the technology, enabling the fabrication of more complex geometries like overhanging, divergent surfaces with wide angles, and mechanically delicate details. In one work, PCL thermoplastic was printed alongside a decellularised extracellular matrix (dECM) ink for mechanical support throughout a 14 day cell culturing period [113]; PCL has also been used in other work to provide mechanical support to cell-laden alginate hydrogels [114]. Alternatively, a water dissolvable polyvinyl alcohol (PVA) thermoplastic has been used to provide short-term mechanical support to both PCL and alginate hydrogel structures [115]. In similar work, PEG has also been used as the temporary ink [116]. The combination of PCL and Pluronic F127, a thermoreversible synthetic hydrogel, has been used simultaneously to provide both long-term and short-term support of cell-laden tissue constructs [117], highlighting that hydrogels with sufficient mechanical qualities may also be viable supportive materials to assist

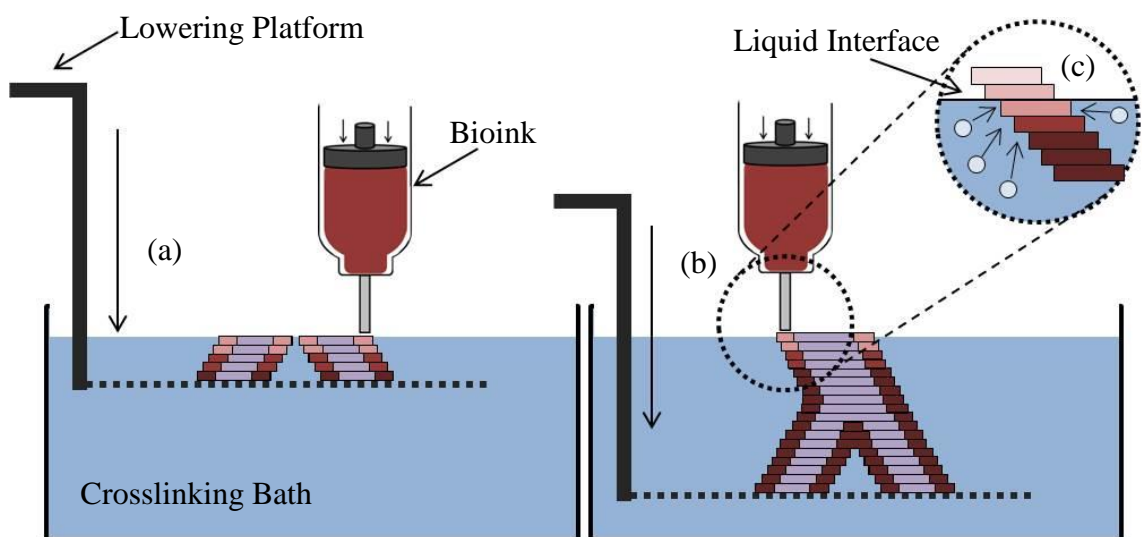
biofabrication. Other literature reports the use of temporary inks not wholly for their mechanically supportive qualities described earlier; rather their temporary nature was employed as a fabrication tool for creating perfusable networks within printed tissues. Scaffolds printed in a logpile configuration using PVA were coated in polydimethylsiloxane (PDMS) and gelled; after gelation the water soluble PVA was dissolved in a water bath to create highly porous scaffolds for cell-seeding with 80% porosity [118]. A carbohydrate glass sacrificial material has been developed for creating perfusable networks within a cell-laden extracellular matrix (ECM), in which the carbohydrate glass is removed from the matrix via dissolution in cell culture media [119]. The use of Pluronic F127 has been utilised for creating embedded vascular networks within cell-laden tissues [120], including thick tissue [121] whereby the inclusion of such channels was attributable to preventing cell death through the provision of nutrients. These methods work to create hollow channels because the volume occupied by the solid-state material is maintained even after the material has been liquefied and washed away (figure 2.9), thus such supportive technologies can support the fabrication of both internal and external features whereby the control of both may benefit tissue engineering research. Whilst the strategy assists the fabrication of geometrically challenging structures and features, there remain several technological caveats. Integrating such a method to fabricate cell-laden constructs requires at least a second nozzle to deposit the support material and, depending on the preferred cell-printing modality, may require the user to integrate a second printing method solely to extrude the support material. Additionally, incorporation of a support material in the described manner means that at least one nozzle cannot be used to print cells as it is instead occupied with the support material – for 3D bioprinters with two extruders for example, this may be the difference between printing mechanically supported and geometrically complex structures with single cells, or printing co-cultures with two cell-types to assess cell-cell interactions. Prolonged fabrication times also remains a potential drawback as each printed layer requires both materials to be printed one at a time, hence doubling the number of required moves to complete a print.



**Figure 2.9** – Schematic diagram showing the fabrication of perfusable and vascularised tissue, adapted from [121] - (a) fugitive Pluronic-F127 and cells printed inside a chip, (b) cell-laden ECM material cast over the chip, (c) fugitive Pluronic-F127 ink removed via cooling and evacuation, (d) hollow internal network perfused to provide nutrition to cells in thick tissue

Instead of dedicating print nozzles to the printing of support materials, some researchers chose to bioprint directly into a crosslinking solution. This method works to crosslink extrudate as quickly as possible post-deposition in order for the bioink to gel, become mechanically strong, retain shape fidelity, and can be utilised to fabricate larger, self-supported structures without needing to dedicate a print nozzle to the extrusion of a supportive material. With this method, alginate is commonly printed into a container filled with calcium chloride solution to induce gelation. In earlier work, this approach was shown to be capable of printing lines, sheets, and HeLa (cervical cancer) cell-laden tubes of alginate with a viability of 70% [122]. It is possible that droplet-based technologies like inkjet printing were initially only able to adopt this approach; due to being a non-contact method of fabrication, the nozzle is never immersed within the crosslinking solution and avoids risks such as the nozzle becoming blocked with crosslinked material. Such a technological restriction may have only applied to

materials with rapid gelation mechanisms like alginate, but to use a similar method with slower gelling materials could hypothetically be more disadvantageous for reasons like material diffusion prior to gelation, particularly if low viscosity inks were to be used, or a loss of print accuracy due to perturbing forces incurred by moving the nozzle through the low viscosity solution. However, since then the method has been developed to incorporate a movable Z-axis platform in various bioprinting modalities such as inkjet [123][124], laser [125], and extrusion [55][126]. In this manner the supportive method functions similarly to standard SLA printing processes; the idea may have even been conceived by this observation. In these approaches any potential detrimental effects on the printability are avoided by printing onto the platform which rests at the solution's surface. Once a layer has been printed the platform submerges into the crosslinking solution a distance of one layer height prior to printing the subsequent layer and so forth (figure 2.10). Whilst the use of such support baths has enabled bioprinting technologies to fabricate to a greater scale and complexity, the range of printable geometries remains limited by the inability of calcium solution, or other similarly low-viscosity crosslinking media, to suspend inks and thus large overhanging features are still a challenge to print. In this regard, printing into a crosslinking solution does not provide the same level of mechanical support as the use of the aforementioned sacrificial inks for example.

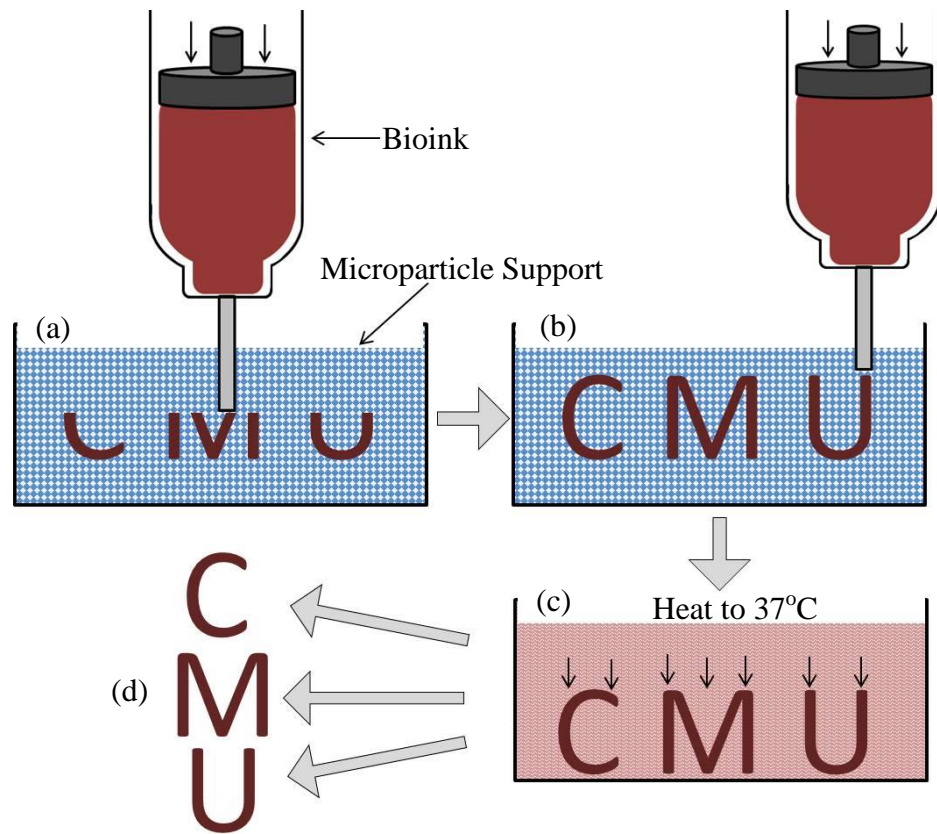


**Figure 2.10** – Schematic diagram of supported fabrication by means of printing into a crosslinking solution, adapted from [55] – (a) bioink extruded onto a porous platform is lowered into a bath of crosslinking solution, (b) lower layers become rigid enough to support upper layers due to crosslinking, (c) printing is conducted close to the crosslinking bath's surface for quick crosslinking to maximise shape fidelity



Developments to specifically address the shortcomings of the crosslinking solution support approach involve establishing a means of suspending extrudate in 3D space within the crosslinking medium itself. Creating such a supportive medium involves creating a network with complex rheology which is solid enough to mechanically support material whilst simultaneously being fluid enough for a nozzle to translate through the medium unhindered and without disturbing previously dispensed bioinks and cells. One method of creating such a ‘solid-and-fluid’ system involves the creation of a gelled microparticle network, alternatively referred to as granular gels or fluid gels. Such microgel networks become fluidised when they are subject to a small amount of shear stress, like the stress induced by moving a print nozzle through the medium, and re-solidify once the stress has been removed [127]. The literature has documented a range of process-able gels with various qualities which have found successful application as a bioink-supportive medium. Carbopol (i.e. carbomer synthetic polymer) microgels have been utilised to support the printing of highly complex structures using silicone [128], fluorescent microsphere/PVA ink [129], cell pellets mixed with hyaluronidase [130], alginate/gelatine ink mixtures [131], and PDMS [132], and can be washed away with water or phosphate buffered saline (PBS), depending on the literature, to remove the printed construct from the medium. Whilst Carbopol is capable of producing supportive fluid gels, the range of compatible materials may be restricted due to Carbopol’s instability to divalent cations which are often used to crosslink certain biopolymers; thus the use of such polymers as bioinks would be less feasible without engineering such inks with a secondary crosslinking mechanism. Furthermore, whilst Carbopol microgels have been mixed with cell culture media, the range of suitable cell culture media is potentially limited by said divalent cation instability which may restrict the range of cell types which can be supported by this material. Instead of potentially harmful synthetic polymer support baths, naturally derived materials like agarose have been processed into microparticle gels to the same effect [133]. In this work cell-laden gellan gum (low acyl) was extruded into the agarose fluid gel bath, thermally crosslinked, and then later supplemented with calcium ions via nozzle injection to induce secondary crosslinking whilst inside the support. However the resolution of printed structure was not quite as high as those printed into Carbopol baths; a possible explanation for this could be related to the low rheological properties of the agarose fluid gel which may have allowed the low viscosity bioink solution to diffuse slightly before the ink could be fully crosslinked, although a nozzle with a much wider diameter was also used which would also affect the resolution. Despite this, agarose is a

relatively inert biopolymer and thus should be more compatible with a wider range of materials. In other work, gelatine microparticles were used in a method called the ‘Freeform Reversible Embedded Printing of Suspended Hydrogels’ (FRESH), and is unique in that the gelled gelatine microparticles can be melted away at a temperature of 37° Celsius (figure 2.11) [134]. Gelatine microparticles are prepared with calcium chloride to crosslink alginate-based bioinks during printing into the support bath as opposed to the printing-then-crosslinking approach described in the aforementioned work with agarose fluid gels; as a result, the print resolution of structures printed using the FRESH method appears greater than with agarose fluid gels. The FRESH method has also been adapted for the fabrication of perfusable microfluidic devices [135]. Having addressed the concerns of biocompatibility and print resolution, as well as having access to a wider range of compatible materials than Carbopol, gelatine-based fluid gels may be a more attractive material for supportive bioprinting. However creating gelatine microparticles demands particularly delicate process control, requiring that the temperature is cold enough throughout the entire process to prevent the gelatine from melting and that the material is correctly blended at the right speed for the right time with parameters detailed for a single brand of blender. Recently the FRESH protocol was revised; the current approach, now referred to as FRESH V2.0, uses complex coacervation to produce gelatine microparticles which are smaller and more uniform than what was possible in FRESH V1.0 [136] and also resolves the blending processing issue from the older method. Lastly, alginate-based microparticles have been employed to print small-scale cellularised human hearts, complete with blood vessels using decellularised bioinks derived from human omenta [137]. The range of suitable materials which can be processed into microparticles can be vast and largely depends on whether the polymer can be gelled or not based on the reviewed literature. In any case, the use of a microparticle-based support bath is shown to be highly adept in the replication of complex anatomical geometries with soft bioink materials.



**Figure 2.11** – Schematic diagram for structures fabricated with a microparticulate support bath, adapted from FRESH [134] – (a) microparticle baths support bioinks in 3D space during (b) and after printing, (c) structures fall out of suspension by melting the supportive microparticles (d) and can then be safely retrieved

Other support bath networks which are functionally similar to the described microgels to suspend extruded biomaterials in 3D space involve Laponite nanoclays [138][139][140], chemical complexation [141][142], block copolymer self-assembly [143], and direct extrusion into aqueous Pluronic F127 solution [144][145]. Of the supportive methods discussed in this section, printing within microparticulate support baths is arguably the method most capable of producing highly complex anatomical models from soft cell-laden materials which are suspended delicately within the medium itself. The technology favours the use of extrusion-based bioprinting modalities due to the requirement of depositing material precisely in 3D space inside the medium. Printing techniques like inkjet and LIFT are probably incompatible with the support method without some process modification as they lack the control to position droplets at a pre-defined Z-axis depth, despite having good positional control along the X/Y plane. Hence this supportive technology is highly poised to enable extrusion-based

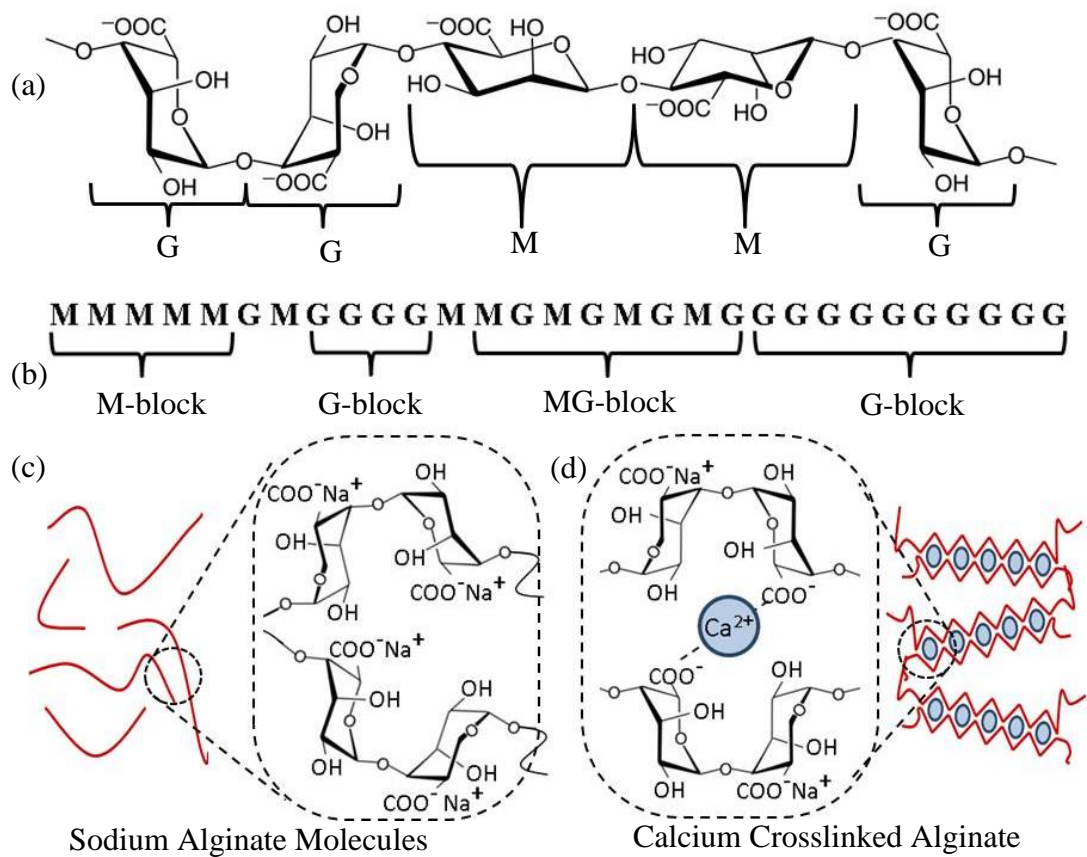
bioprinting techniques to specifically address the mechanical challenge of fabricating geometrically complex cell-laden soft-tissues.

## **2.4 Materials for Biofabrication**

The printing of cells is seldom conducted without the incorporation of some biomaterial in a liquid or gelled state to suspend the cells. Such materials are employed to better provide printed cells with a highly aqueous supportive environment to proliferate and grow as tissues whilst providing the mechanical rigidity to create cell-laden constructs in 3D. As mentioned prior in the discussion of bioprinting techniques, the printing modality will influence the choice and concentrations of materials used based on their viscosity and surface tension properties like inkjet and valve-based bioprinting methods; other methods like extrusion-based methods are better capable of printing mechanically stronger gels and viscous pastes at higher polymer concentrations. Some materials excel in their structural properties but have poor cell compatibility and vice-versa, therefore the choice of biomaterial for bioprinting applications is a key parameter to acknowledge and will now be discussed.

### ***2.4.1 Alginate***

Alginate is a naturally derived biopolymer hydrocolloid obtained via extraction of the material from brown seaweed and has been used in various biomedical applications such as drug delivery [146], wound dressing [147], creating dental impressions [148], and the regeneration of various tissue types [149][150][151]. The overall mechanical properties of alginates are related to the ratio of (1,4)-linked- $\beta$ -D-mannuronate and (1,4)-linked- $\alpha$ -L-guluronic monosaccharides, referred to as M and G respectively, which makes up the molecular structure of alginate itself [152] and the concentration and type of divalent cations used for crosslinking (figure 2.12); divalent cations such as  $\text{Ca}^{2+}$ ,  $\text{Ba}^{2+}$ , and  $\text{Sr}^{2+}$  each have a different crosslinking affinity for G blocks, thus the choice of cations, their concentration, and even the source of cations can drastically alter the mechanical properties of alginates [153][154]. Alginate extracted from different species of seaweed will have varying compositions of G and M blocks [155] thus different alginates can create softer or firmer gels which may be appropriately matched to replicate the mechanical properties of various tissue types.



**Figure 2.12** – The chemical structure of sodium alginate [156] consists of (a) (1,4)-linked- $\alpha$ -L-guluronic acid and (1,4)-linked- $\beta$ -D-mannuronic acid residue called G and M respectively, (b) residues of G and M are arranged in 'blocks' throughout the polysaccharide chain, (c) alginate chains form crosslinks with other chains when exposed to divalent cations and forms an 'egg-box' structure [157][158][159]

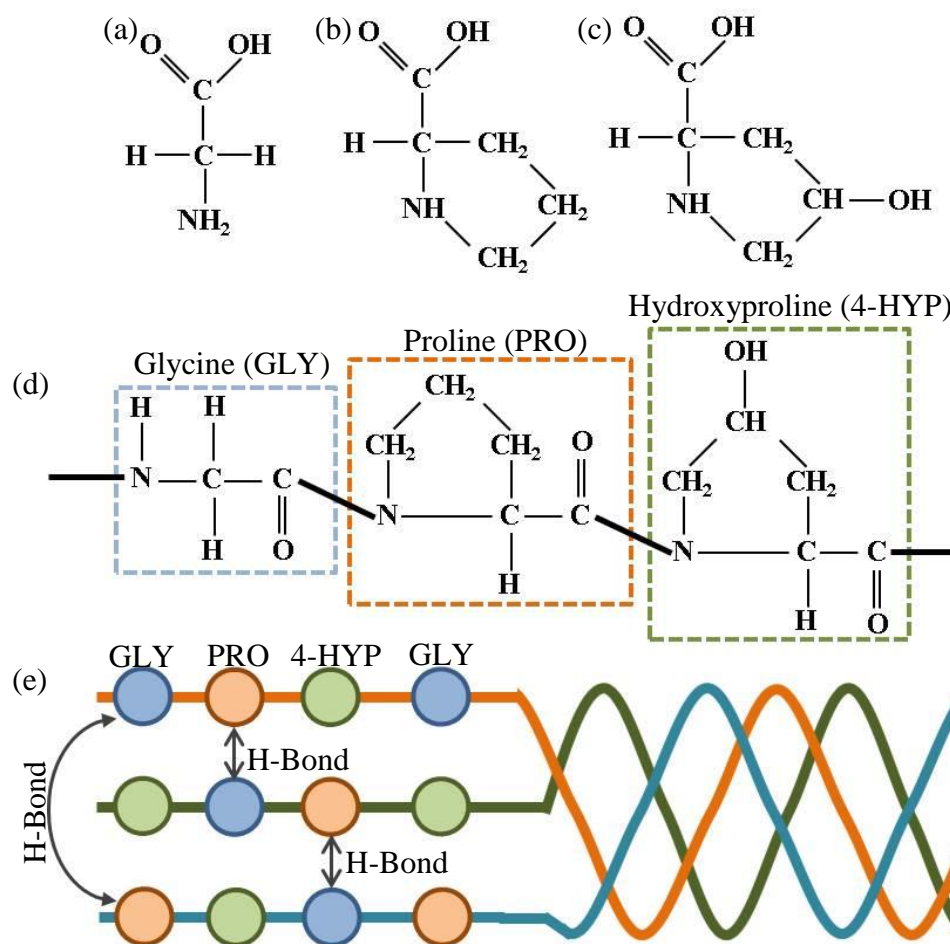
Alginates have commonly been used as the biomaterial of choice for many bioprinting-related applications. Alginate solutions have been deposited onto gelatine/calcium gelled substrates via a piston-based extrusion method whereby the alginate would crosslink with the calcium ions after the gelatine has melted away post-print in an incubator [160]. Alginate solutions may be extruded through coaxial nozzle systems to print rigid filament which are either internally solid [64] or hollow [126] depending on whether the alginate is extruded via the core or shell material streams. Alginate may also be mixed with other biomaterials to infer a multitude of benefits such as to enhance the printability of mixtures, incorporate controllable degradation via the chelation of ions to improve cell proliferation and viability [161].

Alginate hydrogels, whilst a popular bioprinting material, have been viewed as limited in terms of their proliferative capacity for cells. It has been suggested that cells

embedded in alginate structures have hindered proliferative and differentiation capacities, namely as a result of being unable to relocate within the matrix and an inability to degrade the surrounding alginate [113]. It is possible to enhance the degradation rate of alginate based structures through the addition of materials which chelate the calcium ions, such as sodium citrate or ethylenediamine tetraacetic acid (EDTA). However a study in the use of the alginate recovered cellular method concluded that sodium citrate was cytotoxic to mesenchymal stem cells, as suggested by diminishing cell viabilities [162]. Contrary to this finding Wu et al. had successfully demonstrated the printing of human corneal epithelial cell laden structures with a gelatin/alginate/collagen solution hydrogel; the degradation mechanics were controlled by the use of sodium citrate and were shown to enhance cell proliferation [161].

#### **2.4.2 Collagen**

Collagen is a protein consisting of three polypeptide or  $\alpha$ -chains connected in a triple helix formation having a repeating structure in the format of Gly-Xaa-Yaa, where 'Gly' is glycine and 'Xaa' and 'Yaa' can be a variety of amino acids; the  $\alpha$ -chains are most typically tripeptides comprising of glycine, proline and hydroxyproline (figure 2.13) more-so than compositions involving the other amino acids which make up collagen [163][164][165]. These three polypeptide chains wrap around each other and form fibrils which are held together by covalent and hydrogen bonds [166]. Collagen is a hugely attractive material in tissue engineering because of its capability to satisfy many biological needs that cells have [167]. The material exhibits properties which are supportive of cell growth, proliferation, differentiation [152], and is antigenic [161]. Collagen is also a very abundant protein found in all animals and is the most common component in the extracellular matrix of humans [168][169]. Due to collagen's biological supportive role and its abundance in the ECM of many tissues, it is a highly desirable biomaterial which has been used in a multitude of bioprinting applications [170][136][171][172][173].



**Figure 2.13** – The chemical structure of a collagen consists primarily of three amino acids (a) glycine, (b) proline, (c) and hydroxyproline, (d) joined by peptide bonds. Repeating glycine-proline-hydroxyproline units form polypeptide  $\alpha$ -chains (e) which are hydrogen bonded with other  $\alpha$ -chains which forms the triple-helical molecular structure characteristic of collagens [174][175][176][177]

Whilst collagen is effective at supporting cells by mimicking the ECM, it suffers from poor mechanical strength – collagen’s mechanical weakness in bioprinting stems from its use at concentrations much lower than generally present in living tissue [152]. To improve the strength, collagen may be crosslinked by controlling the pH or temperature to induce fibrillogenesis (self-assembly of the collagen fibrils) [178][179]. Crosslinks may be formed when the collagen is heated above its lower critical solution temperature (LCST). Collagen is relatively hydrophilic at temperatures below the LCST; water molecules bind to collagen’s polypeptide chains due to a favourable enthalpy of mixing, ensuring hydration and complete solubilisation in the solvent and results in a homogeneous single-phase system. However, increasing the temperature above the LCST causes the system to become thermodynamically unstable and separates into a

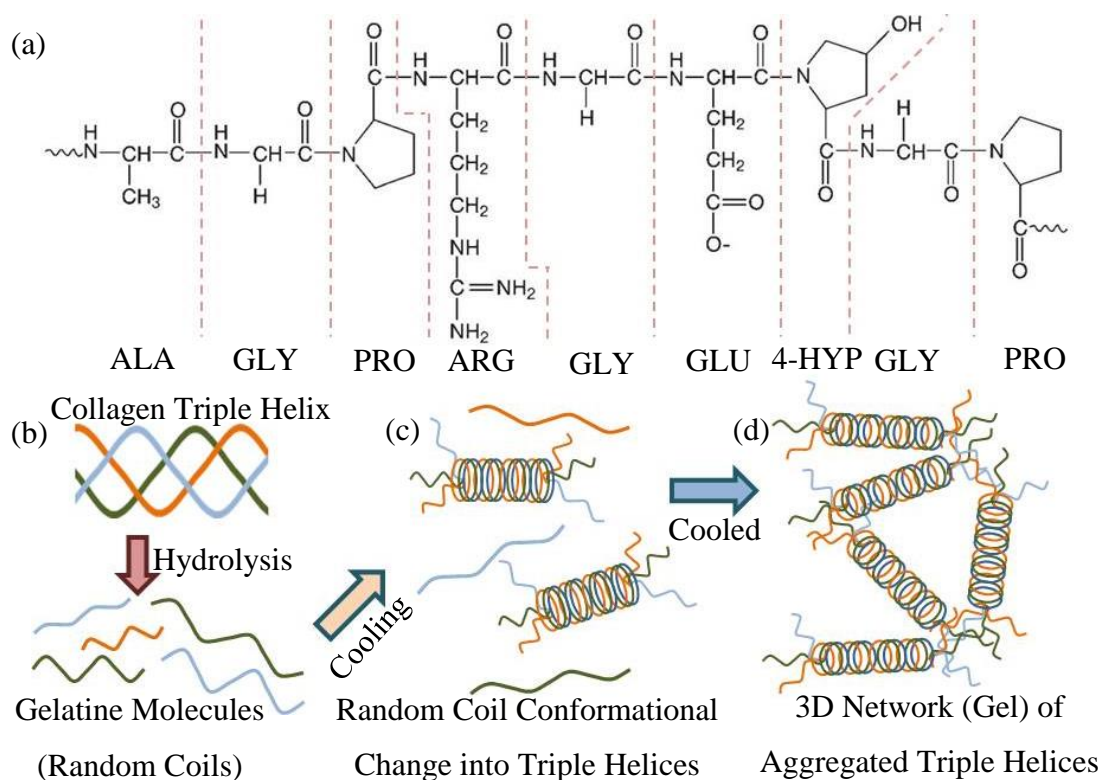
mixed-phase system in an entropy-driven process. Considering Gibbs free energy of mixing, the increase in the entropy of mixing ( $T\Delta S$ ) becomes more significant than the increase in the enthalpy of mixing ( $\Delta H$ ), thus the system favours the entropic disordering of water molecules more than the enthalpy of hydrogen bond formation with collagen's polypeptide chains [180]. Collagen then begins to exhibit hydrophobic behaviour as the water molecules become separated from the polypeptide chains, resulting in partial dehydration of the collagen [165]. The polypeptide chains then undergo a spontaneous self-assembly process to minimise the exposure of the hydrophobic chains to the surrounding water i.e. fibril formation occurs [181]. Despite this, crosslinking of collagen is a relatively lengthy process and resulting gels are still mechanically very weak compared to other hydrogels [152], thus rendering some structural support strategies such as gelation during printing ineffective. For these reasons, collagen may be mixed with other mechanically stronger biopolymers as an effort to balance collagen's biological supportive functions with another biopolymer's structural integrity such as in the works of Wu et al. [161], and Yang et al. [182].

### ***2.4.3 Gelatine***

Gelatine is a protein produced by the hydrolysis of collagen from animal tissues such as cattle hides and pork skins whereby purified collagen is exposed to an acid, such as hydrochloric acid, and then washed with hot water to recover soluble gelatine [183]. Gelatine is comprised of a mixture of multiple polypeptide chains derived from the collagen itself (figure 2.14), with each chain having different compositions and molecular weights [184] which bestow the various types of gelatines with different strengths and viscosities [185]. Gelatine forms thermoreversible gels by dissolving its powder in water above 40° Celsius followed by cooling – random coils of gelatine molecules aggregate into triple-helices when cooled which creates a physically crosslinked gelled network [186] which can be reversibly broken and reformed by temperature control [187]. Gelatine's thermogelling properties are hence contrary of the collagen from which it is derived, exhibiting an upper critical solution temperature (UCST) instead of an LCST. Gelatine is hydrophilic and soluble at temperatures above the UCST, and the gelatine molecules exist as random coils as the entropy of mixing is more favourable than the enthalpy of mixing. As the solution cools to a temperature below the UCST, the entropic constituent ( $T\Delta S$ ) diminishes and the enthalpy of mixing ( $\Delta H$ ) becomes the dominant term in the Gibbs free energy of mixing. In this enthalpy-driven process, the gelatine molecules spontaneously change physically in conformation



and the single-phase system separates into a mixed-phase system. Gelatine undergoes a desolvation process, becoming insoluble and hydrophobic at lower temperatures due to the exclusion of water from gelatine's polypeptide chains leading to contraction and hydrophobic collapse [188]. This results in stronger interactions between adjacent polypeptide chains which outweighs the interactions between the polypeptide chains and the solvent [189], causing gelatine to undergo the coil-to-helix transition. Therefore the thermogelling properties of gelatine is fundamentally different than its parent collagen; gelatine's gelling process is enthalpy-driven which results in more favourable intermolecular attractions between polypeptide chains at temperatures below its UCST, whereas collagen's gelling process is entropy-driven at temperatures above its LCST due to the increased disordering of water molecules which results in their exclusion from the polypeptide chains [190].



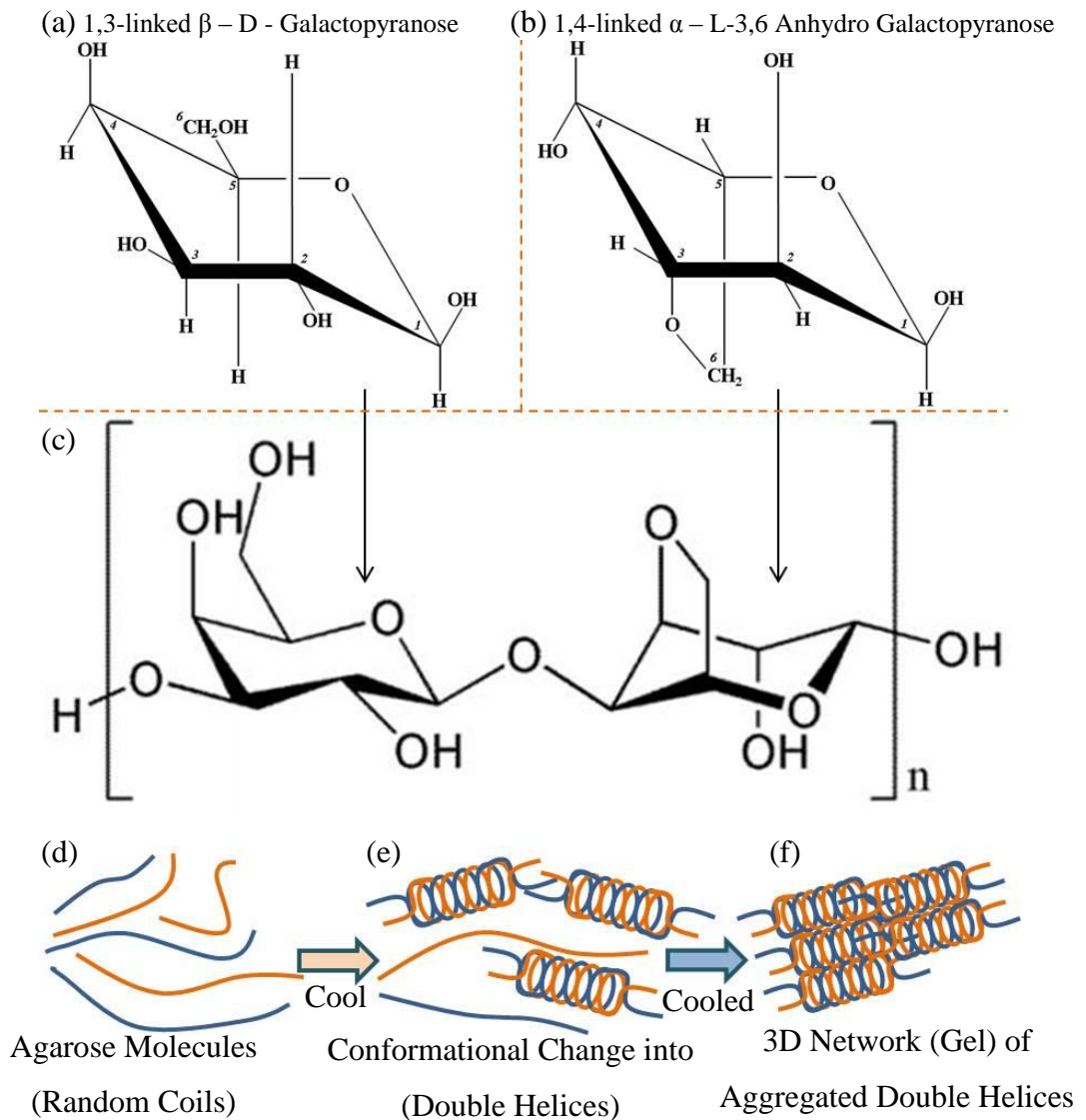
**Figure 2.14** – Gelatine's chemical structure (a) contains a large proportion of glycine, proline, and hydroxyproline amino acids like collagen, (b) denatured collagen produces gelatine molecules, (c) renaturation of molecules into collagen-like triple helices (d) and aggregate into a 3D gelled network when cooled [183][191][192][193][194]

Gelatine shares several similarities with collagen in that it caters to the biological needs of cells by promoting cell adhesion, proliferation, and migration [195], and can be used

to mimic the ECM [196]. Unlike collagen however, gelatine is water soluble and is therefore a hydrocolloid [184] more like alginate and guar gum. The thermoreversible nature of gelatine is both an advantageous and disadvantageous material quality and depends on the material's application. Temperatures typically below 30° Celsius are required to maintain gelatine in its solidly gelled state which means that fabricated cell-laden gelatine structures will melt when stored in an incubator or *in vivo* and is thus unstable in this manner. Furthermore, thermal gelation is a slow process and can take up to 15 hours in order for such gels to attain full gel strength [186]. The mechanical and gelation properties of gelatine can be enhanced through chemical modification, such as the incorporation of methacrylate groups to create GelMA which grants dual-crosslinking capabilities via thermal and UV crosslinking to improve its stability [197]. Chemical modification however may pose some risk to cell viability depending on the chemical used, such as glutaraldehyde [198], which may deter its use in biofabrication. Whilst gelatine may be considered somewhat difficult to print with due to its relatively poor stability, it can be highly advantageous as a supporting material [134][199] because of its physiologically relevant melting temperature, making it a simple and effective material to assist in the fabrication of geometrically complex structures in a cell-friendly manner.

#### **2.4.4 Agar-agar/agarose**

Agar-agar (or 'agar') is a hydrocolloid derived from red algae, like alginate, and is a mixture comprising of mainly two linear polysaccharides components: agarose and agarpectin [200]. Unrefined agar is the extracted raw material from the algae and is generally obtained by boiling the algae in slightly acidic conditions under pressure [201] and in this form is most commonly used as a low-cost ingredient in many culinary applications as a highly effective gelling and stabilising agent, even at low concentrations [202]. The strongly-gelling agarose (figure 2.15) content may be purified from the agar and separated from the weakly-gelling agarpectin using precipitation and chromatography techniques [203][204]. The production of agarose increases the cost of the material but removes the lower molecular weight, more sulphated agarpectin [205]; this may infer multiple benefits including the production of gels with greater strength [206] by means of increasing the substance's average molecular weight through the purification process. Agarose may be preferred over agar in certain applications such as gel electrophoresis [207].



**Figure 2.15** – Chemical structure of agar’s gelling constituent, agarose, comprises of (a)  $\beta$ -D-galactopyranose and (b)  $\alpha$ -L-galactopyranose, (c) which form glycosidic bonds and makes up agarose’s repeating structural unit [208]: (1,3)-linked- $\beta$ -D-galactopyranose and (1,4)-linked- $\alpha$ -L-3,6-anhydro-galactopyranose. (d) Random coils of agarose molecules, (e) conformation change into double helices upon cooling, (f) aggregation into agar’s 3D gelled network [209][210]

Agar is a relatively insoluble material and requires heating to a high temperature in order to dissolve, after which agar forms a thermoreversible gel once the solution has been sufficiently cooled. The mechanism of agar’s gelation is debated [211][156] but may be related to the aggregation of double helices formed from the agarose molecules after exhibiting a coil-helix transition due to the cooling of a hot agarose solution [212], after which these double helices aggregate to produce a three-dimensional gelled network [213] and are held together by reversible physical hydrogen bonds [214]. In

this regard, agar's thermogelling behaviour is similar to gelatine's as it also exhibits UCST behaviour; the random coils become more ordered and adopt a double-helical conformation in response to an enthalpy-driven spontaneous process induced when solutions of agar are cooled below the UCST.

A unique property of agar is that it exhibits significant thermal hysteresis, whereby the difference between the gel-setting (<38° Celsius) and gel-melting (>85° Celsius) temperature is quite large [215] and thus agar gels are considered quite stable unlike gelatine. Whilst known to be mechanically strong and biocompatible [216], agarose, like alginate, has poor biomechanical properties [217] which could prevent anchorage-dependent cells from adhering to the ECM and eventually lead to cell death [218]. Agarose has seen application within the field of bioprinting as a bioink constituent [219][220] and as a supporting material to produce temporary fibers [221] and fluid gel networks [133][222].

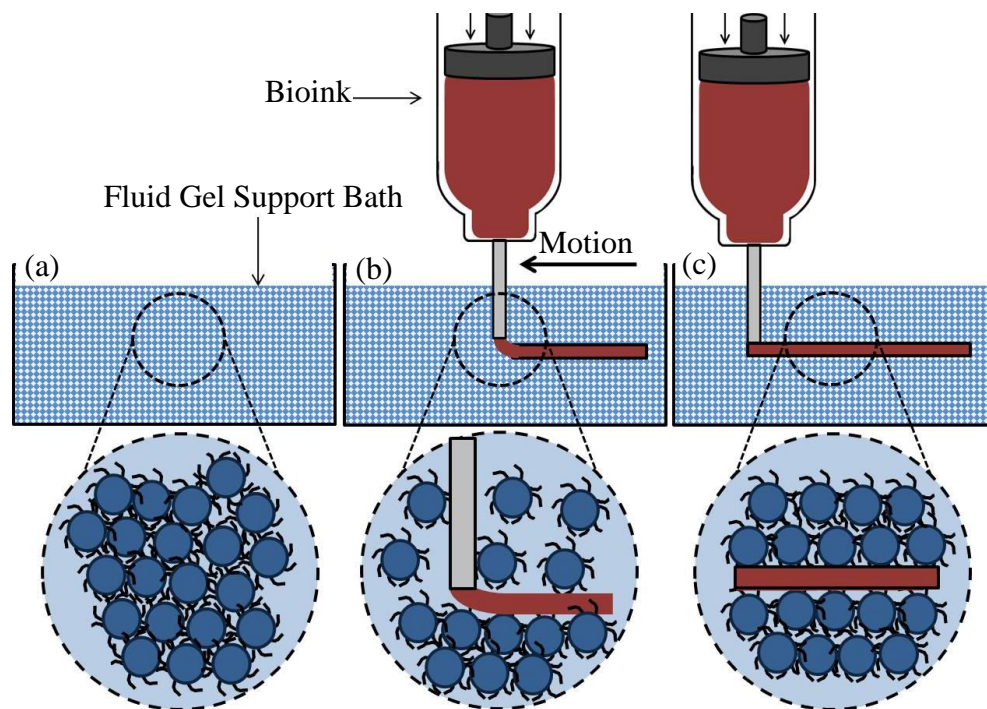
#### ***2.4.5 Fluid gels***

Fluid gels are not a particular material but rather a description of the material's state. Fluid gels may be described as a medium which embodies many micro-sized gelled particles created by the introduction of shear during the gelation of a biopolymer solution [223]. The interactions between the microparticles grant the medium both liquid-like and solid-like properties which are commonly used to create non-settling suspensions in the food and drink industry [224]. Such contradictory behaviour can be most easily understood by considering a model based around 'hairy' microparticles (figure 2.16). In such a model, gelled microparticles are hairy and may form bonds via hair entanglement with adjacent particles, creating an interconnected network and bestow the fluid gel with solid-like qualities; these fluid gels yield once an applied stress is strong enough to disentangle the network of interconnected hairs which induces material flow [225][226], a liquid-like property. The solid-like quality of a fluid gel is restored upon removal of the stressor, an indication that the bonds between particles have been reformed once more.

Fluid gels may be produced in various manners including droplet generation (via nozzle, atomising spray, jetcutting rotating disk, or otherwise) and ejection into crosslinking solution [227], complex coacervation [136], mechanical breakup of the bulk gel [134], and shear-induced gelation [133]. The mechanism for creating gelled particles involves segregating the gel nuclei so that they cannot aggregate as a unified,

infinitely gelled network; the incorporation of a shear field prevents aggregation of the biopolymer's molecules beyond a certain size related to the shear and gelation rates, thus small gelled particles are formed [228][229].

In biofabrication the use of naturally derived fluidised hydrogel networks has already been discussed as a supportive material strategy and demonstrated in a number of works [134][133][137], but its incorporation as part of the bioink is seldom reported in the literature. Despite this, the use of fluid gel bioinks has been used to suspend cells to mitigate against cell settlement [230] and enhance the structural properties of low viscosity inks [231] in inkjet-based bioprinting. In these works, the use of a fluid gel has addressed two major technological disadvantages of the inkjet-based bioprinting modality, therefore it could be argued that fluid gels can some-day become an engineering factor for the development of novel bioinks. Bioinks comprising of a fluid gel component can achieve a wide range of complex rheological profiles depending on the fluid gel's processing parameters, choice of biopolymer and concentration [232][233][234], but this benefit may be offset as the fluid gel is mechanically much weaker than its wholly gelled counterpart. Whilst the use of fluid gels is relatively new in the field of bioprinting, such reasons could indicate why it is more often used as a supportive technology rather than a bioink component.



**Figure 2.16** – Illustration of fluid gel’s supportive mechanism in a bioprinting context based on hairy particle analogy – (a) network at rest maintains solid-like characteristics due to hair entanglement with neighbouring particles, (b) particles local to the stressor become untangled and exhibit fluid-like characteristics; particles far from the stressor remain entangled, (c) removal of stressor allows untangled particles to become entangled again to exhibit solid-like behaviour [225][226]

## 2.5 Summary

The literature review has discussed the beginnings of 3D printing and the advent of customisable open-source technologies, through to the development of bioprinting and the various types of bioprinters as research tools to assist with tissue engineering. In addition to this, a review of various supportive strategies to provide mechanical support to printed structures throughout the fabrication process has been conducted as well as a brief review of some naturally derived biomaterial hydrogels to enable the fabrication of soft tissue-like structures.

The discussion on 3D bioprinting technologies has briefly examined the relative merits and downfalls of each particular modality. The relatively low cost and simplicity of creating an extrusion-based machine is more attractive than attempting to incorporate a laser-based system which is very costly and more difficult to set up, requiring extensive and technical prior knowledge of laser technologies, and is further restricted in material choice as only light-curable biopolymers are compatible. The prospect and relative

advantage of combining laser-based approaches like projection and STL with current trends in supported manufacture is not clear. Laser-based technologies operate by crosslinking a photocurable polymer solution at the solution's surface. Considering this, the use of STL or light-projection methods to selectively polymerise material deep inside, for example, a fluid gel supportive network mixed with the photocurable polymer would likely not succeed because (a) all material between the surface and the desired depth becomes entirely polymerised by the light travelling to the desired position, or (b) be unable to reach the desired depth at all due to polymerised material at the surface preventing light from travelling deeper into the solution - both outcomes also assume that the integration of a fluid gel network does not interfere with the projection of laser light which, whilst presently not documented, could be subject to potentially detrimental light scattering phenomena such as the Tyndall effect (i.e. colloidal particle scattering). As laser-based technologies, like those described, crosslink material at the bath's surface, any benefits associated with being able to fabricate and suspend material deep within a support bath cannot be realised.

An extrusion-based method is potentially more capable of printing structures to a more relevant anatomical scale within a more acceptable timeframe compared to droplet-based technologies like inkjet or valve for example, which from the literature are less commonly used in conjunction with supportive techniques and is entirely absent in more recently developed support baths. The reason for this may be related to difficulties of droplet-based technologies to dispense material with enough force to penetrate the surface of a support bath and with enough kinetic energy to travel to the correct Z-position/depth without incurring cell damage, or may require the support bath material to be added layer-by-layer simultaneously whilst printing the primary construct and would therefore significantly prolong fabrication times. In the former case, the force required to penetrate and translate through a support bath is fulfilled by the nozzle of extrusion-based modalities and is not dependent on the bioink's properties and depositional conditions. Whilst a droplet-based bioprinter like inkjet or valve, but not LIFT, could technically be lowered to the point where a nozzle intersects the support bath, it lacks the depositional control of certain extrusion-based techniques, like a plunger, to retract material and maintain a high print quality between long travel moves by preventing material ooze. Droplet-based technologies are furthermore restricted in terms of compatible material usage as the bioink has to be in the form of a solute with suitably low viscosity and surface tension for successful ejection; extrusion-based

modalities can extrude both solute and partially gelled/hydrogel forms of bioinks, the latter being not necessarily of a 'high viscosity' but is mechanically stronger, and may provide better depositional control due to bearing a more complex solid- and fluid-like rheology, granting such hydrogels with a yield stress which could be more stable than a solute within a supportive medium. Considering all of these aspects, extrusion-based bioprinting in conjunction with support bath technologies seems to be the best way forward.

Current trends in supportive strategies have developed to the point where total encapsulation of the bioink as it is extruded is a highly feasible method to assist the fabrication of highly complex anatomical models using low viscosity inks to create mechanically soft, cell-laden tissue-like structures. Such supportive techniques are capable of holding ink in their deposited location securely and gently throughout the entirety of the printing process. Such techniques can be viewed as a viable strategy to increase the scale of fabrication in applications whereby the fabrication of complex structures from soft materials would otherwise be impractical. Furthermore, this encapsulated supportive strategy is seemingly most synergistic with extrusion-based bioprinting modalities based on the amount of literature combining these two approaches together, and therefore it would make sense to develop such supportive networks using the developed extrusion-based bioprinter proposed.

Lastly, a brief discussion on a range of biopolymers as well as fluid gels as a class of materials highlighted the relative merits and disadvantages of their use within the field of bioprinting. Alginate was considered for use as the primary biomaterial of choice due to its quick gelation mechanism, biocompatibility, and ability to produce strong structures once suitably crosslinked. Gelatine was preferred over collagen due to being easier to handle whilst providing a simple thermoreversible gelation mechanism. Gelatine is unique in this aspect as melting occurs at physiologically relevant cell-friendly temperatures and makes it a highly interesting material for further development as a support bath. In this function, gelatine has great potential as a naturally derived, highly biocompatible material that can cater to the biological needs of cells, comprises of many useful ECM components and has a very simple and gentle gel-melting mechanism – this is unlike other materials (such as Carbopol and laponite clay) which are synthetic and do not natively possess the biological qualities of naturally derived materials or have release mechanisms that are not as effective as gelatine's. However, current methods for preparing gelatine baths are lengthy and moderately complex



whereby the preparation can fail at multiple stages in the preparation process. Therefore there is potential for development if the preparation process can be simplified which could increase the reliability and repeatability of gelatine bath preparation processes and make the method easier to adopt.

Agar and agarose are materials of interest for the development of supportive strategies more-so than its use as a bioink for the reason that gelation is not quite as simple to control as other materials such as alginate. Alginate's strength can be finely tuned by exposure to various cations at various concentrations to provide a range of strengths with rapid gelation times, whereas agar requires hot extrusion and a suitably large temperature drop in order to induce gelation at a quick rate. However it can be argued that fluid gels can be prepared more simply with agar instead of alginate due to this difference in crosslinking mechanism, rendering agar as a viable support material for further investigation. In this application, agar may be a better support material than gelatine due to its greater thermal stability at physiological conditions. Whilst gelatine's physiological melting temperature enables embedded structures to be removed simply by heating to 37° Celsius, it cannot facilitate bioprinting at physiological conditions as the heat impairs the supportive qualities of such baths and is thus a significant drawback; agar on the other hand can retain its gelled state at temperatures up to 85° Celsius and therefore has great potential to support printing at a more cell-friendly 37° Celsius and furthermore could enable technological scale up by allowing the fabrication of larger cellular structures over prolonged print times simply by maintaining cell viability for longer.

## **2.6 Aims and Objectives**

Having completed a review of the literature, the research aims and objectives of the work documented in the following chapters will be based on:

- The development of an open-source, RepRap-inspired, extrusion-based 3D bioprinting platform as a low-cost, highly modular, and customisable tool to facilitate the fabrication of soft tissue-like, cell-laden bioink structures.
- The development of support bath technologies compatible with the aforementioned extrusion-based bioprinting platform and is capable of satisfying several fabrication criteria: (1) suspension of cell-laden, low-viscosity bioinks, (2) replication of complex anatomical geometry, (3) production of high resolution structures, (4) produced in a manner which is simple to follow and

easy to replicate, (5) and can be separated from printed structures with a low-risk of compromising the structural integrity of the construct.

## **2.7 Structure of Thesis**

The structure of the thesis after the preceding introduction (chapter 1) and literature review (chapter 2) is as follows:

- Chapter 3 details the materials and methods utilised to conduct the experimental work.
- Chapter 4 details the construction of the extrusion-based bioprinting platform to conduct experiments pertaining to the extrusion of material into support baths.
- Chapter 5 details the development of a quiescently gelled gelatine-based support bath.
- Chapter 6 details the development of a supportive fluid gel bath derived from commercially available agar.
- Chapter 7 details the development of the aforementioned agar fluid gel systems with respect to control over the bulk rheological properties for support bath bioprinting.
- Chapter 8 summarises the key achievements of the thesis and details perspectives for future studies.

## Chapter 3 –Materials and Methods

### 3.1 Introduction

The following sections detail the range of techniques, materials, and equipment used to conduct the research documented within this thesis. The sections will specifically discuss the research equipment and machinery to fulfil particular research needs, material preparation of the ink and support baths, the biological methods for managing cells before and after bioprinting, and the operational methods pertaining to the use of the developed bioprinter.

### 3.2 Equipment and Machinery

#### 3.2.1 Laser cutter

A laser cutter was employed to fabricate the extruder housing of the developed bioprinter. The Trotec Speedy 300 laser engraver (figure 3.1) is a computer numerically controlled CNC machine, similar to a 3D printer, with an X and Y carriage for planar positioning, a laser mounted onto the moving X-axis, and a movable Z-axis bed for setting the appropriate distance for optimal laser cutting. The machine uses a 120 Watt CO<sub>2</sub> laser which allows for a wide range of materials to be engraved or cut, such as the acrylic plastic PMMA sheet used to house the bioprinter's extruder. The laser cutter has a work area of approximately 726 millimetres by 432 millimetres, which is large enough for plastic sheets to be placed onto the bed for cutting.

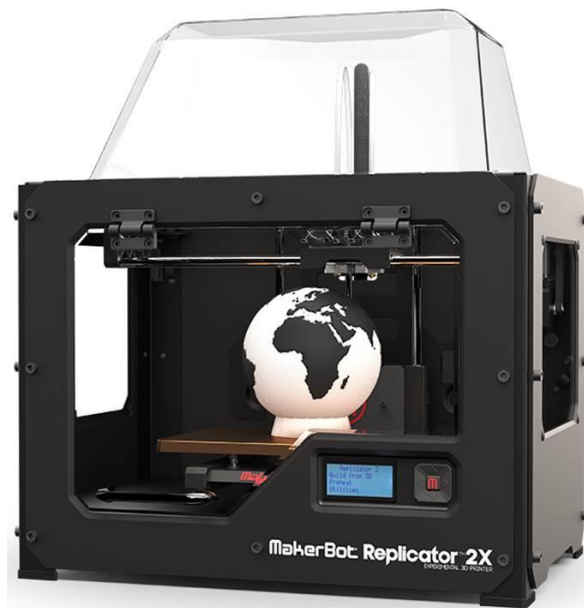


**Figure 3.1** –The Trotec Speedy 300 Laser Engraver [235]

The laser cutter is operated by Trotec's proprietary software JobControl. The software is compatible with various drawing software packages such as CorelDraw for importing drawings in a .DXF format which is then readable by the JobControl software. DXF files in CorelDraw were highlighted and exported into JobControl using the 'Print Selection' option which exports the drawing out from CorelDraw and onto the plater's view within JobControl. Once the file is imported into JobControl, the drawing may be moved around the plater into an appropriate location corresponding to where the cutting material is positioned within the laser cutter itself. The plater can handle multiple files simultaneously and cut them in order which saves time by avoiding the need to conduct laser cutting operations individually. After defining the laser cutter settings such as specifying cutting operations instead of engraving, cutting speeds, laser power, and number of laser passes, the safety guard is lowered and the cutting operations can start and the laser cutter begins trace the drawings loaded within JobControl onto the PMMA sheet inside the machine.

### ***3.2.2 3D printer***

The Replicator 2X 3D printing machine (figure 3.2) developed by MakerBot was used to manufacture bespoke components. Like many 3D printers on the market, the Replicator 2X is suited for extruding thermoplastic filament using FFF (Fused Filament Fabrication) such as ABS (Acrylonitrile Butadiene Styrene) or PLA (Polylactic Acid) into defined geometries. The 3D printer requires a 3D CAD model in the .STL format to be imported into MakerBot's proprietary software MakerWare for slicing and generating the g-code for the printer to execute. The machine has moving X- and Y-axes, an extruder on the X-axis carriage, and a heated printbed which can be raised or lowered in the Z-direction for layering. The printer has a build volume of approximately 246 millimetres wide, 163 millimetres length, and 155 millimetres tall with a positional precision of 11 microns in X and Y and 2.5 microns in Z.



*Figure 3.2 – The MakerBot Replicator 2X 3D Printer [236]*

The Replicator 2X was used to manufacture smaller components necessary for the build of the bioprinter, such as the mounts for the electronics and to connect the feet to the machine. The fabricated models were designed in house using SolidWorks 2012 CAD software.

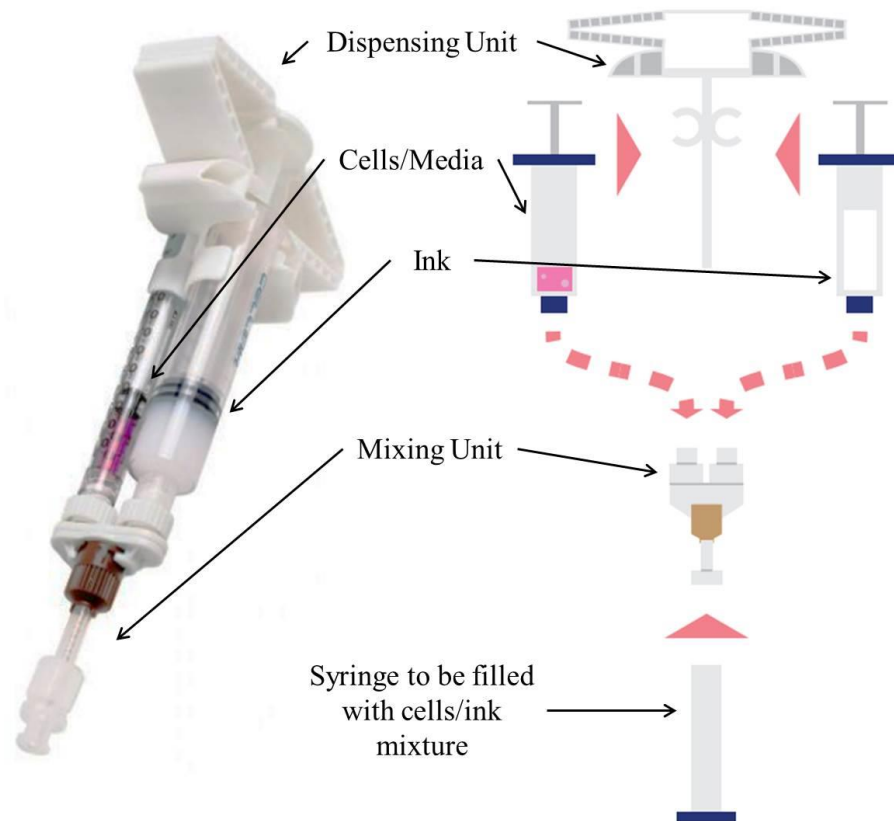
### **3.2.3 Centrifuge**

A centrifuge was used for two applications: to pellet cells during the preparation of cell-laden bioinks and to remove the air bubbles from supportive agar fluid gels. The centrifuge (Herarus Multifuge 3 S-R) is a large machine which operates by spinning liquid materials stored in a centrifuge tube, held by a rotary arm, at a fast speed to separate and redistribute its contents based on the relative densities of the constituent components. Thus when the centrifuge is employed to remove air bubbles trapped inside agar fluid gels, the agar being the more dense material is forced to the bottom of the tube, displacing the air bubbles to the surface and out of the mixture.

When using the centrifuge to remove air bubbles in agar fluid gels, the speed of the centrifuge was set to 1000 revolutions per minute for a time of five to ten minutes depending on the amount of air bubbles and rheological properties of the fluid gel. When spinning diluted fluid gel baths with water, setting a speed too great causes the water to separate out from the fluid gel which then requires re-mixing. For pelleting cells, the centrifuge speed was set to 1000 RPM for 5 minutes prior to resuspension in cell culture media and hydrogel.

### 3.2.4 Cellmixer unit

The cellmixing unit (figure 3.3), developed by CELLINK, is a tool which helps promote homogeneous mixing and distribution of cells throughout the bioinks used for bioprinting. The unit was shipped in multiple parts: the mixing unit, a 12 ml syringe for the ink, a 1 ml syringe for cells and media, and a pushing device to depress both syringes' plungers at the same time. However the mixing unit was used independently as this was the only necessary component of the assembly.



**Figure 3.3** – Schematic of the Cellink Cellmixing unit and its components [237]

The method employed to load syringe barrels for bioprinting was to first pre-load the mixing unit with material to force as much air out as possible. This was achieved by forcing the hydrogel into the mixing unit whilst capping one of the two possible outlets; once material started to flow out of one outlet, this outlet was then capped, the other outlet was then opened, and more hydrogel was forced through to ensure all the mixing unit's channels were filled with hydrogel. With this step complete a syringe loaded with cells and media was fixed on one end of the mixing unit and the hydrogel-loaded syringe placed on the other, and material was passed back and forth between the two syringes for homogeneous distribution; the resulting cell-laden hydrogel was considered

sufficiently mixed once the ink was evenly dyed the same colour as the cell-culture media used with the cells. Finally, with all material loaded into a single syringe, the appropriate syringe barrel to fit the bioprinter's extruder housing was affixed to the receiving end of the cellmixing unit and all of the cell-laden hydrogel material was loaded into the barrel for bioprinting. Whilst this approach involves many steps, it was found that multiple passes back and forth through the unit was worthwhile and pre-loading the mixing unit to remove air bubbles worked well to stop air bubbles from being trapped within the cell-laden hydrogel which are otherwise too difficult to remove once the cells have been added. For figures describing the method of preparing cell-laden bioinks, refer to Appendix A – Mixing Material with the Cellink Cellmixer Unit.

### ***3.2.5 Magnetic stirrer and hotplate***

For dissolving powdered raw materials into solutions of water, a 2-in-1 magnetic stirring hotplate (Starlab N2400-3010) was used. The machine has variable control over the spinning rate in revolutions per minute as well as temperature control to heat up the plate. The machine needs to be used in conjunction with a magnetic stir bar which come in various lengths and designs but ultimately achieve the same end goal of stirring the mixture for homogeneous dissolution. The magnetic stirrer and hotplate plays an integral role in preparing hydrogels for printing as well as creating both the gelatine baths and agar fluid gels.

The materials used in conjunction with the magnetic stirrer and hotplate were mixed at the highest allowable revolutions per minute without causing the magnetic stir bar to spinout. This is achieved by initially starting at a low mixing speed and gradually raising the speed as much as possible – when spinout occurs, take note of the RPM value, restart the magnetic stirrer and slowly raise the speed to below this value. As the materials being mixed exhibit different viscosities from each other, optimal mixing speeds differ between them and may also change over the course of dissolution due to increases in temperature and proportion of powder dissolved. The temperature of the hotplate was set to around 60° Celsius to heat up solutions and lower their viscosities to promote quicker mixing times; such a temperature is also warm enough to dissolve gelatine and is a suitable temperature for preparing gelatine baths. In the case of agar, the temperature was set to the highest value of 280° Celsius as to try and quickly heat up the mixture to a temperature between 95° to 100° Celsius to activate the agar powder and begin dissolution.

### ***3.2.6 Immersion blender***

The process of converting agar from a fully gelled state into a fluid gel state is conducted by the use of an immersion blender to mechanically break up the gel into many gelled microparticles, creating the unique supportive rheological properties. The immersion blender (George Home, 600W hand blender GHB101B) is ideal for the application because the long slender neck of the blender can be easily inserted into beakers containing the gelled agar, with room for manual stirring in conjunction with blending to ensure as much of the gel is broken up as possible. The blender has a slider to control the speed from low to fast, and a turbo option to further increase the speed, although it was found that the slowest speed was apt enough to appropriately break up the agar gels into fluid gels without building up excessive heat within the blender. The blender is also easy to clean as the blending head can be removed from the body for rinsing out any residual gel sticking to the blades or the guard.

When initially attempting to break up gelled agar, the blender needs to be activated whilst the blender head is being pushed into the gel. The process of blending does require some forcing to get started initially as the surface of the gel is firm and smooth, so the pushing is necessary to get the blender's blades to bite into the gel. Once this has been achieved, the gel starts to break up into large chunks and becomes progressively easier to break up further into microparticles.

### ***3.2.7 Cell imaging microscope***

For evaluating the viability of cells within printed structures, an inverted fluorescent microscope (Nikon Eclipse TE300, shown in figure 3.4) was used. Inverted microscopes operate on the basis of providing light from underneath the sample being examined, which is necessary to view the cells contained within printed structures. To view the cells and examine their viability, the cell-laden structures need to be stained prior to their observation (chapter 3.4.3 Cell viability assessment). The staining would label the DNA of each cell a different colour, which would show up in the digital images taken by the computer when the appropriate coloured filter was applied (green for live, red for dead).





**Figure 3.4** – *The Nikon Eclipse TE300 inverted fluorescent microscope [238]*

The samples for examination would be placed onto the microscope's platform which could then be manipulated along the X and Y axes by turning the corresponding dials on the microscope. A separate dial may be used for adjusting the focus by moving the microscope lenses closer or further away from the sample. The lenses are installed on a disc which can be rotated by hand to switch between lenses with various magnification levels.

### **3.2.8 Incubator**

For culturing cells and for maintaining the viability of cell cultures or cell-laden structures, an incubator (Panasonic MCO-230AICUV-PE) was used. This is a CO<sub>2</sub> incubator, whereby the CO<sub>2</sub> is supplied to the machine at a concentration of 5% to create a more suitable environment for cells – the CO<sub>2</sub> is provided by two gas cylinders which are stored near the incubator. This incubator has other features such as a full colour LCD touchscreen mounted onto its outer door which provides control and telemetric data of the temperature (~37° Celsius) and CO<sub>2</sub> (~5%) conditions within the incubator itself, and an inbuilt decontamination system to ensure the incubator is cleaned of any potential contaminants.

When moving material in and out of the incubator, both the thick outer and transparent inner doors must be opened to access/deposit cellular material on the various shelves within the incubator. Cellular material must be secured within a sealed vessel such as a

culture flask, petri dish, well-plate, etc. to provide a barrier between cells and the external environment and reduce the risk of cross contamination. The doors should not remain open for a prolonged length of time, else the incubator will experience a temperature drop and fluctuation of CO<sub>2</sub> levels which may pose a risk to the cells within and takes time to re-stabilise.

### **3.3 Materials**

#### ***3.3.1 Preparation of partially crosslinked alginate-based bioink***

The method of partially crosslinking alginate-based hydrogels is adapted from Tabriz et al., [55]. Protanal LF10/60 FT (FMC Biopolymer), a variety of sodium alginate, is prepared as a solution by weighing out the powder and adding it to a solution of distilled water filled to the corresponding volume to create an alginate solution at double the desired concentration for preparing the partially crosslinked bioink. The powder should be added gradually, poured directly into the vortex formed whilst stirring as to promote better dispersion of the powder throughout the solvent, else the powder will aggregate together and form clumps which are more difficult to separate and disperse. The beaker used for preparing the alginate solution should be large enough to accommodate a blender for mixing at a later stage, and the total volume should be small enough to add a secondary solution and blend without the contents overflowing from the beaker used.

A separate solution of calcium chloride dihydrate (Sigma-Aldrich) was prepared by weighing out the powder and adding them to distilled water solvent and stirring. The concentration of the calcium chloride dihydrate solution should be double the desired concentration for the partially crosslinked bioink. The volume of the calcium solution should match the volume of the alginate solution as the two solutions will be mixed at a 1:1 ratio.

With both the protanal alginate and calcium chloride dihydrate solutions, insert the immersion blender into the alginate solution occasionally tilting the blender head to try and remove air bubbles from the blender head as it is inserted into the solution. The calcium solution is then added and the blender is quickly turned on to mix the alginate and calcium together as effectively as possible to ensure even dispersion of calcium ions to all of the alginate to attain more homogeneous ink properties. Better blending is achieved when the blender head is moved around the beaker, both concentrically and vertically, to ensure the mixing is as effective as possible. The mixed contents were

then stored in a fridge for a day to gradually crosslink homogeneously over the period of 12 hours to reach steady state mechanical properties.

Once the prepared partially crosslinked hydrogel has been left to crosslink for some time, the contents were spooned into conical tubes and centrifuged to remove as many air bubbles as possible. With as little entrained air as possible, the centrifuged partially crosslinked alginate is then carefully aspirated with a large syringe and long, wide nozzle to load the syringe with material, which is then transferred slowly in the bioprinter's syringe barrel via a female luer lock adaptor to fill up the bioprinter's 10 cc syringe barrel with as little air as possible.

### ***3.3.2 Preparation of quiescently gelled gelatine support baths***

Support bath solutions were prepared by weighing out calcium chloride (anhydrous, granular, C1016-2.5KG, MW 110.98, Sigma-Aldrich) to strengths of 0, 4, 8, and 12 milliMolar and mixed with water to the appropriate volume. 0.6% to 1% w/v gelatine (from Porcine skin, Type A, ~300g bloom, G1890-500G, Sigma-Aldrich) were then weighed out, added to the calcium solution, filled to volume with warm water and then allowed to mix until the powder had dissolved entirely at approximately 60° Celsius. The solution when sufficiently mixed is then poured into containers until they are nearly filled to capacity and stored in a fridge at 4° Celsius for at least 12 hours to allow the solution to set. Once set, the gelatine support bath behaves as a soft-solid gel which is rigid enough to withstand inversion but simultaneously permeable enough for a nozzle to travel through and heal itself. To improve the printability into prepared gelatine baths, residual liquid resting on top of the gel may be removed by aspirated gently or dried away with paper towels.

For preparing gelatine support baths for cell-printing applications, the Gelatin powder was sterilised by gamma irradiation and weighed out inside a sterile LEV hood to the appropriate mass for 0.8% w/v concentration. CaCl<sub>2</sub> was weighed out to the concentration of 8 mM and mixed with the gelatine powder, using distilled water as the solvent and filled to volume. The materials were mixed together thoroughly at 37° Celsius using a mixer to dissolve the gelatine powder with the CaCl<sub>2</sub> solution. Once dissolved, the contents were poured in equal distributions into each well of a 6-well plate. The lid was then sealed and stored in a fridge at 4° Celsius for 12 hours/overnight to reach steady state gelation.

### ***3.3.3 Preparation of agar fluid gel support baths***

Supportive agar fluid gels were formulated by dispersing commercially available agar powder (agar-agar, Special Ingredients) weighed to concentrations between 0.2% to 2% w/v were added to calcium chloride solutions between 0 to 40 milliMolar concentrations. Agar powder does not clump like the protanal alginate powder does, so all of the powder was added at once. Whilst being stirred, the mixture was heated to a temperature of 95° to 100° Celsius to activate the thermo-gelling properties of the agar powder; once this temperature had been reached, the mixture was left to mix at this temperature for three minutes before being removed from the hotplate. Once removed from the hotplate, the solution was left to cool. Gelation occurs quickly once the solution cools to a temperature of around 40° Celsius, and theoretically could be processed immediately – however the agar was left overnight for at least 12 hours in a fridge to ensure steady state mechanical properties beforehand.

Once the agar was suitably gelled, the immersion blender was used to mechanically break up the gel into gelled microparticles. This was achieved using the lowest speed setting on the blender and moving the blender head around inside the beaker as much as possible to ensure that all large chunks of gel had been blended. Over the course of blending, the texture and consistency of the gel changes – initially the texture is rough as the gel chunks are relatively large, but eventually the consistency of the gel becomes smoother which is an indication that the gel has become fluidised.

Once blending has been completed, the agar fluid gel is stored en masse in the fridge for preservation. Prior to use as a supportive medium, agar fluid gel is poured into centrifuge tubes and spun in the centrifuge to remove air bubbles which may have become entrained during the blending process. Once this is done, the fluid gel is ready to be poured into a container to support the fabrication of alginate-based structures. When diluting the fluid gels, the agar and secondary solutions are added to centrifuge tubes at respective volume ratios of 3:1, 1:1, or 1:3 (agar-to-diluent), and then pre-mixed by shaking the tubes by hand and then removing any entrained air bubbles via use of the centrifuge.

## **3.4 Biological Methods**

### ***3.4.1 Cell culture***

HepaRG cells, were maintained in a 2D cell culture with Williams' E media, supplemented with 10% foetal bovine serum (FBS), insulin, hemisuccinate, GlutaMAX,

penicillin, and streptomycin. Cell cultures were maintained in cell culture flasks and stored in an incubator to grow. The cultures were examined every two-to-three days to assess their growth to check for confluency, after which cells were split into multiple cell culture flasks at a split ratio of 1:4, or if there were enough cells they were incorporated into the partially crosslinked alginate hydrogel to create cell-laden bioinks or formed into cell aggregates. The cells were used between passage 6 and 10.

### ***3.4.2 Preparation of cell-laden bioinks***

To prepare cell-laden bioinks, cells were removed from their cell cultures by dissociating the cells from the flask's surface with TRYPLE, which was added to the flask for three minutes before being neutralised twice with PBS. Cells adhering to any surfaces were mechanically detached from the flask's surfaces after exposure to TRYPLE by tapping the flask. Williams' E media is then added to the detached cells in the flask and pipetted up and down to break up any clumps prior to their removal into a centrifuge tube. The cells were then centrifuged to pellet them and then resuspended in HepaRG media at a density of  $10 \times 10^6$  cells per millilitre, twice the desired cell density for bioprinting. The cells and media were mixed at a 1:1 ratio with the partially crosslinked 2% protanal to produce bioinks which were 1% w/v alginate by final concentration with a cell density of  $5 \times 10^6$  cells per millilitre.

For HepaRG aggregate encapsulation and printing, HepaRG aggregates were formed using standard, non-adherent agarose microwell plates over 4 days, with 100 cells used per aggregate/well. After 4 days, aggregates were gently pipetted out of the wells, and lightly pelleted at a slow speed. The supernatant was removed and the aggregates were then re-suspended in HepaRG media and mixed with the partially crosslinked alginate as described previously to a final aggregate density of approximately 25,000 aggregates per millilitre.

Cells were incorporated into the syringe barrel with the use of the cellmixer tool. The mixing unit was fitted with two-material filled syringes: one being the HepaRG cells and media, the other being the partially crosslinked 2% protanal hydrogel. On the other side of the mixing unit, an empty syringe barrel to be filled with the cells, media, and hydrogel mixture. Ensuring that the mixing unit has been pre-loaded with hydrogel, the two materials can be depressed simultaneously to have their contents transferred into the empty syringe barrel, whilst occasionally forcing material back and forth through the mixing unit to ensure better mixture homogeneity.

### ***3.4.3 Cell viability assessment***

Cell viability in both the cell-culture and cell-aggregate printed structures were assessed using fluorescein diacetate (FDA) to label live, metabolically active cells, and propidium iodide (PI) to label the exposed DNA of dead cells. FDA and PI solutions from stock were mixed with the cell culture media for the HepaRG cells at concentrations 1  $\mu\text{l/ml}$  and 6  $\mu\text{l/ml}$  respectively. Structures were incubated in FDA/PI for 20-30 minutes before washing once with PBS and imaging on the inverted fluorescent microscope. The viability of both single cell and cell aggregate bioprinting was assessed at day 0, 2, and 7 when the experiment was terminated.

## **3.5 Operational Methods**

### ***3.5.1 Modelling***

3D printing is most typically conducted using a computer generated 3D CAD model to obtain the geometric data necessary for replication. Many of the CAD models were generated manually using SolidWorks 2012 CAD software. Using such software is advantageous for quickly creating simple geometries such as cubes, cuboids, cylinders, spheres, etc. as such geometries do not require lengthy or otherwise complex processes.

For more complex models, such as hearts, noses, ears, etc. where the geometry is not simple or quick to generate in SolidWorks, searches were conducted for existing models on Thingiverse and GrabCAD online CAD model libraries. The major benefit of using online libraries is that highly detailed models can be obtained, sometimes being generated from more sophisticated 3D modelling techniques such as data from computerised tomography (CT) scans for anatomical models.

Any model irrespective of whether the model was created manually in SolidWorks or obtained from an online source was viewed and assessed for geometric defects in the Netfabb software. Netfabb allows for erroneous 3D models to be repaired, resolving geometric issues such as empty holes and tessellation errors for example which may cause prints to fail in some regions. Furthermore, all orientation and positioning-related operations were conducted within Netfabb as the software offers better positional control than the version of Slic3r used; Slic3r could only orientate models around the Z-axis whereas Netfabb allows for model rotation around the X, Y, and Z axes.

### ***3.5.2 Slicing and g-code generation***

Once a 3D model had been generated or obtained from a library, the models were imported into Slic3r (version 1.1.7), which is open-source slicing software, in STL file format. The software offers a high amount of control over all aspects of the print settings, allowing the user to specify layer heights, print speeds, extrusion multipliers, nozzle diameters, infill patterns and densities, retraction control, horizontal and vertical shells, etc. With the model imported into the software and the settings all defined, the model may then be sliced and exported into g-code for the printer to read and execute.

When the use of Slic3r was deemed insufficient to achieve particular goals, such as continuous Z-axis motion as opposed to stepped layering, Excel software was used to plan and create simple executable g-code from scratch. Excel was only used for printing spiral or spring-like structures during coaxial printing. The plan for writing g-code in Excel was to split the tasks into two: plotting the X/Y plane co-ordinates and plotting the Z-axis coordinates. Springs and spirals resemble a circle when viewed from above onto the X/Y plane, so a circle with a defined diameter can be split up into a finite number of X and Y coordinates by dividing a full 360° circle into many small angular increments; dividing a circle into 100 data points will provide an X and a Y coordinate at every 3.6° of the circle which are calculated using sine and cosine functions at the respective angle. The Z-axis was calculated to have an equal number of data points as the X/Y plane so that the start and the end of the g-code would match up together. The Z-axis coordinates were determined by defining a total structure height and pitch to create structures with the desired number of circle revolutions. Excerpts of the Excel spreadsheet for creating custom g-code spirals are included in Appendix B – Using Excel for Spiralling Structure G-code Generation.

### ***3.5.3 Printing***

Printing with the developed bioprinter was achieved by storing the generated g-code files on an SD card inserted into the LCD2004 display which can then be read by the machine and executed. Files were moved from the PC to the SD card via a supported SD card slot on the PC itself.

When connected to the bioprinter with the USB type A cable, the Pronterface software may be used to send g-code files to the machine for execution. As an SD card was preferably used, Pronterface was not used for this purpose. However when coaxial printing was conducted there was a need for simultaneous control of two material feeds.

The biprinter would handle the core material feed using data within the file's g-code found on the SD card, and a secondary microcontroller board connected up to a syringe pump controlled by a PC running the Pronterface software by directly sending a controllable extrude command to drive the shell material feedline.

#### ***3.5.4 Systematic strategy for optimising print quality***

A method for iteratively improving the quality of prints was developed and utilised throughout the period of support bath printing research. This method was used primarily when little or no prior print quality data was available. The method works by careful control and consideration of the relationship between extrusion rate and translational speed of the nozzle [126]. For this method, the overall extrusion rate is considered as the product of the extrusion speed multiplied by the extrusion multiplier. This realisation was made whilst tuning the settings within Slic3r - doubling the print speed without changing the extrusion multiplier actually doubles the extrusion rate because the total extruded material volume is deposited in half the time. Thus if the next print were to be conducted at double the print speed and half the extrusion multiplier, the extrusion rate is maintained consistent but the nozzle can be moved faster; controlling the speed in this manner allows for thinner, or thicker, lines to be extruded without exceeding the motor's extrusion capabilities.

The initial print settings are arbitrarily defined within reason whilst conducting the first print and the user must assess the print quality of the finished structure. There are several outcomes which can then be used to feedback into the optimisation strategy for the next iteration of printing: (1) the structure is overextruded, (2) the structure is underextruded, (3) the extruder's gears struggle to extrude at the set extrusion rate, or (4) the print quality is good. Taking note of the print speed and extrusion multiplier, if the outcome is an overextruded or underextruded structure then the ratio of extrusion rate to translational speed needs to be tuned – when overextruded, the extrusion multiplier needs to be reduced and print speed increased and vice versa for underextrusion. If there is evidence of the extruder struggling to extrude, most noticeably observed by a knocking noise coming from the extruder's gears, then the overall extrusion rate is too great and both the print speed and extrusion multiplier need to be reduced; such an outcome only occurs when the extruder's torque is too low to extrude viscous material at too great an extrusion rate.



Starting from reasonably arbitrary speed and extrusion multiplier values, convergence towards an optimal outcome can be quickly achieved by making the correct observation and doubling/halving the corresponding settings and then printing again. With the second set of print data, if the structure remains overextruded or underextruded then the corresponding values may be scaled by a factor of two again until the quality of printed structures begins to improve. Over multiple iterations, overextrusion or underextrusion related issues should begin to disappear and the structure should see significant improvement in print quality. At this point, smaller adjustments may be made to fine tune the print parameters to optimise the print quality of structures printed with a consistent nozzle size.

### ***3.5.5 Releasing printed structures from gelatine support baths***

Upon completion of the printing process, gelatine support baths with encapsulated structures were taken to a release bath to free the structures in a similar manner to FRESH [134]. Release baths are large volume, low concentration calcium chloride solutions which are gently heated above the melting point of gelatine to liquefy and separate the support from the printed material, releasing and further crosslinking the encapsulated structure within. The concentration of the release bath can be fine-tuned to ensure appropriate crosslinking depending on the size and wall thickness of the structure being released. The total exposure time of structures to calcium solution can also be varied between short to long crosslinking times – sufficient crosslinking times are dependent on the size and wall thickness of the structure as well as the calcium concentration used.

For printing alginate structures without cells, the structure may be left in the release bath for long periods of time at high calcium concentrations to produce strong structures which can easily be handled manually. Large or dense structures need prolonged exposure to calcium at increased concentrations to thoroughly crosslink deep into the structure; otherwise structures will be internally too soft to support their shape.

To release the cell-laden structures 50 milliMolar barium chloride ( $\text{BaCl}_2$ ) was dissolved in HepaRG media, warmed to 37° Celsius, added to the well on top of the gelatine bath, and then incubated for 30 minutes at 37° Celsius to allow the gelatine to liquefy. To clarify, the use of  $\text{BaCl}_2$  was strictly to permanently crosslink bioprinted structures and was not employed in the preparation of gelatine baths. Liquefying the gelatine in the incubator enabled the HepaRG media and  $\text{BaCl}_2$  to mix with the printed

cell-laden structure to simultaneously provide nutrients and further crosslinking. Released structures were then thoroughly washed with PBS, before being submerged in HepaRG media. Cell media was changed every 2-3 days.

### ***3.5.6 Releasing printed structures from agar fluid gel support baths***

Structures printed within agar fluid gel support baths may be released by adapting the prior method of releasing gelatine support baths. Vessels containing printed structures were submerged in a release bath filled with 10 millimolar calcium chloride. The fluid gel surrounding the structure was removed by carefully jetting release bath liquid manually around and under the structure using a syringe fitted with a wide and long nozzle (1.5 inch 18 gauge nozzle). Jetting the liquid underneath the structure within the print vessel causes the attached fluid gel and structure to lift out of the container and into the release bath, making it easier to remove the fluid gel surrounding the structure. The structure, now supported by the buoyant forces of water, can be rotated around by slowly stirring the release bath to induce some vorticity which in itself can help to remove residual agar fluid gel from the structure in conjunction with manual jetting. Liquid should never be jetted perpendicularly to the surface of the printed structure as the forces may cause structural damage; instead the liquid may be jetted at angles parallel to the surface to remove adherent agar on the structure's walls. With the structure now fully released and all surrounding agar removed, structures could be further crosslinked within the release bath via prolonged exposure to the calcium content there, or may be scooped out of the release bath carefully using another vessel with appropriate dimensions to fit into the release bath and hold the structure securely. Structures stored in their new containers could be further crosslinked by adding  $\text{CaCl}_2$  or  $\text{BaCl}_2$  to further enhance their mechanical rigidity, depending on the size and complexity of the structure.

## **Chapter 4 – Development of a Modular Extrusion Based 3D Bioprinting Platform**

### **4.1 Introduction**

Of the numerous bioprinting strategies available, the extrusion-based bioprinting method was chosen with the key advantage of being capable of affixing a long nozzle to the extrusion system for insertion within a supportive medium to assist with the 3D bioprinting of more complex geometries. The extrusion-based approach, whilst considered to have a lower resolution compared to other techniques, can have a moderately quick fabrication speed and thus would be beneficial in the respect that cells would be outside of an incubator for less time compared to other methods when fabricating structures of a similar scale.

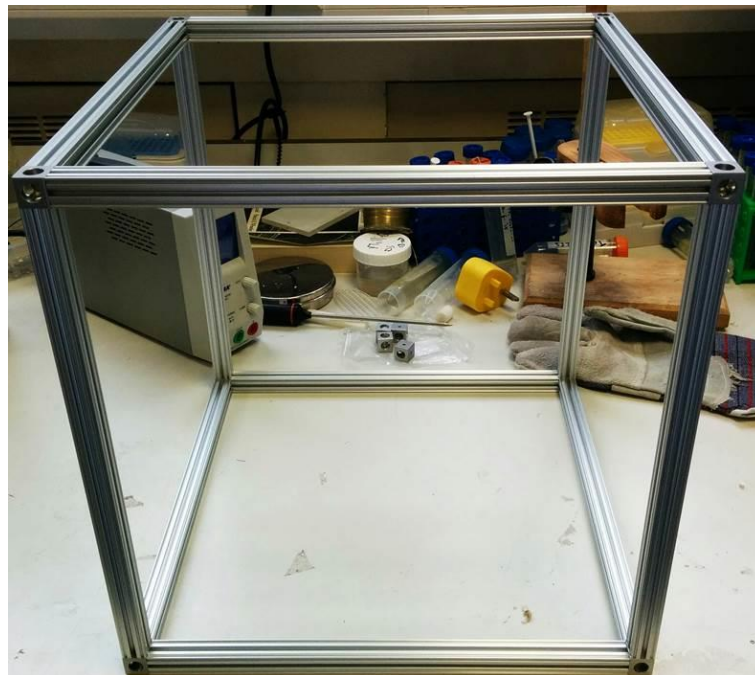
The designed extrusion-based bioprinter was built with modularity in mind. The benefit of a modular design is that modularity innately lends itself to scalability, so long as suitably smaller or larger components of the same profile can be obtained. An eventual goal of integrating multiple interchangeable printheads within a single bioprinting system would be more easily realised in a modular system; a system could be designed to cater for large volume fast printing, small volume high resolution printing, and every trade-off in-between by swapping between extrusion-based printheads for a droplet-based printhead or other modality to meet the fabrication needs of the bioprinted structure in question. However, the current goal is to develop an extrusion-based bioprinting system to accommodate support bath printing.

In addition to design modularity, the incorporation of open-source technologies was also intended as a key design feature; the reasoning for this was to accelerate the development process of the printer and begin 3D bioprinting as quickly as possible. Many technical and difficult challenges regarding the construction of a RepRap-based 3D printer have already been solved, exist online, and are readily distributable with an open source license. Therefore a lot of development time is spared by simply creating a bioprinter which follows the relevant, readily available open-source technologies that exist online. Furthermore, as there are many open-source technologies in the field of 3D printing, there are many options to choose from with regards to which software(s) are best suited for the particular 3D bioprinting-related process at hand.

## 4.2 Hardware

### 4.2.1 Bioprinter frame – creating the X/Y/Z axes

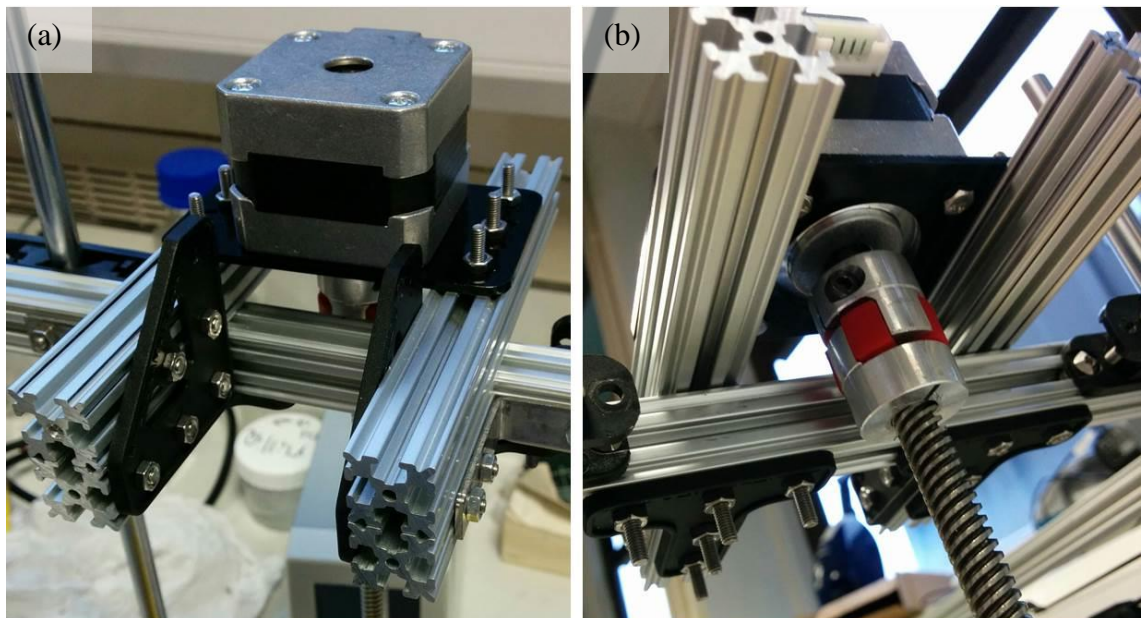
The frame of the bioprinter was constructed from modular aluminium extrusions (OpenBeam) as part of a construction kit. Each aluminium extrusion has a 15 mm x 15 mm square profile and comes in lengths of 30 mm, 45 mm, 60 mm, 90 mm, 120 mm, 150 mm, 210 mm, and 300 mm. To maximise the available printing space for 3D printing, the largest extrusions were used to build a cubic frame giving the printer external dimensions of 330 x 330 x 330 mm<sup>3</sup> with an internal volume of 300 x 300 x 300 mm<sup>3</sup> (figure 4.1). Each beam was connected together via corner cubes which help to ensure that the assembly is maintained ‘square’ throughout the assembly. Each corner cube consists of three small holes for fastening the aluminium extrusions with M3 x 6 mm button head socket bolts, and three larger holes to provide access for a hex key driver to tighten said bolts into the beams; this required an internal thread to be cut into the centre holes of the beam’s profile using an M3 sized tap prior to being fixed to the corner cubes.



**Figure 4.1** – The 3D bioprinter’s frame consists of 12 beams fastened together with 8 corner cubes. The empty space within the frame has a volume of 300 x 300 x 300 mm<sup>3</sup>

The next assembly step was to affix the NEMA 17 stepper motors for the Z- and Y-axes onto the frame. For the Z-axis, a linear stepper motor with leadscrew was attached to a NEMA 17-sized motor mounting bracket, allowing the motor to be affixed to the frame.

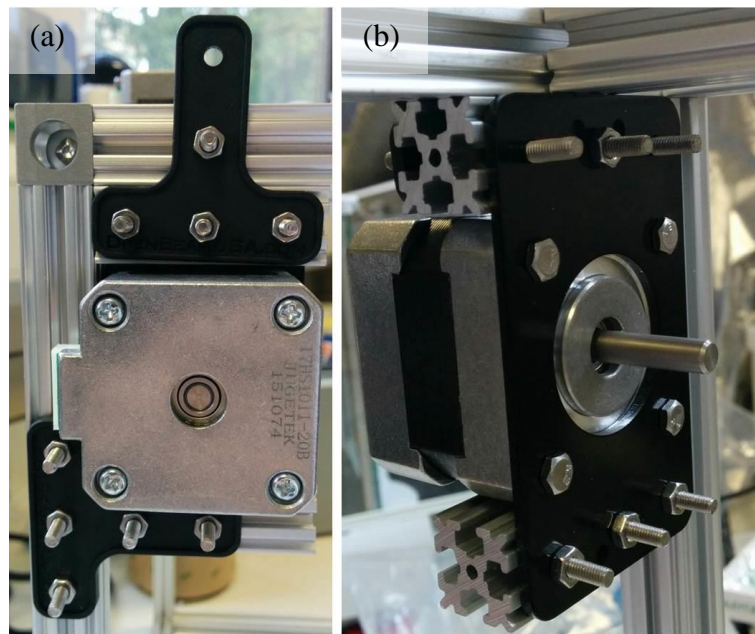
The specific motor used had a 350 mm long tr8\*8(p2) leadscrew built into it, which would mean that the leadscrew would jut out from the bottom of the frame unless the assembly was taller or the leadscrew was cut to length; to avoid unnecessary risk of damage to the leadscrew's threads, the assembly was designed to be taller at the Z-axis motor's mounting point. This was achieved by using some of the smaller beams to simultaneously raise the motor's height by 15 mm whilst also providing a fixing point offset from the back of the frame for the motor mounting bracket to affix to (figure 4.2), and doing so slightly increased the amount of free space available along the Y-axis for printing. The unaccounted 5 mm difference between the frame's dimensions plus the motor assembly and the motor's leadscrew length was addressed by the inclusion of adjustable feet underneath the printer, which raised the frame by the required distance and provided better stability.



*Figure 4.2 – (a) the Z-axis motor mounting assembly consists of a NEMA 17 motor affixed to a mounting bracket which are bolted onto beams below, which are affixed to the frame with corner brackets, 'L' brackets, (b) and 'T' brackets.*

The Y-axis stepper motor is affixed externally onto the frame from the left-hand side. Similarly to the Z-axis, the Y-axis motor required an assembly of two smaller 45 mm beams, two 'T' brackets and a NEMA17 motor mounting bracket in order to be successfully mounted onto the side of the printer. As before, the NEMA 17 motor is attached to the motor mounting bracket, but is then fixed to the two 45 mm beams which are then fixed to the frame with the two 'T' brackets (figure 4.3). At any point

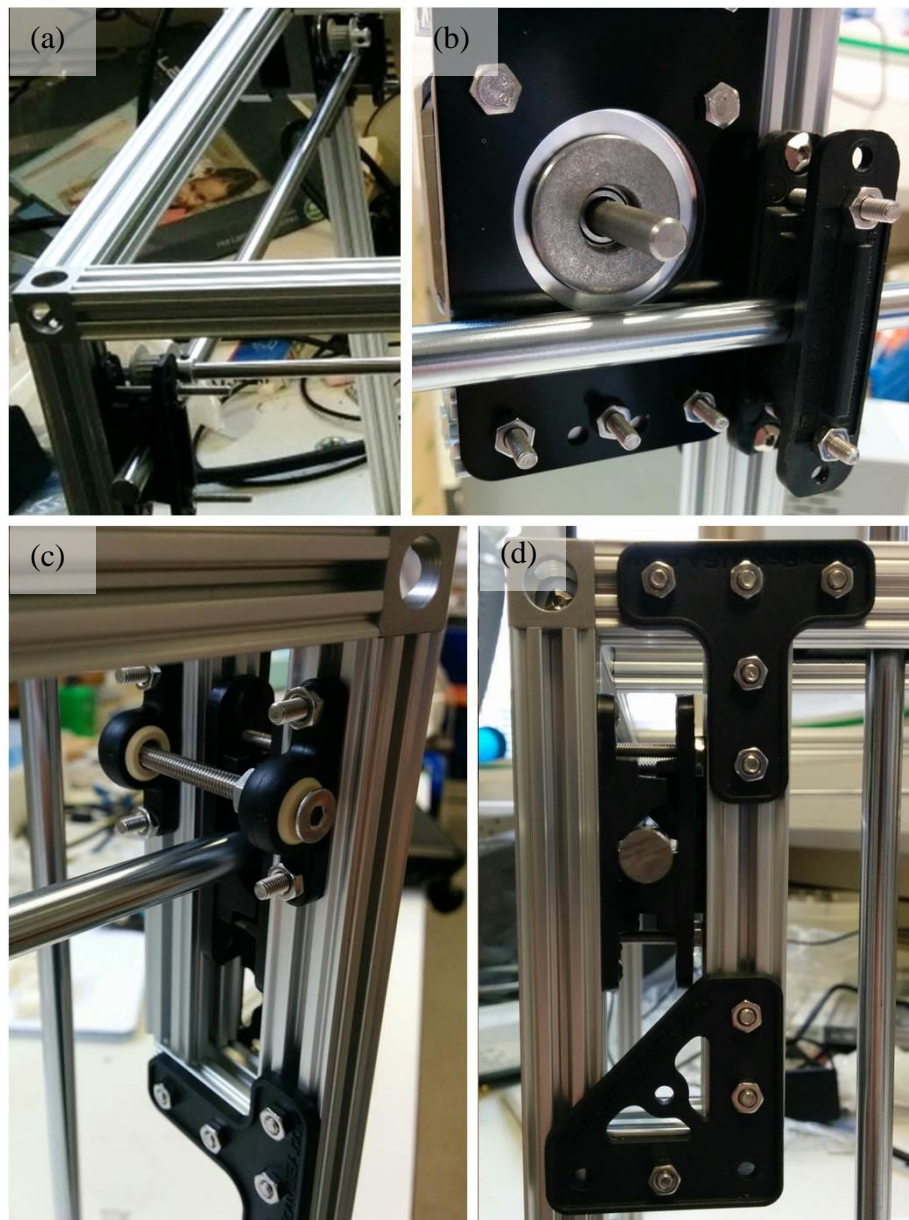
from now, a GT2 20 tooth pulley may be affixed to the flat edge of the Y-axis stepper motor's motor pin by tightening a grub screw situated on the pulley's hub.



**Figure 4.3** – (a) Y-axis stepper motor attached to the frame using two ‘T’ brackets and two 45 mm beams (b) to affix the motor’s mounting bracket to the frame

Once both the Z- and Y-axis stepper motors have been mounted to the frame, the next stage of the assembly was to add the respective linear rods. The rods allow for a carriage to be directed along a single axis with the drive provided by the stepper motor. The Z-axis linear rods are affixed to the frame at equidistant points from the Z-axis stepper motor using OpenBeam’s shaft clamps. The Y-axis has its linear rods positioned at a height slightly below the stepper motor’s pin, and are affixed internally to the left and right sides of the frame. The left side linear rod is simply affixed to the back end of the frame using shaft clamps, but the right side rod required a small assembly to enable the incorporation of an idler pulley. This assembly used a 30 mm beam, a 90 mm beam, two ‘T’ brackets, one ‘L’ bracket, a pair of shaft clamps, and two pedestal bearings, and a bolt with a nut to hold a ‘shaft’ in place for a pulley to rest on. Both linear rods have a corresponding set of shaft clamps positioned at the front of the printer to correctly support them and ensure their accurate positioning on the frame. The positions of both Y-axis linear rods are shown in figure 4.4.

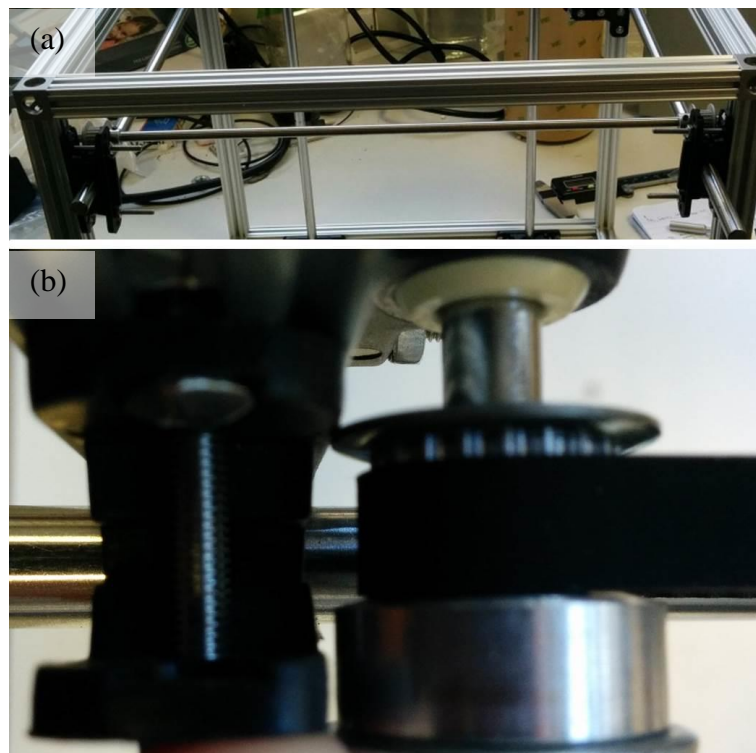




**Figure 4.4** – (a) View of the left Y-axis linear rod for guiding the Y-axis carriage – (b) the rod runs slightly beneath the motor’s pin, (c) at the printer’s right side, an assembly of beams and brackets allows for locating of an idler pulley’s shaft and (d) fixing of the linear rod

As there is only a single Y-axis stepper motor, a coupling is required to translate the drive from the left side to the right to balance the pulling forces at either end of the X-axis carriage when moving along the Y-axis. This was achieved by having a 333 mm long, 5 mm diameter steel rod fitted with two GT2 20 tooth pulleys which when belted and driven by the motor will cause the rod to rotate, transmitting rotational movement from the left side of the Y-axis to the right side which when belted onto the secondary Y-axis carriage can then be converted back into linear motion, providing a driving force

on right side of the X-axis carriage. The coupling rod was supported by two pedestal bearings mounted onto the printer's frame at the front of the printer, and two shaft collars were used to linearly constrain the rod along the horizontal plane whilst still allowing rotational motion (figure 4.5). Each pulley was aligned directly above the linear rod to maintain a parallel relationship between the belt and the rod which in turn keeps the axis movement as smooth and balanced as possible. The heights of the coupling rod and pulleys were positioned to correspond with their respective pulleys at the back of the frame; the pulleys are only locked in place with a grub screw once the GT2 timing belts have been added.

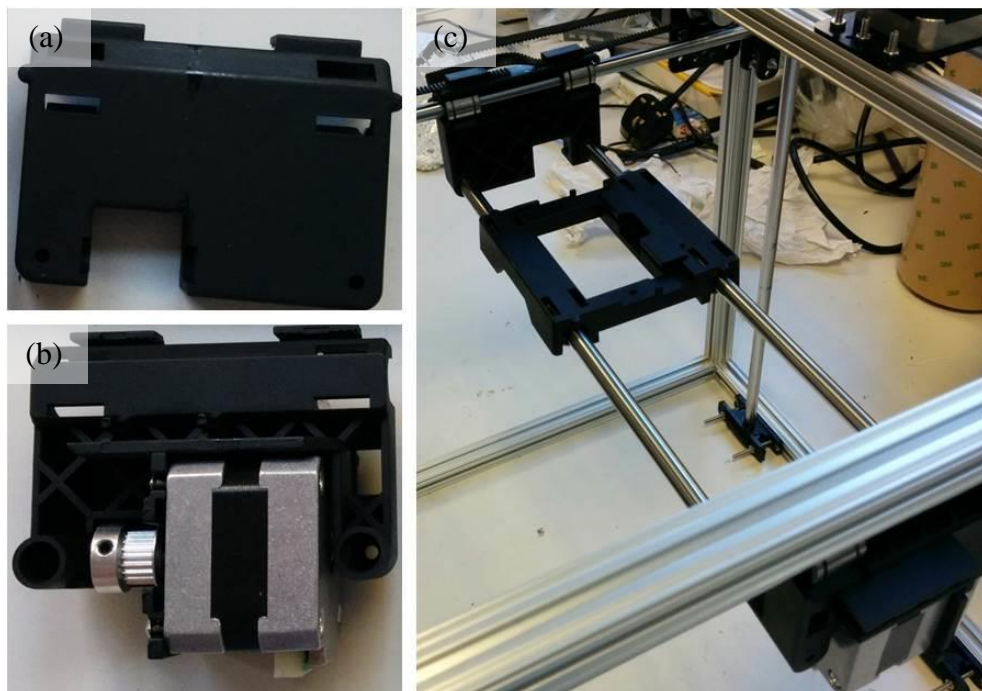


**Figure 4.5** – (a) The Y-axis coupling rod at the front of the frame is supported by two pedestal bearings positioned above the shaft clamps behind the vertical beams, (b) a close up view showing a GT2 pulley and belt aligned parallel with the linear rod

At this point, the carriages for the X- and Y-axes can now be added. The X-axis carriage consists of a central plate which will later support the extruder, fitted with four linear LM8UU bearings which slide onto two linear rods along the X-axis. Before the X-axis is connected to the Y-axis carriages, the X-axis stepper motor should to be affixed to the secondary Y-axis carriage in the corresponding space – this is most easily done prior to being placed on the printer for ergonomic reasons. The X-axis linear rods can be fitted into the corresponding holes on the primary and secondary Y-axis



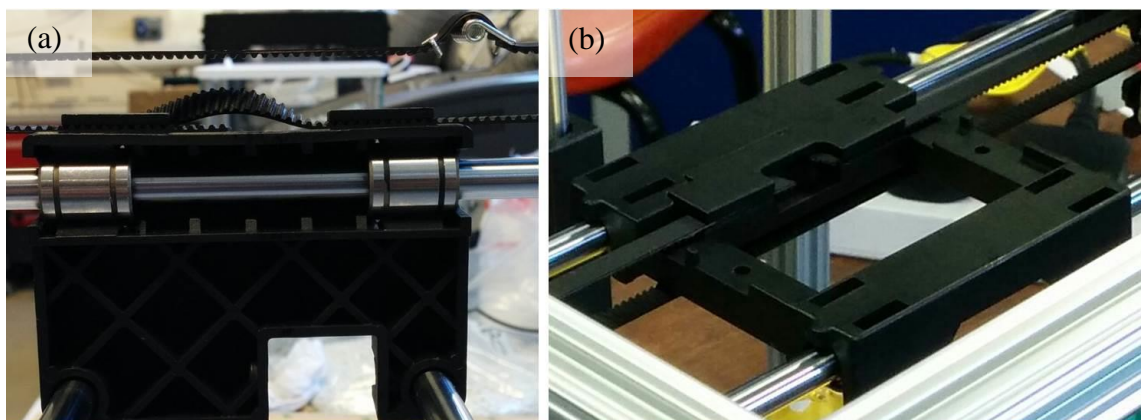
carriages at the left and right hand side of the printer. Once this has been done, each Y-axis carriage fitted with two linear bearings each is inserted onto the Y-axis linear rods added earlier (figure 4.6). Doing this requires that the respective Y-axis shaft clamps are temporarily removed to allow the carriages to slide onto the rods. The primary Y-axis carriage has a slot for locating an idling shaft; as one was not readily available an idler shaft was fabricated using a metal turning lathe to turn a steel rod down to the correct diameter and length to be inserted within a pulley and rest within the slot. The idler shaft and pulley is necessary to return the X-axis belt back to the stepper motor's pulley on the other side of the axis.



**Figure 4.6** – (a) The primary Y-axis carriage (b) with space for a NEMA17 stepper motor to drive the X-axis, (c) the complete carriage assembly showing the positions of all carriages including the X-axis carriage

Once the carriages have been added, the GT2 timing belts can be attached to each axis and slotted into the respective grooved slots on the carriages to provide the pull necessary for linear motion when driven. The belts are open-loop sections and are fitted slightly differently on the X- and Y-axes. Starting at one open end of the belt for both the Y-axis carriages, the belt is slotted into the grooved profile on the carriage, looped around the nearest pulley at one side of the frame, then looped around the pulley at the opposite side of the frame and then fixed into the second set of grooves in the Y-axis carriage as tightly as manageable; belt tension on the Y-axis is improved by affixing a

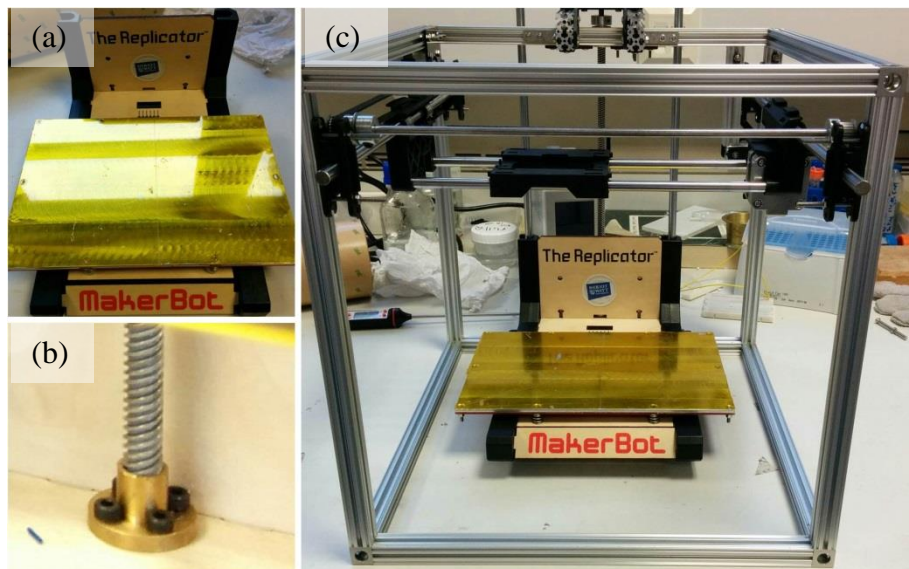
belt tensioning spring to the bolt section at a position above the carriage when situated around the midpoint along the Y-axis (figure 4.7). The X-axis carriage differs from the Y-axis in that the belt is held with a push-fit clamp with a toothed profile which matches the belt as opposed to the grooved slots which were seen on the Y-axis carriages. This makes affixing the X-axis belt more difficult as too much tension can cause the clamp to pop open and release the belt unintentionally, thus both hands are needed; one to hold the clamp down in place as tightly as possible, the other manages the looping. If this step proves too difficult, an assistant may be necessary. Starting from the open end of the belt affixed to one side of the X-axis carriage, clamp the belt down into the toothed profile, loop the belt around the stepper motor's/idler shaft's pulley, bring the belt around to the other pulley, loop the belt around and then clamp the belt down as tightly as possible into the other side of the X-axis carriage. This belt cannot be tensioned as tightly as the Y-axis due to the nature of the push fit clamp - attempting to add a belt tensioning spring causes the belt to pop out from the clamp and will need to be belted again; however the extruder housing (affixed later) will be attached onto the carriage and positioned over the push fit clamp which when bolted can apply some additional clamping force to hold the belt in place as tightly as possible.



**Figure 4.7** – (a) View of the primary Y-axis carriage from the perspective of the X-axis carriage showing the belt tensioning spring and affixed GT2 belt, (b) the X-axis carriage showing the GT2 belt held in position with a push fit clamp

With the X- and Y-axis carriages fitted onto the frame and belted, the Z-axis platform can be added. The platform is the same as the ones used in the original MakerBot Replicator series of 3D printers because the components were readily available for use in the lab and offers robust support and resistance to cantilever bending to help maintain accurate Z-axis positioning during printing – the importance of this is emphasised when

considering the fact that the weight of a support bath can be significant, particularly since the density of a support bath is at least that of water and scales with the print volume necessary to fabricate structures of larger scale. The platform consists of two 'L'-shaped arms at each side, which secures the horizontal print stage with (inactive) hotplate and vertical back panels firmly in place. Between the vertical back panels is a slot for a tr8\*8 (p2) leadscrew nut which corresponds with the leadscrew profile of the Z-axis stepper motor. Located at the side of the 'L'-shaped arms are slots for two linear bearings each, which should align with the Z-axis linear rods affixed to the frame earlier – if the linear rods do not align with the bearings on the platform's arms then this can be corrected by re-measuring and repositioning the linear guide rods and shaft clamps. When everything is ready to be positioned, the Z-axis linear rod's shaft clamps at the bottom of the printer should be temporarily removed to allow the platform to be raised up into the printer from below. The platform may then be secured to the frame by aligning the linear rods and leadscrew with the respective parts on the platform and manually rotating the leadscrew by hand so that it is driven into the nut which then lifts the platform up into position (figure 4.8) – the detent torque of the Z-axis stepper motor is sufficient to hold the platform once in position and the Z-axis linear rod's shaft clamps may be tightened once again.

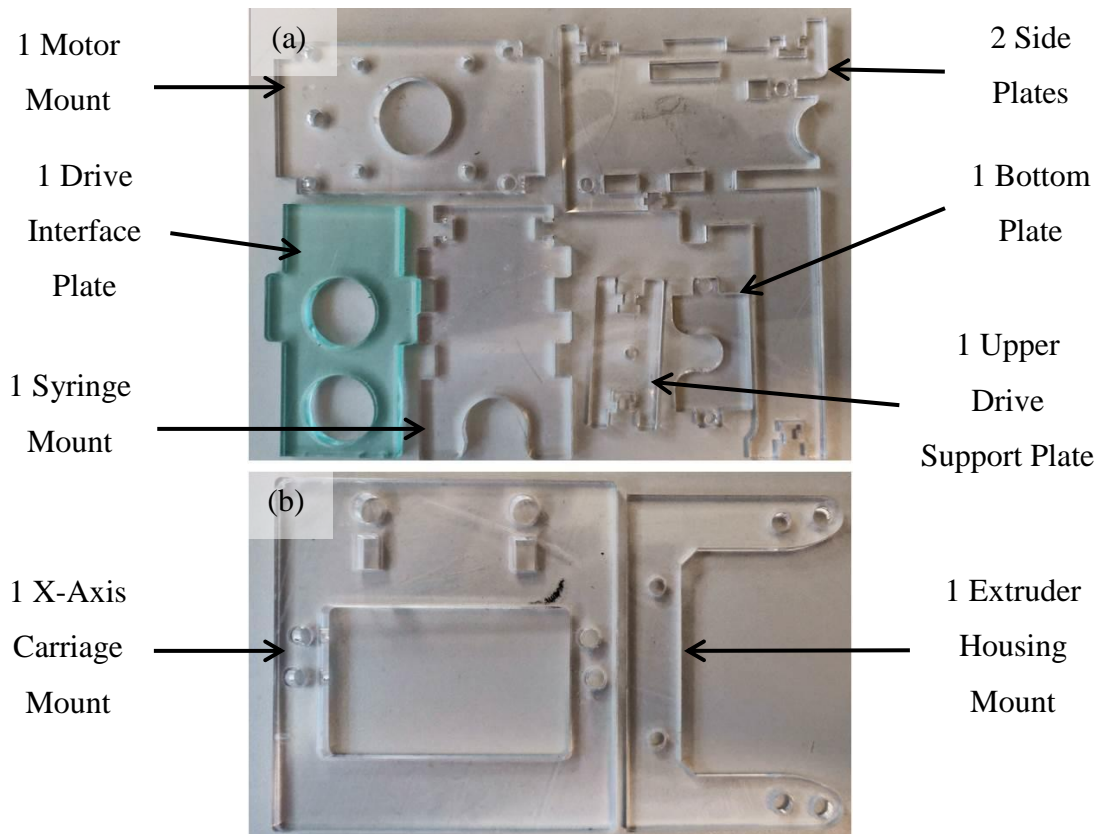


**Figure 4.8** – (a) The Z-axis platform is that of the original Makerbot Replicator 3D printer, (b) the Z-axis leadscrew is joined to the platform between the two back panels with a tr8\*8 (p2) nut, (c) the platform is attached to the frame from underneath by aligning the bearings and nut with the leadscrew and linear rods respectively

#### ***4.2.2 Extrusion system***

The developed bioprinter's extrusion system was inspired and adapted from the Fab@Home model 2 multi-material 3D printer, which notably utilised a screw-driven plunger and syringe barrel to control the deposition of liquid- and gel-like materials through a nozzle [239][240] – a feature which is highly suitable for the deposition of cell-laden hydrogel materials. Additionally the housing to hold the syringe barrel, plunger, and motor could all be readily fabricated from PMMA acrylic sheets with the aid of a laser cutter. The use of a laser cutter to fabricate custom parts to fit an extrusion system to the bioprinter would not be modular in principle, but the open-source license attached to the Fab@Home design would allow for the components to be readily modified to fit modular components such as a NEMA 17 stepper motor, metric nuts and bolts, and 10 cc syringe barrels. The extrusion system comprises of two sub-assemblies: the extruder housing and the screw-driven plunger system.

The extruder housing consists of nine components which fit together with slotting profiles to locate the components and bolts to fix them securely in place (figure 4.9). There is a motor mounting plate at the top for fixing a NEMA 17 stepper motor, with space underneath for affixing two gears to translate the rotary motion of the motor to a threaded rod which vertically displaces a plunger. Underneath the motor plate and gears is the drive interface plate with profiles which keeps the gears in position. Following the drive interface plate is the syringe barrel mount which is circumferentially a push fitting tolerance for the syringe barrel with the barrel's flange resting above the panel. Positioned at the end of the syringe barrel is another plate which secures the syringe barrel's luer locking hub profile in place with a push fit. These four plates are slotted into and bolted onto two identical side panels which hold the extrusion system together. Lastly, the assembled extrusion system is affixed to the extruder housing mount which is secured onto the X-axis carriage mounting panel and connects the extrusion system to the bioprinter's moving axis.

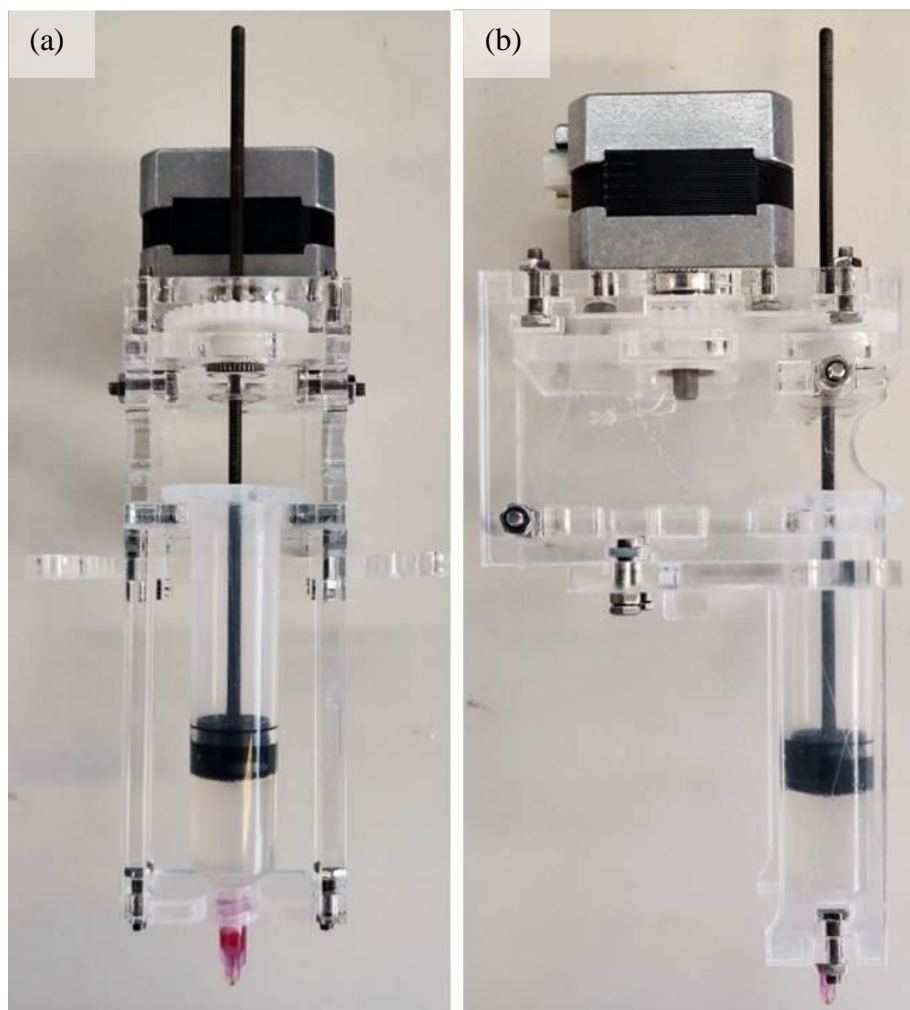


**Figure 4.9** – Laser cut components for the extruder housing assembly, (a) the components for housing the extrusion system, (b) the components for affixing the extruder housing to the printer's X-axis carriage

The screw driven plunger system consists of a NEMA 17 stepper motor, two 0.8 module 35 tooth spur gears with hub and brass insert with a bore size of 5 mm and 6 mm respectively (SDP/SI), an M3 sized 18-8 stainless steel knurled head flanged thumb nut (McMaster-Carr), a threaded rod with M3 profile, a 10 cc plunger, and an M3 sized DIN 467 thin thumb nut (Boneham & Turner). As the stepper motor used does not directly drive a linear rod it cannot be used to directly displace a loaded syringe barrel, therefore the gears are necessary to translate the rotary motion along the extruder housing to a location directly above the syringe barrel with a threaded rod and plunger for material deposition. Using the grub screws with the gears, the wide bored gear may be fixed to the stepper motor's pin and a flanged thumb nut can be fixed to the smaller bored gear. As the flanged thumb nut is fixed to the smaller bored gear, the rotational movement of both components is constrained to each other, allowing for a threaded rod to displace vertically when the gears are driven by the stepper motor. The thin thumb nut is permanently bound to a 10 cc plunger and the M3 threaded rod with a rubber and metal compatible superglue (Loctite), and left for a day to dry and form a strong bond.



The assembly order of the screw driven plunger/extruder housing should start by affixing the NEMA 17 stepper motor to the motor mounting plate, then adding the motor's respective spur gear before being slotted loosely, not bolted, into the side panels. Then the drive interface plate is added to the respective slots underneath the motor plate. The M3 threaded rod with superglued plunger/M3 DIN 467 thin thumb nut is inserted through the small holes located in the motor plate, interface plate, and through the M3 flanged nut inserted within the second spur gear which rests in the space between the two plates and meshes with the gear affixed to the stepper motor. This completes the screw driven plunger system, so the extruder housing is finished when the syringe barrel and luer hub plates are added to the assembly and slotted into the side panels, which may now all be bolted to secure the housing (figure 4.10). The housing is added to both the extruder mount and X-axis carriage mount with slots to locate and bolts to secure the assembly to the moving axis.



**Figure 4.10** – (a) Front view of the assembled screw-plunger extruder based on the Fab@Home system, (b) side view of the extrusion system

### ***4.2.3 Miscellaneous hardware***

The design of the custom built bioprinter includes components which are non-critical to the function of the machine but were added for ergonomic reasons. Such features help the user with machine operation and keep the majority of components together for ease of handling and packing during transportation. Such components are the 3D printed panels for the RAMPS 1.4 microcontroller board, 3D printed mounts for the LCD2004 display, 3D printed fittings to better locate the mechanical endstops on the machine, and 3D printed parts to affix rubber feet to the base of the printer for stability and levelling. Details of such components can be found in Appendix C – Miscellaneous Hardware.

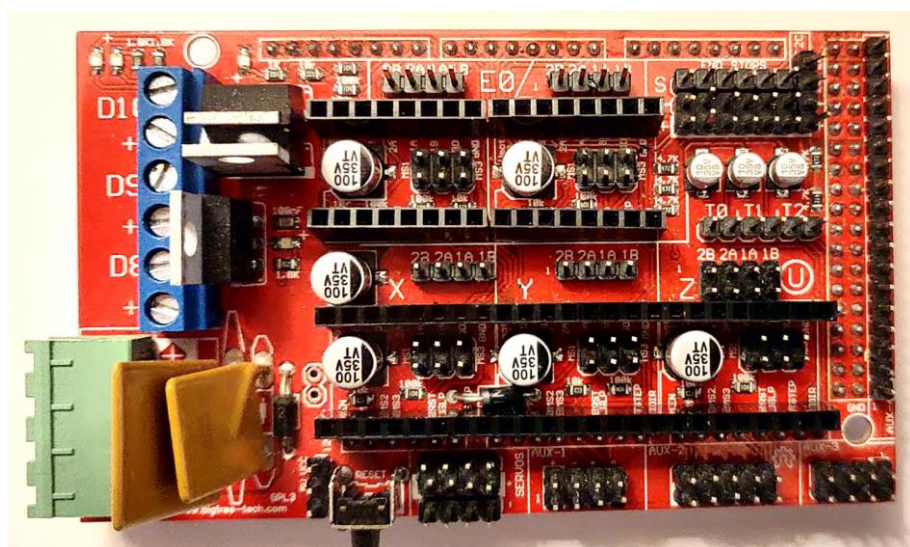
## **4.3 Electronics**

### ***4.3.1 RAMPS 1.4 microcontroller***

Typical 3D printers operate as a CNC machine, taking commands from a central logic unit and operating independently without human intervention except for the initial print setup. The way in which 3D printers achieve this is with a microcontroller which takes a set of inputs in the form of g-code and translates them into physical outputs in the form of motor motion. The developed bioprinter uses a RAMPS 1.4 (Reprap Arduino Mega 2560 Polulu Shield) microcontroller which manipulates the X, Y, Z, and E-axes during printing, and can be connected to a nearby computer via a USB type ‘A’ cable to send commands or to flash the board with new logic.

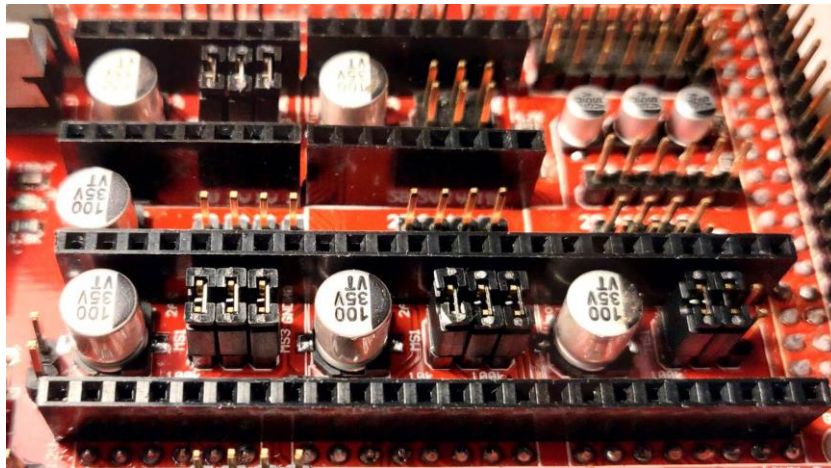
This particular microcontroller was used as it was an easily obtainable commercially available solution based on Arduino technology, an open-source, reprogrammable electronics development platform, which is specifically adapted for RepRap-inspired custom DIY 3D printers. The kit comprised of the Arduino Mega 2560 unit itself and a ‘shield’ (or expansion): the shield adds all the electronic connecting pins to fit up to six motors (one motor in X and Y, up to two Z axis motors, up to two motors for extruders), five Polulu A4988 stepper drivers with heatsinks, and up to six mechanical endstops, and with an adaptor can add an LCD2004 screen with an SD card slot to read g-code files from. The Arduino microcontroller can be considered a modular unit as different shields with various functions can be interchangeably fitted onto the Arduino board as long as the power supply unit (PSU) can adequately satisfy the power requirements – shields may be purchased individually from various electronics/3D printer component vendors or be developed in-house. The stepper motors, jumpers, and PSU were not included as part of the kit and purchased separately.

The RAMPS 1.4 board was pre-soldered so no extra soldering work was necessary for the build; the remaining components were packaged individually and thus required some minor assembly. The shield (figure 4.11), the component to be placed atop the Arduino, needs to have the jumpers installed (figure 4.12) to enable microstepping functionality. The microstep resolution is based on the number of jumpers and the order in which they are installed. The three pins MS1, MS2, and MS3 can either be set as ‘low’ (0) or ‘high’ (1) by either leaving the pins empty or by installing a jumper respectively. With reference to the stepper driver’s datasheet [241], the pin configuration of the jumpers correspond with the stepping modes listed in table 4.1. For attaining the greatest positional resolution, sixteenth-step mode was set by installing a jumper in each of the three MS pins on the shield. Some stepper drivers are capable of greater positional resolution by enabling 1/32<sup>th</sup>, 1/64<sup>th</sup>, and up to 1/256<sup>th</sup> microstepping, but the A4988 stepper drivers that were provided with the RAMPS kit is limited to 1/16<sup>th</sup> by their design. Furthermore, having more microsteps enabled decreases the incremental torque-per-microstep which can be below the motor’s detent torque rating, meaning that enabling too many microsteps can actually hinder positional accuracy if a poorly matched motor is used. The 1/16<sup>th</sup> microstepping capable of the provided A4988 stepper drivers should be comfortably paired with the NEMA 17 stepper motors intended for use, providing a balance of positional accuracy and resolution.



*Figure 4.11 – RAMPS 1.4 pre-soldered shield*





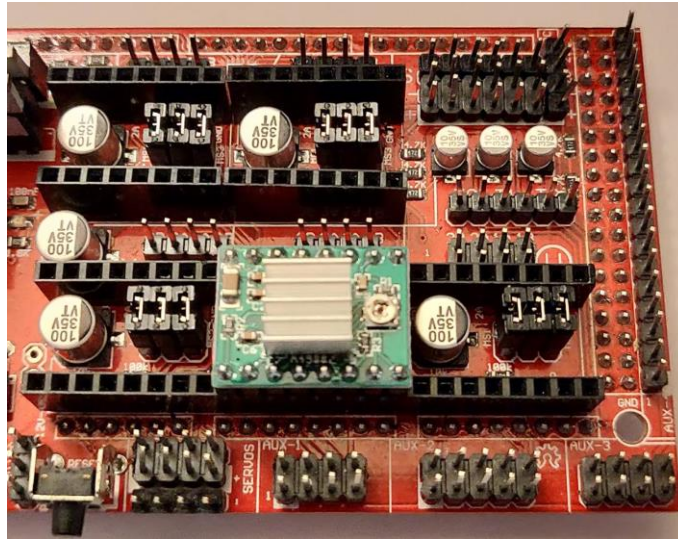
*Figure 4.12 – Jumpers are inserted into their respective pins to enable microstepping*

*Table 4.1 – Pin configurations for various microstepping modes*

MS 1	MS 2	MS 3	Microstep Resolution
0	0	0	Full step
1	0	0	Half step
0	1	0	Quarter step
1	1	0	Eighth step
1	1	1	Sixteenth step

Once the jumpers are installed, the stepper drivers are inserted into their respective slots on the board. Each stepper driver is positioned above the previously installed jumpers in the corresponding locations for E0, E1, X, Y, and Z axes – even when two motors are running concurrently in the Z axis, only a single stepper driver is necessary to control their movements. The orientation of the stepper drivers is critical to ensure the successful operation of the board – for the A4988 stepper drivers provided, the potentiometer of each stepper driver must be on the right hand side of the unit in order for the driver’s GND, VDC, MS, VMOT (etc.) pins to match the corresponding slots on the shield (figure 4.13). If the stepper driver is installed the wrong way around, the stepper driver can be destroyed and incur damage to the RAMPS board itself. Next, the heatsinks that came packaged with the stepper drivers are positioned directly on top of

the black chip, located centrally on each driver, with the pre-prepared adhesive found on the underside of each heatsink.



*Figure 4.13 – The A4988 stepper driver inserted into its respective pins on the board*

Lastly, the current limit is set on each stepper driver to match the rated current of the NEMA17 stepper motors used – to do this, the VREF voltage and  $R_S$  resistance needs to be known. The VREF value was obtained by using a multimeter with the positive red probe touching the potentiometer (corresponding to the VREF voltage) and the negative black probe touching ground. With the power on, the multimeter will display the VREF voltage corresponding with the current position of the potentiometer – with a small Phillip’s head screwdriver, adjusting the potentiometer clockwise increases the VREF voltage and counter-clockwise rotation decreases the VREF voltage.  $R_S$  is the resistance of the sensing resistors S1 and S2 on the stepper driver – the A4988 drivers show these to be labelled as R100 which corresponds to a resistance of 0.1 Ohms using the 4 digit SMD (surface mount device) coding system. With reference to equation (4.1) [241] the VREF and  $R_S$  values are inserted into the equation to obtain the maximum trip current  $I_{\text{TripMax}}$  which should be tuned to a value no greater than 1.2 Amperes to match the rated current of the 17HS3001-20B stepper motors for the X, Y, and E axes and the 17HS3001-350N stepper motor for the Z axis; this corresponds to a VREF value of 0.96 Volts. For general safety and to enhance the longevity of the motors, the current limit was set to 1 Ampere which has a corresponding VREF of 0.8 Volts.

$$I_{\text{TripMAX}} = \frac{V_{\text{REF}}}{(8 \times R_S)} \quad (4.1)$$

To complete the assembly of the microcontroller, the cables for the LCD2004 screen were inserted into the corresponding pins on the respective shield which fits on top of the stepper shield. Once connected, the power can be turned on and the display should light up. Once the microcontroller has been flashed with 3D printing firmware, the screen should display some text such as the name given to the printer – if the text does not appear or appears scrambled, then the cables may have been inserted into the wrong pins or even be inserted upside down, in which case rotating the cable by 180° is enough to remedy the issue.

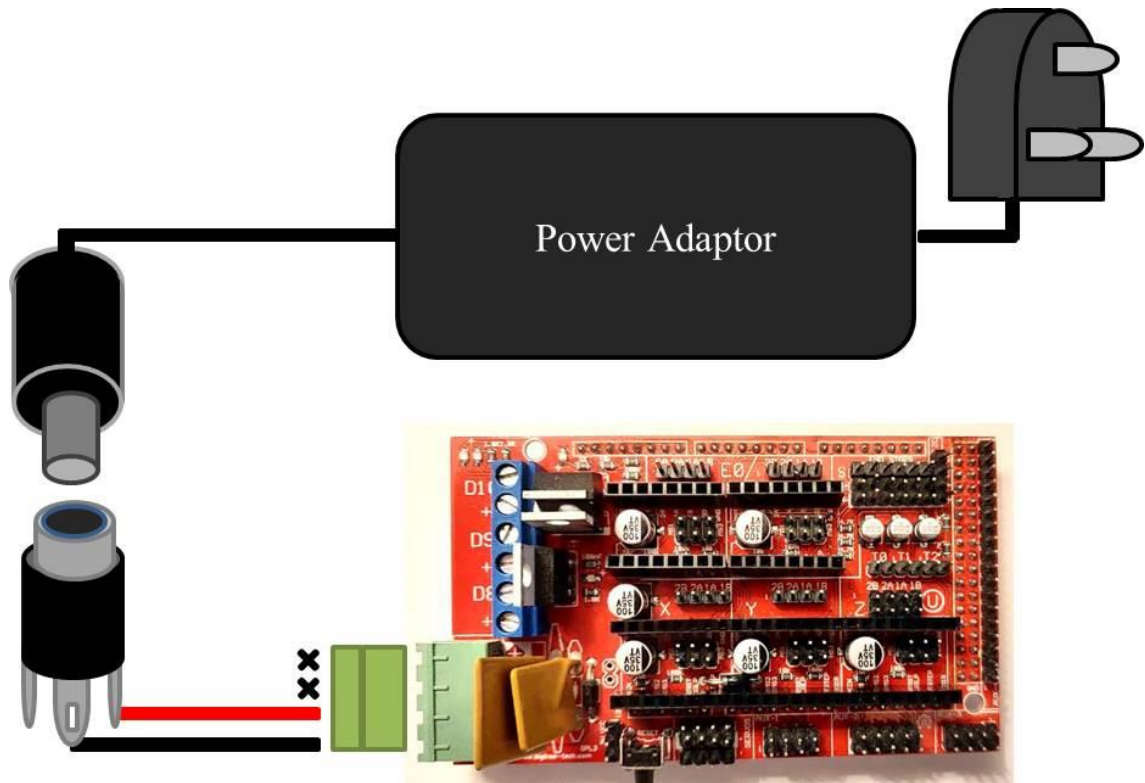
With the microcontroller correctly set up and assembled with the display, the components can be mounted onto the 3D printer's frame using the 3D printed parts described in Appendix C – Miscellaneous Hardware.

#### ***4.3.2 Power supply unit***

The RAMPS 1.4 microcontroller board did not come with its own power supply, thus an appropriately sized power supply unit needed to be sourced to ensure that the Arduino and the 3D printer could function as necessary. The microcontroller requires a power supply unit capable of delivering 12 Volts and a current of at least 5 Amperes to be able to sufficiently power the 3D printer without a heated bed. Printers which incorporate a heated bed require the use of a larger power supply unit; such a bed was considered unnecessary for the developed 3D bioprinter. When extruding cell-laden materials into tissue-like structures, the heat provided by the bed could cause harm to printed cells if the bed was operating too hot. Furthermore, the application of heat from the underside of the structure creates an uneven temperature distribution whereby the top of the structure is always colder than the bottom which makes equilibrating the temperature more difficult for larger structures. A better solution when temperature control and maintenance is critical would be to conduct the print inside an incubator - the temperature is tightly regulated and the provision of carbon dioxide in the air provides a more appropriate environment for cells.

The adaptor (GS60A12-P1J-60W 12V 5A, Meanwell) was appropriate to deliver power to the 3D bioprinter. This adaptor meets the power requirements of the RAMPS board and is a compact solution compared to PC PSU's for example which can be quite bulky. The adaptor does require some minor electrical work in order to connect to the RAMPS board; this was achieved with a DC power connector jack socket (JR1819-ROHS

(PSG01769), Farnell) which fits over the adaptor's output centre positive jack plug, and is then wired and connected into the microcontroller's power input (figure 4.14). The adaptor itself is connected to a mains power supply socket with an IEC (C13) kettle lead.



*Figure 4.14 – Schematic showing the connection between power supply unit and the RAMPS 1.4 board*

### **4.3.3 Motors**

As mentioned earlier, the motors planned for use with all axes on the 3D bioprinter are NEMA 17 standard stepper motors. The reasons for choosing stepper motors over servos or DC motors is the modularity of stepper motors and their capability to balance between having a high torque and good positional control, making their use very practical for 3D printers whereby the torque is needed to move the loads (extruder, X-carriage, Y-carriage) and the positional control is needed for the fabrication of high quality structures. The positional resolution of stepper motors is integrated into their stepping design – each full motor step rotates the shaft by a fixed amount called the ‘step angle’, and a full revolution of the motor comprises of a fixed number of steps. Therefore one can calculate how much a motor-belted pulley assembly will linearly translate per single step of the motor. In conjunction with microstepping, the stepper motors are capable of having more unique steps per motor revolution as each full step is

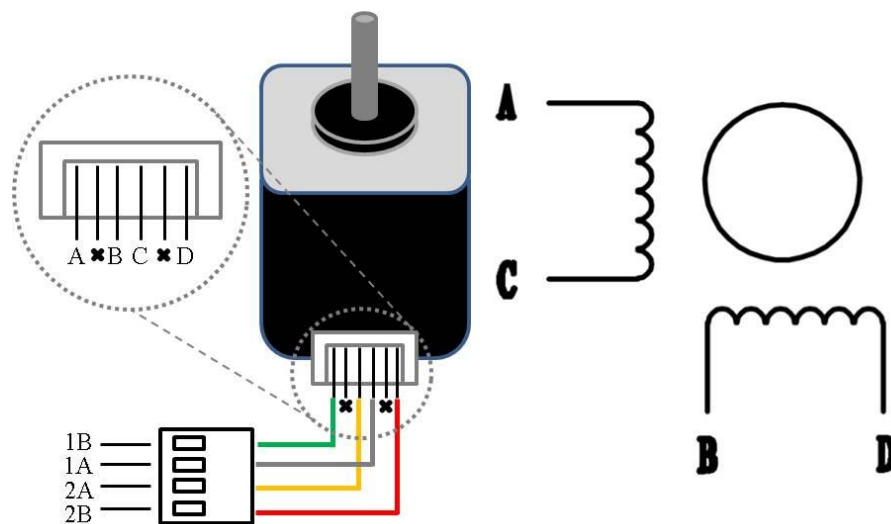
divided equally into half steps, quarter steps, eighth steps, etc. Thus a 200 step-per-revolution motor with sixteenth microstepping would have 3200 microsteps per motor revolution. As the RAMPS microcontroller board can support microstepping, the use of stepper motors is naturally synergistic.

The NEMA standard is used to characterise the profile of the four threaded holes for fitting purposes and is not a strict expression of the power or torque rating of such motors; however motors with a larger NEMA standard, such as NEMA 23, are typically larger in size which usually correlates with greater torque and power requirements. NEMA 17 was the standard of choice based on being very commonly and successfully used in many RepRap inspired 3D printer builds. Furthermore, NEMA 17-sized stepper motor mounting brackets were the only NEMA standard supported by OpenBeam and therefore their purchase ensured that the motors could be successfully affixed to the 3D printer's frame. Whilst the profiles of larger NEMA standards could be readily obtained, fabricating such brackets in-house or sourcing alternate vendors for such brackets was unnecessary as the NEMA 17 standard is known to be very suitable for custom 3D printer builds.

The stepper motors used for the X, Y, and E-axes were the 17HS3001-20B models which have a step angle of  $1.8^\circ$  equating to 200 steps-per-revolution, a rated voltage and current of 2 Volts and 1.2 Amperes respectively, and a holding torque of 0.4 Newton metres [242]. The Z-axis stepper motor (17HS3001-350N) has similar specifications, also being a  $1.8^\circ$  step angle, 200 steps-per-revolution motor rated at 2.3 Volts and 1.2 Amperes with a holding torque of 0.32 Newton metres [243]. The main difference between the two motor models is that the Z-axis motor has an integrated leadscrew with four-starts and an 8 millimetre lead (ACME tr8\*8 profile with a 2 millimetre pitch (p2)) which when rotated can linearly raise or lower the printer's platform when threaded through an ACME nut fixed into the platform with matching profile. As the X and Y-axis motors do not have an integrated leadscrew, they require a pulley to be affixed to the shaft and belted in order to convert rotational motion into linear motion for their respective axes.

The stepper motors are shipped with their 4-pin connecting cables which directly plug into the motor and the microcontroller board. Whilst motors are typically shipped with the cables in the correct order, some vendors do not supply the configured cables and thus require cables to be sourced from another vendor. In this case the cables need to be

manually configured to cater for 2-phase bipolar stepper motors and requires crimping at both ends to fit into the 4-pin housing at the microcontroller end and a 6-pin JST connector at the motor end. With reference to the respective datasheets of the stepper motors and with reference to the motor's terminals on the RAMPS board, the objective is to pair the positive and negative 'A' terminals (pins 1A and 2A on the board) and 'B' terminals (pins 1B and 2B) with the motor's pins labelled AC and BD on the wiring diagram (figure 4.15). This creates two circuits, an 'A' loop and a 'B' loop, which is necessary for energising both phases (groups of coils) of the motor for correct operation. Wiring the motors incorrectly will not likely result in damage, but the motor may rotate in the opposite direction than intended or may not move at all, in which case one of the coil's wiring could be in the reverse order thus causing the phases to work against each other - such an issue can be resolved by checking the order of the wires, for instance if 1A to A and 1B to C does not work, reverse the polarity by changing 1A to C and 1B to A.



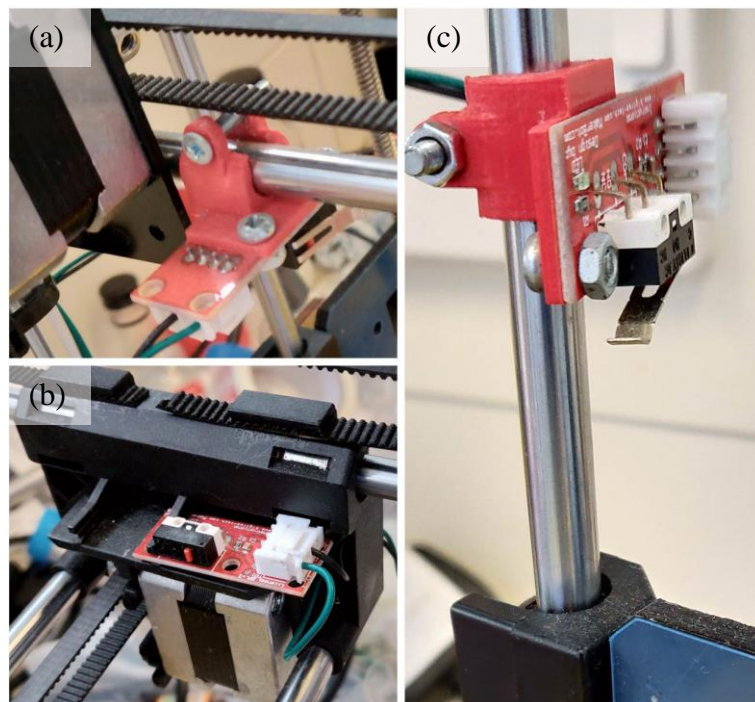
*Figure 4.15 – Schematic showing the wiring for correct operation of NEMA 17 stepper motors*

#### **4.3.4 Mechanical Endstops**

Endstops are small sensing switches which send a low or a high output back to the microcontroller board when the switch on the device is depressed. Endstops serve two purposes: to prevent accidental damage to the machine by restricting movement when the endstop is active, and to 'home' each axis prior to printing so that the extruder can move to a central datum position. Thus the endstops are useful components to ensure both the safety of the machine as well as maximise the largest print sizes possible by



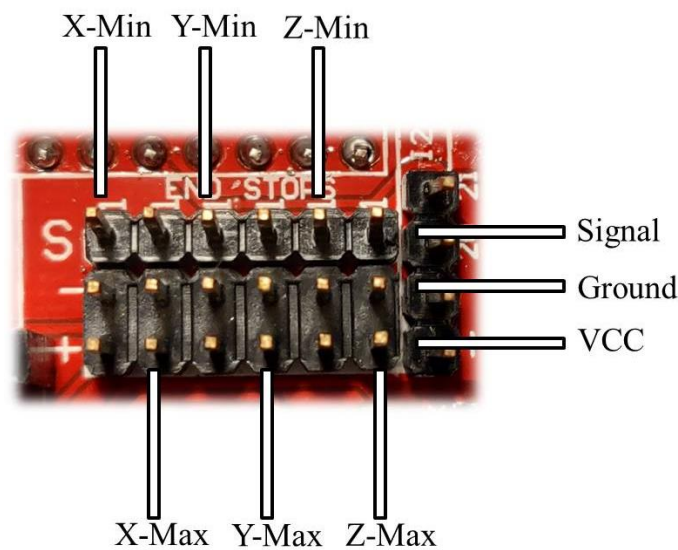
aligning the extruder with the very middle of the platform. Whilst mechanical endstops act as a physical barrier to stop the moving axes from crashing into other components of the 3D printer, they are not strictly essential for 3D printer operation. Within the firmware there are configurable settings to enable software endstops, the digital equivalent of mechanical endstops, which will cause the controller to move no further than the distance specified for each axis without the use of a mechanical endstop - although this is not fool proof as the distance is relative to the extruder's starting position when the machine is first turned on and not the more reliable homed datum position. The position of each endstop is shown in figure 4.16.



**Figure 4.16** – (a) Endstop position on the Y-axis endstop, (b) X-axis, (c) and Z-axis

With the endstops in their respective positions, the endstop cables need to be connected up to the RAMPS board. With the board's green power input facing left, the endstop pins are located towards the top-right hand side of the board. From left-to-right, the endstops correspond with X-min, X-max, Y-min, Y-max, Z-min, and Z-max which relates to the minimum and maximum positions of each of the three moving axes. Only three mechanical endstops are needed in conjunction with software endstops, one to specify either a maximum or minimum position for each axis. The cables were inserted into the min pins on the RAMPS board, but at this point the pins used were arbitrary as the endstops as well as the positive and negative directions of each axis will need to be configured in the firmware, which will be discussed later in section 4.4 Firmware. The

endstops which were sold as part of the kit had cables provided with three wires – one for the signal (S), one for ground (-), and one for VCC (+). These correspond with the three rows of endstop pins on the RAMPS board – in the convention of the board’s green power input facing left, the top row of endstop pins are designated (S) for signal, the middle row is designated (-) for ground, and the bottom row is designated (+) for VCC (figure 4.17). Care should be taken to ensure that the wires are inserted into the correct positions on both the endstop unit and on the RAMPS board to prevent accidental electrical damage to the components.



**Figure 4.17** – Diagram showing which RAMPS 1.4 pins correspond with minimum and maximum axis position, signal (S), ground (-), and VCC (+)

For printing into support baths, it may be more useful to manually position the extruder by hand prior to printing. Doing this ensures that the nozzle can be set to an appropriate depth within the bath and be concentrically aligned with the support bath’s container. This does mean that the homing function at the start of the print needs to be disabled within the Slic3r software and renders each endstop redundant for such a purpose. This is to stop the nozzle from crashing into the walls of the bath’s container to reach the X- and Y-axis endstops, and to stop the nozzle from crashing into the bottom of the container along the Z-axis – crashing the nozzle can break the nozzle, particularly fine nozzles, and thus would need replacement. To disable the homing function at the start of each print, go to the ‘start g-code’ window (‘printer settings’ > ‘custom g-code’) and comment out the ‘G28’ command with a semicolon so that the line reads ‘;G28’ instead. This converts the command into a comment, preventing the microcontroller from executing the home function altogether. Whilst this disables the homing function, it



does not disable the endstops thus the machine still has a failsafe should any carriage try to move outside the bounds of the axis. Furthermore when manually setting the depth of a nozzle within a bath, the Z-axis endstop's 3D printed mount can be physically moved to be engaged when at the desired depth – this then allows for the extruder's nozzle to be moved out from the bath for any reason and can be reinserted reliably to the same depth without further manual calibration. This is beneficial when printing into many support baths with identical dimensions, as the nozzle's depth will be the same in each bath so long as the same nozzle is used consistently throughout all subsequent prints.

#### **4.4 Firmware**

The firmware of a 3D printer can be described as the programming code which is flashed (loaded) onto a microcontroller board which grants the 3D printer the logic to translate input g-code into physical outputs such as what motors to move, at which speeds, to which positions, what to do when an endstop is engaged, etc., as well as process user commands input using the LCD2004 unit. If the microcontroller is analogous to being the brain of the 3D printer, the firmware can be considered to be the thought process by which tasks are ordered and executed. Upon receiving digital signals from the g-code, such as a line of code to move linearly along the X-axis from point A to point B for example, the firmware processes that information and commands the X-axis motor to rotate at a defined speed until the sufficient number of motor steps has been taken to travel the necessary distance.

Creating 3D printing firmware from scratch was considered to be an ineffective use of research time given the complexity involved in programming such logic which can successfully integrate every aspect necessary for correct manipulation of a CNC machine with four moving axes. Instead, open-source firmware was leveraged to very quickly make the machine ready for conducting 3D bioprinting research. By nature of the open-source license, specific aspects of the firmware's code can be changed to suit a specific machine build which is much more straightforward and intuitive than creating working firmware from scratch which would involve extensive prior programming knowledge and expertise.

Several open-source 3D printing firmware exist online for download and integration with custom-built 3D printers. Fundamentally they all provide the means to achieve the same end: to fabricate 3D structures from a g-code input. Different varieties of

firmware may have certain programmed functions which do not exist or are unsupported in other firmware – commands such as ‘G10’, a retraction command, is supported in the Marlin firmware but not in Sprinter for instance - a full list of compatible g-codes for each firmware exists on the RepRap website [244]. Additionally one type of firmware may not support the same electrical components that other firmware can, as such it is important to check that the firmware planned for use is compatible with the purchased components – such information is sometimes included in the microcontroller’s product description or by typing the board’s name into a search engine. As there are many varieties of firmware to choose from which have many subtle differences between them, they will not be listed here.

For the developed 3D bioprinter, the Marlin firmware was deemed appropriate for use. This was primarily because the Marlin firmware is supported by the RAMPS board, but is also advantageous to use due to being a popular choice and having a large user base meaning that many issues have been discussed and resolved on their forums. As the RAMPS board is based on an Arduino, the firmware needs to be opened in the Arduino IDE (integrated development environment) software in order for changes to be made and to flash the firmware onto the microcontroller board. The firmware can only be successfully flashed to the board if the code can be compiled successfully, else the compiler will fail and will prevent the board from being flashed. When compiled successfully without errors, the microcontroller board can be connected to the computer via a USB type A cable between the Arduino board itself and a USB port on the computer with the Arduino IDE software and flashed to upload the firmware onto the Arduino board’s integrated memory.

Marlin can be readily downloaded from the Marlin’s github website [245]. The version of Marlin used with the developed bioprinter is version 1.0.2-1, released in January 2015, and is compatible with Arduino IDE version 1.0.5-r2. Newer versions of Arduino IDE and Marlin currently exist but the Marlin 1.0.2-1 and Arduino IDE 1.0.5-r2 were compatible with each other and offered the features necessary for the developed bioprinter, whereas compiling would always fail when the same version of Marlin was used with a more up to date version of Arduino IDE.

The settings which require configuration in order to work properly with the developed bioprinter are the basic settings to define the machine, thermal settings to disable any temperature related functions, mechanical settings to denote the axis directions and axis’

linear travel per motor step etc., and some additional settings for compatibility with the LCD2004 display provided in the RAMPS 1.4 kit. Details of specific changes made to the firmware are documented in Appendix D – Firmware Configuration.

#### 4.5 Theoretical Resolution

With all of the components attached to the bioprinter, the theoretical positional resolution of each axis may be approximated. For the following calculations the minimum positional resolution is the distance travelled per single microstep of each particular axis, and takes into consideration whether the axis is driven using GT2 belts and pulleys or a threaded rod/leadscrew.

##### 4.5.1 Positional resolution of belted X- and Y-axes

As the X- and Y-axes utilise belts and pulleys which share the same GT2 profile and are driven using similar NEMA 17 stepper motors, the calculated positional resolutions are identical. With reference to equation (4.2) below [246], the NEMA 17 stepper motors have a step angle of 1.8° and thus 200 steps are required for a complete 360° revolution, the RAMPS board is configured for 1/16<sup>th</sup> microstepping mode, the pitch of GT2 belts is 2 mm, and there are 20 teeth on the GT2 pulleys. This results in 80 steps per millimetre of travel (equation (4.3)); the inverse of this value provides a travel distance of 12.5 µm per single motor step for both the X- and Y-axes (equation (4.4)).

$$\text{Steps/mm}_{\text{Belted Axis}} = \frac{\text{Steps per revolution} * \text{Microstepping}}{\text{Belt Pitch} * \text{Number of Pulley Teeth}} \quad (4.2)$$

$$\text{Steps/mm}_{\text{Belted Axis}} = \frac{200 * 16}{2 * 20} = 80 \text{ steps per mm} \quad (4.3)$$

$$\text{mm/Step}_{\text{Belted Axis}} = \frac{1}{80} = 0.0125 \text{ mm} = 12.5 \text{ } \mu\text{m per step} \quad (4.4)$$

##### 4.5.2 Positional resolution of leadscrew Z-axis

The Z-axis differs from the belted axes in that it comprises of a leadscrew instead of a belt and pulley assembly to translate rotational motion into linear motion. Furthermore, the profile of the leadscrew is different from that of the extruder's threaded rod/screw-plunger system and thus will be calculated independently. With reference to equation (4.5) below [246], the number of motor steps required to travel a distance of 1 mm is related to the motor's steps per revolution and microstepping mode as before, the

leadscrew's pitch and number of thread starts (the product of these two is known as the 'lead') which is 2 mm and four starts respectively. This calculation results in 400 steps per millimetre (equation (4.6)) which corresponds with a travel distance per step of 2.5  $\mu\text{m}$  (equation (4.7)).

$$\text{Steps/mm}_{\text{Leadscrew Axis}} = \frac{\text{Steps per revolution} * \text{Microstepping}}{\text{Thread Pitch} * \text{Number of Thread Starts}} \quad (4.5)$$

$$\text{Steps/mm}_{\text{Leadscrew Axis}} = \frac{200 * 16}{2 * 8} = 400 \text{ steps per mm} \quad (4.6)$$

$$\text{mm/Step}_{\text{Leadscrew Axis}} = \frac{1}{400} = 0.0025 \text{ mm} = 2.5 \mu\text{m per step} \quad (4.7)$$

#### 4.5.3 Depositional resolution of threaded rod E-axis

Unlike both the belted X- and Y-axes and the leadscrew Z-axis, which handle the positioning of the printhead relative to the printbed, the extruder's axis, E, is responsible for the deposition of bioink. However as the extruder is driven by a motor and threaded rod/screw-plunger assembly, the minimum travel distance per step corresponds with the minimum extruded material volume and is thus calculated similarly. The extruder's threaded rod has a single start thread and a pitch of 0.5 mm which provides 6400 steps per mm of travel (equation (4.8)); the inverse provides a result of 156.25 nm of linear travel per single step (equation (4.9)). By multiplying this minimum linear travel distance per step by the internal cross-sectional area of the 10 cc syringe barrel used (internal diameter 15.75 mm) (equation (4.10)), the theoretical minimum depositional volume is approximately 0.03  $\text{mm}^3$  (equation (4.11)) which is equivalent to 30 nl when converted from  $\text{mm}^3$  to ml ( $1 \text{ mm}^3 = 0.001 \text{ ml}$ ).

$$\text{Steps/mm}_{\text{T.Rod Axis}} = \frac{200 * 16}{0.5 * 1} = 6400 \text{ steps per mm} \quad (4.8)$$

$$\text{mm/Step}_{\text{T.Rod Axis}} = \frac{1}{6400} = 1.56 \times 10^{-4} \text{ mm} = 156 \text{ nm per step} \quad (4.9)$$

$$\frac{mm^3}{Step_{T.Rod\ Axis}} = A_{XSA,10cc} * mm_{Step} = \frac{\pi D_{ID}^2}{4} * mm_{Step} \quad (4.10)$$

$$\frac{mm^3}{Step_{T.Rod\ Axis}} = \frac{\pi * 15.75^2}{4} * 1.56x10^{-4} = 0.03 mm^3 \quad (4.11)$$

It should be stressed that the positional resolution of each axis is purely derived from a theoretical standpoint; positioning experiments were not conducted to validate the accuracy of the developed bioprinter in relation to the calculated resolutions. There are various factors which likely restrict the bioprinter from achieving such resolutions in practice, such as backlash in the stepper motors when changing direction, incremental torque at 1/16<sup>th</sup> microstepping possibly being insufficient to successfully drive the load and requiring multiple steps, and step-skipping when driving at fast speeds. However the theoretical values are comparable to what has been achieved amongst other 3D printers/bioprinters. X, Y, and Z resolutions are comparable to those of commercialised RepRaps like the Mendel and Prusa i3 models. E depositional resolutions as low as 1 nl has been documented using NEMA 17 stepper motors driving an 8 mm diameter leadscrew which pushes a tungsten plunger into pulled glass capillary pipettes with inlet diameters of approximately 1 mm [247]; whilst the cross-sectional area of the glass capillary is approximately 225 times smaller than a 10 cc syringe barrel, its extruder's leadscrew has a greater pitch than the developed bioprinter. Although not explicitly documented in the work, the leadscrew and nut assembly looks identical to the tr8\*8(p2) profile used as the Z-axis in the developed bioprinter, thus the developed bioprinter's extruder could have a lead which is up to 16 times more resolute if the leadscrew is a four-start thread, 8 times more resolute for two-starts, and 4 times more resolute for a single-start. Factoring such details, a dispensed volume of 1 nl multiplied by the ratio of syringe cross-sectional area and leads results in a range of depositional volumes between 14 nl to 56 nl and thus indicates that the calculated E-axis depositional resolution is reasonable.

#### 4.6 Summary

Discussed in this chapter is the complete development of the 3D bioprinting platform which was used in this thesis. As far as possible, the machine was built with two concepts in mind: component modularity and open-source technology.

Constructing a modular machine was desirable to reduce the overall complexity of construction with readily available standardised components, but is also useful when considering the purchase of spare parts in case of emergency repair work or for constructing similar machines at various scales in future projects. Component modularity ensures that any part can be interchangeably replaced by another component sharing the same standards, thus larger or smaller machines may be constructed using the same beam profile should suitably-sized beams be sourced. Where modularity could not be maintained, single-part multifunctional components such as the X- and Y-axis carriages were used as they were capable of fulfilling the needs of clamping belts, affixing linear rods, and affixing stepper motors all as a single component. Lastly, where such solutions did not exist, 3D printing and laser cutting was necessary to fulfil the remaining requirements of the printer, such as the laser cut housing to fix the extruder to the X-axis carriage, or the parts to secure the LCD2004 screen and RAMPS 1.4 microcontroller board to the printer.

Leveraging the use of open-source technologies was critically significant to the construction of the 3D bioprinter. Without specialist knowledge and expertise in programming and electronics, the development of firmware and software to interface with the 3D printer would have been an insurmountable challenge for a single researcher to undertake in conjunction with building the machine. Especially in the context of 3D printing, there are already many resources available to help accelerate the average hobbyist to quickly get started with 3D printing, so there would be little sense in trying to recreate software solutions for technical challenges which have already been solved unless a particularly niche application demands it. Thus the merit of utilising pre-existing open-source technologies is to save developmental time so that 3D bioprinting research can be conducted sooner rather than later.

Based on the components used, the theoretical resolution of the 3D printer can be approximated as linear distance per motor step. This is the inverse of the steps per millimetre calculation, so assuming that the incremental torque of each microstep surpasses the detent torque and assuming no skipped steps, the positional resolution in the X- and Y- axes is 12.5 microns, and 2.5 microns along the Z-axis. The theoretical resolution of the extruder configuration is approximately 156 nanometres for a single extruder microstep, which corresponds to a displaced volume of approximately 30 nanolitres with the 10 cc syringe barrels used.

In relation to currently available bioprinters on the market, the developed 3D bioprinter compares well with various printers in the low- to mid-price range such as the Allevi 2, but pales in comparison to the high-end machines like RegenHu's 3DDiscovery as summarised in table 4.2. Observing the qualities of various bioprinters, features such as the number of printheads, precision, temperature control, the capability of printing multiple-modalities simultaneously, etc., add value to the technology which warrants greater prices; however high technological costs has historically been a major limitation of the field [248][249], and machines such as the 3DDiscovery may yet remain inaccessible for many research groups today. The developed 3D bioprinter's main benefits include being relatively low cost, its compatibility with open-source technologies, and largely modular frame design; these factors may be more desirable for new research teams attempting to break into the field of bioprinting. The developed bioprinter's main drawback is that it is currently restricted to a single printhead and print modality; however this could be addressed by redesigning the X-axis carriage so that it may accommodate multiple printheads and better conform to more modern trends in bioprinter design. Whilst the developed bioprinter was constructed at a relatively low cost, it is also possible to simply buy a conventional plastic FDM 3D printer and modify the extruder for bioprinting applications. In 2015 Hinton et al. converted a MakerBot Replicator 2X and demonstrated the FRESH method of supportive bioprinting [134], and in 2019 the Anet A8 3D printer was converted into an extrusion-based bioprinter for as little as €150 (~£135) [250]; such an approach is arguably the most accessible by being the cheapest and requiring minimal assembly, however the lessons learned from designing and building one's own 3D bioprinter has value beyond that which can be measured by cost alone.

**Table 4.2 - Comparison of the developed 3D bioprinter's cost and functionality with commercially available options**

<b>Bioprinter Model</b>	<b>Print Method(s)</b>	<b>Printheads</b>	<b>Build Volume</b>	<b>Precision</b>	<b>Temperature Control</b>	<b>Price</b>	<b>Other Notes</b>
<b>Developed Bioprinter</b>	Extrusion	1	225 x 145 x 150 mm	X, Y: 12.5 $\mu$ m Z: 2.5 $\mu$ m	None	~£600 to build	Largely modular design
<b>Allevi 2</b> [253]	Pneumatic	2	130 x 90 x 60 mm	X, Y: 5 $\mu$ m Z: 1 $\mu$ m	Temperature control on extruders	Quoted \$15,000 (£12,300)	405 nm photocuring module built-in
<b>RegenHu 3DDiscovery Evolution</b> [254]	Extrusion, Droplets, melt electrospinning	6	130 x 90 x 60 mm	5 $\mu$ m (each axis not specified)	Yes	Estimated £160,000+ [251][252]	Modular, climate control, photoinitiation, cameras
<b>Modified FDM 3D Printers: MakerBot Replicator 2X</b> [255], <b>Anet A8</b> [256]	Extrusion	MakerBot: 2 Anet: 1	MakerBot: 246 x 163 x 155 mm Anet: 220 x 220 x 240 mm	MakerBot: X, Y: 11 $\mu$ m Z: 2.5 $\mu$ m Anet: X, Y: 12 $\mu$ m Z: 4 $\mu$ m	Yes, heated build plate and FDM extruders	MakerBot: ~\$2000 (£1635) at launch in 2012 Anet: £135 [250]	Could modify one MakerBot extruder for hydrogels and use the other for thermoplastics



## **Chapter 5 – A Quiescently Gelled Gelatine Supportive Medium to Facilitate 3D Soft Tissue Biofabrication**

### **5.1 Introduction**

There are numerous limitations in the context of extrusion-based bioprinting which hinders the ability of such technologies to create relevant anatomical structures. The shape fidelity of bioprinted structures becomes compromised when attempting to maintain high cell viability by using low concentration, low-viscosity inks due to the tendency of such materials to spread laterally. Fabricating relevant anatomical models with such inks presents many difficult mechanical challenges – a lack of mechanical strength compounded with the fabrication of geometrically complex features like sloping surfaces and overhangs may result in complete print failure. To address the lack of mechanical strength in biologically more favourable ink conditions, supportive strategies have been developed. Strategies such as FRESH cater to the mechanical needs of bioinks by suspending extruded material within a supportive medium throughout the fabrication process.

Analysing FRESH specifically, this method's key advantage revolves around the choice of material used to prepare the microparticulate gel network: gelatine. Gelatine is a very relevant biomaterial for supportive technologies due to its melting temperature comparable to that of the human body. This is hugely advantageous for cells as the release condition, to liquefy the gelatine, matches the physiological temperature condition for cells to remain viable, proliferate, and grow into tissue. Gelatine also has greater material compatibility than other candidate support materials like Carbopol which exhibits intolerance towards divalent cations like calcium cations; this intolerance makes printing with ionically crosslinked materials like alginate less feasible unless a secondary mode of crosslinking is utilised such as making an alginate/gelatine copolymer ink to induce thermogelation from within the carbopol support prior to its removal from the bath and followed by ionic crosslinking thereafter [257].

Incorporating the FRESH method involves dissolving gelatine powder in water, cooling this solution in a chilled environment for a period of 10+ hours to gel, and then blending the resulting 'puck' of gel with chilled calcium solution at a set speed for a specific time to produce gelatine microparticles of average size dependent on the blending parameters. The removal of entrained air and excess soluble gelatine from the

interstitial fluid is achieved by centrifugation which packs the microparticles closer together. The microparticles are mixed with more chilled calcium solution and centrifuged multiple times until all excess soluble gelatine is removed – the process is complete once the interstitial fluid is completely clear, after which the densely packed microparticles may be stored in a fridge for later use or re-suspended in chilled calcium solution to produce a supportive slurry with the appropriate rheology to suspend printed structures in 3D.

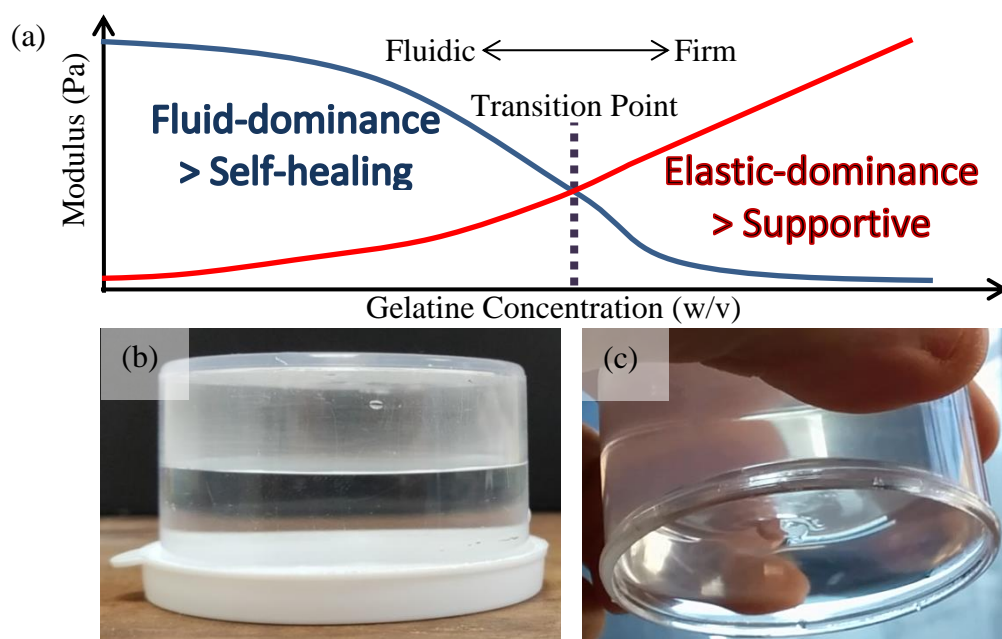
FRESH is however deceptively difficult to successfully incorporate due to its preparation. Multiple modes of failure exist at the preparation stage; should failure occur post-gelation then the process needs to be restarted, requiring at least another 10+ hours to prepare a new batch. The blending process can incur mechanical failure of the microparticles by blending for too long or too fast, or thermally whereby the blending process generates enough heat to melt the particles which becomes easier to do the longer and faster the gelatine is blended. The centrifugation process is iterative and poses a significant risk to the sterility of the gelatine due to the repeated opening and re-sealing of the gelatine-filled centrifuge tubes whilst removing the supernatant and adding calcium solution, and the gelatine can fail again thermally if the temperature throughout this whole process is not maintained suitably low. Thus it can be argued that the FRESH preparation process demands a certain level of ‘know-how’ to successfully implement.

To overcome the preparatory difficulty of FRESH, a new supportive method was developed with the objective of simplifying the preparation process as much as possible. This method is distinguished from other approaches such as FRESH and Carbopol methods in that the support network achieves its function with being microparticulate in nature. However, like FRESH, gelatine is used as the candidate support material for its simple thermogelation qualities. Soft tissue-like constructs can be supported using low-viscosity inks in this two-step process: mixing of the gelatine solution and its subsequent gelation in a fridge. This two-step approach significantly reduces the likelihood of failure by not requiring blending or repeated opening/sealing of the containers. Through control of the fluidic and elastic properties of the gels as governed by gelatine concentration, the baths can functionally achieve this supportive role in biofabrication. This is hence a ‘quiescent’ approach due to the bath’s ability to generate the necessary qualities for supportive behaviour on its own without processing post-gelation.

## **5.2 The Influence of Gelatine Concentration on Bath Properties**

In order to create a support bath with appropriate rheological properties, the factors which constitute an ideal support bath should be known. It is understood that ideal support baths should be: (1) capable of supporting and suspending extruded material internally, (2) capable of rapid self-healing after a nozzle translates through it, (3) be of low viscosity to minimise viscous forces acting on the nozzle during movement, and (4) have a mechanism in place to remove structures post-print.

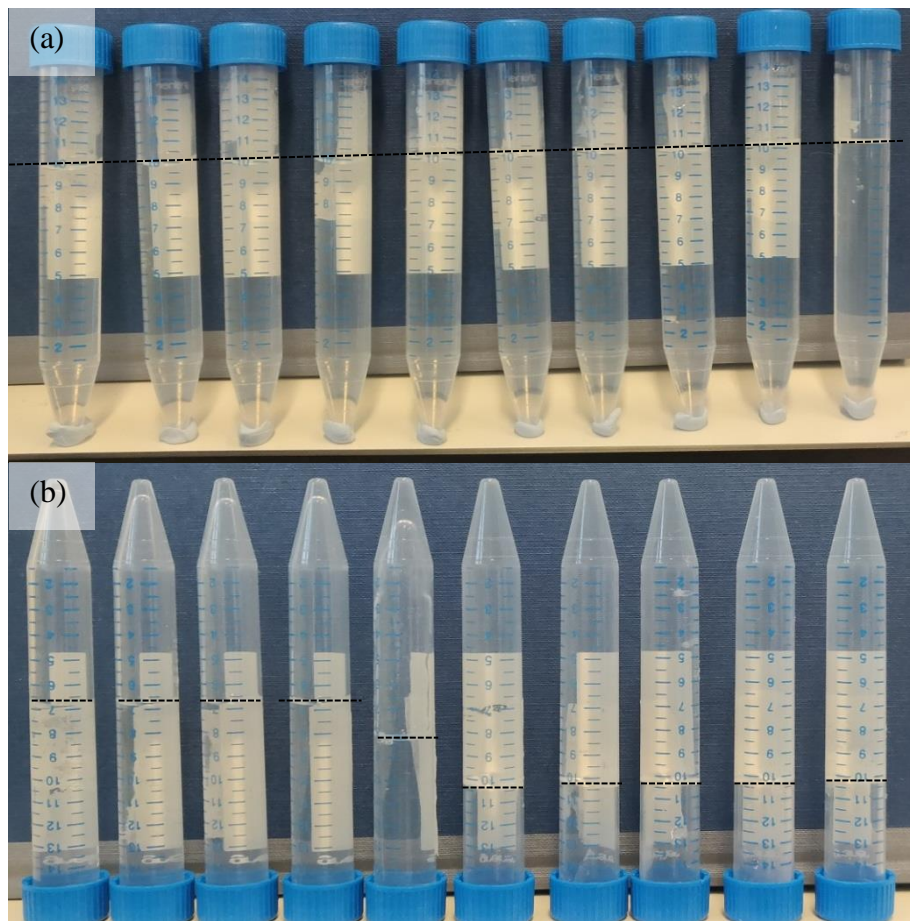
By tuning the concentration of gelatine, produced gels can be more elastic and stiff at increased concentrations, or more fluidic and runnier at decreased concentrations. Adopting the method of tabletop rheology, the bulk properties of the produced gels can be visually assessed and compared with each other by simply inverting the gelatine-filled containers post-gelation – any sudden change of results post-inversion between two adjacent gelatine concentrations indicates a transition between elastic and fluidic dominant behaviour. The schematic diagram shown in figure 5.1 describes this relationship between fluidic and elastic dominant behaviour with varying gelatine concentration. Materials exhibit fluid-like flow behaviour when the loss modulus exceeds the storage modulus, and conversely materials exhibit solid-like behaviour when the storage modulus exceeds the loss modulus. The point where the storage and loss moduli intersect each other corresponds with a change in the material's bulk behaviour and indicates the concentration required for gelation occur in hydrogels. More concentrated gels are stronger because there are more molecules that aggregate into their triple helical conformation during the thermogelation process and thus will remain upright upon inversion, whereas concentrations that are fluid dominant will yield and flow to the bottom of their containers.



**Figure 5.1** - (a) Schematic representing the crossover between fluidic and elastic dominance with increasing gelatine concentration, (b) different gelatine concentrations are inverted to check for fluidic dominance, (c) or elastic dominance

To establish the conditions that result in gels with fluidic-dominance or elastic-dominance, a systematic study of gelatine concentrations between 0.1% to 1% w/v in increments of 0.1% was conducted. Gelatine solutions were prepared in 15 ml centrifuge tubes, stored overnight in a fridge to gel and inverted the next day. Each condition was positioned next to each other for visual assessment and comparison of each concentration's bulk behaviour. An intermediate concentration between the maximum fluidic-dominant condition and the minimum elastic-dominant condition is considered the transition point between fluidic- and elastic-dominant states.

The inversion study (figure 5.2) shows that gelatine concentrations in the range of 0.1% to 0.5% w/v are fluid-dominant and concentrations in the range of 0.6% to 1% are elastic-dominant. The result implies that the transition point between fluidic- and elastic-dominant states exists between a gelatine concentration of 0.5% and 0.6% w/v.

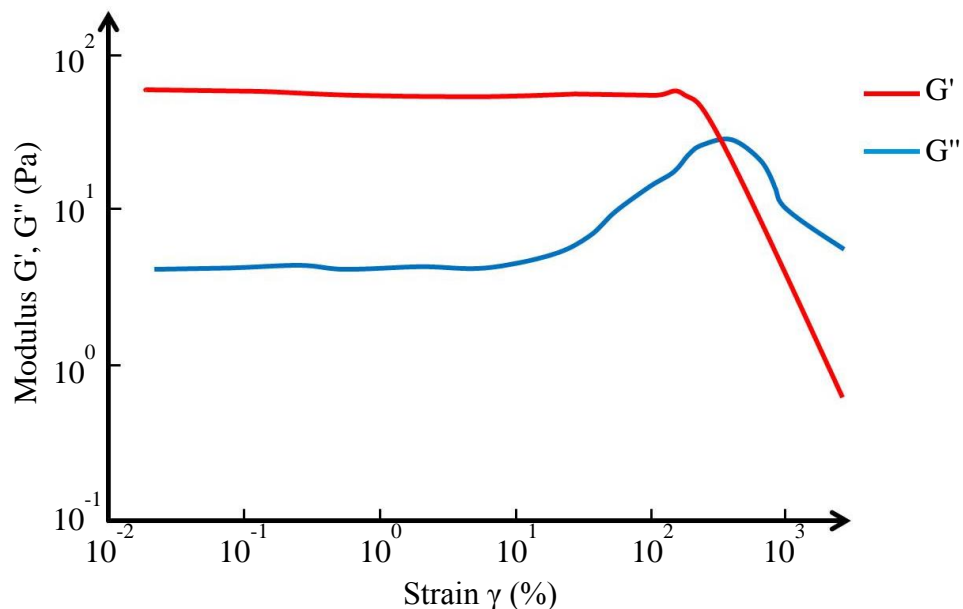


**Figure 5.2 -** (a) Ten 15 ml tubes arranged left to right with 0.1% to 1% gelatine concentration prior to inversion, (b) tubes in the same order after inversion. The dotted line corresponds with the fluid/gel level

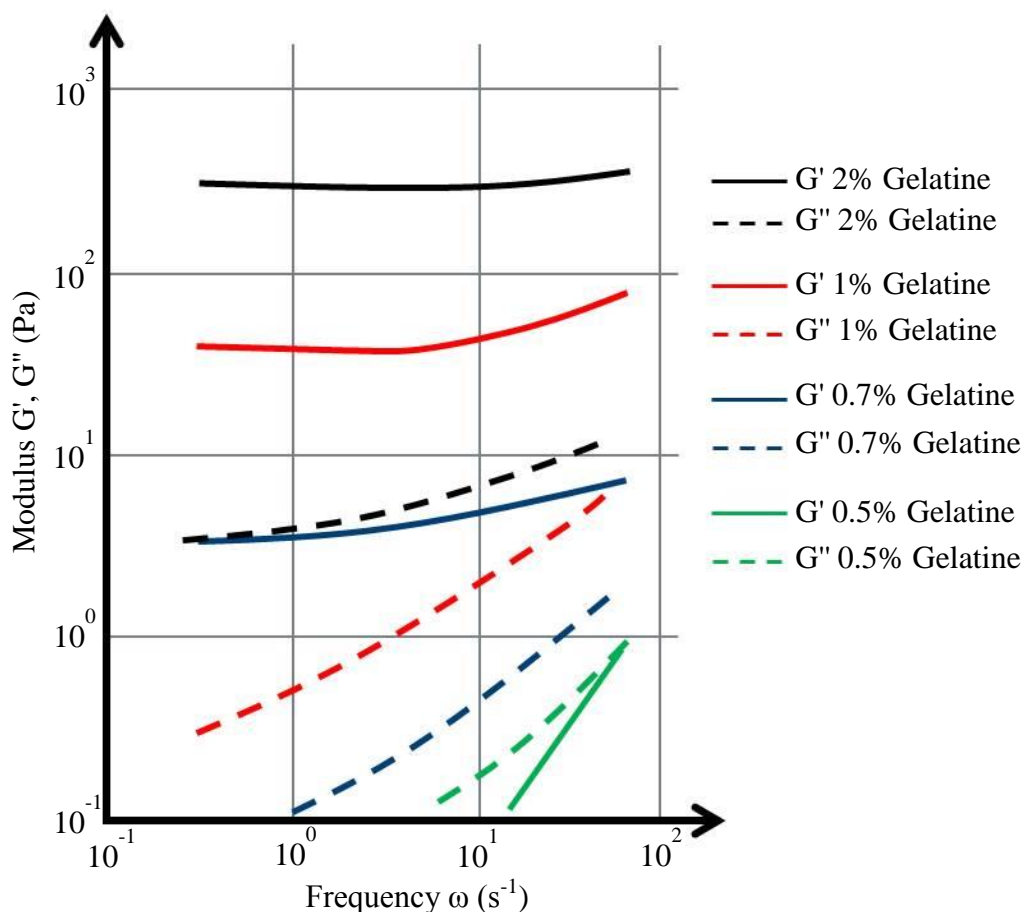
Concentrations below the transitional value either completely failed to gel (0.1% and 0.2% w/v) or lacked the mechanical strength for self-support post-inversion (0.3% to 0.5% w/v). In the case of 0.1% and 0.2% w/v gelatine concentrations, it is speculated that the concentration is too low for gelatine molecules to aggregate and form their structurally stable triple-helical conformation. Conditions in the concentration range of 0.3% to 0.5% w/v appeared to exhibit some mixed-phase characteristics when tilted slightly, seemingly separating into both gel- and liquid-phases. However, such concentrations exhibited fluid-dominant behaviour upon inversion. The mixed phase phenomenon may be once more related to an insufficiently low gelatine concentration; there are not enough gelatine molecules for aggregation into a mechanically strong, sufficiently dense triple-helical network that is able to occupy the entire solvent volume and thus the molecules settle and gel at the bottom of the tube, leaving a liquid supernatant on top.

Concentrations above the transition point were capable of remaining upright after inversion. However, the 0.6% w/v condition only achieved this for a period of minutes before flowing to the bottom of the tube. The convergence of elastic and fluidic properties by increasing the concentration may have granted the illusion of self-supportive behaviour briefly, thus this condition is considered fluid-dominant due to being unable to remain upright post-inversion. Gelatine concentrations between 0.7% and 1% w/v remained distinctly in a solidly gelled state for the duration of the study and are thus considered elastic-dominant conditions.

Gel formation can only occur once a critical concentration has been surpassed which is influenced by the average molecular weight of the polypeptide chains which varies by gelatine source and type; gelatines with greater molecular weights tend to have lower critical concentrations for gelation. However the average molecular weight is related to the bloom strength [183] therefore high bloom strength gelatines, such as the 300 bloom gelatine used in this experiment, have low critical concentrations. Such gelatines tend to have critical concentrations in the range of 0.4% to 1% [258] indicating that the results from the inversion study is in good agreement with the literature. Rheological data adapted from the literature on low concentration gelatine gels (figure 5.3) and solutions (figure 5.4) is shown below.



**Figure 5.3** – The storage modulus ( $G'$ ) and loss modulus ( $G''$ ) of 1% gelatine at a temperature of 14° Celsius, adapted from [259]



**Figure 5.4** – Frequency sweep of 0.5% to 2% gelatine solutions showing the storage modulus  $G'$  and loss modulus  $G''$  at a temperature of 10° Celsius, adapted from [260]

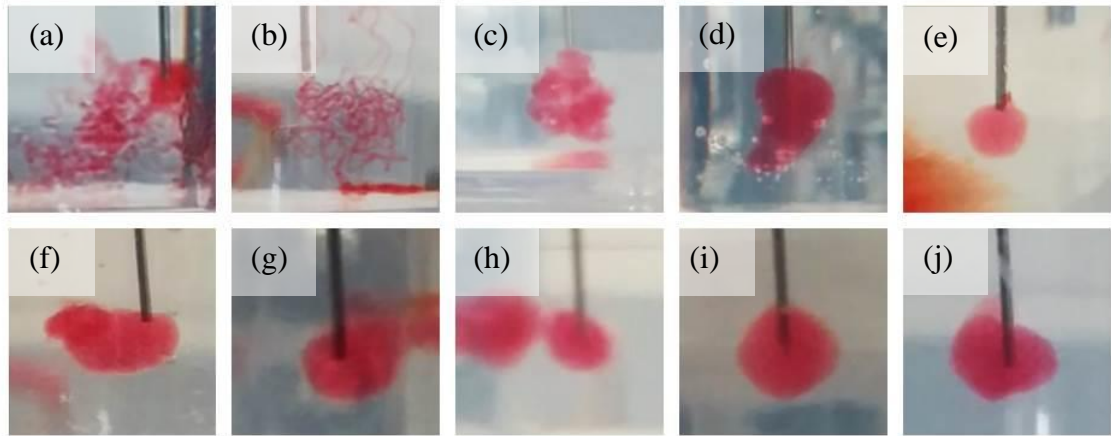
### 5.3 Extrudate Flow Behaviour within Support Baths

An investigation into the supportive properties of various gelatine concentrations is conducted by manually extruding ink into each bath. This work aims to understand if a correlation exists between supportive behaviour and fluidic- or elastic-dominance in gelatine gels via visual assessment and comparison between conditions. Furthermore, partially-crosslinked alginate hydrogels and red dye solutions were manually extruded into the gelatine baths to compare the suspension of inks with different rheology.

#### 5.3.1 Manual extrusion of partially crosslinked alginate into gelatine baths

Figure 5.5 shows the result of manually extruding a partially-crosslinked alginate hydrogel into each of the ten gelatine support bath concentrations. Gelatine concentrations of 0.1% and 0.2% w/v demonstrate a complete absence of suspensive capability and correlates with the tabletop rheological assessment results in that such conditions do not form gels.





**Figure 5.5** – Partially crosslinked alginate hydrogel manually extruded into gelatine baths of concentration (a-e) 0.1% to 0.5% w/v and (f-j) 0.6% w/v to 1% w/v

Suspensive behaviour in fluidic-dominant baths is first realised at gelatine concentrations of 0.3% w/v – extruding partially crosslinked alginate shows slightly suspensive behaviour below the nozzle outlet, indicating that fluidic-dominant gelatine baths can bear supportive properties and may be viable for the application. This trend is maintained in the remaining fluid-dominant conditions with gelatine concentrations between 0.4% and 0.6% w/v. However, conditions between 0.4% and 0.6% w/v appeared to exhibit more rounded and better defined extrudate when compared to the 0.3% w/v condition. A common trait between all the fluidic baths is poor dynamic stability. These baths exhibit a significant oscillatory response when subject to perturbations, such as those incurred by the nozzle moving through the medium, which results in the ink displacing back and forth within the bath - the extent at which this occurs is much greater at lower concentrations like 0.3% w/v. This oscillatory behaviour is representative of the gelatine's rheology – with reference to figure 5.4 shown previously, less concentrated gels exhibit a greater oscillatory response due to their dominant loss modulus (viscous component) and deficient storage modulus (elastic component). As the gelatine concentration increases the storage modulus becomes the dominant factor, and when the discrepancy between both the storage and loss modulus continues to grow with increasing gelatine concentration, the baths become dynamically more stable and exhibit a reduced oscillatory response.

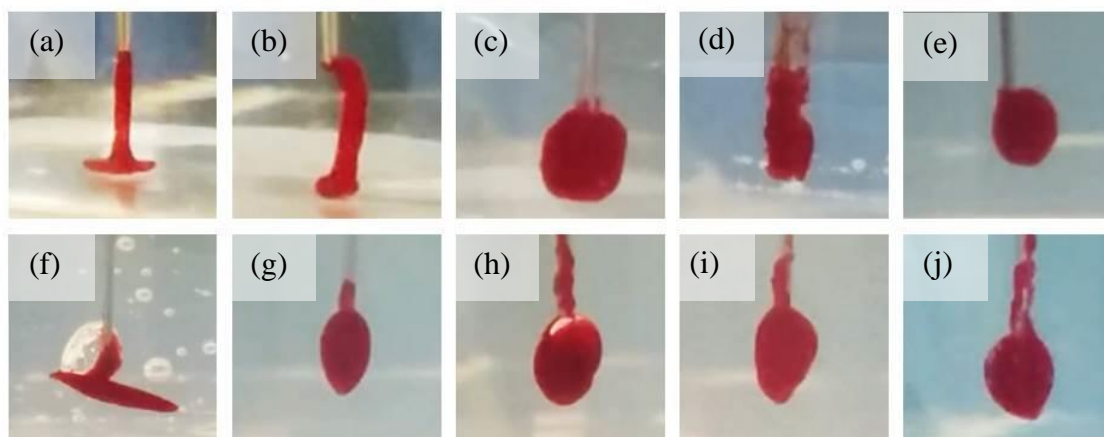
Suspensive behaviour is maintained in each of the elastic-dominant gelatine conditions of 0.7% to 1% w/v. As the gelatine concentration increases, the dynamic stability continues to improve even in these elastic-dominant baths. The rounded morphology of



extrudate is maintained whilst extruding into these conditions, but a slight change in extrudate behaviour compared to the fluidic-dominant conditions is observed. In elastic-dominant baths, extrudate forms a bead around the nozzle outlet. This phenomenon may possibly be related to the material stream being obstructed by the strongly gelled gelatine bath, resulting in a build-up of the ink's internal pressure at the nozzle's outlet, leading to circumferential yielding of the bath around its midpoint which coincides with the nozzle outlet. This is different in fluidic-baths whereby bead formation occurs below the nozzle, possibly due to the bath being weak enough to yield and permit material flow below the nozzle. Therefore the change in extrudate behaviour here correlates with the transition from fluidic- to elastic-dominant baths.

### 5.3.2 Manual extrusion of red dye solution into gelatine baths

Figure 5.6 shows the results of manually extruding red dye solution into each of the aforementioned gelatine bath conditions. The difference between this red dye solution compared to the partially crosslinked alginate hydrogel is an absence of an elastic modulus and lower viscosity. Without an elastic modulus, the red dye solution will readily flow in any direction under the application of stress, or in the case of support baths, will flow more readily within the medium under the build-up of pressure.



**Figure 5.6** – Red dye solution manually extruded into gelatine concentrations of (a-e) 0.1% to 0.5% w/v and (f-j) 0.6% to 1% w/v

Like before, gelatine concentrations of 0.1% and 0.2% w/v fail to show evidence of any supportive qualities and the material stream jets directly downwards until it collides with the bottom of the bath and again correlates with the tabletop rheological assessment results.

Extrusion of red dye solution into gelatine baths of concentrations 0.3% w/v and greater tends to result in the formation of a bead below the nozzle as before. The discrepancy observed at a bath concentration of 0.4% w/v is due to the presence of air within the ink; the upwards strands of ink occurred due to the buoyancy of the air bubbles leaving the bath which was then subsequently occupied with red dye solution. The 0.6% w/v condition is unique in that the red dye solution spreads laterally within the medium when extruded deep enough into the bath. This may be an indication of some biphasic bath consistency whereby the extrudate readily flows downwards through the fluidic-dominant component, but is obstructed by the strongly gelled elastic-dominant component and forces the ink to suddenly change direction. This may also correlate with the result of the tabletop rheological assessment conducted for the 0.6% w/v condition, whereby the bath remained upright after inversion for a period of minutes before eventually yielding and flowing.

Gelatine concentrations in the range of 0.7% to 1% w/v are also met with a change in flow behaviour. In the case of extruding red dye solution, a bead forms but shares a centroid which approximately coincides with the nozzle outlet much like as observed in the extrusion of partially crosslinked alginate. However unlike the extrusion of alginate, some red dye solution protrudes upwards to the bath's surface along the side of the nozzle. This observation is unique to elastic-dominant baths, and thus is likely related to the stiffness of the gel. Inserting a nozzle into the bath cuts it and requires self-healing characteristics to re-seal. It is possible that the self-healing efficiency is poor, resulting in structurally weak regions within the gel which are more prone to yielding. Such regions are located around the nozzle which acts to stress and cut the bath; therefore with a sufficient build-up of the ink's internal pressure, the regions situated around the nozzle yield first and allows for the projection of red dye solution up to the surface. This observation is not made when extruding partially crosslinked alginate into the same bath conditions, and thus is likely related to the lack red dye solution's rheological properties. The low viscosity and absence of an elastic modulus bears such solutions with no yield stress and thus cannot withstand the build-up of internal pressure as capably as partially crosslinked alginate and flows more readily.

Generally, the flow behaviour of partially crosslinked alginate and red dye solution is similar during extrusion into the developed gelatine baths – however partially crosslinked alginate is likely a more stable ink on account of not being projected upwards along the side of the nozzle like red dye solutions extruded into baths between

0.7% and 1% w/v. The results of the tabletop rheological assessment correlate well with the extrusion behaviour of inks – evidence of gel formation, even at conditions that produce a biphasic substance, tend to correlate with some level of supportive ability. Suspensive qualities are apparent at gelatine concentrations as low as 0.3% w/v but more idealised conditions are likely presented nearer concentrations of 0.6% and 0.7% whereby the balance between fluidic- and elastic-dominant qualities is more closely matched, bearing better dynamic stability than lower concentrations yet better self-healing capacity than greater concentrations.

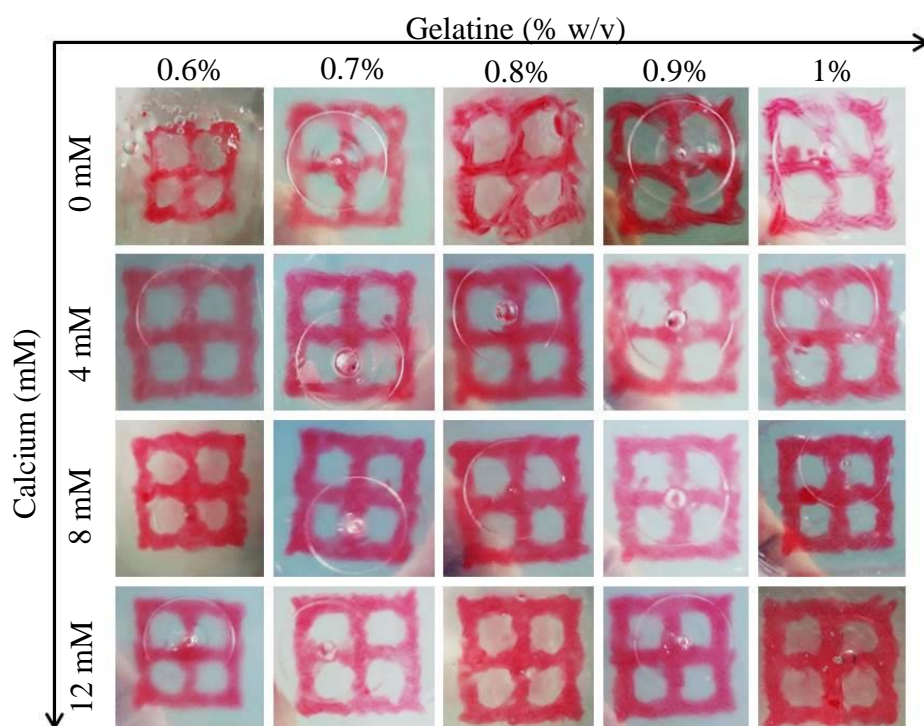
The observations made here are in general agreement with the work of O’Bryan et al. whereby exceedingly fluidic or rigid baths can inhibit the feasibility of support bath printing. O’Bryan discussed that exceedingly fluidic baths can cause extruded inks to break up into droplets or were prone to buoyant displacement, and that exceedingly rigid baths could cause irreparable damage to the support network resulting in the formation of trenches extending from the nozzle tip to the surface [143]. Whilst the breakup of ink into droplets at low gelatine concentrations was not observed, it can be agreed that an insufficiently low concentration is detrimental to the extrusion quality, and stronger gelatine concentrations show the tendency for inks to flow upwards and thus could be indicative of the trenches described by O’Bryan et al. Based on the experimental work shown and O’Bryan’s observations it was anticipated that the optimal support bath should have both fluidic and elastic qualities. An appropriate balance of the two contrasting qualities provides the bulk gel with the beneficial properties of both the elasticity to support and suspend structures throughout the printing process and the fluidity to allow the bath to recover swiftly. For these reasons, it is speculated that such characteristics likely exist at gelatine concentrations situated around the transition point between fluidic and solid-dominant behaviour.

#### **5.4 Printability Study of Support Baths**

The extrusion of partially crosslinked alginate into the developed support baths requires the addition of crosslinking ions to further solidify the bioink and form rigid structures. Therefore a systematic study is conducted to establish a range of appropriate crosslinking conditions which is compatible with the developed gelatine supportive baths. The amount of crosslinking ions added to the gelatine baths (at preparation) needs to be high enough to enable the formation of rigid structures, yet low enough to avoid depositional issues.

The discussion of an appropriate gelatine concentration for the support bath in chapter 5.2 The Influence of Gelatine Concentration on Bath Properties concluded that a bath condition which is situated around the fluidic/elastic-dominant transition point is most likely to provide the best support bath qualities. Based on this discussion, baths with gelatine concentrations ranging from 0.6% to 1% w/v are considered in the following printability experiments. Calcium chloride is added to gelatine solutions at the preparation stage at concentrations of 4, 8, and 12 mM and is compared to a control without calcium chloride. A simple 20 mm x 20 mm x 2 mm grid structure with four equally spaced square 4 mm x 4 mm holes was used as the test piece for printing, which was conducted with a 1 inch long 25 gauge nozzle at a print speed of 10 mm/s.

The printability study (figure 5.7) shows that multiple bath conditions exist with the capability to successfully fabricate grid structures. All grids printed in conditions varying from 0.6% to 1% w/v gelatine and 4 to 12 mM  $\text{CaCl}_2$  maintain a fair representation of the designed CAD model. Grids printed into baths without any calcium appear somewhat distorted and are more erratic in their geometry compared to any of the results with  $\text{CaCl}_2$ . If not supplemented with further crosslinking for solidification, the partially crosslinked alginate will eventually diffuse into the bath. Furthermore, without any crosslinking it is highly unlikely that a successful structure can be released from the bath. The addition of  $\text{CaCl}_2$  at concentrations as low as 4 mM produces grids without the visual distortion that is present in the calcium-free baths, and implies that the crosslinking is sufficient to mitigate diffusion.



**Figure 5.7** - Systematic study of grid printability at various gelatine and  $\text{CaCl}_2$  concentrations

Support bath conditions which comprise of greater gelatine concentrations such as 0.9% and 1% w/v are shown to exhibit less effective self-healing properties. This is evidenced by the trapping of air bubbles within the medium during the printing process. In a perfectly fluid system, self-healing is instantaneous; in stiffer gels such as the 0.9% and 1% conditions, a delayed self-healing response allows air to enter the bath via the wounds generated by the nozzle translating through the medium. This may lead to fabrication issues when larger structures are printed as deposited material will not be suspended within the gel, it will instead fill the volume of the air bubble and result in a loss of depositional control. This effect was not observed at concentrations of 0.8% w/v and below.

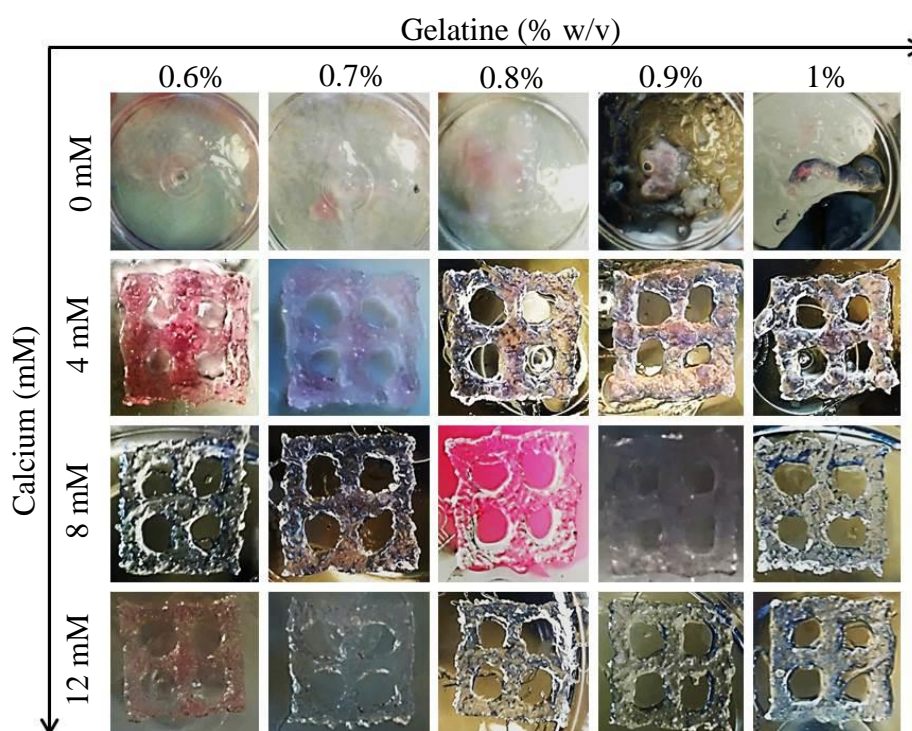
It was found that printing was easier to conduct when the gelatine baths had lower calcium concentrations. At 12 mM  $\text{CaCl}_2$  levels, some minor depositional issues were present during the fabrication process, presented in the form of trailing filament – a phenomenon whereby extrudate is crosslinked too much and sticks to the nozzle instead of being deposited. Whilst this did not result in print failure in the experiment, it could be more problematic when printing larger structures as the trail of filament grows larger and can disrupt previously deposited layers of material. This issue was not evident at

calcium concentrations of 4 and 8 mM, therefore a balance exists between better printability and crosslinking strength.

It has been documented that the presence of divalent cations in gelatine hydrogels can reduce the stiffness and melting temperatures of such gels [261]. However such an effect was not observed in this experiment. The  $\text{CaCl}_2$  levels may be minute enough to not noticeably impact the mechanical properties of the gelatine baths. However if a different, less ionically sensitive alginate were to be used, it stands to reason that greater  $\text{CaCl}_2$  levels would be needed to crosslink such inks which may then be sufficient to affect the mechanical properties of the gelatine baths, although this may potentially be remedied by an increase in gelatine concentration.

### 5.5 Release Study of Support Baths

Following successful printing, the embedded structures are removed from their supportive baths. A 500 ml beaker was filled with 11 mM  $\text{CaCl}_2$  solution, as per the FRESH protocol, with the grid-embedded support bath immersed. The application of heat gently warms up the release bath/calcium solution which in turn melts the gelatine baths and releases the grids from their supports. The result of the release-ability of printed grid structures from the various bath conditions is shown in figure 5.8.



**Figure 5.8** - Systematic study of grid release-ability at various gelatine and  $\text{CaCl}_2$  concentrations

The inability to successfully retrieve fabricated constructs is consistent in all prints conducted into support baths without any calcium, despite the presence of calcium at the release stage. This confirms that the presence of  $\text{CaCl}_2$  within gelatine baths is necessary, imbuing the embedded alginate structures with the rigidity to hold themselves together and prevent diffusion. The release study also confirms that a minimum  $\text{CaCl}_2$  concentration of 4 mM is sufficient to achieve a successful release. Lastly, the release study also confirms that a calcium concentration of 12 mM is not too excessive to prevent the fusion of subsequent layers of alginate, evidenced by the release of a grid with congruent layers. The success of the release of these structures is also likely in part related to the  $\text{CaCl}_2$  levels present within the release bath, therefore higher or lower  $\text{CaCl}_2$  levels in the release bath could be experimented with to obtain mechanically stronger or weaker constructs. Therefore the results indicate again that there exist many viable support bath conditions which allows for some degree of tunability in bioprinting applications.

The dynamic stability of gelatine baths is important not just for printing, but also logistically as the baths need to be transported from the bioprinter to the release bath. This poses a risk to the structural integrity of the bath's contents due to perturbing forces which are exerted upon the bath during manual handling. The more fluidic-dominant condition of 0.6% w/v gelatine is therefore subject to greater risk than the more elastic-dominant gels with gelatine content 0.7% w/v and greater which are more resilient to flow.

Each bath condition is compared to establish which one is most optimal for further experimental work. For obvious reasons, all support baths which do not consist of any crosslinking  $\text{CaCl}_2$  is excluded as such conditions fail to yield a structure at the end of the fabrication process. By superimposing the print and release data, and considering the aforementioned discussions regarding the self-healing ability, the crosslinking conditions, and logistical aspects, a bath comprising of 0.8% w/v gelatine and 8 mM  $\text{CaCl}_2$  is considered most optimal and best suited for further work. It is perceived as capable of printing the strongest structures with minimal risk of encountering depositional issues, is elastic-dominant in nature and thus can be handled more easily yet has sufficient self-healing response to avoid the entrapment of air within the medium.

## 5.6 3D Printing of Dense Anatomical Structures

A range of more challenging structures were printed to evaluate the fabrication limits of the developed support baths. The need to accurately deposit and support extrudate during printing is a key challenge faced by bioprinting technologies and this gelatine support bath method is potentially able to achieve such a goal. The previously printed grids may be considered as simple 2D shapes projected into 3D and does not accurately represent the geometries found in human anatomy. Thus the fabrication of more complex structures both single-walled and thick and mimic some parts of human anatomy is proposed.

For these experiments, a tubular model (10 mm tall, 6 mm outer diameter, 0.2 mm wall thickness), a 'Y' shaped branching blood vessel-like structure (20 mm tall, 13.3 mm branch outer diameter, 1.65 mm wall thickness), and a nose (45 mm wide, 28.2 mm long, 17.8 mm tall) were printed using a 1 inch long 30 gauge nozzle at layer heights of 0.16 mm.

The tube was printed first in an upright orientation and used primarily as a test piece to optimise the ratio of material flow rate to nozzle translational speed. Balancing these two parameters allows for the extrusion of thinner lines and can mitigate overextrusion - a good balance was found at a print speed of 10 mm/s and extrusion multiplier of 0.8. This was deemed a good strategy to optimise the extrusion characteristics as a single-walled structure relies solely on the fusion between layers for its strength. Therefore if the extrusion properties were too low, gaps would form along the walls and thus the structure would fail. These settings were also used for printing branching blood vessel-like structures and noses.

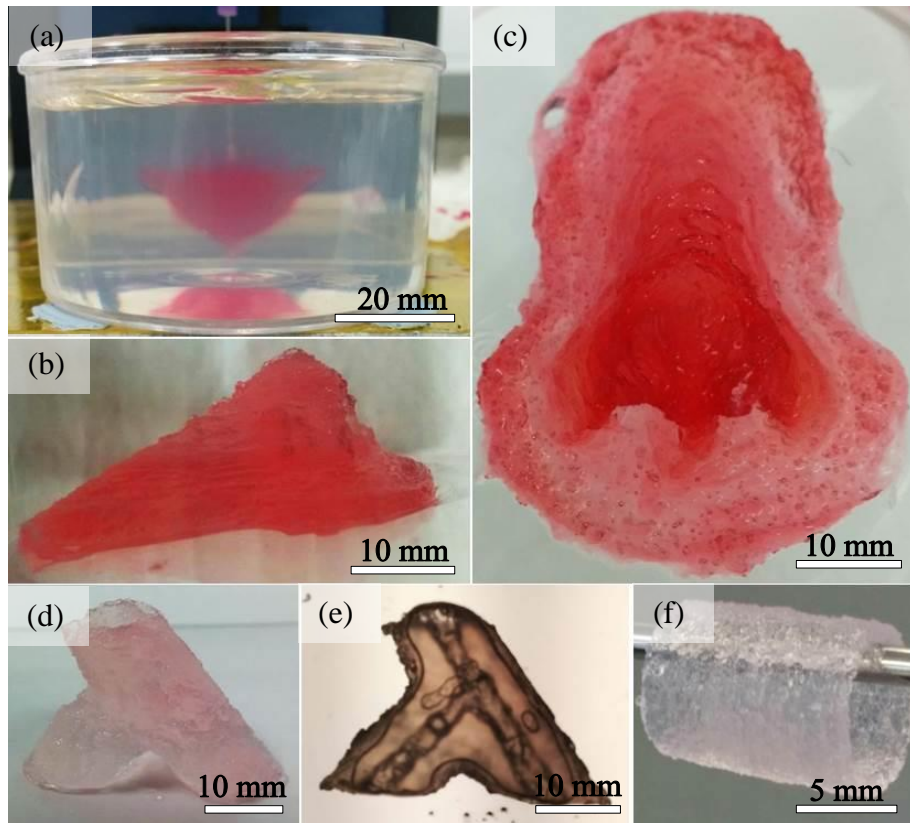
The supportive nature of the developed gelatine baths grants the user with greater freedom in terms of structure orientation, allowing fabrication in orientations which would conventionally be considered impractical without such a bath. To assess the bath's ability to achieve this, branching blood vessel-like structures were printed in a horizontal orientation. Whilst orienting circular details along the Z-axis may yield prints of a higher quality, printing this blood vessel-like structure in a horizontal orientation (circular details along the X- or Y-axis) enables better utilisation of the bath's volume and the size of the structure can be maximised.

During printing, a surface quality defect, termed 'fluff' in this thesis, was observed. This phenomenon is most evident when printing larger and thicker constructs and is



characterised by vertically aligned strands of ink which protrude from the top surface of the printed structure. This is generally a detriment to print quality and is capable of blocking internal channels if not controlled. Reducing the extrusion multiplier was found to reduce the amount of fluff present on structures at the end of the printing process; doing so led to the successful fabrication of a blood vessel-like structure with clear internal channels. Despite this, the occurrence of fluff was not able to be completely eliminated, just merely reduced to more acceptable levels

In certain geometries, it was possible to work around fluff defects by considering the orientation of the structure being printed. Printing structures in an upside-down orientation and designing a thick raft on the model's base keeps all defects on the underside - this was applied to nose printing and is possible due to the divergently aligned surfaces when printed in this orientation. It was the intention that such thick, rafted bases would be removed later in a post-processing stage, but this was never conducted. Noses printed in this manner are distinguishable and resemble a human nose reasonably well with clearly defined nasal passages. The result of the nose printing, as well as the branching blood vessel-like structure and tube is shown in figure 5.9.



**Figure 5.9** – (a) Photograph of a nose during fabrication within a gelatine support bath, (b) side view (c) and top view of the printed nose after successful release, (d) a self-standing branching arterial-like model (e) with a clear internal network, (f) a thin, single-walled tube held up by an 18 gauge nozzle

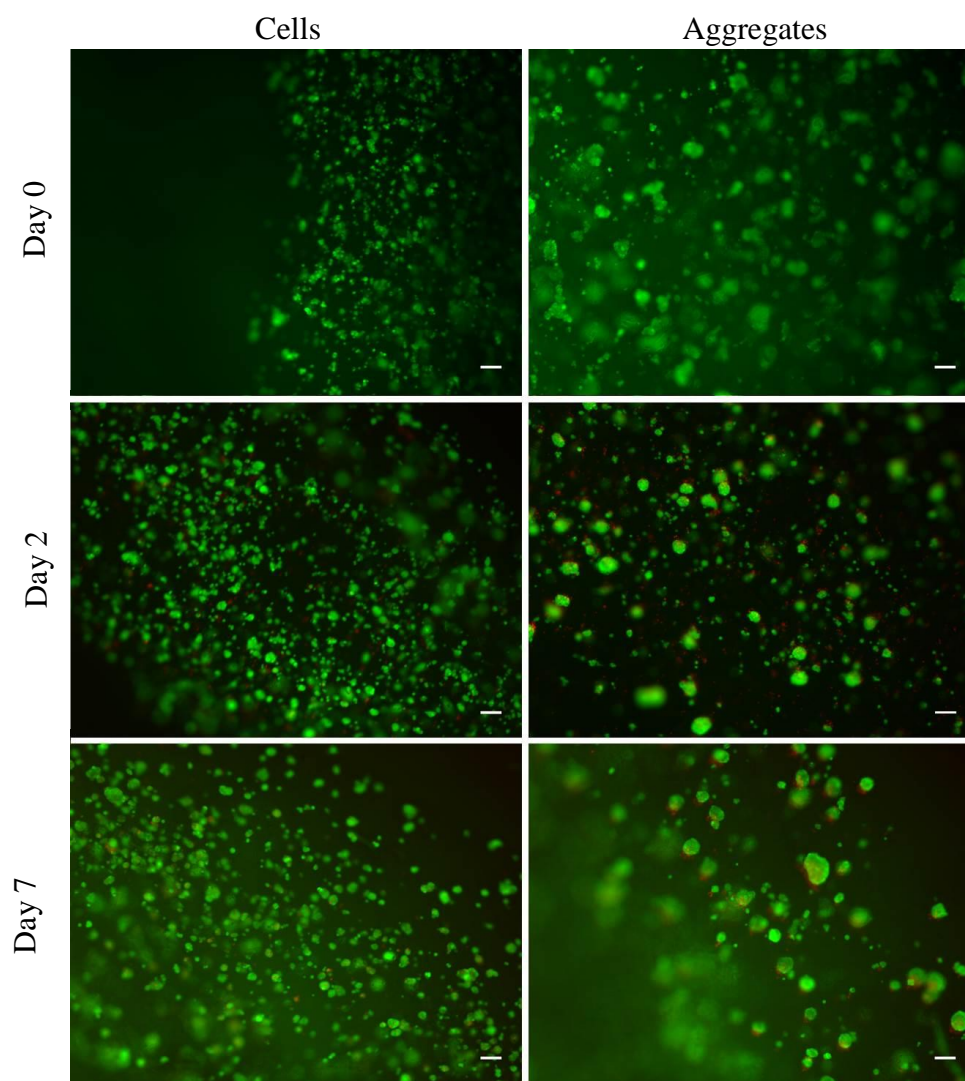
The sensitivity of alginates to crosslinking ions is related to their G-block content, and may cause alginate gels to swell [262]. However, Protanal alginate contracts when exposed to crosslinking ions. This feature of Protanal could allow for the fabrication of even more resolute structures by printing at the maximum possible resolution which then becomes even more resolute as it contracts due to crosslinking. At the calcium concentrations used, printed noses on average shrunk to 74.7% of their original size, as determined by measuring the printed structure's length, width, and height and comparing these to the model's dimensions in CAD.

### 5.7 3D Bioprinting Live Cells into Gelatine Support Bath

For these experiments, a simple ring model was designed in CAD and printed into the gelatine baths with a 1.5 inch 25 gauge nozzle, at a print speed of 10 mm/s; each ring structure was printed once per well for a total of 6 structures, 3 of which were cell-culture-laden structures and 3 which were cell-aggregate-laden structures. The wells were filled to approximately half the height with the support bath gelatine, thus the long

nozzles were necessary to print deep into the well. Once printing was complete, the wells containing the structures were covered in barium chloride and media in approximately equal volume to the gelatine and moved to the incubator to liquefy and further crosslink. The mixed gelatine/calcium/barium solution was removed via pipetting, the structures were washed twice in PBS, fed with fresh cell culture media, and stored in the incubator again to grow.

A LIVE/DEAD assay was conducted on both the cell-culture-laden and cell-aggregate-laden structures at various timepoints after printing and confirmed that cells were capable of surviving the gelatine support bath printing process. The staining process ‘fixes’ cells, meaning that any ongoing biochemical reactions are terminated and further proliferation is ceased; thus each bioprinted structure can only be used to provide cell viability data at a single time point before disposal. The low calcium concentration of the bath in conjunction with a short release time and controlled exposure to barium are believed to be the key reasons for good cell viability post-printing. The fluorescent assay showed cells remained viable in both conditions post-print. The viability of cell-culture-laden structures was assessed at day 0, 2, and 7 post-print and shown in figure 5.10. Live cells were present at all time points, with very little cell death seen in the cell-culture-laden structures, however aggregate-laden structures were noted as having more dead cells which seemed to increase over time. These cell viability assays show that cell viability in the bioprinted structures is robust post-printing and can be supported for at least one week after printing and possibly longer. HepaRG cells, like most epithelial cells, are adherent dependent cells and often undergo anoikis when they do not have an appropriate substrate to anchor to - this makes the viability results of the cell-culture-laden structures quite interesting as a gradual decline in cell viability over the week due to progressive cell death was expected. The measured viabilities of cell-culture-laden constructs and cell-aggregate-laden constructs at day 0, 2, and 7 is 96%, 92%, and 94%, and 93%, 80%, and 79% respectively.



**Figure 5.10** – Viability of HepaRG cell- and aggregate-laden partially crosslinked alginate printed into 0.8% gelatine 8 mM CaCl<sub>2</sub> support bath at day 0, day 2, and day 7. Scale bars: 200 μm. Green: live cells. Red: dead cells

Whilst the cell viability data is promising for both cell-cultures and cell-aggregates and shows that the developed bioprinter achieves cell-friendly bioprinting conditions, the assay only shows the cell viability of a particular structure at a particular time point and does not show cell growth within a single structure over a time period. For cell-culture-laden structures this was not considered given that anoikis was expected to occur due to the cell's anchorage dependency for proliferation and result in a diminishing viability over time; however given the unexpectedly high viability over the 7 day period, a continuous assay may have provided more insightful data to verify if anoikis was indeed occurring or if the cells were dead as a result of the printing process. Furthermore, an assessment of aggregate proliferation over time within a single bioprinted sample would also warrant the use of a non-fixative, continuous assay such as an MTT assay.

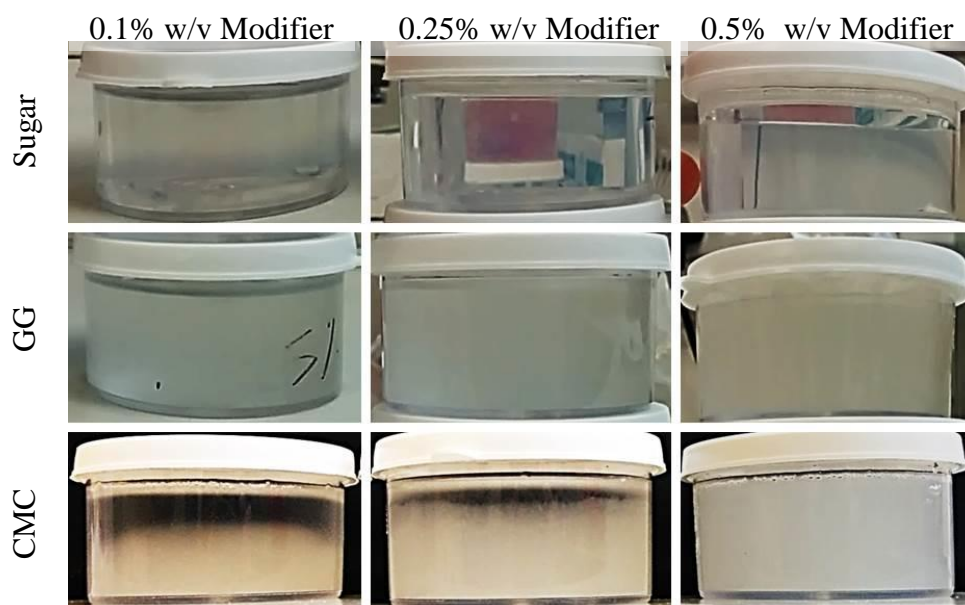
## **5.8 Viscosity Modification of Gelatine Support Baths**

Currently there is difficulty in managing the dynamic stability and the overall gel strength of the gelatine support baths. The matter is complicated in that the dynamic stability to hold extrudate in place is related to the gelatine concentration which in turn affects the gel strength and the gel's self-healing capability. Thus a single parameter, gelatine concentration, dictates two outcomes: gel viscosity and elasticity. This means it is not possible to tune a single characteristic without also affecting the other. If the viscosity of the support bath could be increased, the baths should become more resilient to perturbing forces such as those incurred by a nozzle moving through the medium. Doing so could dampen the oscillatory response of the gel and make material deposition at faster speeds more accurate and reliable than currently achievable.

### ***5.8.1 Influence of viscosity modifiers on gelatine behaviour***

Three different viscosity modifiers, sugar, guar gum (GG), and carboxymethylcellulose (CMC) are mixed with gelatine solutions at the preparation stage in an attempt to influence the bulk viscosity of support baths. Sugar solution is considered to induce a minor viscosity change, whereas GG and CMC are believed to incur a significant change in the viscosity due to their rheological properties. GG and CMC are two common hydrocolloids used to thicken liquids and exhibit thixotropic (shear-thinning) behaviour when stressed, resulting in a temporary decrease in the solution's viscosity. The opacity of GG compared to CMC may be a detrimental factor as it could obscure the print and impair visual assessment during fabrication; however GG is highly effective at increasing a solution's viscosity even at low concentrations.

Each viscosity modifier was prepared to concentrations of 0.1%, 0.25%, and 0.5% w/v with a corresponding gelatine concentration of 0.6% w/v. The gelatine concentration was set as such as this condition can only be inverted briefly before flowing; this is a useful condition as it should be immediately clear if any mixture induces a change in gel behaviour by assessing whether the bath flows immediately upon inversion or remains upright for a prolonged period, respectively. The resulting bath mixtures are shown in figure 5.11 and the results of their inversion are shown in table 5.1.



**Figure 5.11** – Turbidity of 0.6% w/v gelatine mixtures with sugar, GG, and CMC at concentrations of 0.1%, 0.25%, and 0.5% w/v

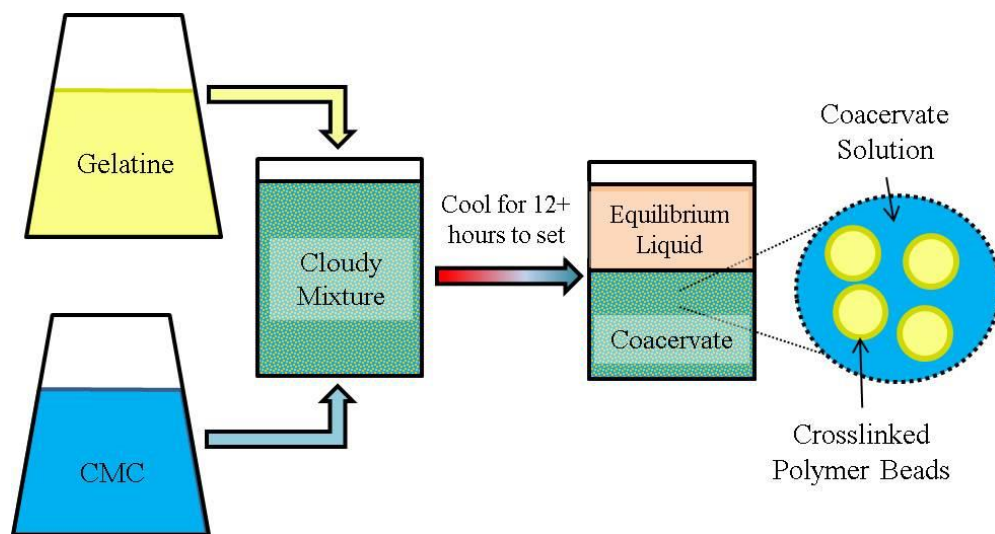
**Table 5.1** - Invertibility assessment results of 0.6% w/v gelatine mixtures with sugar, GG, and CMC at concentrations of 0.1%, 0.25%, and 0.5% w/v

	<b>0.1% w/v</b>	<b>0.25% w/v</b>	<b>0.5% w/v</b>
<b>Sugar</b>	Invertible	Invertible	Invertible
<b>GG</b>	Invertible	Non-Invertible	Non-Invertible
<b>CMC</b>	Non-Invertible	Non-Invertible	Non-Invertible

The data suggests that sugar in conjunction with gelatine is able to maintain the clarity and invertibility of 0.6% w/v gelatine baths. This is likely due to the sugar concentration being too low to induce any significant change in bath behaviour rather than an indication of compatibility. Sugar concentrations at the experimented levels behave largely like water and not as a viscous, syrup-like substance. However the values used were as such in order to keep the concentrations equal between the different viscosity modifiers for a fair comparison.

Mixtures with GG are shown to significantly obscure gel clarity even at concentrations of 0.1% w/v. Clarity may be a desirable attribute of support bath to aid in visual inspection during fabrication but is a non-essential quality that does not affect function. GG mixtures remain invertible at a concentration of 0.1% w/v but fail to do so at concentrations of 0.25% and 0.5% w/v. This implies that GG at greater concentrations interferes with the expected gelling behaviour of gelatine. Deliberate perturbation of the GG mixtures to induce an oscillatory response was noticeably reduced compared to the gelatine baths developed before viscosity modification.

Mixtures with CMC resulted in an unexpected interaction known as complex coacervation between the two biopolymers. This interaction was made apparent by the immediate clouding of the mixed solution, despite the fact that gelatine and CMC solutions are both optically clear. Complex coacervation is an attractive process of electric charges between a positively charged protein and a negatively charged polysaccharide, like gelatine and CMC respectively. During this process, the negatively charged CMC coalesces around the positively charged gelatine molecules and separate into two solutions: the coacervate and the equilibrium fluid (figure 5.12). Gelatine microparticles exist within the coacervate; this is due to the surrounding CMC preventing the gelatine molecules from aggregating at a global level and thus a globally gelled network fails to form. The absence of a global network prevents mixtures with CMC from being successfully inverted and is therefore deemed unsuitable to control the viscosity of gelatine baths.



*Figure 5.12 – Schematic depicting the complex coacervation process exhibited by gelatine/CMC mixtures*



This investigation of viscosity modification of gelatine baths has led to only a single condition to be potentially viable for further experimentation: 0.1% GG with 0.6% gelatine. This condition was the only one which provided a noticeable improvement of the gelatine bath's dynamic stability, most likely due to an increase in the bulk gel's viscosity, without a complete reduction in the gelatine's gelling ability. Reasons for this condition's compatibility are likely related to the low concentration of GG to avoid impeding the gelatine's gelling efficiency, and its non-ionic nature prevents unfavourable interactions such as the complex coacervation phenomenon observed in gelatine mixtures with CMC. However, the ability of GG to control the overall viscosity of gelatine gels is restricted as concentrations of 0.25% w/v and greater negatively impact the formation of gelatine gels. Therefore the compatibility of gelatine and GG is dependent on the concentrations of the two materials: both materials may be miscible and coexist as a mixture at sufficiently low concentrations but becomes unstable once a critical total concentration has been exceeded.

### ***5.8.2 Printing into guar gum/gelatine support bath gels***

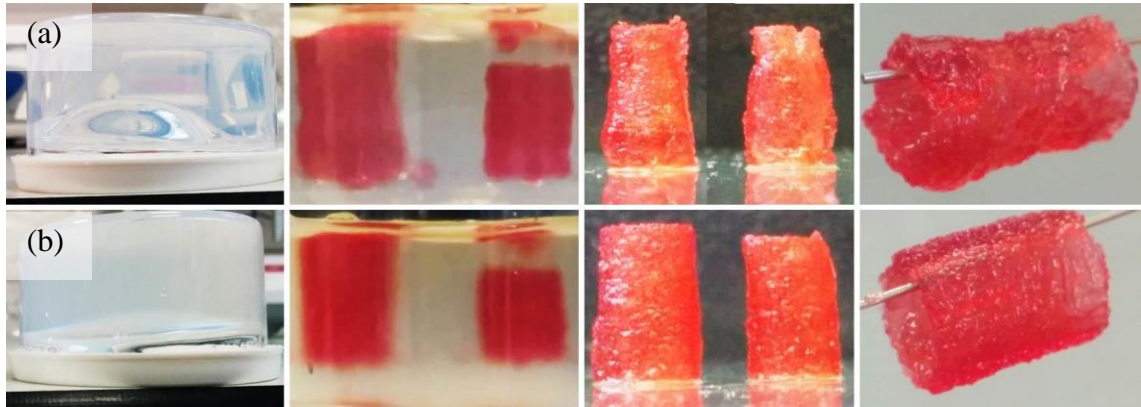
To evaluate if the addition of 0.1% GG is truly beneficial to improving the printability of hydrogels within the support bath, it is necessary to conduct some printing experiments into the baths to ensure that it is still possible to retrieve fabricated structures successfully.

The printing of two simple tubular structures, 15 mm tall and 6 mm in diameter, was conducted at two different print speeds into 8 mM CaCl<sub>2</sub> 0.6% gelatine support baths with and without 0.1% w/v GG using a 1 inch long 25 gauge nozzle. By keeping all other print settings the same, the only difference being the speed, the relative effect of printing into a viscosity-modified bath compared to a standard bath can be visualised.

The results of printing at faster and slower speeds into baths with and without GG viscosity modification is shown in figure 5.13. Both baths exhibited a similar trend in that the print quality tends to diminish at faster print speeds. The reduction in print quality however was far more significant in gelatine baths which did not have its viscosity modified. Regardless of the print speed, tubes printed into baths with GG bore a more consistent diameter and therefore the tubes are printed straighter. The increase in bath viscosity is likely responsible for this improvement as the structures are better held in their deposited location due to having a greater resistance to flow when stressed. By holding the structure more reliably in place during printing, the released tubular



structures have a more aesthetically pleasing surface finish which could be considered an improvement of the print resolution. It can be argued that the print quality of the tube printed into the viscosity modified bath at 60 mm/s even exceeds that of the tube printed into the standard bath at 15 mm/s, an indication that better rheological control of the bath can simultaneously improve both the print quality and fabrication time.



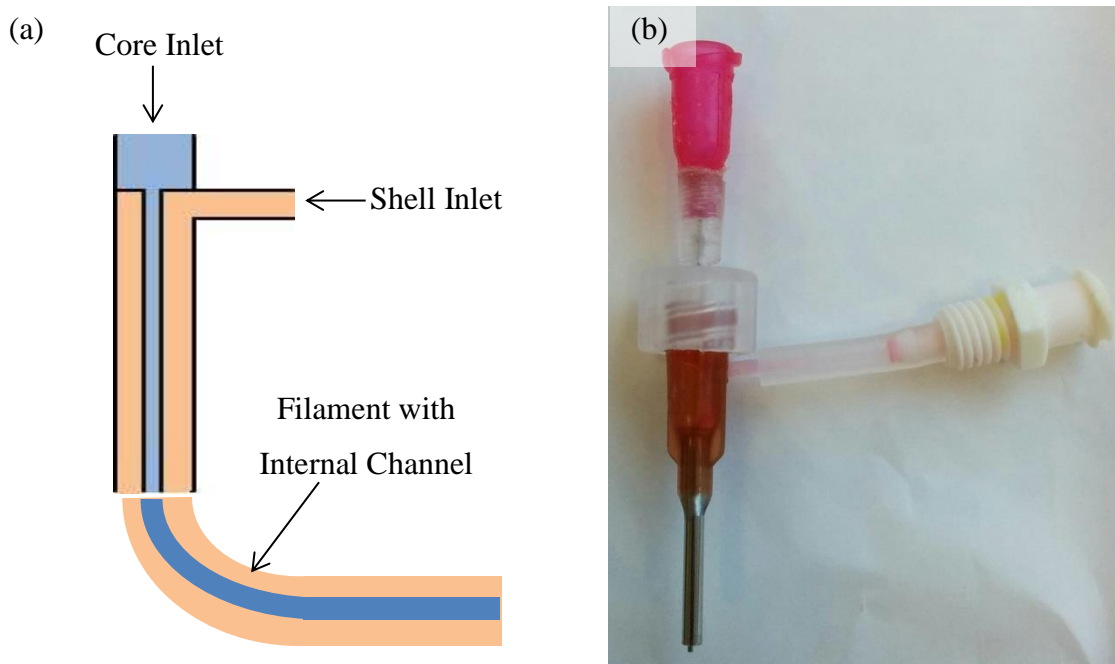
**Figure 5.13** – (a) 0.6% w/v gelatine bath without viscosity modification and (b) with 0.1% GG modification. Tubes on the left were printed at 15 mm/s speeds; tubes on the right were printed at 60 mm/s speeds.

## 5.9 Coaxial Nozzle Printing into Quiescently Gelled Gelatine Support Baths

The combination of coaxial nozzle printing with the supportive nature of the developed baths has synergistic potential. With supported fabrication it is possible to break away from the norm that is layer-by-layer fabrication, and freeform fabrication in true 3D can be realised. This may benefit coaxial nozzle printing strategies as a single, continuous internal perfusable network can be formed and maintained throughout printed structures, as opposed to fabricating a single channel on each layer in the traditional support-free approach.

### 5.9.1 Manufacture of a custom DIY coaxial nozzle

Coaxial nozzles may be described as two nozzles of different sizes that are combined together in such a way that they are both aligned along a single axis. Coaxial nozzles have two material feeds: a core material feed for the internal nozzle, and a shell material feed for the external nozzle. With these definitions, a custom DIY coaxial nozzle was assembled as shown in figure 5.14 below. The DIY coaxial nozzle shown is assembled with a wide 0.5 inch 15 gauge nozzle (1.372 mm internal diameter) for the shell and a long 1.5 inch 25 gauge (0.26 mm internal diameter) nozzle for the core.



**Figure 5.14** – (a) Schematic diagram showing the core and shell assembly of a coaxial nozzle, (b) the assembled DIY coaxial nozzle

The shell's material inlet was formed by punching a hole into the side of the 15 gauge nozzle using a nail – the diameter of the punched nail was matched closely to the diameter of available microfluidic tubing. This microfluidic tubing is then connected to the barbed side of a female luer adaptor with a sleeve – the female luer side of the adaptor can then be connected to a syringe for material to be driven into the shell. This subassembly is completed by fitting a straight barbed-to-male luer lock adaptor on top of the shell nozzle.

The core nozzle is first modified by removing the flanges on its hub using a craft knife. The outlet of a 1 cc syringe barrel is cut away from its syringe and is used to create a connection between the nozzle and a straight barbed-to-male luer lock adaptor. A secure connection between the 1 cc luer slip section and the core nozzle is formed by creating an external thread on the hub of the nozzle and a matching internal thread within the cut 1 cc luer slip section, using an M3 nut and M3 bolt respectively. The nozzle is screwed into the 1 cc luer slip section, and the luer slip section is fitted over the barb of the male luer adaptor which is affixed to the shell nozzle's subassembly.

When the coaxial nozzle was first assembled, it was found that the core nozzle's outlet can jut out from the shell nozzle's outlet and is not perfectly aligned concentrically. This is largely attributed by the DIY nature of the manufacture using components which

are not designed to be assembled in this manner. However it was also found that the core nozzle's outlet can be retracted and realigned slightly by gently twisting the core nozzle and 1 cc luer slip fitting as to ensure the core and shell outlets are flush and centrally aligned.

### ***5.9.2 G-code generation for coaxial printing***

The manner in which Slic3r generates g-code, particularly in the layer-by-layer fabrication approach, may be poorly suited for coaxial printing strategies. The reason for this becomes clearer when complex geometries are loaded into the software for g-code generation – layers may not be possible to complete as a single path and, if enabled, multiple retract operations could cause the internal channels to become disconnected from the rest of the layer. This would be problematic during perfusion as the media would not be able to flow throughout the entire structure as intended, leading to a build-up of fluid somewhere inside the structure and some regions being absent of nutrients entirely. Two cases where Slic3r may be viable in conjunction with coaxial printing would be if the entire structure could be printed in one continuous toolpath, including Z axis movements, or if each layer could be printed as a continuous segment and each layer be perfused separately.

Furthermore, the bioprinter has only a single extruder mounted onto the X-axis carriage. Therefore to concurrently drive material through both the core and shell of the coaxial nozzle, a syringe pump was needed. The syringe pump's stepper motor was controlled by a spare RAMPS 1.4 microcontroller board which had been flashed with the Marlin firmware and could be driven continuously using the Pronterface software via USB cable. Based on the geometry of the manufactured coaxial nozzle, its fittings, and the bioprinter itself, the syringe pump was only suitable for feeding material into the shell nozzle. Whilst the method of material extrusion through the core and shell nozzles relies on two independent systems, the two can be controlled so that they run simultaneously and flow at similar rates.

To overcome the perceived restrictions of Slic3r in the context of extruding material through the coaxial nozzle's core using the bioprinter, custom g-code was written in Excel to formulate the data points necessary in the X, Y, Z, E (extruder) axes, F to set the speed, and G to set the command. For testing the feasibility of coaxial printing into the gelatine support baths, a simple spiralling tubular construct was planned for fabrication. The idea was that the structure could be perfused at an inlet situated at the

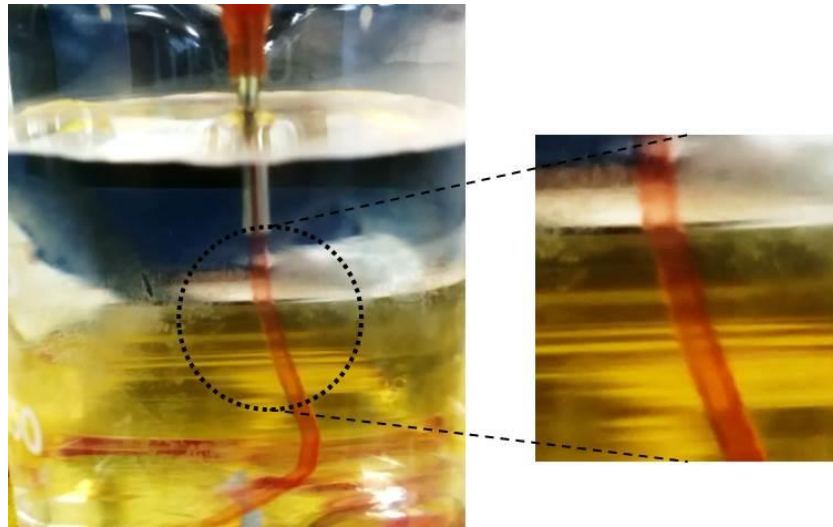
base of the structure and the pressure would drive the liquid up along the inside of the structure in a spiral path and leave at an outlet at the top. Details of custom g-code generation may be found in Appendix B – Using Excel for Spiralling Structure G-code Generation

### ***5.9.3 Coaxial extrusion into calcium solution***

Prior to experimenting with the coaxial extrusion of material into a gelatine support bath, an experiment was conducted to ensure that the flow rates of both the core and shell were compatible with each other to produce perfusable tubes. To do this, the coaxial nozzle was immersed in a beaker filled with calcium solution to crosslink the external surfaces of the extruded filament whilst the core, also loaded with calcium solution, crosslinks the internal surfaces. This allows for a working set of extrusion parameters to be identified before any support bath printing takes place.

The fabrication of hollow filament is realised when the flow velocity, not flow rate, of both core and shell streams are matched. This means that both the core and shell material streams leave their outlets at the same speed and join together as one congruous filament. The flow velocities are matched mathematically by understanding the volumetric flow rate – the ratio between the diameters of the core and shell is equal to the ratio between the flow rates of both material streams. The extrusion rates of each material stream for unified flow velocity is determined by dividing the respective stream's flow rate by its syringe barrel's cross-sectional area.

Coaxial extrusion was achieved by executing a g-code file to command the printer to extrude material for a set length of time, but was maintained stationary along the X/Y plane by disconnecting the stepper motors on the respective axes – this ensures that a single continuous stream of filament is produced. The shell material feed was connected to a 3 cc syringe barrel driven by the syringe pump to extrude partially crosslinked alginate. The core material stream's 10 cc syringe barrel was filled with CaCl<sub>2</sub> solution at a concentration of 20 mM (dyed green) to form the internal channel of extruded filament. Coaxial extrusion was conducted within a 500 ml beaker filled with 8 mM CaCl<sub>2</sub> to crosslink the external surfaces of the extruded filament as shown in figure 5.15.



*Figure 5.15 – Coaxial extrusion into calcium solution shows some evidence of internal channel formation*

There is evidence of two distinct material streams within the extruded filament as indicated by a lightly coloured central region with dark red regions on either side which indicates the presence of a thickly gelled alginate wall. This suggests that the extrusion conditions are well matched to enable the congruent extrusion of coaxial filament with a hollow internal channel. To confirm this, a section of the coaxially extruded filament was cut and perfused with red dye solution in figure 5.16. The ability of the red dye solution to flow from one end of the cut section to the other without leaking shows that an internal perfusable network had indeed formed and that the walls were sufficiently sealed. Some red dye solution is shown to have spilled onto the surface, but this was due to some back flow of the solution incurred by not inserting a nozzle of sufficiently thick diameter deep enough into the filament. This confirms that compatibility of flow velocities of both material streams.

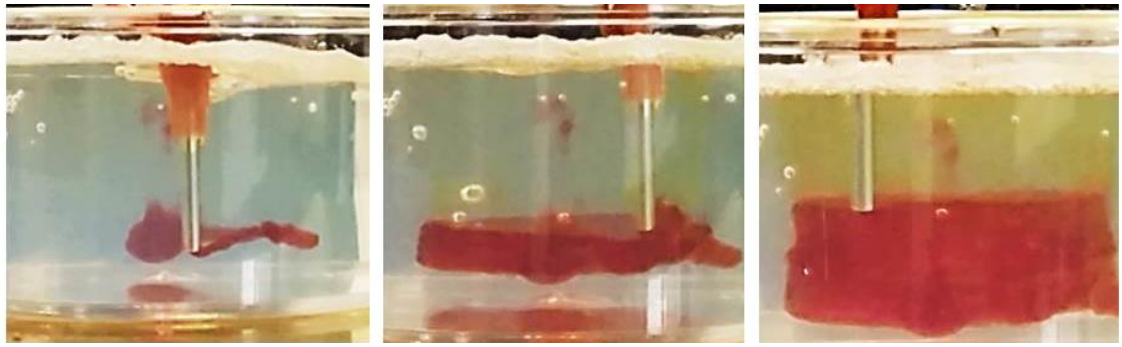


*Figure 5.16 – Cut section of coaxially extruded filament is perfused with red dye solution to show successful internal channel formation*

#### **5.9.4 Coaxial extrusion into gelatine baths**

The flow settings for both core and shell material streams for compatible coaxial nozzle printing into calcium solution is now applied to the fabrication of structures supported by the developed gelatine baths. For these experiments, g-code for a 20 mm diameter, 10 mm tall spiralling structure with 1 mm pitch was generated in Excel, and the X/Y stepper motors were reconnected to facilitate full range of motion once more. In these experiments, the 0.8% w/v gelatine support baths with 8 mM CaCl<sub>2</sub> were used to support the extruded ink.

Fabricating structures within the gelatine support baths first required better optimisation of the conjoined material stream's flow rate and the translational speed of the printhead. Compared to the extrusion of straight filament within a beaker filled with calcium solution, filament extruded into the gelatine support baths was coiling. The coiling phenomenon occurs when the ratio of flow rate to translational speed is too high [126]; therefore the printer needs to either move faster or the flow rates of the core and shell material streams needs to be reduced. The extrusion rate of the shell could not be lowered any further within Pronterface as it was already the lowest available value and subsequently meant that the core material stream could not be lowered without a causing a mismatch between the flow velocities. Therefore the translational speed was increased in Excel from F120 (2 mm/s) to F480 (8 mm/s) which was found to produce straighter filament. With these new settings, spiral structures were attempted to be printed into the gelatine support baths as shown in figure 5.17.



*Figure 5.17 – Coaxial nozzle extrusion into a 0.8% w/v gelatine bath using g-code derived from the developed Excel spreadsheet; the calcium solution core (dyed green) above the structure indicates unsuccessful internal channel formation*

The process of printing spiral structures generated from the Excel g-code generator begins at the base of the gelatine bath, and the nozzle makes circular revolutions up until the top of the structure. The deposition of material into the bath appeared to be reliable, with material suitably positioned in close proximity to the outlet of the coaxial nozzle assembly. Extrudate initially shown the tendency to displace vertically and rise up by a small distance upon deposition, but it is speculated that this is in some way related to the relatively large nozzle diameter used compared to previous prints which used finer 25 and 30 gauge nozzles. This may pose some minor problems such as adjacent lines of filament being moved closer to each other than intended, but can be adjusted by altering the vertical spacing between lines i.e. the pitch. However a more significant problem presented itself and is evidenced by the presence of green dye outside and above the printed structure. Since the only material component which has been stained green is the core material, the fact that green dye is present outside the main body of the spiral structure signifies that the core material stream does not remain inside the alginate shell throughout the coaxial printing process; this is an indicator that an internal perfusable network has not successfully formed. It is speculated that this phenomenon could occur due to the differences between extruding partially crosslinked alginate gel versus low viscosity solutions as observed in chapter 5.3 Extrudate Flow Behaviour within Support Baths. The tendency of liquid-like inks to flow upwards post-deposition was believed to be related to the support bath's gelatine concentration; hence it was proposed that a less concentrated gelatine bath could better accommodate the coaxial extrusion of perfusable filament. Additionally there were no observed problems with the formation of hollow filament when the materials were extruded into calcium solution which has a significantly lower viscosity than gelatine despite not



being able to support structures due to the absence of an elastic modulus. This may be an indicator that the bulk rheology of the gelatine support baths needs to be altered in order to facilitate better compatibility with coaxial extrusion practices.

Releasing the coaxially printed spiral structure confirmed the absence of any internal perfusable network (figure 5.18); the presence of green dye outside the structure in the support bath correlates with an absence of any internal network when released. Additionally the fusion of subsequent layers of alginate was not optimal as not all sections were connected in a satisfactory manner; some regions were not connected at all and as a result just peeled away from the rest of the structure.



*Figure 5.18 – Coaxially extruded structure released from 0.8% w/v gelatine support bath*

A difference that cannot be deduced between the gelatine baths versus simple extrusion into a bath filled with calcium solution is whether the geometry of the spiral structure is the problem. The ratio of lateral (X/Y plane) movement compared to the vertical (Z axis) movement causes the filament to bend sharply, almost orthogonally. The alginate shell of the coaxially extruded filament may be most affected by this and shield the core from the shear stresses incurred when moving through the gel. The alginate shell when subject to the shearing stress realigns its flow from being vertical to horizontal, whereas the core may remain more vertically aligned in the absence of as much shear to redirect the flow. Due to the misalignment post-deposition the core material may no longer be centrally positioned within the alginate which allows the walls to come into contact with each other, thus sealing the filament without a channel.

Another possible explanation for the absence of an internal channel could be that the calcium concentration of the core is not high enough to crosslink the alginate fast enough to enable the walls to hold their shape sufficiently. However 40 mM is already



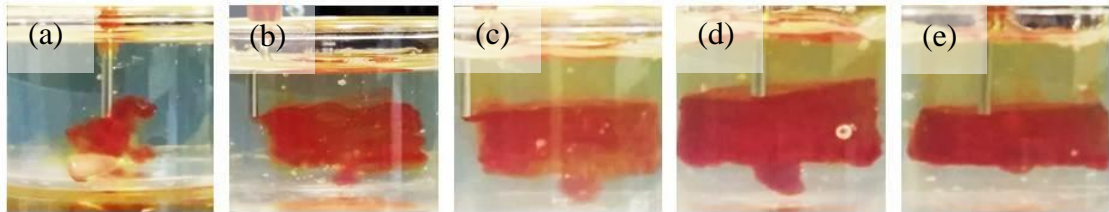
a moderately strong concentration to expose the protanal alginate to, given its highly sensitive nature to divalent cations – furthermore it has already been shown that entirely self-standing structures can be produced at much lower concentrations of 8 mM and in the interest of cell viability, less calcium is better. Perhaps the use of a different core material, one with more complex rheology, would be better for the purpose of maintaining a core. For instance, a calcium enriched gel could be used to improve the mechanical strength of the core and potentially better support the formation of an internal network within the extruded filament. This may encourage the core's material stream to maintain a more circular cross-section compared to a purely liquid stream.

A third perceivable problem could be simply that the core material stream simply does not strictly have anywhere it can flow to. Unlike the extrusion into a calcium bath where both the core and shell can flow freely from the coaxial nozzle's outlet down to the bottom of the bath, the gelatine bath's strength does not readily permit material flow once it has been deposited. Instead what is observed when gels are extruded is the formation of a bead at the nozzle outlet until the nozzle is moved whereby longitudinal lines are formed; when liquid is extruded the bead grows in size until the internal pressure is sufficiently large to cause the liquid to flow along the path of least resistance, which is upwards along the side of the nozzle as such regions are weaker requiring self-healing from the nozzle intersection. For a perfusable channel to form the core material likely needs to be flowing in a consistent and steady stream, which cannot be the case if the material forms a bead at the nozzle outlet due to the gelatine preventing such behaviour.

Exploring the idea that the gelatine concentration of the support bath was a potential problem for coaxial extrusion, the remaining concentrations which were known to have some supportive qualities (0.3% to 0.7% w/v) were prepared with 8 mM calcium chloride for crosslinking. It was thought that the conditions for successful coaxial extrusion might exist at lower gelatine concentrations to facilitate the fabrication of perfusable structures in an even gentler manner.

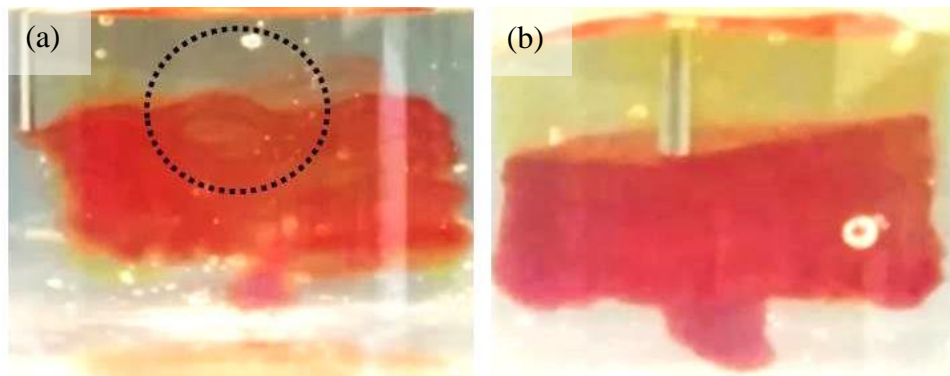
Figure 5.19 shows the coaxial printing of the generated spiralling structures using support baths with gelatine concentrations in the range of 0.3% to 0.7% w/v. At 0.3% w/v, it can be seen that whilst there is some suspensive behaviour, the overall rheology is inadequate to support the printing of structures. The shape fidelity and repeatability of the printed spiral structures continues to improve as the gelatine concentration is

increased from 0.4% to 0.7% w/v; however the presence of green dye solution above the structure is presented at concentrations of 0.5% w/v and greater, indicating that the formation of an internal network becomes less likely at conditions which are more favourable for maintaining the shape of printed structure. The most optimistic condition for coaxial fabrication is hence 0.4% w/v gelatine.

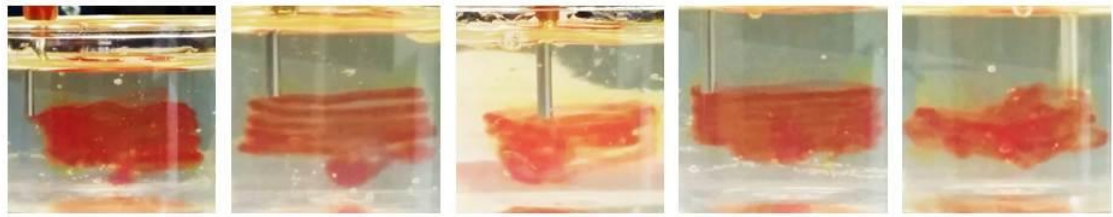


**Figure 5.19** – Coaxial extrusion into support baths with gelatine concentrations of (a) 0.3% to (e) 0.7% w/v

Figure 5.20 shows some evidence supporting the formation of an internal channel within a 0.4% w/v gelatine bath and is compared to a 0.6% w/v bath, despite the presence of some green dye solution around the structure. However unlike the 0.6% w/v condition the repeatability of printing into 0.4% w/v gelatine baths is very unreliable, yielding results wherein the adjacent lines do not fuse, become tangled, are printed straight or wavy, print successfully or fail catastrophically (figure 5.21).



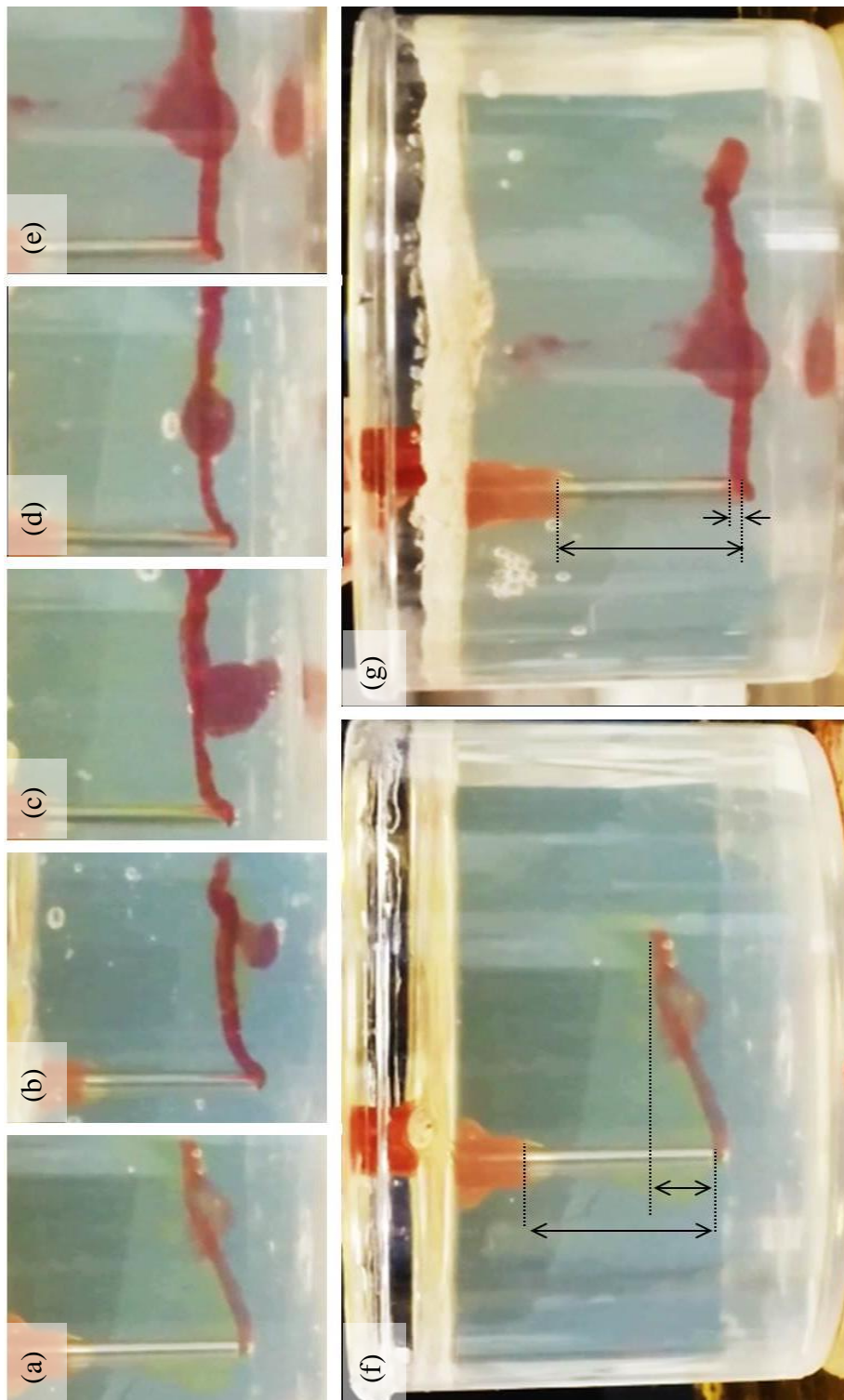
**Figure 5.20** – Comparison of coaxially printed structures into baths with (a) 0.4% and (b) 0.6% w/v gelatine; extrusion into 0.4% w/v gelatine baths shows some evidence of internal channel formation at a loss of printability



*Figure 5.21 – Assessment of print repeatability of coaxial extrusion into 0.4% w/v gelatine baths*

The current hypothesis to explain the observations made whilst attempting to coaxially print structures within the developed gelatine support baths is that the core material does not have anywhere where it can easily flow to. In the case of the stronger, more elastic-dominant baths, the yield stress of the gelatine may exceed the jetting force of the core material stream and thus cannot be reliably inserted within the medium. With subsequent extrusion, the build-up of internal pressure causes the weaker self-healing regions beside the nozzle to yield, allowing the calcium to slip and project upwards above the structure and fails to produce an internal perfusable network; alginate does not exhibit this characteristic (as observed in chapter 5.3 Extrudate Flow Behaviour within Support Baths) which is why alginate can be reliably deposited but calcium cannot. This hypothesis is supported by evidence of an internal network being formed only at a fluidic-dominant 0.4% w/v gelatine support bath in which the bath is weak enough to yield in favour of internal channel formation whilst retaining some suspensive characteristics; however the printability into such baths is very poor on account of its low elasticity.

Another characteristic of coaxial printing into the various concentrated gelatine baths is the phenomenon of filament rising up post-deposition. At a low concentration of 0.4% w/v, filament rises more significantly compared to printing into 0.8% w/v gelatine baths (figure 5.22). This could correlate with print-repeatability issues present in less concentrated baths, whereby risen filament is more susceptible to becoming entangled around the nozzle as it makes subsequent passes to print adjacent lines.

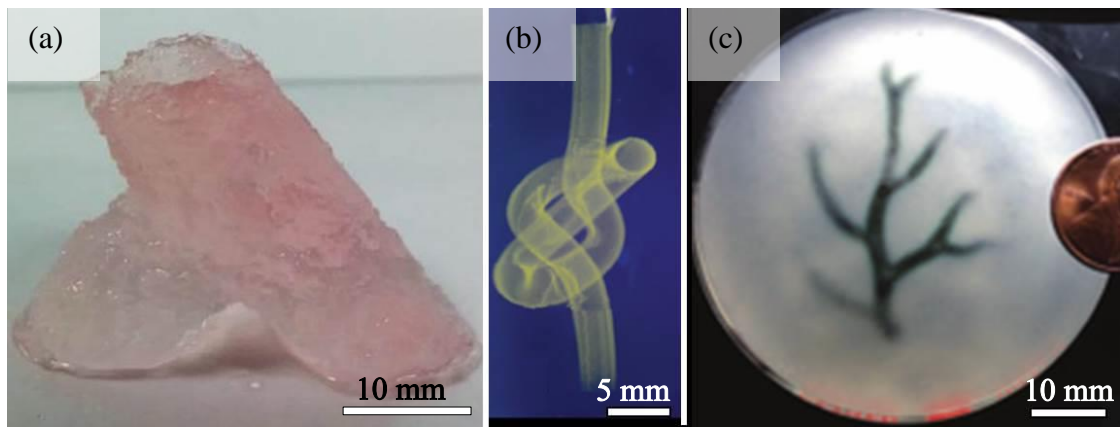


**Figure 5.22** - Rising filament phenomenon when coaxially extruded filament is printed into various gelatine baths (a) 0.4% to (e) 0.8% w/v. The difference in vertical displacement between (f) 0.4% and (g) 0.8% w/v is measured relative to the nozzle size and is shown to be significantly greater at lower gelatine concentrations

A contradictory set of conditions exists which requires fluid-dominant behaviour for reliable formation of an internal network ( $\sim 0.4\%$  w/v) and simultaneously requires more elastic-dominant behaviour for print repeatability and shape fidelity ( $\sim 0.8\%$  w/v). Even at conditions closer to the fluidic/elastic-dominant transition point ( $\sim 0.5\%$  to  $0.7\%$  w/v), the formation of an internal network could not be achieved. As a result of these contradictory conditions, a balance of the properties was not successfully met.

### **5.10 Summary**

The work described within this chapter documents the development of a new support network via quiescent gelation which is fundamentally unlike other methods based on the formation of microparticulate networks. Primarily the developed gelatine-based support baths aimed to eliminate as many of the processing and preparation challenges that are present in the FRESH method. This was achieved and a large number of processing steps were removed simply by preparing the supportive material in a manner which was ready to use immediately post-gelation without any further work. The mechanical qualities of the prepared quiescently gelled gelatine support baths can be tuned slightly by changing the concentration of gelatine at preparation, offering some flexibility whilst establishing more idealised print conditions. With this simplified approach, it was possible to suspend and support structures throughout fabrication and can print HepaRG cells with a high viability. Whilst the preparation process is significantly simplified in these quiescently gelled support baths, making it simpler to incorporate support bath printing into one's research, the resulting quality of the printed structures is not as high as exemplified by other methods as shown in figure 5.23. This is largely due to the presence of surface quality defects which causes strands of alginate to protrude vertically outwards from the printed structures - a detrimental property specific to the developed support baths which hinders the resulting print resolution, and is not an indication of poor print settings.



**Figure 5.23** – Comparison of 3D structures printed from (a) the developed quiescently gelled gelatine support bath, (b) a Carbopol-based granular gel support bath [128], and (c) the gelatine-based FRESH method [134]

Developments to enhance the fabrication speed whilst maintaining or improving upon the depositional accuracy of extruded inks through the addition of GG to modify the viscosity was fulfilled in 5.8.2 Printing into guar gum/gelatine support bath gels. This enabled the fabrication of simple tubular structures with greater print quality at faster speeds compared to baths without viscosity modification; however the effective tuneable range of viscosities is severely restricted to 0.1% w/v GG due to an incompatibility between gelatine and GG once a critical material concentration has been exceeded. To circumvent such a limitation, the search for a more appropriate and compatible viscosity modifier may need to be conducted.

The integration of a coaxial nozzle fabrication strategy was unsuccessful on account of an unsuitability of the gelatine baths to facilitate such printing. A balance between suitable bath properties and core/shell material properties could not be met that would allow for the fabrication of structures with a continuous internal perfusable network. At the time, there was no known literature of coaxial nozzle printing specifically into a support bath in a manner similar to FRESH or otherwise; however a new, alternative supportive technique has been reported very recently (February 2020) to assist in the fabrication of interconnected prevascular networks [263]. In this work, coaxial nozzle printing was conducted into a partially crosslinked gelatine solution which was fully gelled after printing was complete to securely encapsulate the printed construct within. It is hence speculated that a fluid-dominant support bath is perhaps more desirable than one which is elastic-dominant; partial crosslinking of the gelatine in combination with its use at high concentrations (up to 12% w/v) allows the support bath to exhibit fluid-

dominant behaviour with sufficiently high viscosity to maintain good dynamic stability for printing, whilst partial crosslinking provides the appropriate elasticity for supportive behaviour. This method's approach and application (printing prevasculature into a highly concentrated, partially crosslinked solution then inducing gelation) is quite different than the method developed in this thesis (printing structures into low concentration pre-gelled gelatine); whilst it has excelled at demonstrating coaxial printing within a supportive medium, it is not yet clear if such a support bath can print large or thick structures coaxially or otherwise.



## **Chapter 6 – Supported Fabrication of 3D Structures within an Agar- Agar Fluid Gel Medium**

### **6.1 Introduction**

Supportive strategies can be considered a key technology to progress the biofabrication of highly viable soft tissue-like structures, as explored earlier in Chapter 5 – A Quiescently Gelled Gelatine Supportive Medium to Facilitate 3D Soft Tissue Biofabrication. The need for an appropriate supportive network stems from the shortcomings observed in traditional ‘printing on glass slides’ approaches, such as the poor capability of producing overhanging features and generally low mechanical strength of structures that are unable to support themselves. Efforts to improve the structural qualities of structures often involve the use of a stronger pre-gelled, high viscosity ink or more extreme crosslinking conditions which typically results in poorer cell viability; such is the dilemma faced by the biofabrication of high resolution and highly viable cellular structures.

Whilst the use of the developed gelatine-based support bath has several merits, notably its ease of preparation and simple release mechanism, there were some aspects which needed improvement; features such as the ‘fluffing’ defects (the presence of vertically aligned strands of alginate protruding out from the structure’s surface) commonly observed during fabrication as well as the gradual thermal degradation of the bath’s mechanical strength due to the gel’s low melting point, a material property of low concentration gelatine, were the main concerns with that strategy. The observed fluffing defects were likely caused by the quiescently gelled nature of the gelatine which would have more likely behaved as a single block of soft, permeable gel; this is in contrast with other established support methods like FRESH which break up the gelatine gel into discrete microparticulate gelled slurries, producing baths which do not behave as a single gelled mass and from their respective image data do not exhibit such printing defects.

Here, the use of commercially available agar-agar (agarose-agaropectin, or simply ‘agar’ referring to the non-purified substance), a thermogelling biopolymer which in culinary practice is often regarded as a gelatine substitute for making jellies, is proposed. The qualities of agar as such are similar to those of gelatine in that firm-cutting, strong but brittle gels are produced when the molecules are activated upon heating the powder in water for dissolution, followed by a period of cooling to induce

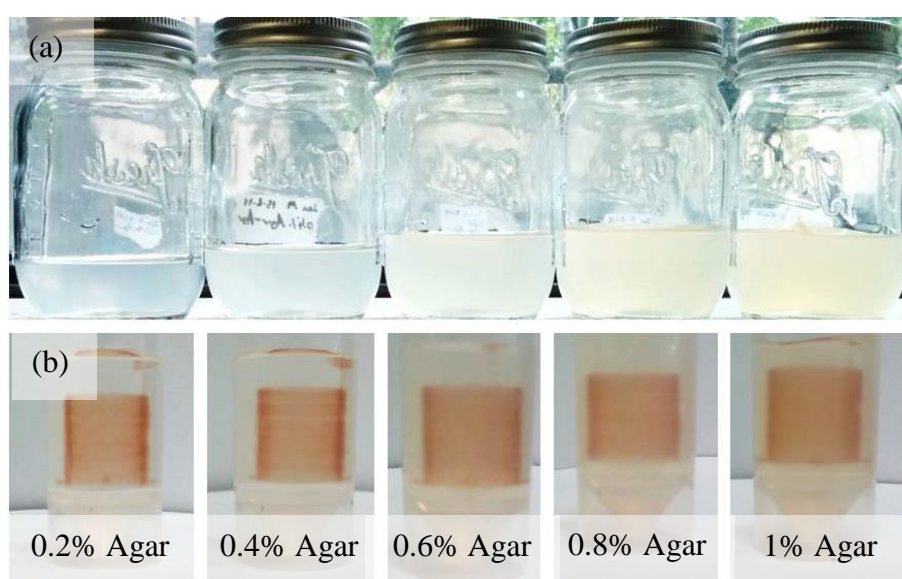


gelation. However the difference between the two biomaterials is that agar is derived from seaweed and is not animal-based like porcine, bovine, or fish gelatine. Agar, whilst thermogelling like gelatine, has a greater dissolution temperature of around 100° Celsius and rapidly forms a gel upon cooling down to around 40° Celsius; however unlike gelatine, agar exhibits thermal hysteresis whereby the gel will not re-melt until the temperature reaches 100° Celsius again, thus making agar the more thermally stable biomaterial. Additionally, and related to agar's thermal hysteresis, the resulting gels can be readily blended without causing the gel to re-melt due to the build-up of frictional heat, a common problem experienced when blending gelatine gels due to their much lower melting temperature. Consequently the agar's hysteresis quality means that releasing printed structures in the formally adopted manner, the application of heat to liquefy the medium, is not practical for the preservation of printed cellular structures due to the extreme temperatures required to re-melt the agar; instead the supportive fluid gel can be washed away with water or cell culture media in a controlled manner so long as the liquid is not directly jetted forcefully onto the structure itself.

The principal reason for using commercially available agar instead of agarose is to keep the costs minimal. Whilst printing, the support bath's volume will greatly exceed the extruded volume of printed structures thus a lot of raw material is needed which can become costly very quickly. As far as the constituents of agar are concerned, the content of the strongly gelling agarose component varies and depends on the algal source. In one study, the ratio of agarose to agaropectin from agars derived from Korean *Gelidium amansii* and Chilean *Gracilaria* sp. was 1.5:1 and 20:1 respectively [264]; the agaropectin content is largely regarded as non-useful compared to agarose and usually discarded [265]. Therefore the relative disadvantage of commercially available agar powder is that the more expensive agarose tends to be more translucent and forms stronger gels. At equivalent concentrations, the agarose may be disadvantageous because of the additional strength of the gel and greater microparticulate volume resulting in a network which may be too strong and too viscous, but would otherwise be advantageous for visual assessment during fabrication at greater expense. However once the feasibility of agar fluid gel baths has been understood, the relative value of its purified variant, agarose, may then be investigated and compared.

## 6.2 Systematic Evaluation of Agar and Calcium Concentration on Supportive and Print Qualities

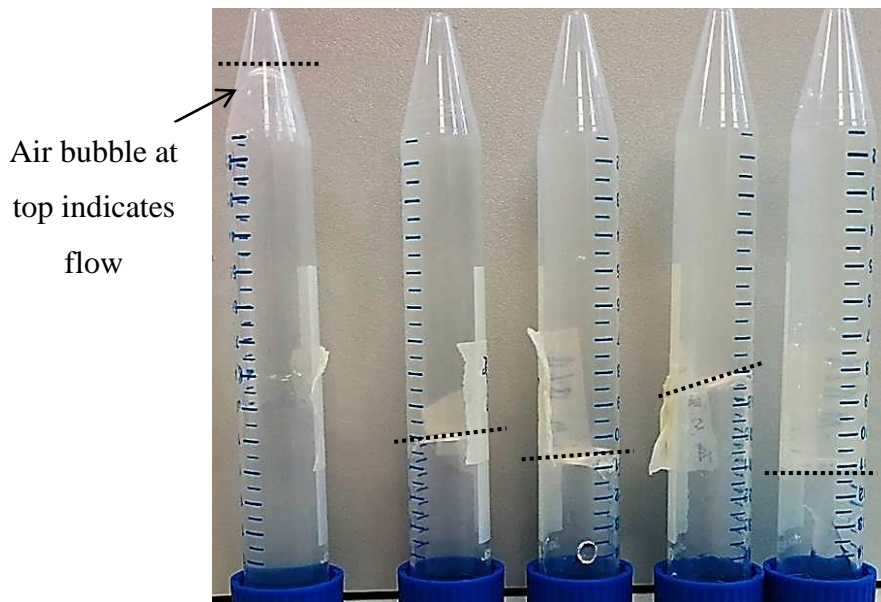
The first step necessary for bath printing is to establish what agar concentrations are appropriate, and which are not, to support structures throughout the biofabrication process. A simple and systematic process of trial and error was employed to test the range of agar fluid gel concentrations of 0.2%, 0.4%, 0.6%, 0.8%, and 1% w/v – the conditions were initially tested without any crosslinking calcium present as the fluid gel component is the responsible constituent for structure suspension and support throughout the fabrication process. For each of the five concentrations analysed, test prints of simple single-walled tubular structures were conducted to evaluate each bath's ability to support and suspend the extruded partially crosslinked alginate ink throughout the printing process using a 1.5 inch long 25 gauge nozzle (figure 6.1). The vessel for the support bath was a 50 ml conical tube cut circumferentially around the midpoint to reduce the bath's volume, preserving the agar fluid gels for as long as possible by reducing the amount used per print per prepared batch.



**Figure 6.1** - (a) comparison of the relative clarities of fluid gels at concentrations from 0.2% to 1% w/v, (b) and the gel's ability to support printed simple tubular structures at those concentrations

As the concentration of the agar increases, so does the opacity of the gel and is expected behaviour for non-clear dissolvable material. In addition to the increased opacity, the viscosity and strength of the fluidised gel increases and as such so should the supportive qualities too; however at the tested concentration range of 0.2% to 1% w/v the agar proved to be capable of supporting the extrudate adequately in position and shape. Agar

fluid gels prepared at 0.2% and 0.4% w/v would flow smoothly when poured from one vessel into another like a liquid, whereas concentrations of 0.6% to 1% were substantially thicker and would flow in an unsteady, blob-like manner. An inversion test was also conducted to provide a visual assessment of each concentration's rheology, revealing that agar is reasonably strong at most of the prepared concentrations except for 0.2% w/v which exhibited material flow upon inversion (figure 6.2). Much like the gelatine baths discussed earlier, fluid gels made with greater concentrations of agar remained dynamically more stable during the printing process compared to lower concentrations which where the motion of the nozzle translating through the bath would easily perturb it. At this point, any of the tested agar concentrations could be suitable for supported biofabrication.

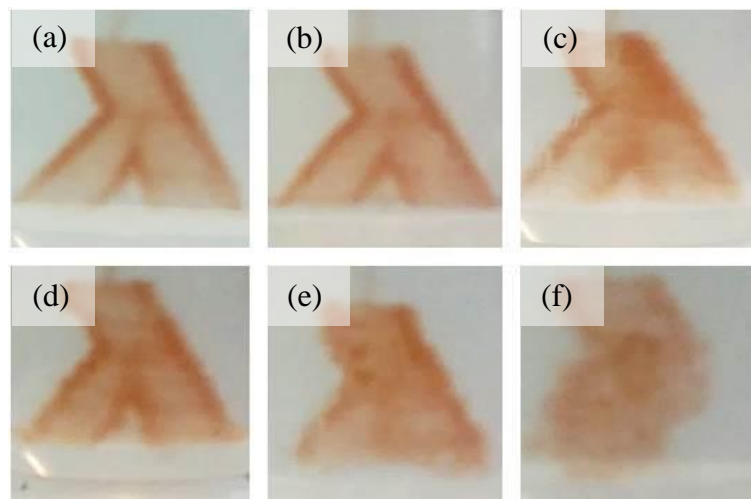


**Figure 6.2** – Results of tabletop rheological assessment of five agar fluid gel concentrations from 0.2% to 1% w/v, left to right. All concentrations were successfully inverted except for the weakest 0.2% agar condition

As the supportive qualities of the agar had now been tested, which had shown supportive qualities throughout, the next development step for the agar fluid gel baths is to evaluate an appropriate calcium concentration to suitably fuse and crosslink the layers of partially crosslinked alginate to produce rigid structures. The manner by which calcium was added to the gels was during the preparation stage – calcium chloride granules were weighed out and added to a water filled beaker with the agar powder to produce calcium enriched gels which would then be blended to form the support baths. The alternative method to add calcium to the gels would be to have a

separate calcium solution and mix it with the already fluidised gel – however this approach could be problematic due to (a) the reduction in fluid gel volume fraction by essentially diluting the fluid gel with calcium solution would cause the gelled microparticles to disperse further away from each other and reduce their supportive rheological qualities, and (b) the mixing ratio and the respective concentration of the calcium solution with the fluid gel; a separate set of experiments would be necessary to determine whether or not high concentration low volume or low concentration high volume calcium solution would be better for fabrication, and it is uncertain if the continuous liquid phase's calcium concentration would equilibrate with the gelled agar microparticles or not which could mean that the calcium concentration would be greater than the mixture's intended concentration. Therefore the method of diluting the fluid gel with calcium solution was not utilised for the discussed concerns.

The investigation of crosslinking conditions began with choosing an agar concentration and then preparing the fluid gels with the various calcium concentrations. For the first experiment, the agar concentration of 0.2% w/v was evaluated with calcium concentrations ranging from 2 to 10 mM followed by a print quality assessment of a simple branching blood vessel model (figure 6.3). This experiment would provide data regarding the effectiveness of various crosslinking conditions using the least supportive agar concentration.



**Figure 6.3** - Branching blood vessel-like structures printed into 0.2% agar fluid gel baths with various calcium concentrations (a) 0 mM (control), (b) 2 mM, (c) 4 mM, (d) 6 mM, (e) 8 mM, (f) and 10 mM  $\text{CaCl}_2$

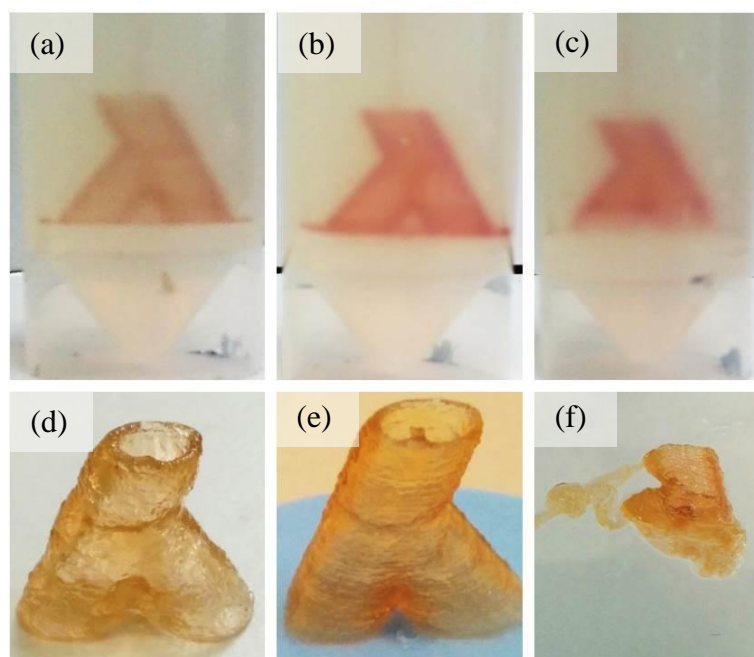
The control condition without calcium to crosslink the alginate is necessary as a reference to compare the print quality of each condition. When material deposition is unhindered from crosslinking effects the print quality is highest; however the absence of calcium within the bath renders the ink incapable of forming crosslinks, which is the mechanism responsible for increasing the strength of the structure. Without crosslinking, the structure cannot hold itself together and the alginate will eventually diffuse into the bath. As the calcium concentration is gradually increased, the printability begins to diminish and the likelihood of encountering deposition problems, such as trailing filament, increases. Such deposition problems have become evident at concentrations of 4 mM and whilst the structure was still successfully printed, the relative print quality of the structure was not as good as what was exhibited in the control or the 2 mM concentration; the depositional defects are relatively minor at such calcium levels and typically do not result in significant print failure, and are most noticeable when looking at the structure's walls as they appear more distorted and do not look as uniform as the control and 2 mM conditions. Calcium concentrations of 8 mM and 10 mM caused considerable failure whereby the print struggled to deposit the material in the correct position. In these conditions trailing filament is a major issue as the filament continues to grow in length but will not separate from the nozzle outlet due to the greater strength of the alginate at increased calcium concentrations, preventing the material from being truly deposited and encourages the filament to be dragged through the bath. As the filament trails and extrusion continues, the trail can collide with previously deposited material and become entangled which ultimately leads to large sections of the structure to fail at the printing stage.

In order to fabricate high quality structures the experimental data would suggest that the crosslinking conditions need to be minimised, but in order for printed structures to become mechanically strong there must exist some reasonable calcium content. Thus the contrasting crosslinking conditions for printing alginate-based structures needs to be suitably balanced to achieve both criteria sufficiently. From this experiment alone the only calcium concentration with any potential to satisfy both factors was 2 mM. As this condition made use of the lowest concentrations of agar and calcium, this was considered as the lower limit for fabrication; however the mechanical rigidity of structures printed at such low concentrations was very poor. Whilst it is possible to further enhance the mechanical properties of printed structures post-release by exposing the structures to more crosslinking ions, the problem is that the structures are so weak

that it is very difficult for them to withstand the initial release process. Increasing the calcium concentration to 4 mM would improve the crosslinking capability within the support at the cost of depositional quality. Even so, a calcium concentration of around 8 mM would be more desirable mechanically as such concentrations are known to produce reasonably strong, self-standing structures based on the gelatine support bath work.

As the prior experiment started with the minimum concentrations to facilitate supported fabrication, the next experiment was planned to investigate what the maximum conditions were and compare their printing performance. The purpose of conducting the experiment in this manner was to try and investigate a set of conditions which would deliberately cause the print to fail and would thus provide data regarding the maximum tolerable limits for successful printing. Additionally, it was not known if the more concentrated agar fluid gels behaved differently than the less concentrated gels at equivalent calcium concentrations during the fabrication process, thus this method was employed to investigate.

As a calcium concentration of 10 mM was the maximum used in the previous experiment with 0.2% agar, the same calcium concentration was used with the prepared 1% agar gels to maintain a fair comparison with the previous data. Whilst calcium concentrations in the range of 4 mM to 10 mM experienced problems or print failure when using 0.2% agar gels, the same problems were not evident during printing into 1% agar gels at 10 mM calcium concentration. Despite the increased opacity of the more concentrated gel, the structures were still visible for examination and it could be seen that the print quality was comparable with the 0.2% agar control and 2 mM calcium conditions and appeared to be of higher quality than the 4 mM and greater conditions. As one of the goals of this experiment was to deduce conditions for print failure, additional baths with 20 mM and 40 mM calcium concentrations were also prepared and printed into in an effort to discover such a condition (figure 6.4). Only at calcium concentration of 40 mM was there any indication of depositional problems whilst attempting to print the structure; 20 mM calcium concentrations exhibited print qualities comparable to that of the 10 mM concentration whilst printing into 1% agar baths as well as the control and 2 mM concentrations of the 0.2% agar baths.



**Figure 6.4** – Relative print and structural qualities of branching blood vessel-like structures printed into 1% agar fluid gel baths with calcium concentrations of (a, d) 10 mM, (b, e) 20 mM, and (c, f) 40 mM  $\text{CaCl}_2$

The results of the printability study into the various 1% agar baths had shown greater tolerance to the greater calcium levels present within the bath, producing much stronger structures with very good depositional quality. Whilst the print data shows the depositional quality at 10 mM and 20 mM  $\text{CaCl}_2$  levels as being similar, the respective surface quality was significantly higher in the 20 mM condition – this is related to the increase in crosslinking content which is commonly known as a means of maintaining shape fidelity in standard bioprinting practice. The 40 mM condition had encountered some depositional issues but seemed to recover during the print; despite this the structure was unable to support itself because of the initial depositional failure related to the excessive calcium levels present within the bath.

It can be hypothesised that the reason why the printability of the ink at greater calcium concentrations is better when the agar fluid gel concentration is similarly greater is due to the strength of the gel. A relationship might exist between the alginate as it is crosslinked and the bath itself which determines the depositional capability of the extruded ink, and could be related by their relative mechanical strengths. If the relative strength of the alginate as it crosslinks is less than the strength of the bath, then the extrudate will yield first, separating from the nozzle outlet and be deposited successfully; conversely should the product of the ink and crosslinking conditions create

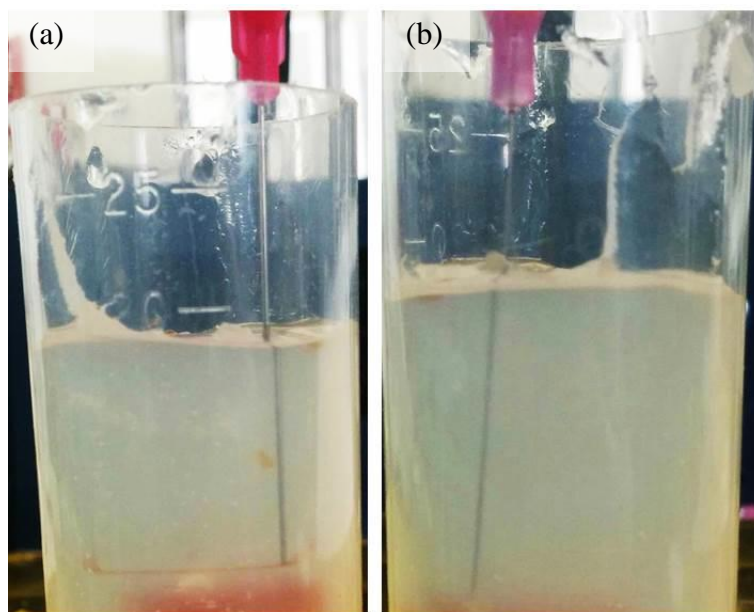
filament which is stronger than the fluid gel bath, the bath would yield first and would be incapable of facilitating successful deposition. Should the hypothesis be correct, this would explain why the 0.2% agar concentration was unable to achieve a good print quality with a calcium concentration of 10 mM whereas the same crosslinking conditions in 1% agar baths could. Due to the relative merits of using the greater agar concentration for the purpose of supported fabrication, it appeared more logical to investigate such baths further rather than to conduct the same experiments with 0.4%, 0.6%, and 0.8% w/v agar baths as they were deemed less likely to improve upon the operational range which 1% baths could offer in the context of selecting the most optimal calcium concentration for maximum mechanical strength and cell viability; functionally it would seem that the 1% agar fluid gel baths could achieve more than what the reduced agar concentrations could.

As the print quality has been established to be good with the 1% agar baths at 20 mM  $\text{CaCl}_2$  concentration using 25 gauge nozzles, an investigation was considered whether the same bath conditions were suitable for higher resolution printing using a 30 gauge nozzle. For the investigation, the same branching blood vessel-like structures were printed again as to allow for a comparison to be made with earlier data.

Prior to printing any complete structures, a problem was observed in that 1.5 inch long 30 gauge nozzles would readily deflect under the viscous forces involved during the fabrication process; this effect was never observed in any of the prints conducted with 25 gauge nozzles of equivalent length (figure 6.5). Deflecting nozzles during the fabrication process is problematic because the depositional accuracy and reliability of extruded ink becomes questionable. As the length of the nozzle is fixed, the degree of bending involved creates variances with how deep the nozzle's outlet is situated in the bath which could potentially lead to structural delamination if the variance exceeds the layer height. Regions of structures printed deeper into the bath will have smaller cross-sections compared to regions printed nearer the top of the bath as the total viscous force acting on the nozzle is reduced; this is because the viscous forces bend the nozzle in the opposite direction to nozzle movement, creating structures with a more trapezoidal profile along the Z-axis rather than square. The constant bending and re-bending of the nozzle as it changes direction could eventually cause the nozzle to break due to fatigue of the stainless steel tips. Such a failure would require many loading cycles and likely the reuse of nozzles which could factor into large-scale fabrication; however this is



unlikely to occur and one would expect nozzles to be disposed of after use in a biofabrication context.

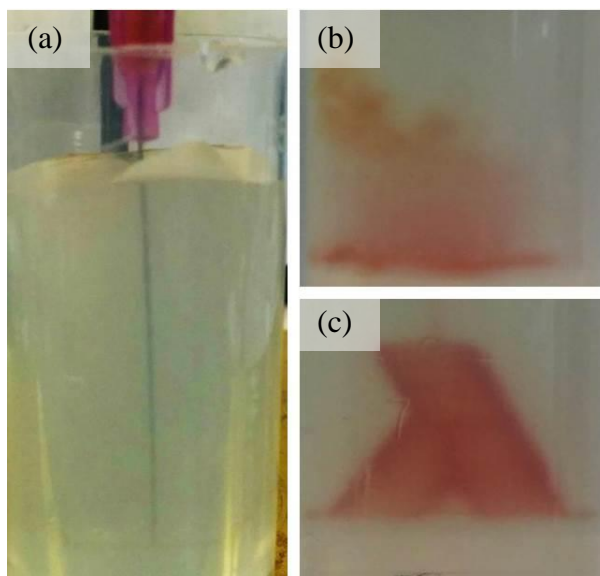


*Figure 6.5 – Nozzle deflection observed whilst moving within a 1% agar bath, (a) thicker 25g nozzles resist deflection whereas (b) thinner 30g nozzles readily bend due to viscous forces acting on the nozzle as they through the medium*

On account for the nozzle deflection problem, there were two conceivable solutions to resolve the issues: dilute the agar fluid gel with a secondary liquid to reduce the volume fraction of microparticles or use a lower concentration of agar, both solutions working to alter the rheology of the fluid gel and reduce its strength. The relationship between microparticulate volume fraction and the supportive qualities of such baths were not investigated and perceived to be outside the scope of the current work, therefore the use of a less concentrated agar fluid gel was considered instead. Therefore the investigation continued with the preparation of a 0.8% agar fluid gel bath with 20 mM calcium chloride for crosslinking to evaluate the suitability of tuning down the bath's strength to mitigate nozzle bending. As before the branching blood vessel-like structures were printed with both 25 gauge and 30 gauge nozzles to provide a comparison with previous print data.

As shown in figure 6.6, the results from printing into a 0.8% agar bath with 20 mM  $\text{CaCl}_2$  remained successful for the 25 gauge nozzles but not with the 30 gauge nozzles. The reason for failure was not related to any nozzle deflection as this issue had been resolved by reducing the bath's rheological properties by reducing the agar

concentration during preparation. The mode of failure much looked much like the issues related to excessive crosslinking of the ink observed in previously obtained data. As the bath's calcium concentration was maintained at 20 mM for both the 25 gauge and 30 gauge nozzle prints, it can be hypothesised that the different outcomes are related to the differences in nozzle size.



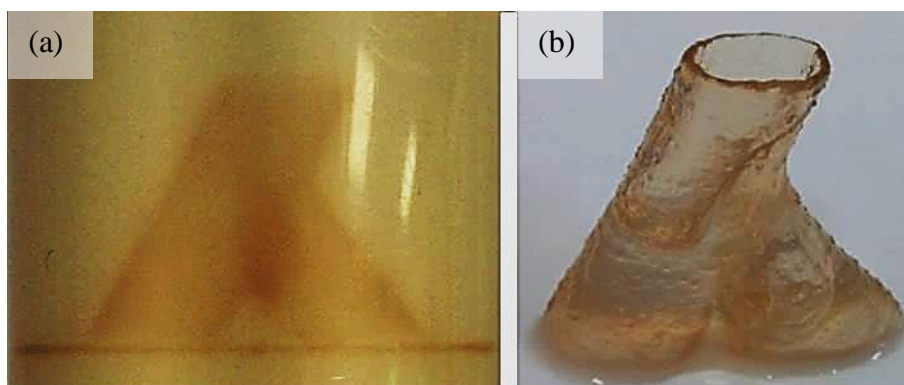
**Figure 6.6** – (a) 30g nozzles retain their straightness in 0.8% w/v agar baths, (b) but fail to print successfully at 20 mM  $\text{CaCl}_2$  levels in a manner symptomatic of excessive crosslinking, (c) unlike 25g nozzles which print successfully at these conditions

If the bath can be considered as an ‘infinite’ source of calcium ions maintained at 20 mM concentration, and considering the cross-sectional volume of alginate as it exits both nozzles, then it could be argued that the ratio of calcium ions to crosslinkable junctions is much higher for the 30 gauge nozzle because the relative extruded material volume is smaller than the 25 gauge nozzle. This would imply that the bath’s relative crosslinking strength is greater when using finer, higher resolution nozzles compared to larger nozzles, despite the bath’s global calcium concentration being fixed to 20 mM and the alginate concentration being consistent in both tests. Therefore the most likely reason why the 30 gauge nozzle print failed, and the 25 gauge print was successful, is that the relative bath calcium concentration is too much to accommodate printing with such a fine nozzle and hence the calcium concentration should be reduced when higher resolution printing is conducted.

To conclude the investigation carried out in this section, a final bath comprising of 0.8% agar 10 mM  $\text{CaCl}_2$  was proposed. It has been shown that 0.8% agar baths have

appropriate rheology to prevent finer nozzles from bending during operation, and by stepping down the calcium concentration by a factor of 2 there is a better chance that the crosslinking conditions would not be too harsh to hinder the fabrication process with such nozzles. The use of a 25 gauge nozzle for this experiment was disregarded based on the knowledge that good working bath parameters have already been established in the range of 1% agar and up to 20 mM  $\text{CaCl}_2$  – the main purpose of this test was to establish good bath conditions which work in conjunction with 30 gauge nozzles as such a functional bath has not yet been discovered in this work.

The result from printing into the 0.8% agar 10 mM  $\text{CaCl}_2$  bath had proven to be a success (figure 6.7), with the bath conditions suitably tuned to enable the reliable deposition of the ink without incurring any unnecessary nozzle deflection. Printing at such resolutions makes visual assessment difficult as the wall's cross-section is very thin and the bath is still relatively opaque at concentrations of 0.8%; however releasing the structure from the bath proved that these bath conditions were indeed compatible with 30 gauge nozzles.



**Figure 6.7** – (a) successful print of blood vessel-like structure with a 30g nozzle within a 0.8% w/v agar 10 mM  $\text{CaCl}_2$  bath, (b) successful release of the aforementioned structure, shown to be self-standing

The work conducted in this section aimed to investigate the support bath conditions which would provide good functionality and facilitate the successful fabrication of soft-material structures. Whilst the supportive aspect of fluid gel baths increases with greater agar concentrations, such concentrations do not necessarily indicate their suitability for the purpose, such as baths with excessive rheological qualities leading to physical problems like bending nozzles. On the other hand, increasing the concentration of agar allows for the use of greater calcium levels which would

otherwise cause depositional issues at lower agar concentrations. It is possible to fine tune and optimise the bath conditions to suit the application; the overall calcium content can be varied to produce softer or harder structures and the rheology can be varied to accommodate higher resolution nozzles. However a factor which is not directly related to the bath yet affects the printability at given bath conditions is the size of nozzle used – finer nozzles are more sensitive than larger nozzles at equivalent calcium levels and as such the calcium content may need to be reduced initially in order to successfully print, but the structure may later be released and exposed to more calcium at a post-processing stage if necessary to attain the correct structural qualities. Bearing this in mind, it was deemed that baths with an agar concentration of 1% and a calcium concentration of 10 mM, in conjunction with 25 gauge nozzles, were good enough for standard bath printing operations; however if higher resolution printing with 30g nozzles was desired then 0.8% agar with 10 mM CaCl<sub>2</sub> was found to be effective.

### **6.3 Supported Fabrication of Macroporous 3D Structures**

Prior to the introduction of support bath technologies, a common biofabrication strategy involved the printing of scaffolds which could later be seeded with cells. The printed structures would often comprise of many orthogonal layers of spaced out lines of some biocompatible thermoplastic material such as PLA. The distance between adjacent lines of filament could be set at either the CAD model generation stage, or controlled at the slicing/g-code generation stage by defining the space between printed lines. The orthogonal printing of subsequent layers creates the mesh pattern, allowing for the fabrication of structures with controlled porosity for cells and media to proliferate into. The degradation rate of the scaffold would often be engineered to match the rate of tissue growth so that high density, larger scale cellular structures can be produced.

The mechanical requirements to print mesh scaffolds imply that the fabrication method is more suited to replicating harder tissues. The necessary mechanical strength required to produce such mesh structures with high shape fidelity requires the use of strong filament, commonly biocompatible and biodegradable thermoplastics, to mitigate problems like material sagging over the gaps which can impair the effective 3D porosity. For such reasons the fabrication of anatomically relevant sized soft tissue models is very difficult, as the mechanical strength to maintain shape fidelity is insufficient even when printing reduced scale models. Consequently, the soft hydrogels and viscous biomaterials used in soft-tissue fabrication have a key advantage of

allowing the encapsulation of cells within the ink during extrusion, a feature which is not possible to achieve when thermoplastic filaments are used.

The advent of new supportive strategies provides new methods for overcoming many of the fabrication struggles when using soft biomaterials for fabricating soft-tissue models, as the supports can delicately suspend and hold weak bioinks in place within the medium. As such, larger mesh structures from soft materials can be fabricated in conjunction with a support bath for instance. Furthermore the combination of printing mesh structures with soft, cell-laden bioinks which can later be seeded with cells creates a new strategy for the production of co-culture systems whereby two compatible cell types can grow as tissue within the single scaffold. Even if a co-culture system was not incorporated, and only a cell-laden alginate bioink was used to print the mesh for example, the porous nature of the structure could drastically improve the rate of crosslinking of larger structures by maximising the surface area that is exposed to crosslinking ions, ensuring that regions deep within the structure are crosslinked as effectively as external regions. Additionally, the largely porous nature of mesh structures could promote better cell viability in thicker tissues by providing a myriad of channels for nutrient delivery and waste removal.

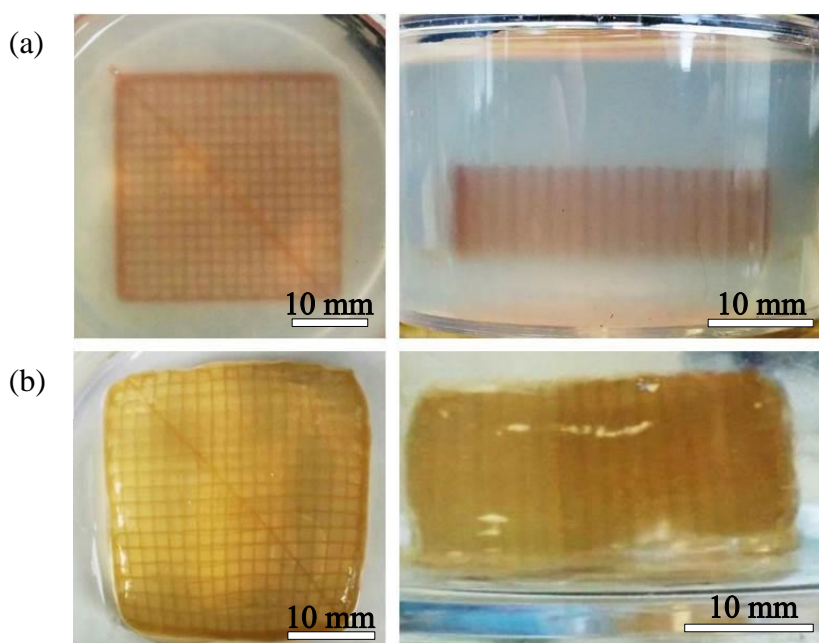
For the context of biofabrication, porosity could be perceived as somewhat ambiguous terminology to either describe the biomaterial's microstructure or the whole structure itself – to which description the term is referring to depends on the context. To clarify the term, 'macroporous' is the nomenclature in this thesis to distinctly discern that the structure's porosity as a whole is being controlled, and not the microstructure of the hydrogel which is a material property rather than a property of the fabrication process.

### ***6.3.1 Fabrication of large, thick macroporous grids***

A significant challenge faced by bioprinting is the fabrication of large scale structures from soft tissue-like materials for reasons described earlier. Thus it was hoped that the developed agar fluid gel support baths could be utilised as a tool to overcome such challenges. To evaluate the feasibility of this, a simple cuboid model was created in CAD with dimensions 30 mm x 30 mm x 11 mm and tessellated for input into Sic3r for g-code generation. The print settings included a single perimeter to form an external wall, rectilinear infill pattern with a fill density of 15%, print speeds of 15 mm/s, and extrusion multiplier of 0.8 to produce thinner lines, using a 25 gauge nozzle with a respective layer height of 0.26 mm and extrusion widths of 0.26 mm. A bath

concentration of 0.5% agar with 4 mM  $\text{CaCl}_2$  was chosen for experiment – whilst this is not the considered optimal conditions as established earlier, the reduced calcium content is to assess if meshes could be printed and released with less crosslinking to produce softer yet self-standing structures.

As can be seen from figure 6.8 the spacing between adjacent struts is consistent throughout the whole structure, which means that the supporting agar fluid gel is dynamically stable enough that the perturbing forces of the nozzle moving through the medium does not cause the printed lines to lose their orthogonality along the X/Y plane. This is also true when looking at the structure from its side; the walls and layers maintain their parallelism throughout the structure's thickness in the Z-direction. The long diagonal line which spans corner-to-corner of the structure is the effect of excess material oozing out from the nozzle due to the pressurisation of the ink and the long travel distance between points – this can be prevented with better control over the extrusion by using faster non-print travel speeds and retract functions.



**Figure 6.8** – (a) Macroporous grid structures printed into 0.5% w/v agar 4 mM  $\text{CaCl}_2$  baths, (b) released grid structures with residual fluid gel trapped within pores

Releasing the structure revealed a phenomenon of the supporting fluid gel remaining trapped inside the structure's mesh. Initially this was seen as a hindrance as the process of removing the trapped agar would be very tedious and involve the delicate aspiration or expulsion of the residual gel using a very fine nozzle. However the residual agar can be considered highly beneficial given that the gel's rheology can continue to support

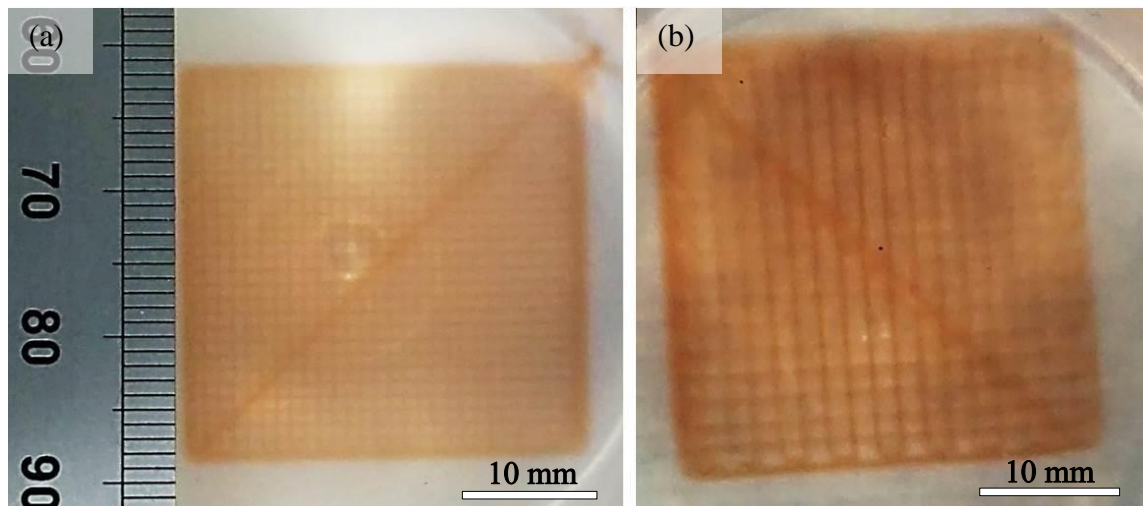
very soft and delicate structures post-release. This could be seen as a method of printing and handling even softer structures with minimal crosslinking which could translate to the fabrication of much softer tissues with better cellular viability. Furthermore, if the trapped agar gel contained cells and were shown to be capable of proliferating through the medium and grow as tissue then the agar itself could be considered a secondary biomaterial for the production of co-culture structures.

The released structure, despite being congruent, is shown to have lost some of its orthogonality (in X/Y) and parallelism (in Z) upon release – this is likely a sign that the supportive agar trapped in the mesh has less than optimal rheology, and that the printed structure itself is not very rigid due to the bath's reduced calcium content. In spite of this, the experiment was still considered a success as it successfully shown the suitability of printing larger scale macroporous scaffolds from soft materials within a supportive network.

It was considered to print the same structure with a finer nozzle to assess if any differences would appear as a result of using a different nozzle. As has been shown in earlier work, an agar concentration of 0.8% or less is soft enough to enable the unhindered printing with 30 gauge nozzles without bending – thus 0.5% agar is well within the working range for using such fine nozzles. Aside from changing the nozzle size (0.16 mm), layer height (0.16 mm) and extrusion width (0.16 mm) to reflect the parameters of the 30 gauge nozzle, all other print setting values were kept the same as before.

For a given infill density, it can be seen in figure 6.9 that the mesh size is smaller and the number of meshes increases when using smaller nozzles. This is expected of the print settings as the fill density is expressed as the ratio of total cross-sectional area to be occupied with material which is extruded with a thinner nozzle extruding thinner lines, thus more lines are required for smaller nozzles to approximate the same ratio as larger nozzles. The more appealing result, other than the fact that more and smaller meshes can be fabricated, is that the difference in nozzle size provides an additional means of controlling the macroporosity. Therefore in addition to varying the infill density, one can change the nozzle itself in order to vary the relationship between extruded line thickness, hole size, and total number of holes to control the overall structure's porosity and tune both the mechanical properties and perfusion capabilities.





**Figure 6.9** – Comparison of nozzle diameter on line thickness and pore size, (a) grid printed with 30g nozzle, (b) grid printed with 25g nozzle

Whilst not assessed in the current work, further experimentation to assess the concentration of agar and its impact on maintaining the shape fidelity of large, soft structures would be of interest. Much like the conditions established in the systematic study of the bath's properties, one can imagine that printing soft material scaffolds into stiffer supportive gel networks would better maintain the shape fidelity of released structures - this assumes that the agar can remain sufficiently trapped within the mesh to better distribute the structure's weight and reduce the loading on the scaffold's struts.

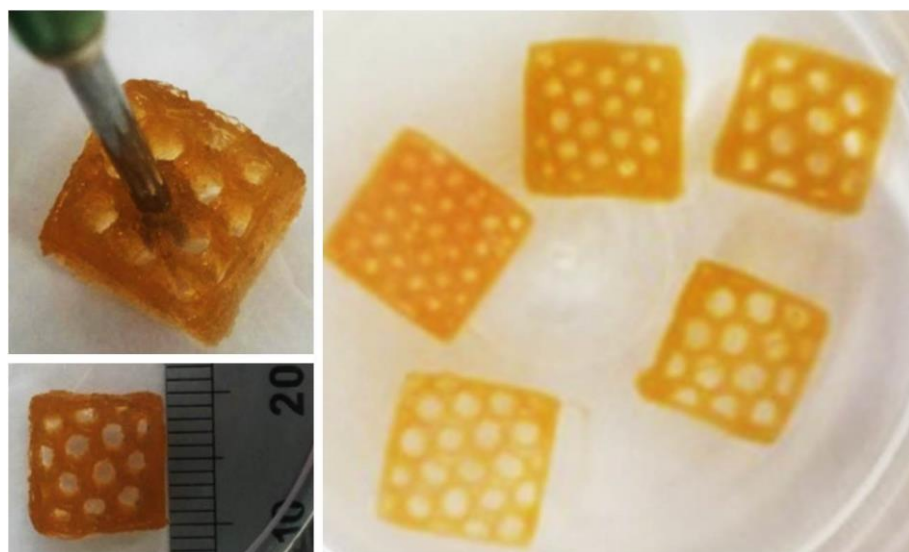
### **6.3.2 Fabrication of honeycomb grids with variable macroporosity**

Whilst control of a structure's porosity is partly related to the size of the nozzle used which determines the range of possible extrusion widths, the primary method of controlling the porosity should be to appropriately tune the infill density. In Slic3r, the infill density can be set to any whole value between the range of 0% (no infill) and 100% (completely dense infill), but the infill itself can be printed in a variety of patterns. Different patterns may bestow different mechanical properties upon the structure as a whole, as well as change the shape of the pores or even alter the relationship between hole size and infill density. For this experiment, smaller scale cuboidal structures with dimensions 12 mm x 12 mm x 6 mm were printed using a honeycomb infill pattern with infill densities ranging from 10%, 15%, 20%, 25%, and 30%. The honeycomb infill pattern is commonly regarded as being efficient at promoting high mechanical strength in 3D printed components at reduced infill densities, which correlates with reduced print times to complete structures compared to other infill patterns such as rectilinear or concentric. The structures were printed into



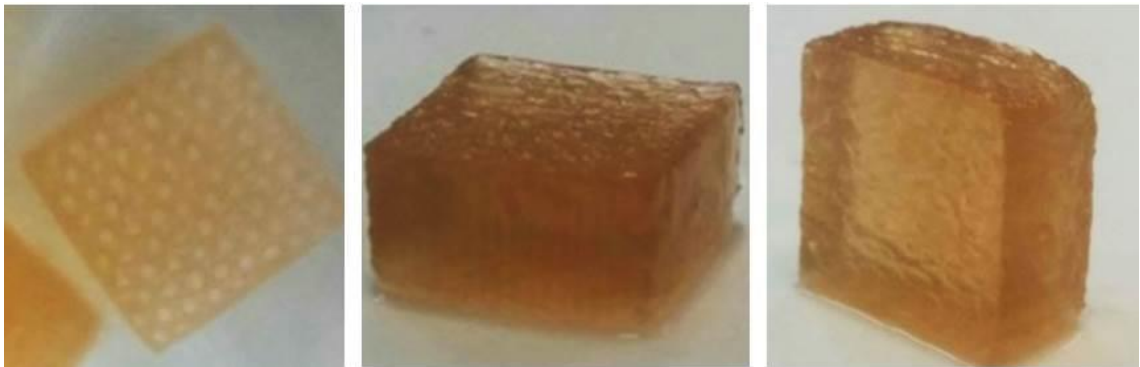
1% agar 20 mM CaCl<sub>2</sub> baths with a 1.5 inch 25 gauge nozzle to ensure the production of strongly crosslinked structures. The print speed was set to 15 mm/s, a single perimeter was used to form a vertical wall around the structure, and an extrusion multiplier of 2 to print thicker lines with 0.26 mm layer heights was used.

The honeycomb infill structures shown in figure 6.10 have shown the potential to fabricate structures with a range of porosities. The honeycomb infill pattern lends itself to producing rounder pores compared to the rectilinear infill patterns for example, which form square pores. The pore geometry may be an important parameter to control - the shape as well as the positioning of adjacently layered struts may encourage better cell adherence to the structure if seeded with cells [50]. If the honeycomb infill pattern were to be used for cell printing, care should be taken to consider the relative cell densities with respect to the infill density used. Whilst greater infill densities attribute themselves to producing stronger structures, in this case should the filament be printed with cellular inks then the total number of cells present within the structure would be proportionally greater too. On the other hand when the infill density is increased, the remaining pore volume is decreased which could make media perfusion more difficult for single cell-culture models, or restrict the total amount of cells within the pores for co-culture systems. Any residual supporting gel within the structures printed at lower infill densities of 10%, 15%, and 20% would readily vacate from the pores during the release process; structures printed with 25% would require physical intervention to remove as would 30% infill density.



**Figure 6.10** – Macroporous grids printed with honeycomb infill patterns, printed with infill densities from 10% to 30% in 5% increments

Increasing the infill density whilst simultaneously using a finer 30 gauge nozzle allows for the fabrication of strong structures with many tiny pores. To illustrate this, figure 6.11 shows the same 12 mm x 12 mm x 6 mm cuboidal structure using 30% honeycomb infill. The pores were printed small enough to successfully trap the supporting agar within the structure throughout the release process, which can arguably further improve the strength of the structure post-release. The structure's pores are most visible whilst the structure is immersed in a clear body of liquid such as water – however when the surrounding fluid is removed, the pores become more difficult to see.



*Figure 6.11 – Honeycomb infill patterned grids printed with 30g nozzle and an infill density of 30% to create tiny pores with trapped agar fluid gel*

The fact that many slicing software, not just Slic3r, can be used to generate g-code to fabricate structures with a variety of infill densities and patterns is nothing new. However it is potentially a highly useful tool to aid in the biofabrication of functional tissue models for the reasons that larger structures can be printed with good strength and less weight given the reduction in extruded material volume, as well as providing a means of ensuring that the deepest regions of the structure can crosslink more rapidly. In addition to this, the porous nature of such printed structures can potentially allow for the delivery of nutrients and removal of waste products deep within the structure, and could even enable the utilisation of cell-seeding strategies in conjunction with cell-laden printing.

#### **6.4 Supported Fabrication of High Resolution and Highly Complex 3D Structures**

To showcase the potential fabrication capabilities of the newly developed agar fluid gel support baths, a range of challenging models were planned for fabrication and their qualities assessed. The different models would challenge various operational aspects of the printing process which not only would be a function of the bath's ability to support structures, but would also be related to the fine tuning of the many print parameters

within Slic3r. The combination of a highly pseudoplastic support bath and well-tuned print settings should permit the fabrication of more complicated geometries - the results of which would be beneficial when printing anatomical models which can be difficult, having a combination of thin walls, non-uniform cross-sections, overhangs, internal features, and diverging/converging geometries.

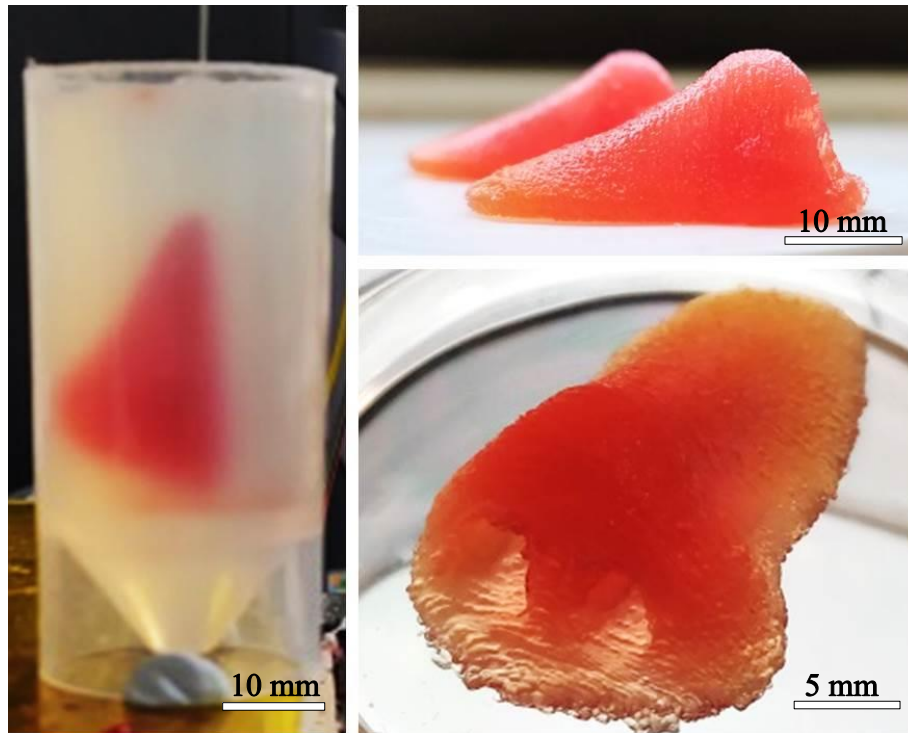
The models considered for printing included a nose, an ear, a bucky ball, and an Eiffel tower. The STL files were obtained from the online CAD model library: Thingiverse. Each model was printed into the standard 1% agar 10 mM CaCl<sub>2</sub> bath using a 1.5 inch long 25 gauge nozzle. The print settings for each structure were configured on a case-by-case basis, as the different models have different printing requirements as will be discussed in their respective sub-sections. All structures were left for a day encapsulated within their support baths to ensure they were initially crosslinked throughout, after which the supporting agar was carefully washed away with water to release the structure and then immersed into a 50 mM BaCl<sub>2</sub> solution for further crosslinking.

#### ***6.4.1 Agar fluid gel support bath – nose printing***

The nose is an easily recognisable anatomical model with the main features of interest being the two nostril channels, the nose tip, and the long sloping nasal bridge. Due to the layer-by-layer approach utilised by 3D printing, and depending on the print orientation, curves can become poorly approximated as staggered, stepped layers rather than a continuous smooth profile. How exaggerated these steps may be is a function of the layer height - bigger layers poorly approximate the profile of a curve when compared to many smaller layers which exclude less geometric data. Therefore, and despite the absence of very small details in the model, the nose still requires high print resolution in order for the sloping nasal bridge to be printed with a smooth-looking finish.

This model was chosen to be printed in an upright orientation in order to attain smoother print detail of the nostrils and slope (figure 6.12) – printing rounded details along the X/Y plane is better as details can be printed more smoothly because those motors are running continuously, whereas Z-axis motion is only active during a layer change which consequently creates rougher surface qualities. To strike a balance between neat surface morphology and strength, two perimeters were printed with a honeycomb infill pattern at 15% fill density. Setting the extrusion multiplier to a value

of 1.5 ensured that there was a high enough flow rate to achieve good layer fusion without leading to overextrusion. The print speed was set to 15 mm/s and the layer height was set to 0.2 mm.

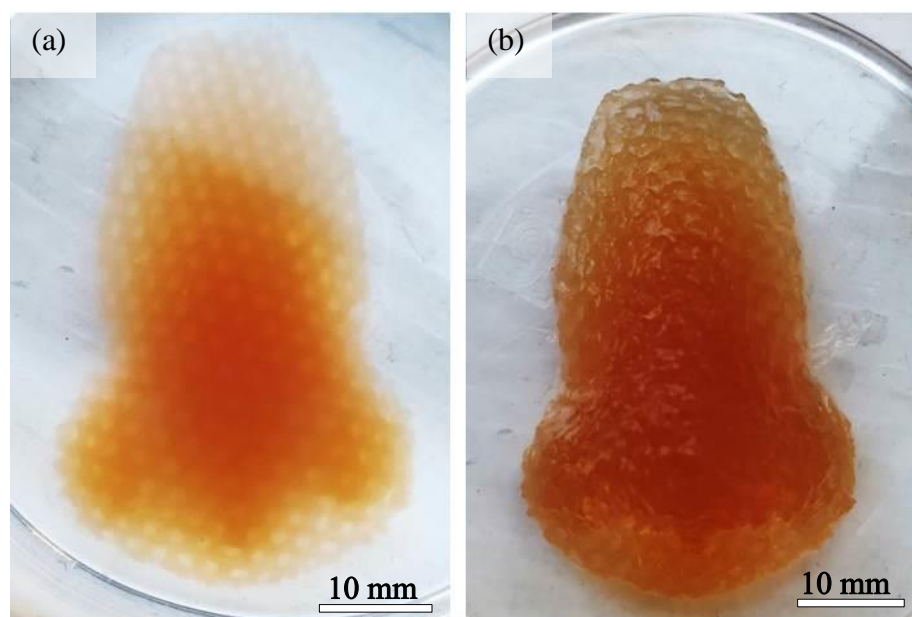


*Figure 6.12 – Noses printed using the developed agar support bath; prints were conducted in a vertical orientation and produced noses with a high print quality*

In addition to this, the same nose model was also printed with purely a honeycomb infill pattern without any vertical walls. Whilst the presence of perimeter walls helps to produce neater looking structures by printing a smooth exterior, it may or may not be necessary to incorporate such operations whilst printing functional cell-laden structures as the walls can impede the diffusion of crosslinking calcium ions and cell culture media to regions deep inside the structure. As such, the knowledge gained from printing macroporous structures was applied to the model of a nose and printed.

The orientation of the macroporous nose was changed so that the largest cross-section would rest flat on a horizontal plane. This orientation distributes the structure's weight over a wider area and is thus more robust, as well as reducing the overall print time by printing the smallest dimension along the slower moving Z-axis. An infill density of 25% was used as it provides a good balance between print speed, macroporosity, and mechanical strength.

As can be seen from the results in figure 6.13, the entirety of the nose has been printed successfully and the porous honeycomb infill pattern can be seen throughout the structure. As before, the infill pattern is most visible whilst the structure itself is immersed in water and is likely related to some light refraction phenomenon of the combined agar fluid gel (trapped between the pores) and the water. The relative thickness at various parts of the construct can be discerned based on the intensity of the red colouring which was used in the ink. Similar to a heat map the deep red segments indicates the presence of more material i.e. thickness, which in the figure correlates with the position of the nose tip. As no external perimeters were printed, the honeycomb infill is exposed which results in a rougher looking surface morphology – this may possibly be improved upon by printing at greater infill densities to reduce the pore size and produce surfaces with a less jarring morphology. However as previously discussed this may not cause detriment when considering that the strategy could be used to print large scale, soft-tissue cellular structures with an integrated method of nutrient delivery and waste removal via control over the macroporosity.



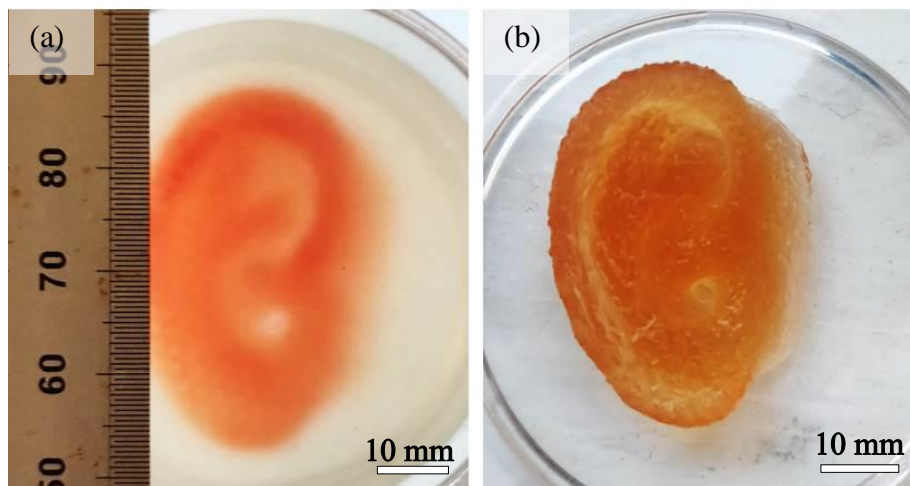
*Figure 6.13 – Agar fluid gel bath-printed macroporous nose structure (a) immersed within water to show pores, (b) out of water to show structure*

#### **6.4.2 Agar fluid gel support bath – ear printing**

Like noses, ears are an easy to recognise part of the human body which is of interest to replicate using 3D bioprinting technology. The surface morphology is more complex than the nose because there are many more curves and folds which make up the auricle of the ear, as well as the overhanging lobule. The settings used to print this structure

were 2 perimeters, 25% honeycomb infill at 15% fill density, extrusion multiplier of 1.5, print speeds of 15 mm/s, and 0.2 mm layer heights.

The overall structure was successfully printed with consideration for all the curves and folds that make up the defining features of the structure as shown in figure 6.14. Whilst immersed in water the folds are easier to discern from the rest of the structure – the curves that make up the helix, antihelix, and antitragus of the ear as well as the hole the cavum conchae are the most profound details replicated in this print. The surface morphology of this structure is not as smooth as the nose was, and the most likely cause for this is related to the moderately wide cross-section of the ear, incurred by choosing to print the structure flat along the X/Y plane, and an insufficient number of perimeters. Printing wider cross-sections without an adequate number of vertical walls or a top and bottom horizontal shell will cause the infill to become exposed to the outside, which can then impair the surface smoothness of affected regions and could explain why the ear appears rougher than the earlier printed noses. If the structure were printed upright like the noses were, the effective cross-sectional area of each layer is reduced and as such the perimeter walls are much more likely to effectively seal the structure with a smooth continuous line.

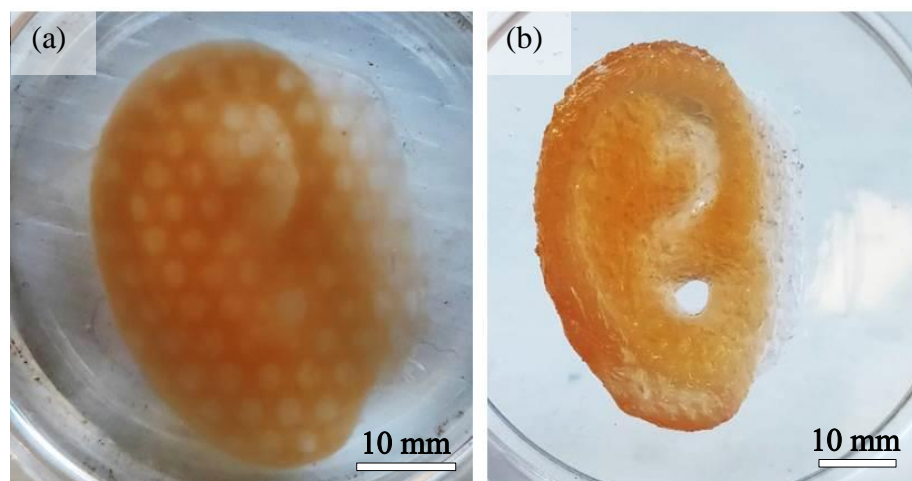


*Figure 6.14 – Agar support bath-printed ear (a) encapsulated within supportive medium, (b) post-release*

The macroporous fabrication strategy was also applied to the printing of an ear. This time, a single perimeter was used in an effort to retain as much of the curved detail as possible. For this print, an infill percentage of 20% was used to produce slightly larger pores while maintaining reasonable structure strength.



As before the pores are capable of trapping supportive agar within the structure which gives the illusion of a completely dense structure, despite water immersion showing that the structure is indeed not completely dense (figure 6.15). The curved details were maintained throughout the print, and are arguably more clearly defined than before when the structure is not immersed in water. The fact that the ear is printed with good shape fidelity, even with moderately large pore sizes, is a good indicator that the macroporous printing strategy can find suitable application when integrates with the developed agar fluid gel support bath strategy.



*Figure 6.15 – Agar support bath-printed ear (a) immersed within water to show pores, (b) out of water to show structure*

#### **6.4.3 Agar fluid gel support bath – bucky ball printing**

The bucky ball is highly complex model which is a hollow sphere with multiple hexagonal shaped holes cut out from the surface. The geometry of the model is what makes printing it so challenging as there is no internal structure to provide any extra strength, and the external surface consists entirely of thin struts which need to be strong enough to hold the shape in place once released. Print-orientation is irrelevant as there is no preferred axis to make the printing process any more reliable due to the spherical nature of the object.

The combination of the standard layer-by-layer fabrication approach and the many empty spaces between struts means that the printer has to ‘hop to ‘X’ position’, ‘extrude’, and then ‘hop to ‘Y’ position’, ‘extrude’,... etc. – the printer cannot simply continuously extrude material and move along a single defined path like what was possible when printing noses and ears. Hence in order to attain good print resolution there needs to be good extrusion control to stop material from accidentally flowing out

from the nozzle between travel moves due to any residual pressurisation of the ink, which would otherwise form strands of crosslinked alginate across each hole and significantly diminish the print quality. Such control can be achieved using Slic3r's retract settings – retracting ink back into the syringe by reversing the extruder motor to mitigate the accidental deposition, or oozing, of ink when unnecessary.

Retraction operations enable the bidirectional flow of material into and out of nozzles, and can be troublesome should the bath's calcium content be slightly too strong. Stronger crosslinking conditions may be better tolerated in unidirectional extrusion as extrudate does not re-enter the nozzle in such a scenario – however when material can flow out of a nozzle via typical material extrusion and back into the nozzle via retraction, the risk of aspirating the bath's calcium and/or crosslinking/crosslinked material is greatly increased which can block the nozzle.

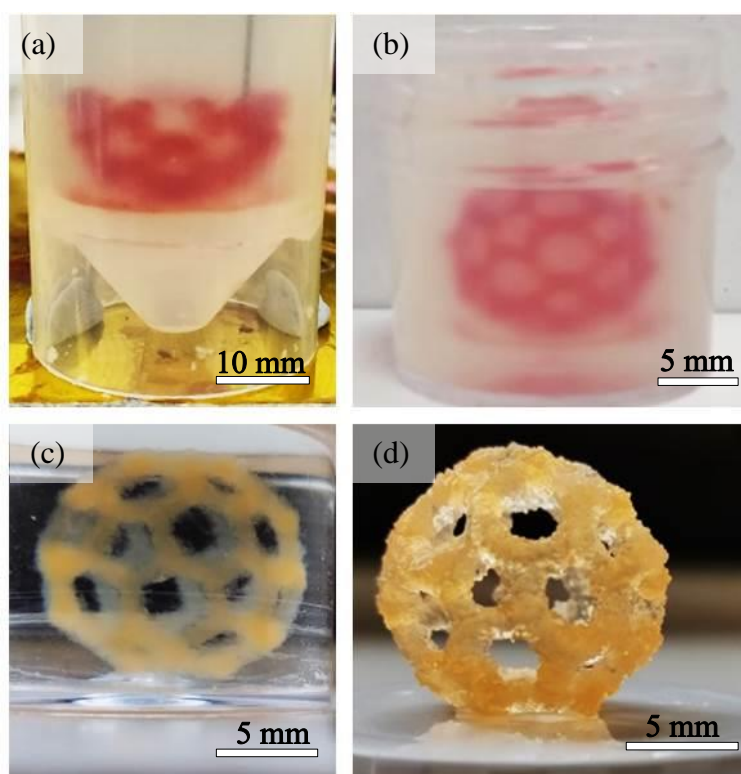
Printing bucky balls can therefore be considered a very challenging print assessment, requiring arguably even greater synergy between the support bath's qualities, the ink's qualities, the nozzle, and the print settings compared to any structure printed before.

It was found through trial and error that the best strategy for printing bucky balls was to print quickly at high extrusion rates with very small layer heights. One of the problems faced when printing bucky balls is the length of time required before the ink becomes suitably pressurised – the sporadic 'on and off' style of printing exemplified here does not allow the ink to become suitably pressurised in time with the same skirt settings as used before, thus more skirts and a greater extrusion multiplier were necessary to ensure a more consistent flow of material throughout the print. Another problem was if the layer heights were too great then the diagonal struts would be poorly connected due to the loss of geometric data incurred when printing at greater layer heights, thus a layer height of 50 microns was deduced as being capable of reliably fabricating the struts. The cross-section of the struts is really thin, so the best method to print them as strong as possible was to use 2 perimeters without any infill – the inclusion of infill or too many perimeters, even as low as 3, was found to contribute to overextrusion as too many lines of material were being deposited too closely to each other.

Despite the difficulties, figure 6.16 shows the successful fabrication of a bucky ball. The holes were maintained clear on account of the retraction settings with fought against oozing filament between the struts. Retraction had to be fine-tuned so that the retracted volume was meaningful to successfully stop ooze yet not be excessive which



would aspirate the calcium-enriched agar from the bath up into the nozzle which risks blockage. Furthermore the retract speed needs to be appropriately set so that the retract function is effective. A retract speed of 1 mm/s was found to be appropriate and a retract length of 0.1 mm was found to eliminate oozing. The structure depresses slightly under its own weight when released – the struts themselves are thin and are forced to bear all the weight of the structure without the presence of any trapped agar post-release to support the structure. Scaling down the structure could possibly improve the rigidity of the structure by reducing the weight, but the resolution challenge of printing smaller struts becomes even more difficult. To improve the print quality the structure could be printed bigger as the layers become proportionally more resolute, but it was deemed that the ink would not be strong enough to grant the structure the rigidity it would require to resemble a spherical object to the same capacity.



**Figure 6.16** – Agar support bath-printed bucky-ball (a) during printing, (b) post-printing, (c) post-release immersed in water, (d) self-standing out of water

Thus to summarise the printing of bucky balls, the best print settings were found to be 15 mm/s speeds, an extrusion multiplier of 5, 50  $\mu\text{m}$  layer heights, 2 perimeters, no infill, 0.1 mm retract length and retraction speed of 1 mm/s, a Z-lift height of 0.5 mm, and 20 skirts to ensure that the nozzle is adequately primed for extrusion.

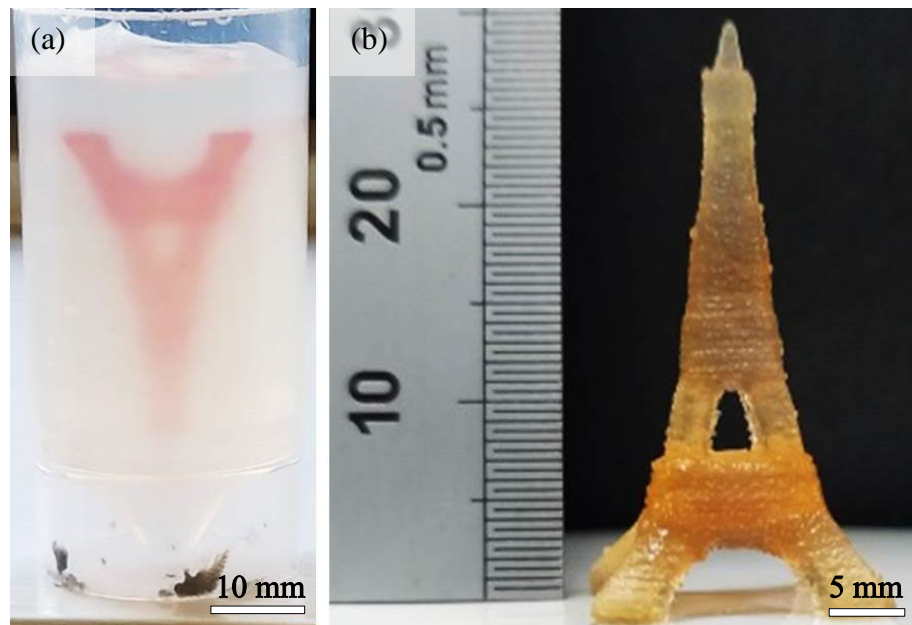
#### **6.4.4 Agar fluid gel support bath – Eiffel tower printing**

A simplified model of the Eiffel tower was chosen as the final challenging structure to test the fabrication capabilities of the support bath. The four legs and the four mid-section struts of the tower require the extruder to hop across the gaps without material oozing out from the nozzle and thus utilises the mitigation methods discussed in the bucky ball print. The top of the tower is relatively long and slender which demands that the bath is dynamically stable enough during printing to ensure that the top is printed straight. Additionally, the feet and mid-section struts are thin, yet they need to be very strong in order to support all the weight of the structure which requires the crosslinked ink to be very rigid.

As the structure is very tall and not too wide, the inverted position was deemed the best orientation whilst printing deep into a tube – this allows for a larger print as otherwise the tube's internal taper at the bottom would interfere with the feet of the tower. As the cross-sections of the feet, mid-section struts, and top are all quite small and the section just above the arch is quite large, the CAD model needed to be split into five subsections each with different print settings in order to fabricate such a structure. The feet and mid-section struts have the smallest cross-sections, and are so small that using any infill density would lead to overextrusion, thus these sections were printed with 2 perimeters only (the feet also had a 2 bottom horizontal shells to seal the inside). The thicker region above the arch was printed with 2 perimeters, 20% honeycomb infill for extra strength, with 2 top and bottom horizontal shells to seal up the areas above and below which would otherwise be exposed. The top of the tower was split into two sections: the bottom half and the top half. As the bottom half is moderately thick, there was enough space to have 10% honeycomb infill to provide the extra strength necessary to hold up the rest of the spire. As the spire tapers to a point, the top half becomes too narrow for the inclusion of any infill material, thus the top half was printed using 2 perimeters only.

The printed Eiffel tower model (figure 6.17) was capable of being printed with good mechanical strength and shape fidelity. The strength of the crosslinked alginate was sufficient to keep the spire of the tower reasonably straight. The moderately thin feet of the tower would deflect slightly due to the weight of the structure, causing the tower to lean slightly towards one side. Despite this, the tower was able to remain stable when placed on a level surface. The arches which separated the feet and the gap in the mid-section remained clear from any oozing filament because of the well-tuned retract

settings established during the printing of bucky balls. The perimeters helped maintain the aesthetic qualities of the structure by ensuring a smooth outline at each printed layer, and the honeycomb infill was strategically placed in regions of the structure where the extra strength was necessary.



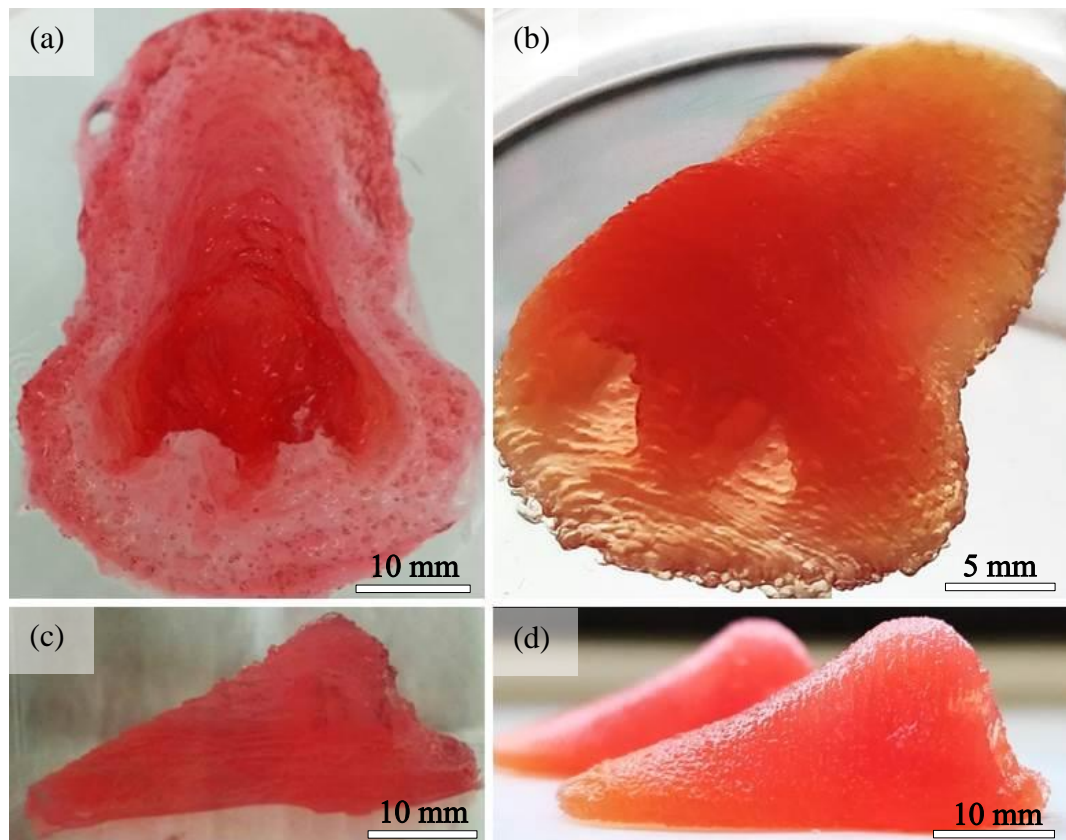
*Figure 6.17 – Support bath-printed simplified Eiffel tower model (a) in an inverted orientation within the medium post-print, (b) self-standing post-release*

## 6.5 Summary

The printed models exhibited in this chapter show the importance of integrating supportive strategies to produce a variety of challenging structures with different logistical needs. In the absence of the supportive agar fluid gel, the fabrication of such structures with the same quality characteristics becomes highly impractical because of the need for high mechanical strength and rapid crosslinking at all times to fight against gravitational effects and lateral spreading of less viscous inks. Therefore it would be a near insurmountable challenge to fabricate such structures at ink concentrations which are more favoured for cell-viability. It is therefore the opinion that the developed agar support baths are very capable biofabrication tools which could increase the scalability of bioprinting with respect to the production of softer tissue-like models.

The agar fluid gel support baths demonstrated here have shown excellent capability as a viable support bath material to assist in the fabrication of complex structures using a partially crosslinked alginate hydrogel, and can be seen as a significant improvement upon the quiescently gelled gelatine support baths discussed in Chapter 5 – A

Quiescently Gelled Gelatine Supportive Medium to Facilitate 3D Soft Tissue Biofabrication – a comparison of a printed nose structure between the two methods is shown below in figure 6.18. The agar fluid gel support baths share the same ideology of the quiescently gelled gelatine baths as both can be prepared in a very simple manner. The developed gelatine support baths are arguably the most repeatable and straightforward to replicate as they only require a specified concentration to prepare. Whilst agar fluid gels are also simple to prepare, there may be some issues regarding the repeatability of obtaining exact mechanical properties between batches - variations in blending time and blending speed may produce microparticles of different sizes which can alter the bulk rheology of fluid gels, however such concerns did not become apparent in the conducted experimental work.



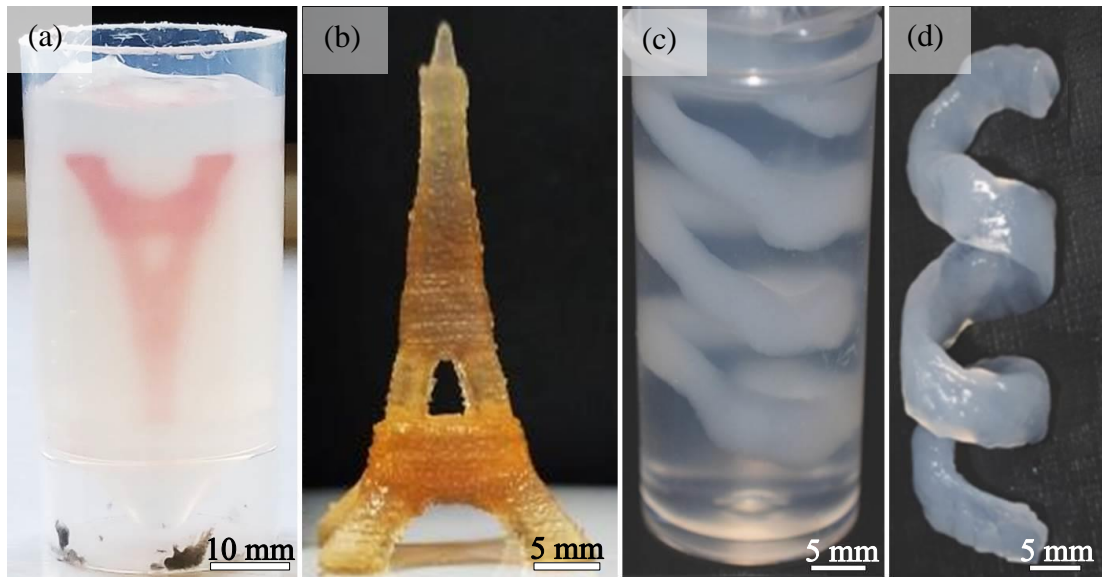
**Figure 6.18** – Print quality comparison of a nose printed using (a, c) the quiescently gelled gelatine support bath and (b, d) the agar fluid gel support bath

There exists published work which adopted a similar approach for biofabrication [133] which used agarose to create the gel, whereas unpurified and commercially available agar was used here. The method to create the microparticles in the published work was different than the method documented within this thesis; the microparticles were formed under sheared gelation with a magnetic stirrer whilst the agarose solution cooled, the

shear stress inhibits the aggregation of molecules so that only small spherical gelled microparticles could form instead of gelling globally as a unified puck then mechanically broken using a blender like the method described in this thesis. Sheared gelation may offer more consistently rounded particle morphology compared to a mechanical breakup approach which induces brittle fracture and results in rough particle morphology – this comparison is seen when comparing the morphology of fluid gel particles created in FRESH v1.0 and FRESH v2.0, whereby the fluid gels prepared in the FRESH v1.0 protocol are blended and are subsequently much rougher and irregularly sized than the coacervation/sheared gelation approach in FRESH v2.0 [134][136]. In the literature, a dual crosslinkable gellan gum bioink was used – the heated gellan gum is deposited into the agarose support bath in a liquid state, which thermally gels as it cools, and is followed by ionic crosslinking with calcium afterwards by injecting the calcium around the printed structure within the bath; this is the primary difference between their method and the method described in this thesis.

It is hypothesised that the use of a partially crosslinked alginate filament and incorporating the calcium into the agar fluid gel bath are the two key reasons for this method's capability to print with good resolution - liquid inks could be more prone to flowing and diffusing out of position as ink will displace due to not having an elastic modulus under the internal bath stresses acting on the ink. When partial crosslinking is employed a runny solution can be made filament-like, boasting elastic moduli with the capacity to withstand the surrounding stress incurred by changes in bath internal pressure and shearing stresses from the moving nozzle, resisting flow and thus can better retain depositional accuracy for maintaining a higher print resolution. Furthermore when partial crosslinking is employed the filament becomes more tolerable to crosslinking cations within the bath and can mitigate some issues related to excessive crosslinking which occurs more frequently with liquid inks. This is in contrast to the literature which avoids the ionic crosslinking of the liquid ink by first inducing thermal gelation of the gellan gum followed by ionic crosslinking only after the extrudate has initially gelled – the time taken for thermal crosslinking is longer than ionic crosslinking, which means there is greater risk of the liquid ink diffusing or flowing out of position before gelation can occur. Therefore there are multiple differences between the literature and the thesis which opens the possibility for further investigation so that the depositional aspects of support bath bioprinting can be better understood and optimised further. The respective print quality of structures printed into the developed

agar fluid gel baths compared to agarose sheared gels is shown in figure 6.19. Although the printed structures bear vastly different geometry, it can be seen that the agarose sheared gel is optically much clearer due to being a more refined product than commercially available agar as well as its use at a moderately low concentration of 0.5% w/w compared to the 1% w/v used in the developed agar baths; this makes it easier to visually assess a structure during printing which helps the user identify any depositional issues which may otherwise ruin fabrication.



**Figure 6.19** – An Eiffel tower structure (a) encapsulated within the developed agar fluid gel support bath before (b) and after release, compared with a helical structure (c) encapsulated within an agarose sheared gel before (d) and after release [133]

## **Chapter 7 – Agar Fluid Gels with Enhanced Tuneability for Further Engineering Control**

### **7.1 Introduction**

To this point, the developed agar fluid gel baths can only be considered tuneable in the respect that the concentrations of agar and calcium can be varied to suit the demands of supported fabrication with consideration for structure size, nozzle size, bath's tolerable calcium levels, and the desired mechanical properties of printed constructs. Whilst this has been shown to be versatile enough to enable the fabrication of complex structures with good shape fidelity and strength, as well as enable the fabrication of structures from nozzles as fine as a 30 gauge (160  $\mu\text{m}$  internal diameter), the currently developed baths have not been assessed in their functional capabilities when the fluid gel is mixed with other materials. This could entice the development of complex baths with an even greater range of rheology which may be useful for catering to specific requirements such as very high resolution printing with thin (<100  $\mu\text{m}$  diameter) glass capillaries, or to add some bio-functionality to long-term and large scale prints with the inclusion of cell culture media.

Further control over the support baths can be achieved by simply mixing the fluid gel with another solution for example; the volume fraction of gelled agar microparticles is reduced, spacing the particles further apart to reduce the attractive strength of adjacent bonds which lowers the bath's bulk rheological properties. Should a bath be considered too strong for the printing operation being conducted, then diluting the gel would allow the user to appropriately reduce the properties to correct the bath conditions rather than having to repeat the preparation process. This could also cut down preparation times when conducting large scale bioprinting operations using multiple machines running in parallel by having a stock of fluid gel which can be readily mixed to the correct conditions for the specific work being carried out, removing the need to prepare a specific bath a day in advance. This could additionally provide the baths with various benefits imparted from the diluting solution, such as mixing with clear solutions to improve the overall clarity of support baths or mixing with cell culture media to grant printed cellular constructs a source of nutrition immediately upon deposition and throughout lengthy and large scale biofabrication.



## **7.2 Influence of the Continuous-Phase on Support Bath Qualities**

The aim of this initial investigation is to understand the effects of diluting the supportive agar fluid gel so that optimal diluted bath conditions can be achieved. To maximise the volume of the secondary solution (such as cell culture media) within the bath, the agar needs to be diluted as much as possible whilst retaining its functional capabilities of suspension, support, and dynamic stability during printing.

To evaluate the effects which dilution has on the overall qualities of the support baths, three different mixing ratios were considered – 3:1, 1:1, and 1:3 which corresponds with the respective amounts of the agar-to-diluter. To assess the effect of different material solutions on the overall bath's rheology, three different materials with different viscous qualities were considered: water, 2% w/v CMC, and 2% w/v GG. Furthermore three different agar fluid gel concentrations of 0.5%, 1%, and 2% w/v were prepared which granted the baths with various undiluted strengths. For each condition, a simple cuboidal grid structure was printed to provide an evaluation of the bath's printability and invertibility characteristics.

An additional evaluated characteristic was the bath clarity - whilst functionally a non-crucial characteristic of a support bath, it does make it easier to obtain visual feedback which can allow the user to more easily deduce whether a print is failing, thus bath clarity is considered an attribute of secondary importance. For such evaluation, a coin was used as a reference image and placed on the underside of a clear dish containing the bath material, allowing for the relative image clarity between different bath conditions to be observed.

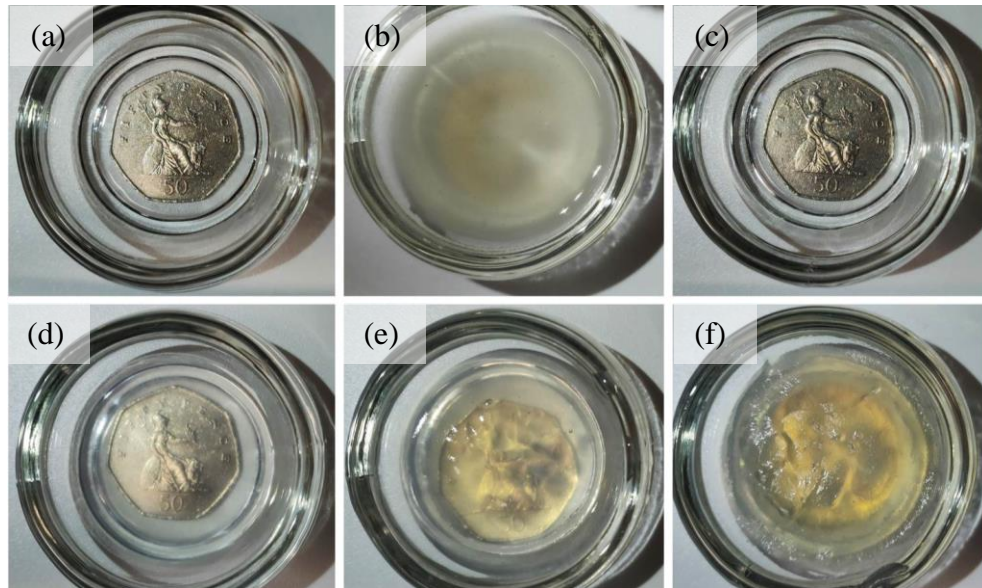
### ***7.2.1 Assessment of fluid gel and diluent constituents prior to mixing***

The qualities of each material (three agar concentrations and three secondary solutions) were evaluated initially to highlight their relative merits and shortcomings prior to any mixing being conducted. The purpose was to show the respective properties of each material to provide an approximation of what the outcome after mixing could be.

Figure 7.1 shows the relative clarities of the three diluents (water, CMC, GG) and the three agar concentrations (0.5%, 1%, and 2%). The materials with the best clarity are the solutions of water and CMC because the solutions themselves are naturally clear. The next clearest condition was the 0.5% agar concentration which exhibited only a minor loss of clarity, followed by the 1% agar concentration in which the coin's details were barely distinguishable but the coin's outline remained discernible. Agar



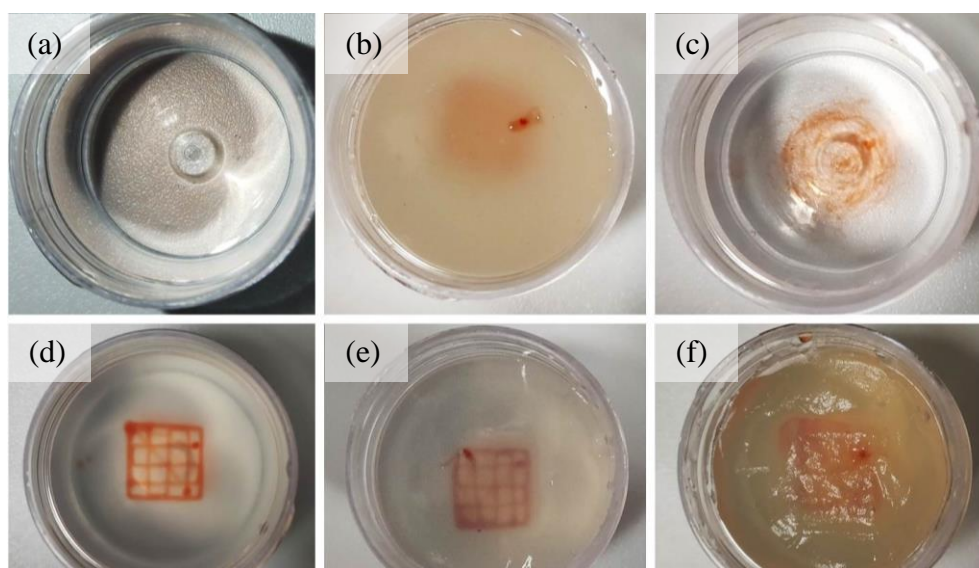
concentrations of 2% were so opaque that the coin's outline could not be clearly deduced, and 2% GG was too opaque to identify the coin underneath. For optimal mixture clarity, a combination of 0.5% or 1% agar with water or CMC would likely produce the best conditions for visual assessment during fabrication.



**Figure 7.1** – Clarity assessment of constituents on their own: (top row) viscosity modifiers (a) water, (b) 2% w/v GG, (c) 2% w/v CMC, (bottom row) agar fluid gel at concentrations (d) 0.5%, (e) 1%, (f) and 2% w/v

The printability of a simple cuboidal grid structure into each of the 6 materials was assessed as shown in figure 7.2 – this was to provide visual data regarding which materials exhibit the best printing qualities. The best conditions for printing were the agar fluid gels at concentrations of 0.5% and 1%; the microparticulate fluid gel network provides the conditions necessary for very reliable printing but has already been established as the basis of the work on supportive agar gels, thus the result was expected. 2% agar fluid gels were expected to show good printability but the material's poor clarity impairs the reliability of such a judgement – by extrapolating from previously obtained data it can be speculated that such concentrations could cause thinner nozzles to bend which could result in less accurate material deposition it, but assessing nozzle deflection was not the experimental objective of this test. Each of the three diluting solutions exhibited terrible printability, an anticipated outcome based on the absence of an elastic modulus thus no supportive qualities exist within the materials. The 2% GG solution presented arguably the best printability of the three solutions, most likely because it bore the greatest viscosity; despite this the structure was printed with

poor shape fidelity, resembling a non-distinct rounded geometry when viewed from underneath and may be related to the nozzle acting like a stirrer during printing, introducing small vortices which causes the material to rotate and mix. A similar observation can be made for the print into the 2% CMC solution, which although failed to print did leave filament strands oriented in a circular manner. Lastly the viscosity of the solution seemed to affect the rate of alginate diffusion – all the alginate had diffused into the water when that was printed into, CMC shown the presence of loosely tangled strands of filament, and guar gum appeared to retain the most of the alginate as indicated by the intensity of the ink's red dye.

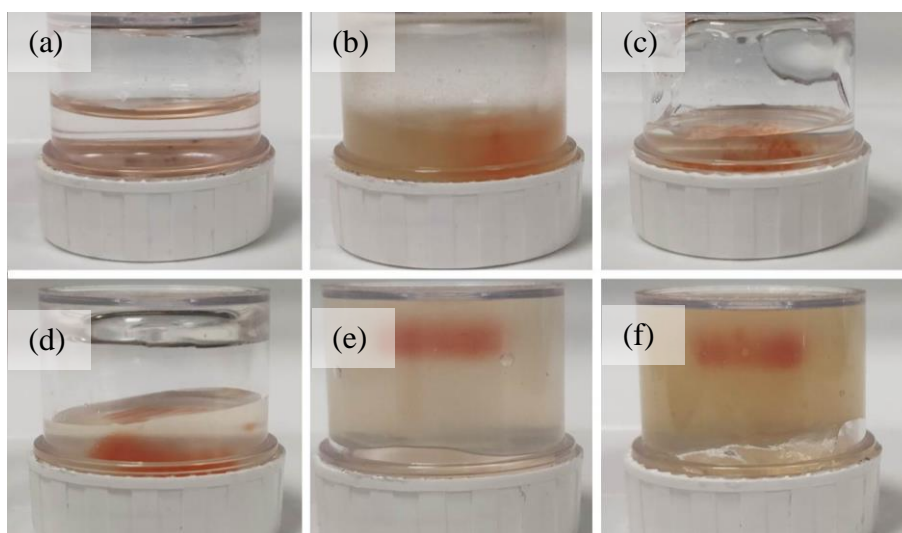


**Figure 7.2** – *Printability assessment into each constituent on its own: (top row) viscosity modifiers (a) water, (b) 2% w/v GG, (c) 2% w/v CMC, (bottom row) agar fluid gel at concentrations (d) 0.5%, (e) 1%, (f) and 2% w/v*

The results from this experiment would confirm that the best printing conditions involve the use of the agar fluid gels, but that is not to say that the three diluting solutions are not useful – diluting the agar fluid gels should be done with consideration of the final bath's qualities, as the use of water or GG for example may produce supportive baths which are too runny or too thick, or there may even be some solutions which can dilute the agar at greater ratios than other solutions whilst remaining as effective. However such speculation will need to be assessed in further experiments.

As per the typical method of evaluating the overall rheological qualities of support baths, figure 7.3 shows the results of inversion tests conducted on each of the materials studied after printing. Each of the diluting solutions failed to remain upright upon

inversion as expected due to not having an elastic modulus to hold the material together nor adhere to the walls of the tub. The 0.5% agar concentration also failed the inversion test but had a textured, non-flat surface which indicates the presence of some strength attributes, as does the relative success of that concentration's printability study. It should be noted that this 0.5% concentration failed the inversion test, whereas earlier in 6.2 Systematic Evaluation of Agar and Calcium Concentration on Supportive and Print Qualities the 0.4% agar concentration passed the inversion test. The inconsistency between these two concentrations is related to the size of the vessel used in their respective inversion tests; the 0.4% agar concentration was inverted in a vessel with a small internal diameter which enabled that condition to be inverted successfully, whereas the 0.5% condition examined here failed the inversion because the vessel's diameter is much greater and the strength of the fluid gel could not be sustained over the larger area. Both the 1% and 2% agar concentrations were successfully inverted with the printed test structures still supported inside. From this experiment the results would suggest that the 1% and 2% agar concentrations are most suitable for supporting structures most securely, however the combination of such concentrations with any of the three diluting solutions whilst retaining some inversion capability may be possible.

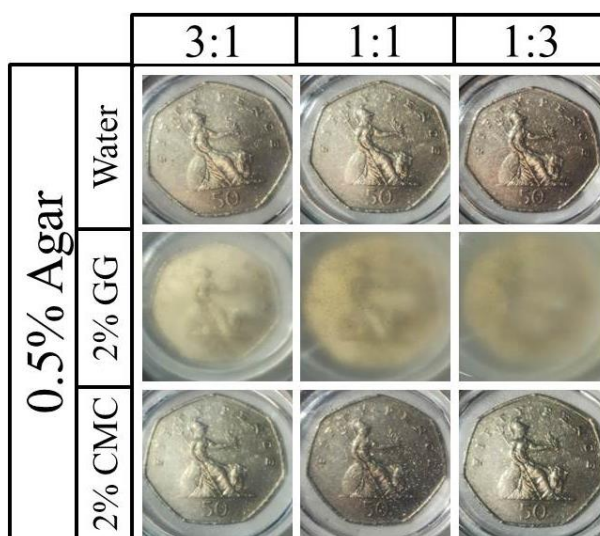


**Figure 7.3** - Printability assessment into each constituent on its own: (top row) viscosity modifiers (a) water, (b) 2% w/v GG, (c) 2% w/v CMC, (bottom row) agar fluid gel at concentrations (d) 0.5%, (e) 1%, (f) and 2% w/v

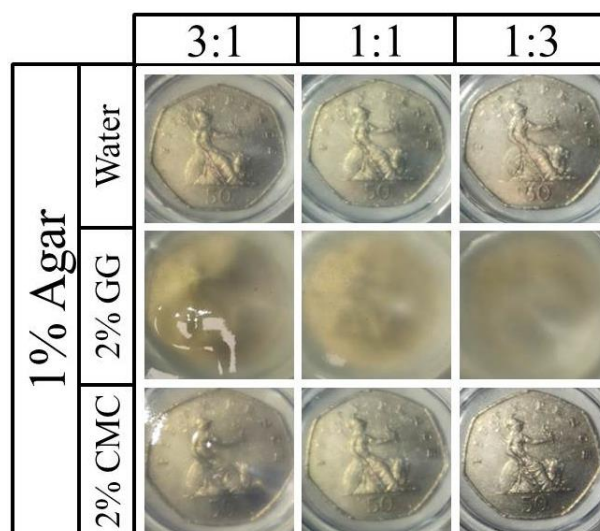
### 7.2.2 Clarity assessment of fluid gel/diluent mixtures

The clarities of each diluted fluid gel mixture with 0.5%, 1%, and 2% agar is presented in figure 7.4, figure 7.5, and figure 7.6 respectively. The overall trend suggests that 2%

GG performs poorly in this aspect, with the only two permissible conditions being when mixed with 0.5% agar at a 3:1 and 1:1 ratio of agar to GG whereby the coin's details remain reasonably visible; all other conditions with GG are too opaque for reliable visual assessment. All conditions mixed with water or CMC were optically similar given that both solutions are naturally clear. In the cases where agar was mixed with water or CMC, 0.5% and 1% agar concentrations granted suitably clear visual conditions at all dilution ratios whereas 2% agar was optically too opaque at a 3:1 ratio to provide a good visual assessment.

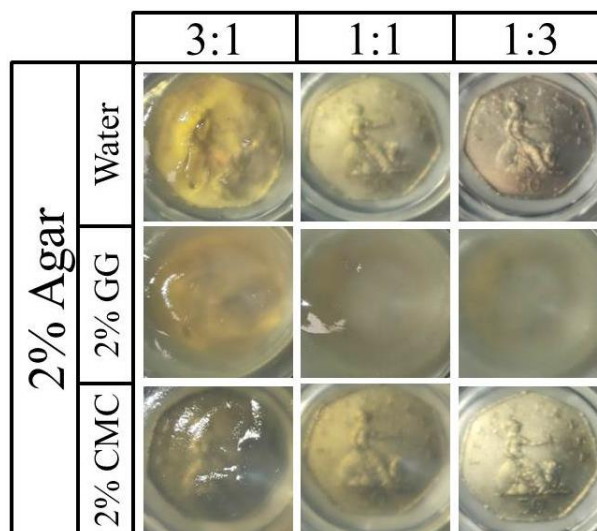


*Figure 7.4 – Clarity assessment of various mixtures of 0.5% w/v agar fluid gel with water, GG, and CMC*



*Figure 7.5 - Clarity assessment of various mixtures of 1% w/v agar fluid gel with water, GG, and CMC*





**Figure 7.6** - Clarity assessment of various mixtures of 2% w/v agar fluid gel with water, GG, and CMC

The dimensions of the vessel used to conduct these bath clarity assessments meant that the bath was not too deep. Baths which are deeper are more difficult to visually assess as more material exists between the object of interest and the camera. This also applies when viewing an object whilst printing from the side of the vessel used – wider vessels similarly can hold more material between the bounds of the vessel and the object of interest and thus makes visual assessment more difficult from that view too. Considering this, one should expect the baths to become less translucent than what is shown in the figures when conducting larger prints which require wider and taller vessels to hold the necessary volume of supportive gel. This means that results which were shown to be not too opaque (such as 2% agar at 1:1 ratio with water or CMC), would be reasonably more difficult to assess whilst printing at such scales.

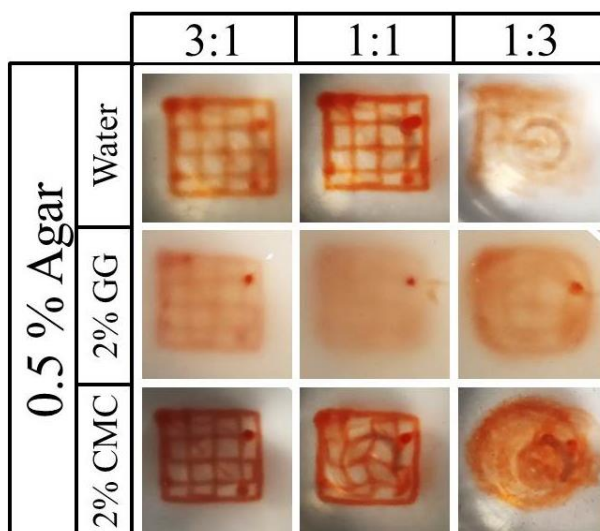
As one could anticipate when mixing the agar with various solutions, the best conditions to maintain the opacity of the support bath would be 0.5% and 1% agar at any ratio of water or CMC to dilute. The relative translucency of agar at lower concentrations coupled with naturally clear solutions for dilution means that the clarity of the mixtures can be maintained very easily, whereas the clarity was severely impacted at the smallest examined ratio of 3:1 when GG was used which required the most translucent agar concentration of 0.5% for the coin to remain discernible.

Alternative methods to improve the clarity of agar fluid gels were not investigated in this experiment. The visual clarity of agar fluid gel mixtures is related to the concentrations of the agar and the diluent, dilution ratio, differences in the refractive

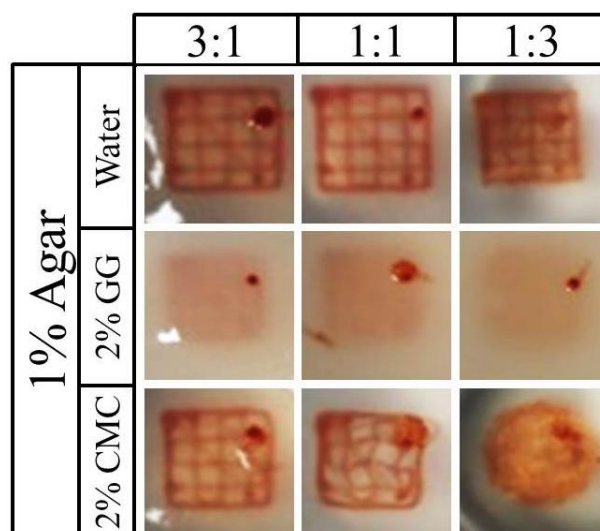
indices of the medium's constituents, the size and shape of the particles, and combinations of these [266], therefore addressing such factors during the formation of supportive fluid gels could enhance their transparency. Some solutions to resolve such factors may already exist such as optical clearing; a process to help visualise thick tissues in biological research. Optical clearing includes various techniques which aim to homogenise the refractive index of all substances in a mixture to allow visible light to pass through more easily, such as immersing the tissue sample in a solution with matching refractive index [267]. Therefore a more appropriate diluent than water or CMC may exist which is able to better match the refractive index of agar's gelled microparticles in the context of support baths. Alternatively, and specifically for fluid gels, reducing the size of the gel particles may improve visual clarity [268] which could be achieved by stronger blending conditions or by adopting a method of shear-induced gelation instead of the current mechanical breakup approach. Lastly, the use of purified agar (agarose) instead of commercially available agar should produce clearer fluid gels due to the removal of agaropectin [269]. If more concentrated fluid gels could be made clearer, then visual assessment of a structure during printing could be made more easily whilst retaining relatively strong supportive qualities which may help in the fabrication of large scale structures.

### ***7.2.3 Printability assessment of fluid gel/diluent mixtures***

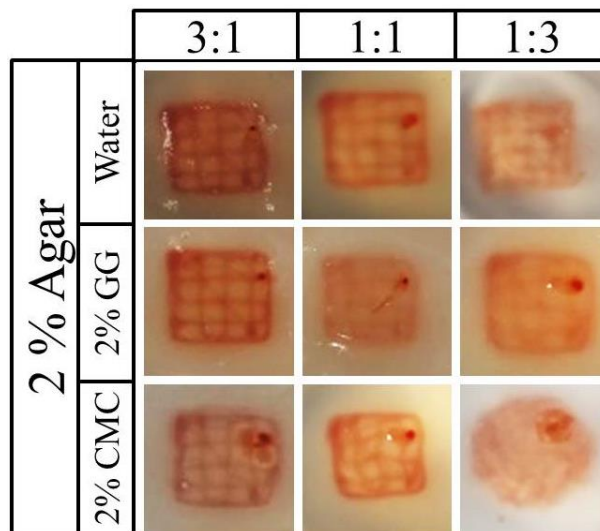
The results from the printability assessments into the 0.5%, 1%, and 2% agar mixtures with water, 2% GG, and 2% CMC are shown respectively in figure 7.7, figure 7.8, and figure 7.9. The observed trend was that mixtures formulated at the 1:3 ratio of agar to diluting solution were functionally too poor for the purpose of supported fabrication, and the overall printability did not seem to improve noticeably when a more concentrated agar constituent was used at such ratios; arguably the only condition which showed any development in printability was when the agar was mixed with water, whereby the ink was readily diffusing when 0.5% agar was used but retained its grid-like geometry when 1% and 2% agar was used.



**Figure 7.7** – Printability assessment of various mixtures of 0.5% w/v agar fluid gel with water, GG, and CMC



**Figure 7.8** - Printability assessment of various mixtures of 1% w/v agar fluid gel with water, GG, and CMC



**Figure 7.9** - Printability assessment of various mixtures of 2% w/v agar fluid gel with water, GG, and CMC

The data implies that the overall printability is governed by the agar constituent more-so than the diluting solution. In all conditions examined, every agar concentration was able to extrude the partially crosslinked alginate ink with reasonably good printability at ratios of 3:1 and 1:1; only relatively minor deviations in the print quality based on the diluting solution used became evident at mixing ratios of 1:1. Therefore this experiment would suggest that the printability is equally valid at 3:1 mixing ratios at each of the three agar concentrations when mixed with any of the three diluting solutions when not considering factors such as the bath's rheology or dynamic stability during printing.

The most intriguing comparison which can be deduced from this experiment is the difference in printability between mixtures with water and mixtures with CMC. Both solutions are similarly clear, however their viscosities differ significantly from each other. The relative print quality and success was greater in mixtures which used water to dilute the bath and poorer in the conditions where CMC was used. This finding suggests that less viscous solutions are better at maintaining the print quality of fabricated structures. The grids printed into the 1:1 mixing ratio baths with CMC were all printed with twisting struts, circling around the midpoint of the structure. The severity of such twisted structural distortions did seem to lessen when greater agar concentrations were used but remained evident to some degree in the condition where 2% agar was used. However the greatest contrast in performance was between water and CMC at mixing ratios of 1:3, whereby all conditions with CMC succumbed to



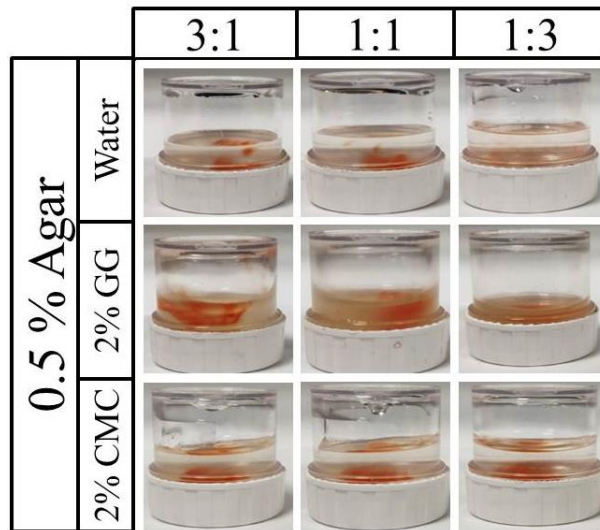
complete print failure and resulted in ink deposition in a rounded and otherwise non-distinct manner – structures printed into the conditions mixed with water at identical mixing ratios largely retained their grid-like geometry. Therefore it can be speculated that the less viscous water cooperates better with the fluid gel microparticles, possibly allowing the particles to reorganise themselves back into a supportive network at a faster rate due to having a low viscosity. This is in contrast with the CMC, being a more viscous material, which greater resists the shear stresses induced by the nozzle moving through the bath and by extension could impede the rate of stress relaxation of the gelled microparticles, thus such mixtures take a longer time to regain their supportive capabilities.

The printability data is overall not very clear regarding the use of GG as the diluting solution, primarily due to the difficulty in providing a good visual assessment on account of the gum's opacity. Despite this, printability data of the GG in the 2% agar experiments was clearer than the data obtained for the same material in the 0.5% and 1% agar conditions. This was unexpected due to 2% agar already being shown to be more opaque than the 0.5% and 1% agar gels, so the result should not have been clearer. The most probable explanation for this is that the structures in the 2% agar experiments were not printed as deep as they were in the 0.5% and 1% conditions. This would explain the sudden increase in structural clarity due to less bath material existing between the structure and the camera as previously discussed. However what can be reasonably deduced from the use of GG as the diluting solution is that it appears to perform better than CMC at equivalent mixing ratios. GG, despite being the more viscous material, does exhibit shear thinning or thixotropic flow behaviour [270] whereby the viscosity of the gum reduces in the presence of a shearing force like a nozzle moving through the medium. As the viscosity near the stressor is lowered, the gelled agar microparticles at local areas may be able to reorganise themselves at a quicker rate compared to CMC. This may explain why the structure's grids remain orthogonal at 1:1 ratios (unlike CMC which distorts), and may even explain the printability's relative success at ratios of 1:3 whereas such ratios with CMC result in failure. Aside from some erroneous rounded details forming at the corners of structures printed into the baths with GG, the results are overall promising from what can be deduced from the 2% agar experiments. However clearer data is needed to confirm with better certainty if GG performs similarly when mixed with agar at concentrations

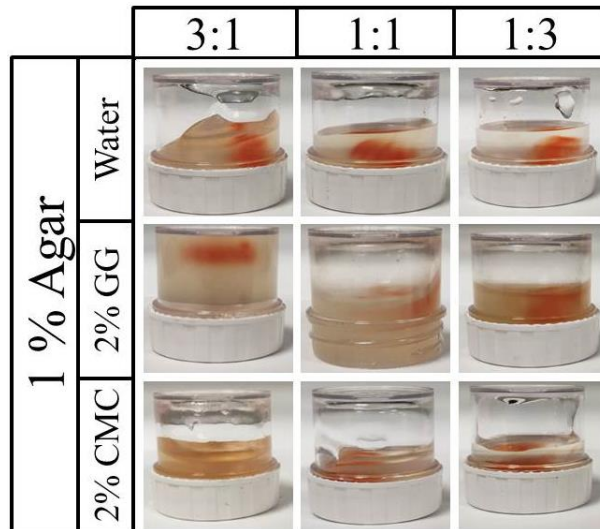
of 0.5% and 1%. From what can be deduced from the data, mixtures with water still appear to exhibit better printability compared to mixtures with GG.

#### ***7.2.4 Invertibility assessment of fluid gel/diluent mixtures***

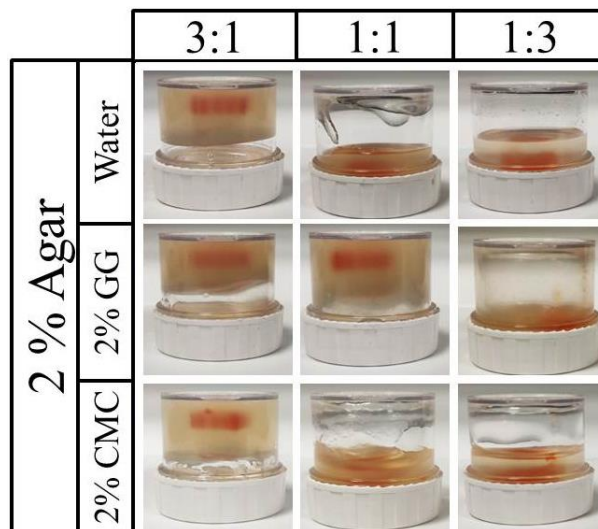
The final assessment of the mixture's properties was an inversion test to evaluate the relative strength of each mixture consisting of the three agar concentrations of 0.5%, 1%, and 2% shown respectively in figure 7.10, figure 7.11, and figure 7.12. The trend follows that greater agar concentrations result in stronger fluid gels, which also applies to their diluted versions as shown. All mixtures containing 0.5% agar failed the inversion test as a result of the bonds between gelled agar microparticles being too weak to prevent material flow; recalling an earlier experiment whereby purely 0.5% agar was inverted without dilution, it can be said that the addition of any diluting solutions did not improve the strength in any noticeable way. 1% agar mixtures with 2% GG successfully showed inversion capability at a ratio of 3:1, whilst water mixtures at the same ratio did not succeed. Despite the fact that water mixtures failed the inversion test, there was still evidence of some strength in the presence of the ridges formed on the gel's surface – this is in contrast to the natural tendency for weaker materials to spread out laterally to flatten the surface like in the 1:1 and 1:3 ratios with water. 2% CMC initially resisted the inversion at a mixing ratio of 3:1 but eventually succumbed to the gravitational forces and fell to the bottom of the container, thus failing the assessment and therefore deemed non-invertible. 2% agar mixtures were invertible with each diluting solution at mixing ratios of 3:1. Of the remaining ratios with 2% agar, only GG retained its invertible behaviour at ratios of 1:1; the remaining conditions were diluted too much, reducing the volume fraction of supportive microparticles, to bear the strength necessary to resist inversion.



*Figure 7.10 - Invertibility assessment of various mixtures of 0.5% w/v agar fluid gel with water, GG, and CMC*



*Figure 7.11 - Invertibility assessment of various mixtures of 1% w/v agar fluid gel with water, GG, and CMC*



**Figure 7.12 - Invertibility assessment of various mixtures of 2% w/v agar fluid gel with water, GG, and CMC**

The 2% agar mixture with 2% GG at the mixing ratio of 1:1 stands out as being stronger than mixtures formulated at the same ratios with water or CMC. It is unclear if this behaviour is related to this condition's high viscosity and thixotropy compared to water or CMC, whereby the time necessary for the material to flow was perhaps greater than the time permitted in the experiment. Alternatively the high viscosity and thixotropy of this mixture could provide so much resistance to flow that the shear stress of the bath at the given shear rate incurred during inversion never exceeds the yield point of the bonds which make up the gelled microparticle network.

#### **7.2.5 Scoring of fluid gel/diluent mixtures with respect to assessment criteria**

To surmise the experimental data and to deduce which condition performed the best overall, a decision matrix (table 7.1) was created to help weigh up the relative scores of each test condition with respect to the functional qualities deemed important for support baths. Each condition has points added ('+' for satisfactory performance, or '++' for good) or subtracted ('-' denotes poor performance, '--' for very poor) based on the condition's ability or inability to meet each criterion. The score of each condition was tallied up in table 7.2.

**Table 7.1 - Decision matrix to score the relative strengths and weaknesses of each agar fluid gel and viscosity modifier mixture at various mixing ratios**

Fluid Gel	→	0.5% Agar			1% Agar			2% Agar		
Diluent	↓	Print.	Invert.	Clarity	Print.	Invert.	Clarity	Print.	Invert.	Clarity
Water	3:1	++	--	++	++	+	+	++	++	-
	1:1	+	--	++	++	--	++	++	--	+
	1:3	-	--	++	-	--	++	-	--	++
2% GG	3:1	++	--	-	++	++	--	++	++	--
	1:1	-	--	-	+	--	--	++	+	--
	1:3	-	--	--	-	--	--	-	--	--
2% CMC	3:1	++	--	++	++	+	+	++	++	-
	1:1	-	--	++	-	--	+	-	--	-
	1:3	--	--	++	--	--	++	--	--	+

**Table 7.2 - Surmised decision matrix to show the relative score for each of the assessed agar fluid gel and viscosity modifier mixtures at the various mixing ratios**

Fluid Gel	→	0.5% Agar	1% Agar	2% Agar
Diluent	↓	Total Score	Total Score	Total Score
Water	3:1	2	4	3
	1:1	1	2	1
	1:3	-1	-1	-1
2% GG	3:1	-1	2	2
	1:1	-4	-3	1
	1:3	-5	-5	-5
2% CMC	3:1	2	4	3
	1:1	-1	-2	-4
	1:3	-2	-2	-3

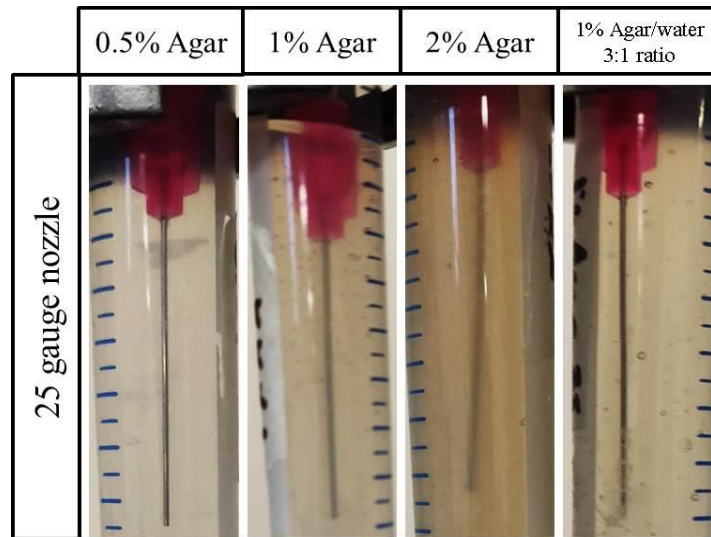
Support baths comprising of 1% agar with water or CMC at a mixing ratio of 3:1 were deemed to exhibit the best overall qualities to facilitate the fabrication of structures, followed closely by their 2% agar counterparts. As the scores for both 1% agar baths were given a value of 4, neither condition could be said to be better or worse than the other so determining a single condition as optimal was not straightforward at this point. Within the same agar concentration, the relative scores for water and CMC at mixing ratios of 1:1 and 1:3 would favour the use of water as the diluent of choice; dilutions with water can better retain more desirable bath characteristics compared to CMC which has been shown to warp the geometry of printed structures, thus it can be argued that a

wider range of mixing ratios could be explored with water, therefore mixtures with water can be considered more tuneable than CMC. Therefore the most optimal bath condition based on the experimental data would be 1% agar mixed with water at a ratio of 3:1.

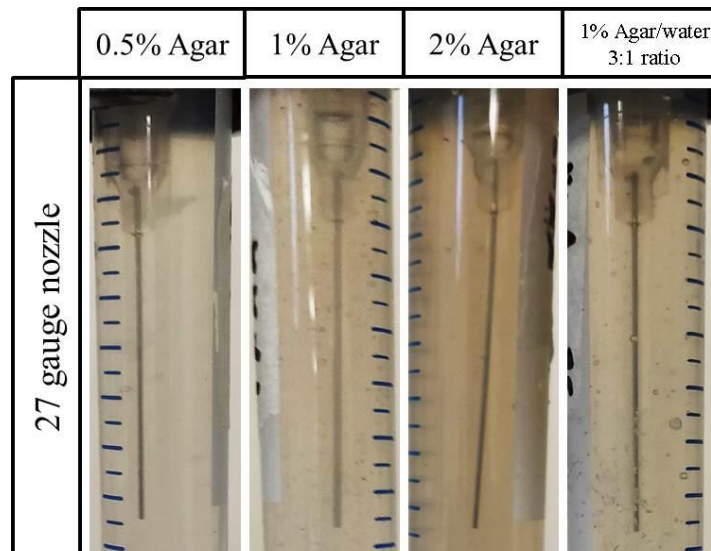
#### ***7.2.6 Nozzle assessment of optimised fluid gel/diluent mixture support bath***

With the optimal bath condition chosen, a final evaluation was conducted to compare the relative impact of the bath on a variety of printing nozzles to assess if the nozzles would bend. Previously the issue of nozzle deflection was addressed by stepping down the agar concentration in chapter 6.2 Systematic Evaluation of Agar and Calcium Concentration on Supportive and Print Qualities, whereas this approach incorporates the dilution of the fluid gel constituent with water to deliberately weaken the network by reducing the effective volume fraction of gelled microparticles within the bath. To check for nozzle deflection, a nozzle was inserted deep into the bath and photographed whilst the nozzle was being moved by hand. Four baths were used to assess nozzle deflection: the optimised 1% agar/water mixture at a ratio of 3:1, and three non-diluted baths with 0.5%, 1%, and 2% agar to serve as a basis for comparison.

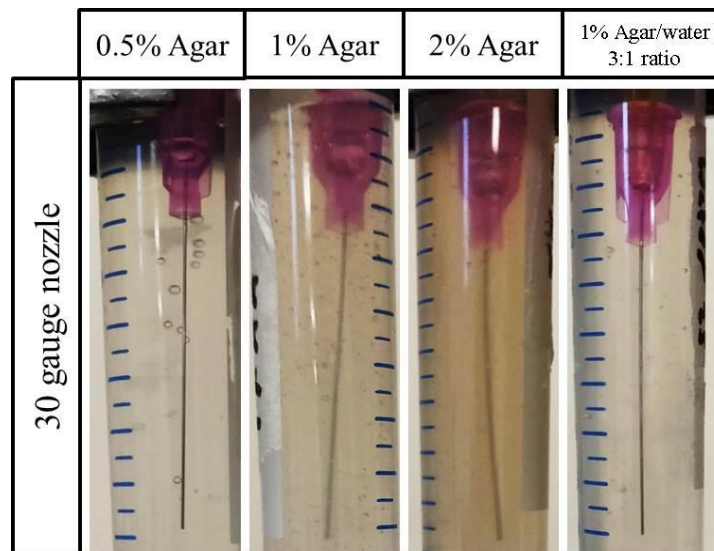
As can be seen in figure 7.13, figure 7.14, and figure 7.15, the optimised support bath is weak enough to avoid bending nozzles at gauge sizes of 25, 27, and 30, corresponding with internal diameters of 0.26 mm, 0.21 mm, and 0.16 mm respectively. In terms of the control conditions of purely 0.5%, 1%, and 2% agar, the data shows that concentrations of 2% are exceedingly strong and cause the thickest of the three tested nozzles to bend – thus the rheology of 2% agar fluid gels is too great for reliable use as a support for fabrication and would require the concentration to be stepped down or be diluted in order to accommodate the use of such nozzles. Agar concentrations of 0.5% were compatible with all nozzles and 1% was only incompatible with 30 gauge nozzles. Nozzle deflection data for 1% agar with 25 and 30 gauge nozzles was initially discovered in chapter 6.2 Systematic Evaluation of Agar and Calcium Concentration on Supportive and Print Qualities but was not investigated to provide further data at the time for various agar concentrations or the intermediate sized 27 gauge nozzle; thus the data is now more complete whilst simultaneously serving as a comparison for the newly optimised 1% agar/water mixture bath.



**Figure 7.13** – Nozzle deflection assessment of 25g nozzles moving through 0.5%, 1%, and 2% agar fluid gel baths compared to optimised 3:1 ratio agar/water support bath



**Figure 7.14** – Nozzle deflection assessment of 27g nozzles moving through 0.5%, 1%, and 2% agar fluid gel baths compared to optimised 3:1 ratio agar/water support bath



*Figure 7.15 – Nozzle deflection assessment of 30g nozzles moving through 0.5%, 1%, and 2% agar fluid gel baths compared to optimised 3:1 ratio agar/water support bath*

The data suggests that the optimised 1% agar/water mixture performs as well as the 0.5% agar fluid gels in the context of mitigating nozzle deflection in addition to performing better overall when considering the printability, invertibility, and clarity as discussed in the decision matrix. Furthermore, the optimised baths can be engineered and optimised further for bioprinting applications when considering that up to 25% of the bath's volume could incorporate a more functional secondary material, such as cell culture media which could meet the nutritional needs of bioprinted cells when printing for prolonged periods of time. For fluid gel mixtures, media would only need to be added as and when necessary for bioprinting and could be readily mixed with the gel immediately prior to printing.

### **7.3 Influence of Calcium Concentration and Distribution within the Gel-Phase/Continuous-Phase on Support Bath Qualities**

The optimisations regarding the dilution of the supportive agar fluid gels was conducted without the presence of any calcium in order to solely gather data on the mechanical functionality of the baths. At the time, optimising the calcium concentration simultaneously would have introduced more variables which would have been difficult to consider whilst focusing on what conditions maintain the best functional qualities. In the case of agar/CMC mixtures at ratios of 1:3 for example, if calcium were present in the mixture then it would not have been clear that the bath conditions were fundamentally the cause of print failure – this would not have been clear until a range of



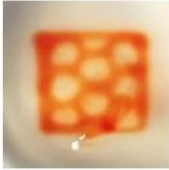
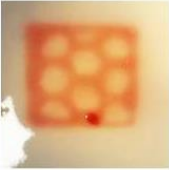
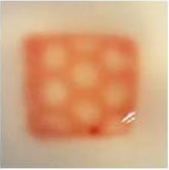
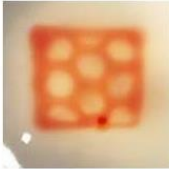
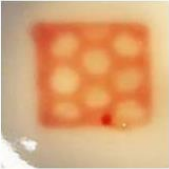
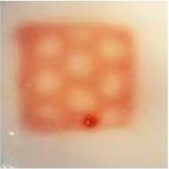
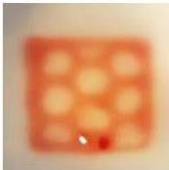

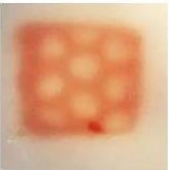
calcium concentrations had been tested in either the gel-phase, continuous-phase, or both phases which would have consumed a lot of time.

Now that an optimal bath concentration has been chosen, a more thorough investigation to establish the range of appropriate calcium concentrations can be conducted. As mentioned earlier, the distribution of calcium within the support bath as well as the concentration is worth investigating as the interactions between partially crosslinked alginate inks and the calcium ions in the gel-phase, continuous-phase, or both phases are not known. The information would be useful to understand, particularly when considering the incorporation of cell culture media, many of which will contain some calcium content and particularly so if the media is mixed with serum; if the support baths exhibit any intolerance to crosslinking calcium ions in the continuous-phase, then the range of appropriate cell culture media may be limited.

### ***7.3.1 Printability assessment into fluid gel 3:1 mixtures with respect to calcium distribution and concentration in the gel- and continuous-phases***

Following is the assessment of three calcium concentrations (0, 10, and 20 mM) and their impact on printability and release-ability in the gel-phase, continuous-phase, and both phases of the optimised 1% agar/water baths at a mixing ratio of 3:1. For this experiment, macroporous structures with a honeycomb infill pattern were printed with 25 and 30 gauge nozzles to evaluate the crosslinking effects when different nozzle sizes are used.

As can be seen from the post-print data (figure 7.17) and post-release data (figure 7.18), the distribution of calcium did not impair the printability into the bath in any noticeable manner and structural integrity was maintained throughout the release stage for most conditions using the 25 gauge nozzle. Structures printed into support baths without calcium in the gel-phase and some calcium in the continuous-phase were prone to structural failure upon release or would be too soft to maintain good shape fidelity.

25g Nozzle		Agar CaCl <sub>2</sub> Conc.		
		0 mM	10 mM	20 mM
Water CaCl <sub>2</sub> Conc.	0 mM			
	10 mM			
	20 mM			






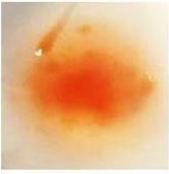
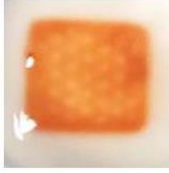

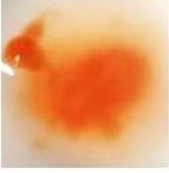
**Figure 7.16** – Impact of CaCl<sub>2</sub> concentration and distribution between continuous/gel-phase in developed 3:1 agar fluid gel/water support baths with 25g nozzles post-print

25g Nozzle		Agar CaCl <sub>2</sub> Conc.		
		0 mM	10 mM	20 mM
Water CaCl <sub>2</sub> Conc.	0 mM			
	10 mM			
	20 mM			






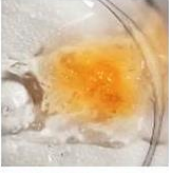



**Figure 7.17** - Impact of CaCl<sub>2</sub> concentration and distribution between continuous/gel-phase of developed 3:1 agar fluid gel/water support baths with 25g nozzles post-release

With a finer 30 gauge nozzle, the post-print (figure 7.18) and post-release data (figure 7.19) show a reduced tolerance to the same crosslinking conditions used with 25 gauge nozzles, as is already known. At sufficiently low CaCl<sub>2</sub> levels, the printability with 25g and 30g nozzles is similar. However with increasing CaCl<sub>2</sub> levels, the 30g nozzle

becomes intolerable of the crosslinking conditions as evidenced in 1% agar 20 mM CaCl<sub>2</sub> with all continuous-phase CaCl<sub>2</sub> concentrations examined. With both nozzles, the best conditions appeared to be with 1% agar 10 mM CaCl<sub>2</sub> with CaCl<sub>2</sub> solutions in the range of 0 to 20 mM.

30g Nozzle		Agar CaCl <sub>2</sub> Conc.		
		0 mM	10 mM	20 mM
Water CaCl <sub>2</sub> Conc.	0 mM			
	10 mM			
	20 mM			

**Figure 7.18** - Impact of CaCl<sub>2</sub> concentration and distribution between continuous/gel-phase of developed 3:1 agar fluid gel/water support baths with 30g nozzles post-print

30g Nozzle		Agar CaCl <sub>2</sub> Conc.		
		0 mM	10 mM	20 mM
Water CaCl <sub>2</sub> Conc.	0 mM			
	10 mM			
	20 mM			

**Figure 7.19** - Impact of CaCl<sub>2</sub> concentration and distribution between continuous/gel-phase of developed 3:1 agar fluid gel/water support baths with 30g nozzles post-release

The results from this experiment so far suggests that the calcium distribution does not matter too much – considering the fact that each bath is mixed in a 3:1 ratio of agar to calcium solution, the majority of the bath's calcium content comes from the agar constituent and not the diluent. Furthermore, it should be noted that 1% agar with zero calcium mixed with 20 mM CaCl<sub>2</sub> solution is not the same as 1% agar with 20 mM CaCl<sub>2</sub> mixed with 0 mM CaCl<sub>2</sub> solution, because the total calcium concentration is 5 mM in the former condition and 15 mM in the latter, because of the 3:1 mixing ratio. This means that the total calcium concentration in each condition is 0 mM, 2.5 mM, and 5 mM for 1% agar 0 mM CaCl<sub>2</sub> baths, 7.5 mM, 10 mM, and 12.5 mM for 1% agar 10 mM CaCl<sub>2</sub> baths, and 15 mM, 17.5 mM, and 20 mM for 1% agar 20 mM CaCl<sub>2</sub> baths – there were no conditions whereby the same total calcium concentration was maintained whilst varying the ratio of gel-phase and continuous-phase calcium concentrations. Hence the data does not differentiate between whether failure was a result of the total calcium level being excessive or if the distribution of calcium was the cause. However if the calcium distribution was important it would seem reasonable that failure could occur at a lower total calcium concentration when high calcium content continuous-phase is used compared to the gel-phase's calcium concentration – as this was not observed in the obtained data, it seems unlikely that the calcium distribution matters greatly. The data thus implies that the calcium levels in both the continuous-phase and gel-phase will equilibrate, leading to the conclusion that the respective calcium levels of each constituent is of minor importance compared to establishing good overall crosslinking parameters for good printability.

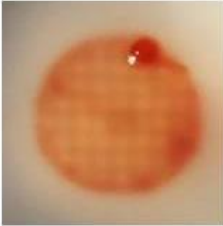
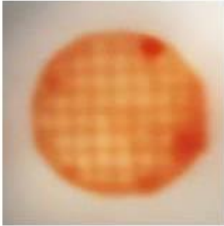

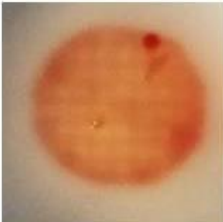
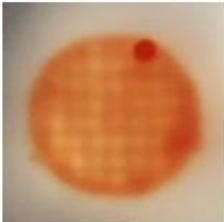
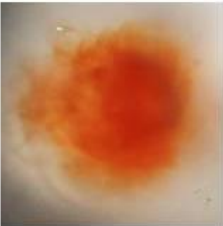
In the case of the dilution of fluid gel systems with calcium in the liquid phase, for most of the cases it would seem that the baths are capable of tolerating total calcium concentrations up to 20 mM when 25g nozzles are used. With this knowledge, the optimised 1% agar/water bath mixed at a 3:1 ratio should confidently be capable of tolerating a range of diluent calcium concentrations such as the levels present in various cell culture media should such a material be incorporated into the mixture for bioprinting experiments.

### ***7.3.2 Impact of mixing ratio on printability with respect to calcium concentration and distribution***

An extended evaluation related to the concentration and distribution of calcium throughout the agar/water support baths would be to consider how the printability varies with the calcium concentration at various dilution ratios. Previous data regarding the







reduction in printability as the agar becomes more diluted without calcium has already been investigated, as has an investigation into the concentration and distribution of calcium between the gel-phase and continuous-phase on its effect on printability into the support bath. By incorporating mixing ratios with both the calcium concentration of the gel-phase and continuous-phase, the relationship between the concentrations of each phase can be varied further.

In this experiment, three agar conditions (1% agar prepared with 0 mM, 10 mM, and 20 mM CaCl<sub>2</sub>) were used as the supportive fluid gel, which were to be mixed in three ratios (3:1, 1:1, and 1:3) with two different concentrations of calcium solution (10 mM and 20 mM). The use of a zero calcium diluent was now disregarded as it was deemed unlikely to provide useful information based on data regarding its use in the earlier experiments. For these experiments, a 25 gauge nozzle was used. The post-print and post-release data for 1% agar 0 mM CaCl<sub>2</sub> baths is shown in figure 7.20 and figure 7.21, the data for 1% agar 10 mM CaCl<sub>2</sub> baths is shown in figure 7.22 and figure 7.23, and the data for 1% agar 20 mM CaCl<sub>2</sub> baths is shown in figure 7.24 and figure 7.25.

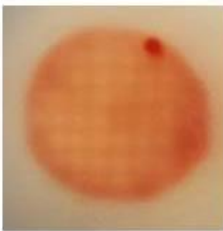
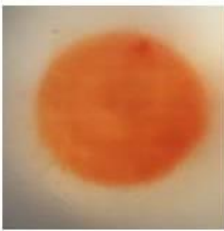

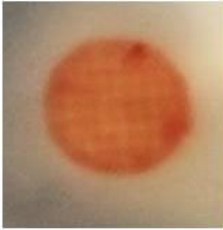


1% Agar 0mM CaCl <sub>2</sub>		Mixing Ratio		
		3:1	1:1	3:1
Water CaCl <sub>2</sub> Conc.	10 mM			
	20 mM			

**Figure 7.20** – Impact of 0 mM CaCl<sub>2</sub> agar fluid gels mixed with 10 mM and 20 mM CaCl<sub>2</sub> at various mixing ratios on macroporous cylindrical structures post-print









1% Agar 0mM CaCl <sub>2</sub>		Mixing Ratio		
		3:1	1:1	3:1
Water CaCl <sub>2</sub> Conc.	10 mM			
	20 mM			



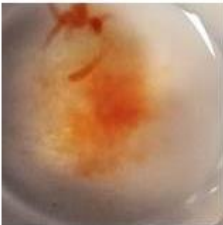



*Figure 7.21 - Impact of 0 mM CaCl<sub>2</sub> agar fluid gels mixed with 10 mM and 20 mM CaCl<sub>2</sub> at various mixing ratios on macroporous cylindrical structures post-release*

1% Agar 10mM CaCl <sub>2</sub>		Mixing Ratio		
		3:1	1:1	3:1
Water CaCl <sub>2</sub> Conc.	10 mM			
	20 mM			







*Figure 7.22 - Impact of 10 mM CaCl<sub>2</sub> agar fluid gels mixed with 10 mM and 20 mM CaCl<sub>2</sub> at various mixing ratios on macroporous cylindrical structures post-print*

1% Agar 10mM CaCl <sub>2</sub>		Mixing Ratio		
		3:1	1:1	3:1
Water CaCl <sub>2</sub> Conc.	10 mM			
	20 mM			

**Figure 7.23** - Impact of 10 mM CaCl<sub>2</sub> agar fluid gels mixed with 10 mM and 20 mM CaCl<sub>2</sub> at various mixing ratios on macroporous cylindrical structures post-release

1% Agar 20mM CaCl <sub>2</sub>		Mixing Ratio		
		3:1	1:1	3:1
Water CaCl <sub>2</sub> Conc.	10 mM			
	20 mM			

**Figure 7.24** - Impact of 20 mM CaCl<sub>2</sub> agar fluid gels mixed with 10 mM and 20 mM CaCl<sub>2</sub> at various mixing ratios on macroporous cylindrical structures post-print

1% Agar 20mM CaCl <sub>2</sub>		Mixing Ratio		
		3:1	1:1	3:1
Water CaCl <sub>2</sub> Conc.	10 mM			
	20 mM			

*Figure 7.25 - Impact of 20 mM CaCl<sub>2</sub> agar fluid gels mixed with 10 mM and 20 mM CaCl<sub>2</sub> at various mixing ratios on macroporous cylindrical structures post-release*

The general trend from the data obtained is that the printability diminishes in accordance with an increase in the total calcium concentration and the mixing ratio of the baths. These outcomes were previously observed when the agar was diluted (a reduction in printability due to diminishing supportive rheology), and during any of the experiments pertaining to the optimisation of the calcium concentration for crosslinking (partially crosslinked ink's tolerable limit to calcium is reduced when the bath's rheology is weaker), thus the newly obtained data is in agreement with prior data.

Due to the relationships between the calcium concentrations of the gel-phase and continuous-phase, the total calcium concentration is held constant whilst the mixing ratio is varied thus provides some information regarding varying the calcium distribution and its impact on the printability and crosslinking into such baths – the conditions where the total calcium concentration was maintained throughout each dilution ratio were 1% agar 10 mM CaCl<sub>2</sub> when mixed with 10 mM CaCl<sub>2</sub> solution and 1% agar 20 mM CaCl<sub>2</sub> when mixed with 20 mM CaCl<sub>2</sub> solution, maintaining a total concentration of 10 mM and 20 mM respectively.

There are also various conditions which share the same total calcium concentration despite being prepared from agar fluid gels and diluents with different calcium concentrations – such conditions are 1% agar 0 mM CaCl<sub>2</sub> with 10 mM CaCl<sub>2</sub> at a ratio



of 1:1 which shares the same concentration as 1% agar 0 mM CaCl<sub>2</sub> mixed with 20 mM CaCl<sub>2</sub> at a ratio of 3:1 (5 mM total concentration), 1% agar 0 mM CaCl<sub>2</sub> at a ratio of 1:1 shares the same total concentration with 1% agar 10 mM CaCl<sub>2</sub> with 10 mM CaCl<sub>2</sub> at all ratios (10 mM total concentration), 1% agar 0 mM CaCl<sub>2</sub> with 20 mM CaCl<sub>2</sub> at a ratio of 1:3 shares the same total concentration as 1% agar 10 mM CaCl<sub>2</sub> with 20 mM CaCl<sub>2</sub> at a ratio of 1:1 and 1% agar 20 mM CaCl<sub>2</sub> with 10 mM CaCl<sub>2</sub> at a 1:1 ratio (15 mM total concentration), and lastly 1% agar 10 mM CaCl<sub>2</sub> with 20 mM CaCl<sub>2</sub> at a ratio of 1:3 shares the same total concentration as 1% agar 20 mM CaCl<sub>2</sub> with 10 mM CaCl<sub>2</sub> at a ratio of 3:1 (17.5 mM total concentration). However when studying the post-print and post-release data for similar total calcium concentrations, the results are heavily varied in that the same total calcium concentration can result in print success or print failure and correlates with the corresponding mixing ratio. As discussed earlier, the more diluted the bath, the more likely print failure will occur due to the relationship between the bath's rheology and the crosslinking strength; when the bath is weak the bath yields first and is unable to facilitate good depositional qualities, and when the bath is stronger the ink yields first, separating successfully from the nozzle outlet and thus good printability is achieved. Therefore a just comparison between similar total calcium concentrations cannot be made because of the differences in the mixing ratios, meaning that relative successes or failures are more likely a fault of the bath's rheology and not related to the distribution of calcium in the gel-phase or continuous-phase.

With the prior point in mind, the only conditions which share the same total calcium concentration and mixing ratios are: 1% agar 0 mM CaCl<sub>2</sub> with 20 mM CaCl<sub>2</sub> shared by 1% agar 10 mM CaCl<sub>2</sub> with 10 mM CaCl<sub>2</sub> (1:1 ratio and total concentration of 10 mM), and 1% agar 10 mM CaCl<sub>2</sub> with 20 mM CaCl<sub>2</sub> shared by 1% agar 20 mM CaCl<sub>2</sub> with 10 mM CaCl<sub>2</sub> (1:1 ratio and total concentration of 15 mM). Both structures printed and released when the total calcium concentration was maintained at 10 mM were successful, whereas both structures printed at a ratio of 1:1 and 15 mM total calcium concentration failed at the printing stage. Comparing both structures printed at a 1:1 ratio and 10 mM total calcium concentration, the structure printed into the 1% agar 0 mM CaCl<sub>2</sub> bath with 20 mM CaCl<sub>2</sub> solution appeared to be printed at a higher quality than the structure printed into the 1% agar 10 mM CaCl<sub>2</sub> with 10 mM CaCl<sub>2</sub> solution which exhibited some minor loss of print quality; in this case there is a minor implication that the calcium content within the continuous-phase is more significant than the calcium in the gel-phase, but given that both structures were printed and

released successfully with only a slight difference in print quality, and with only two pairs of conditions for comparison makes this a weak and unlikely claim overall.

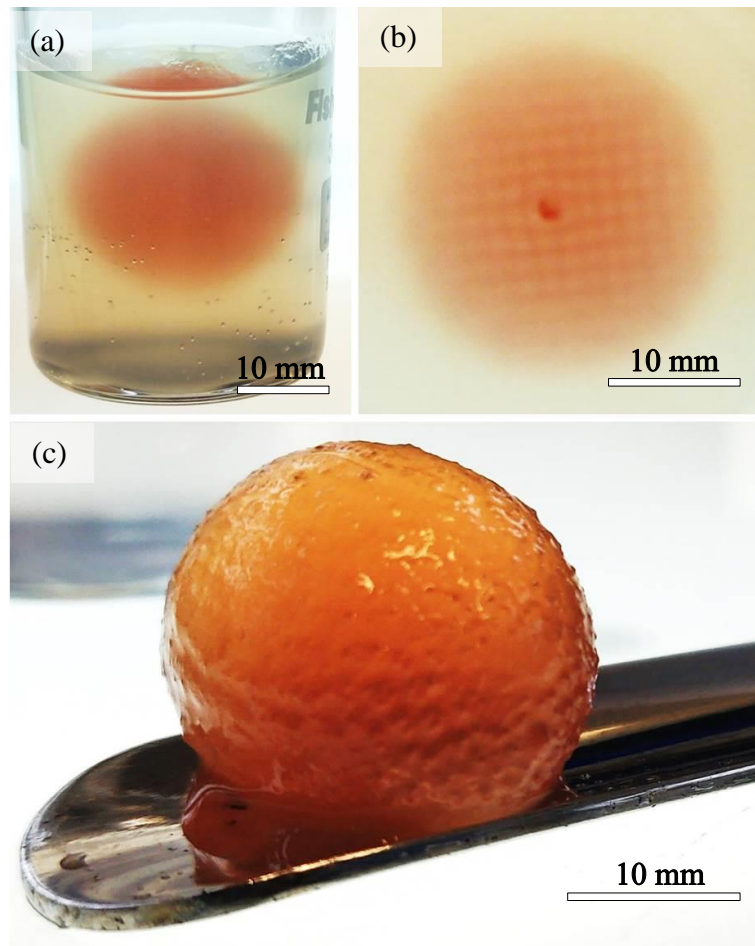
With the data obtained from this experiment and chapter 7.3.1 Printability assessment into fluid gel 3:1 mixtures with respect to calcium distribution and concentration in the gel- and continuous-phases, it is far more likely that the distribution of calcium between the gel- and continuous-phases does not matter and is less important to consider than the bath's total concentration and overall supportive rheology. In a practical sense, this could mean that calcium could instead be mixed with the baths after the agar has been blended into microparticles, instead of being added with the agar powder at the initial gel preparation stage. The practical difference that this makes is not likely significant, and it was still preferential to include the calcium with the agar powder at the initial preparation stage; subsequent blending ensures that the calcium is well mixed and dispersed throughout the bath anyway. In terms of technical difference, the agar gel itself might be prepared with greater clarity as the presence of salts in gelling media could incorporate some undesired turbidity – any differences in clarity between agar gels with and without calcium was not examined in this study.

#### **7.4 Capability of Agar Fluid Gel/Water Mixtures to Facilitate Complex Structure Fabrication**

To highlight the capability of the developed support baths in the context of complex 3D printing, a variety of challenging anatomical structures were printed into the baths to show their functional viability as a good quality support bath which could be adopted for use in bioprinting applications. The printed models utilise a macroporous approach, setting an infill density and printing orthogonally aligned layers generally without perimeters unless deemed necessary for overall detail. Printing structures in the macroporous manner may promote more efficient crosslinking deep within structures to ensure the inside is as strong as the outside.

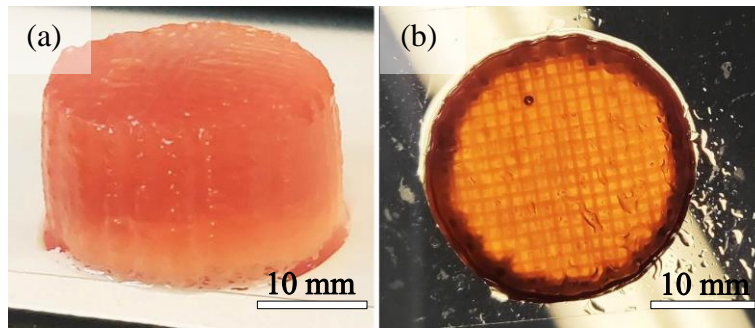
Shown in figure 7.26 is a sphere which consists entirely of orthogonally aligned rectilinear layers without any perimeters. The roundness of the structure is maintained by printing the structure with a moderately high infill density and having both crosslinked material as well as residual agar remaining within the pores of the structure. The structure can be observed whilst within the supportive gel, and when inspected closely the rectilinear mesh detail can be seen on account of the developed agar fluid gel's reasonable translucency. Printing spherical structures without an adequate

supportive strategy in place is quite unfeasible with soft hydrogel inks because of the tendency for the material to spread laterally under loading from upper layers and lacking mechanical strength. In the context of cell seeded scaffolding biofabrication approaches, printing rounded scaffold structures in this way with the developed agar fluid gel could potentially be a viable method to replicate organs like the eyes or testicles.



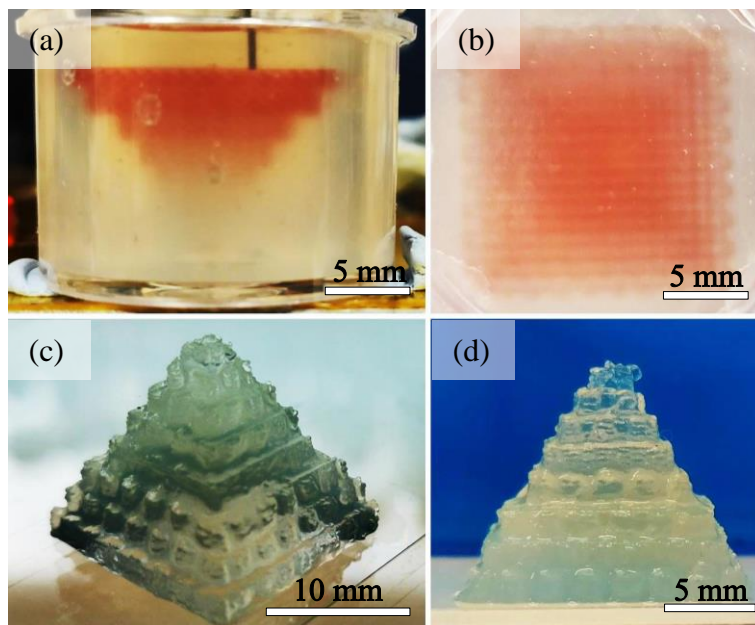
**Figure 7.26** – Macroporous sphere printed into the developed agar fluid gel/water support bath at 3:1 mixing ratio, shown (a) suspended within the support bath, (b) top-down view showing with visible pores, (c) structure after release

Figure 7.27 shows a cylindrical structure printed in the macroporous manner. The structure is relatively wide and thick and printed with a moderately high infill density to produce the structure with residual agar trapped within the printed mesh. Such structures could potentially be used to model bone tissue for example, utilising cell-laden bioinks and cell-seeding strategies with control over the mesh size to approximate the bone's porous structure.



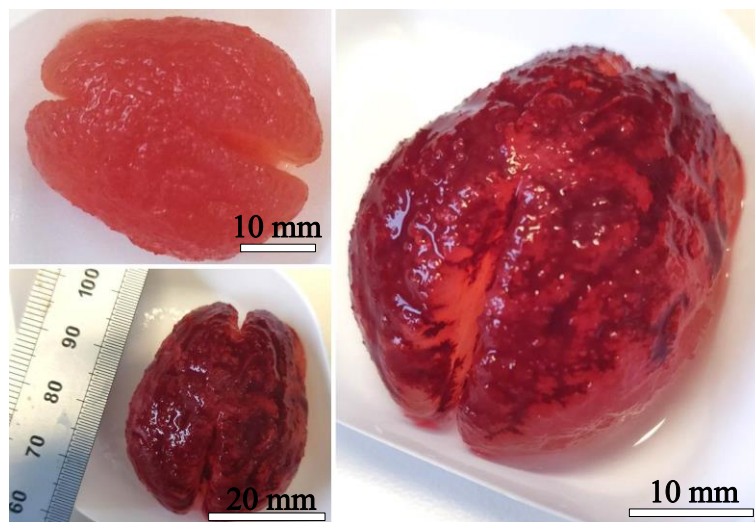
**Figure 7.27** – Cylindrical structure post-release from the developed agar fluid gel/water support baths at 3:1 mixing ratio, shown (a) self-supporting with residual fluid gel trapped inside, (b) held under a light to makes pores visible

As shown in figure 7.28, a stacked pyramid structure was printed upside down from the tip to the base. The tip of the pyramid consists of a small square cross-section which gets increasingly larger with each subsequent step of the structure. Again, a rectilinear infill pattern with moderately high infill density was used to maintain the structural strength as well as trap some residual agar within the mesh, creating a composite alginate/agar fluid gel structure. As can be seen each step is distinctly defined even without the use of any perimeter lines for edge detail, and the strength of the structure is sufficient for the pyramid to retain its geometric detail.



**Figure 7.28** – Stacked pyramid structure shown (a) printed in an inverted orientation, (b) top-down view post-print, (c) isometric view of released structure, (d) front view of released structure

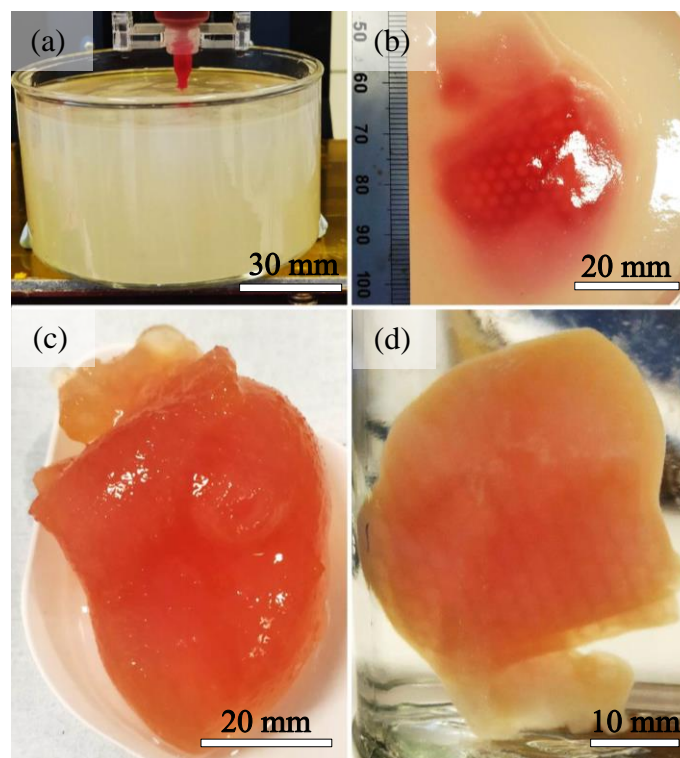
A scaled model of the human brain was chosen for support bath printing because it has a very complex surface morphology in the form of all the folds which make up the brain's soft tissue structure – such folds were replicated successfully as shown in figure 7.29, with the folds themselves being visually emphasised by adding some red dye on top of the structure which pools in such regions. As the model itself was scaled down to match the printer's extruded material volume capabilities, the resolution of a 30 gauge nozzle was necessary to maintain as much print detail as possible. With that being said a real brain would be significantly larger than the printed model shown as well as being having a lower elastic modulus than the than the partially crosslinked alginate ink used; such barriers could be overcome by using a larger extrusion system with sufficient volume to print at the required scale and printing into an appropriately large supportive agar fluid gel bath which can gently suspend very weak bioinks as they develop into soft brain tissue.



*Figure 7.29 – Human brain model printed within developed agar fluid gel/water support bath at 3:1 mixing ratio; red dye is added to highlight the brain's morphology*

The final structure to be demonstrated as printed from the developed agar fluid gel baths was a model of the human heart (figure 7.30). This model was the largest to be printed with the developed 3D bioprinter and required the extrusion of all the stored material within a completely filled 10 cc syringe barrel; the 10 cc capacity is a current limitation of the developed bioprinter's extrusion system and is restricted by the extruder housing's dimensions. The honeycomb infill pattern was used to help maintain the strength but a lower infill density was used to reduce the extruded material volume per layer without reducing the strength too much – by reducing the amount of extruded

material per layer, the saved material was instead used to maximise the scale of the model. The reduction of infill density can be observed whilst looking at the heart whilst it is immersed in water – the hexagonal holes can be seen through the perimeter walls and the pores are larger than observed in previously printed structures for this reason. The model of the heart contains internal cavities which resemble the chambers of the heart for pumping blood, which is connected in the model to the interior vena cava – whilst the internal network is modelled in such a way that fluid flow could be achieved through the heart, perfusion was not conducted in case of accidental damage to the structure as extra force would be necessary to wash out the residual agar fluid gel inside the chambers. Along its biggest axis the printed heart was approximately 60 mm long – comparing this to the size of a real adult human heart, which can be approximated to be around the size of one’s fist, the printed heart is close to around half the size of a real human heart. A printer with a greater ink capacity should be able to print a full sized heart using the developed agar fluid gel support bath, which would show that support bath technology could be used to address the issues regarding the scalability of biofabricated soft-tissue structures.



**Figure 7.30** – Human heart model printed within the developed agar fluid gel/water support baths at 3:1 mixing ratio, shown (a) the large support bath, (b) top-down view of the heart post-print in a horizontal orientation showing its internal honeycomb infill structure, (c) heart successfully released from its support, (d) heart immersed in water



## 7.5 Summary

An important note to consider with regards to support baths is to remember that a one-size fits all approach is unlikely to cater for all the intricate aspects of biofabrication. When considering that two major challenges facing the technology are scalability of fabrication and provision of nutrients to printed cells throughout the entire fabrication process, the developed agar support baths looks to be a solution to both. Demonstrated in Chapter 6 – Supported Fabrication of 3D Structures within an Agar-Agar Fluid Gel Medium, the use of a purely agar fluid gel medium was shown to be applicable for fabrication purposes with good resolution and shape fidelity which could improve the scalability of the technology; whilst this is helpful from a traditional 3D printing standpoint, it offers nothing more to cater to the needs of bioprinted cells. Remembering that cells are taken out of their most hospitable environment when loaded into a syringe barrel for 3D bioprinting, they remain outside their ideal environment without nutrition when they are deposited into a support bath. Therefore improving the scalability of 3D biofabrication solely through the provision of a mechanically supportive bath is rendered moot when considering the time to print large scale structures would likely lead to loss of cellular viability. Hence supportive baths need to do more than merely provide mechanical support to printed structures; they also need to biologically support the extruded cells too. To date, the only known technique to actively incorporate cell culture media with the support bath involves the use of Carbopol [128] which is restricted to media without divalent cations due to its instability.

Establishing that the initial agar support baths could retain their suspensive and supportive qualities after dilution is an important development towards catering to a wider range of supportive needs for 3D biofabrication. Showing that the agar fluid gel constituent can be diluted by at least a quarter whilst maintaining good printing and supportive qualities with water, CMC, or GG opens up the possibility for mixing the fluid gel with many other materials. When the agar fluid gel constituent is the dominant constituent of the mixture, good qualities are maintained; stronger agar concentrations are necessary to retain good support bath qualities at greater dilutions. Of the three diluents considered, lower viscosity options like water tended to maintain better printability compared to more viscous or thixotropic materials such as CMC and GG - however the loss in printability only started to become prevalent when the dilution ratio was 1:1 and 1:3 of agar to diluent. Specifically for bioprinting, the ability to incorporate

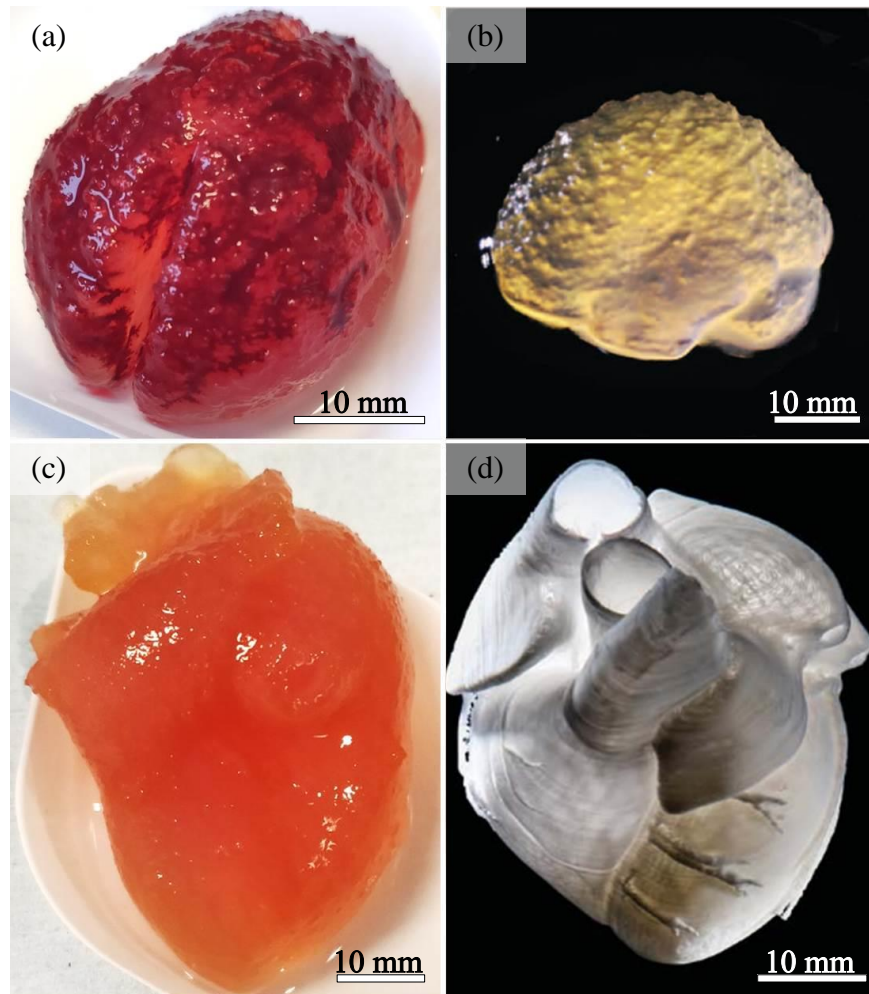
a diluent as a secondary material could be highly beneficial for incorporating biological support in the form of using cell culture media as the diluent of choice. Given that the viscosity of cell culture media is low, similar to water, it stands to reason that the biological support could synergise effectively with the mechanical support provided by the agar fluid gel.

With the intention of adding cell culture media to the developed support baths, experiments were conducted to evaluate if the presence of calcium in the continuous-phase diluent would cause any detriment to the printability. This question had arisen based on the range of cell culture media solutions available, many of which contain calcium chloride in various small amounts which may be significant to the relatively sensitive protanal alginate ink used. The experiments themselves tested the printability into the support bath whilst varying the concentrations and distribution of calcium ions between the gel-phase and the continuous-phase, as well as queried the impact of calcium at the various dilution ratios investigated. The results of these experiments suggested that the distribution of calcium did not matter for a given dilution ratio and that the total calcium content was most likely the determining factor for successful printability. Therefore it is quite likely that cell culture media could be successfully incorporated with the agar fluid gel to help address two major biofabrication challenges: increasing the scalability of the technology and providing a means to keep printed cells fed and viable throughout the process.

The fact that the agar fluid gels could be diluted to alter the bulk properties of the support baths without compromising the fabrication capability is promising for further work. The print quality of structures fabricated using the developed agar fluid gel/water mixtures is compared with the current state-of-the-art techniques below in figure 7.31. It can be argued that the developed agar fluid gel support baths are capable of printing structures of equal or similar quality to structures printed using FRESH V1.0 support baths; however the print quality has been improved significantly with the advent of FRESH V2.0 which is greater than the developed agar fluid gel baths. The increase in print quality is likely related to the technique's divergence from the older mechanical breakup approach with a blender. As reported in the literature, FRESH V2.0 produces gelled microparticles which are uniformly spherical in morphology and smaller in size due to the new coacervation technique [136]. Additionally, it is speculated that such microparticles should be produced more reliably than those from FRESH V1.0. Therefore a new question is proposed: could the agar fluid gel support baths see a



similar increase in print quality by changing the method of microparticle production from mechanical breakup with a blender to a sheared gelation approach similar to Moxon et.al [133]? Despite this, the use of agar as a support material has the advantage of being thermally more stable than the gelatine used in both of the FRESH methods which could help maintain physiological temperatures during printing for prolonged periods, although the process of releasing structures from agar fluid gels remains much more cumbersome than both of the gelatine-based FRESH methods.



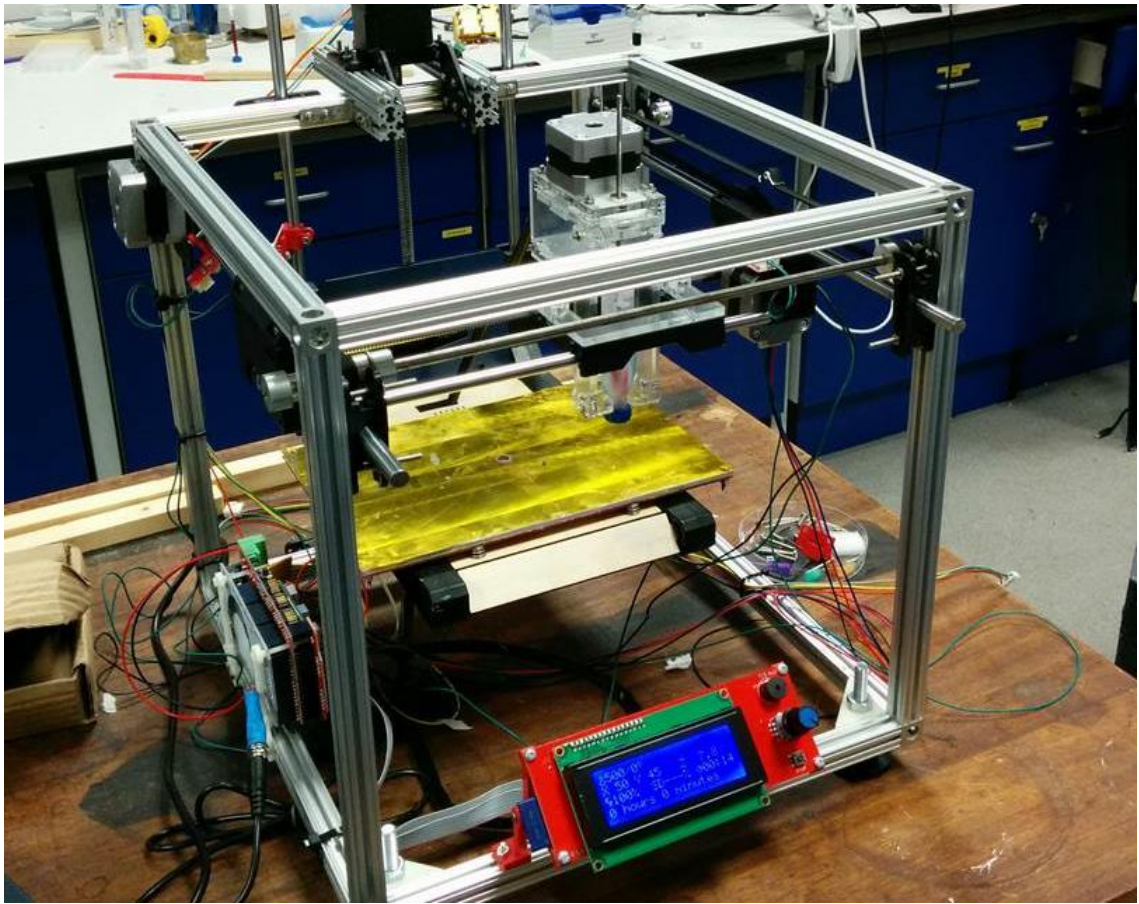
**Figure 7.31** – Comparison of a brain printed into (a) the developed agar fluid gel and (b) FRESH V1.0 [134], (c) and a heart printed into the developed agar fluid gel and (d) FRESH V2.0 [136]

## Chapter 8 – Conclusions and Future Perspectives

### 8.1 Conclusions

The work documented within this thesis centred on the development of support bath strategies which could: (1) reliably suspend cell-laden low-viscosity bioinks, (2) support the printing of complex anatomical geometry, (3) print with a high resolution, (4) using a bath which is prepared in a simple, easy to follow and reproducible manner whilst (5) being capably separated from the printed construct with minimal risk to the structural integrity. Having established these key objectives, two support baths were developed to address a fundamental biofabrication challenge; creating anatomically relevant, complex structures with appropriate mechanical properties at relevant scales using highly cell-compatible bioink conditions. The two developed support baths, a quiescently gelled gelatine-based support bath and an agar-derived fluid gel support bath, were shown to be capable of supporting the fabrication of complex structures which would otherwise be unfeasible to print without such a supportive strategy in place and hence may be beneficial technologies for further biofabrication research.

To test the suitability of the developed support baths based on these five criteria, a DIY custom, Reprap-inspired extrusion-based 3D bioprinting platform was developed as described in Chapter 4. The developed bioprinter was largely modular by its design and was leveraged for experimental bioprinting research using a plethora of open-source resources that exist online within the communities of 3D printing enthusiasts. The bioprinter comprises of many standardised components common in the design of RepRaps such as NEMA 17 stepper motors, GT2 profile belts and pulleys for X/Y planar motion, a tr8\*8(p2) profile leadscrew for the Z-axis, and an Arduino-based microcontroller board (RAMPS 1.4). The developed bioprinter may be considered custom on account for swapping out the thermal extruder, commonly seen in RepRaps for plastic deposition, in favour of a screw-plunger design with a 10 cc syringe barrel based on the Fab@Home extrusion system - a method which is highly suited for the extrusion of high and low viscosity inks or soft hydrogels such as cell-laden bioinks. Overall the printer performs well and is able to conduct essential 3D printing operations with a positional resolution of (theoretically) 12.5 microns along the X and Y axes, 2.5 microns in the Z-axis, with a minimal depositional volume of approximately 30 nanolitres in conjunction with the 10 cc syringe barrel. The completed developed 3D bioprinter is shown in figure 8.1.

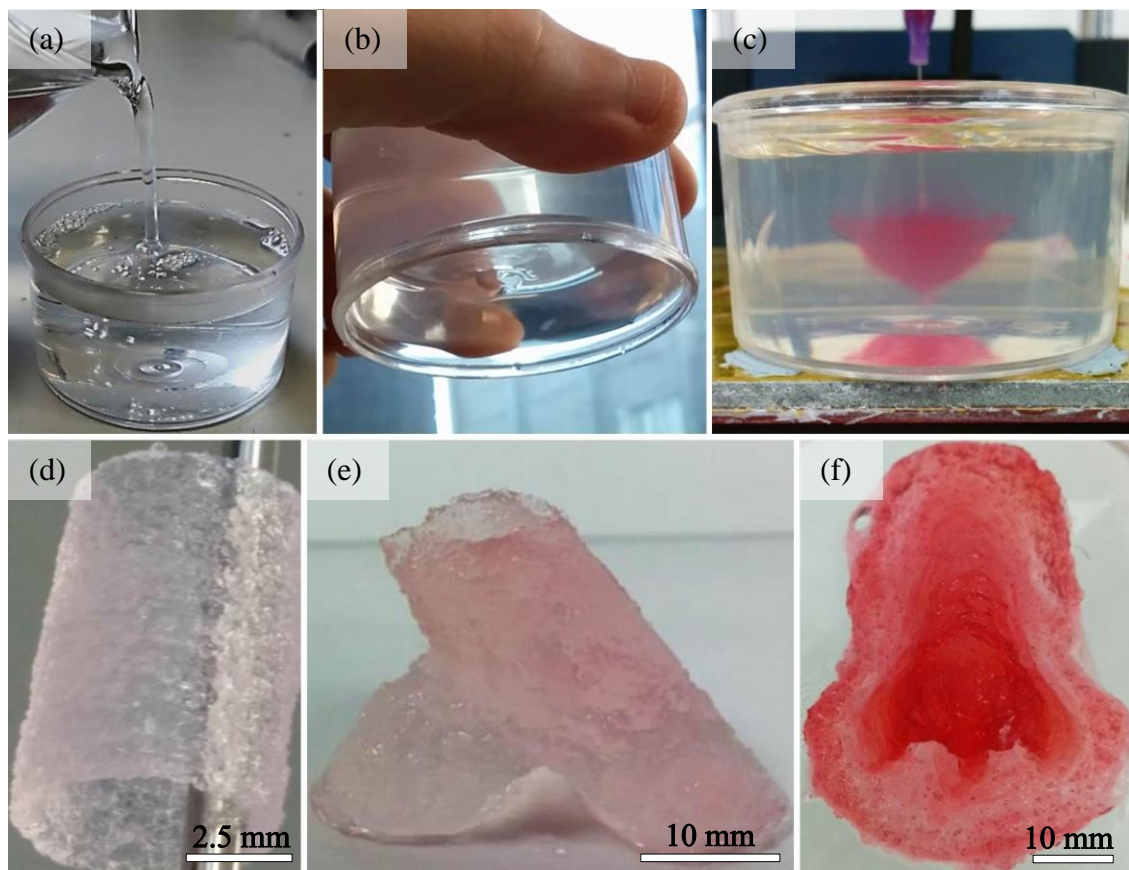


*Figure 8.1 – Photograph of the developed RepRap-inspired 3D bioprinting platform*

The two supportive strategies developed in this thesis are the quiescently gelled gelatine-based support bath and the agar-based fluid gel support baths. The capability of these baths to satisfy the five established criteria of a highly functional support bath will be concluded in turn.

The quiescently gelled gelatine-based support bath documented in chapter 6 has been shown to capably support the extrusion of cell-laden bioink and thus meets criterion (1). The baths were capable of facilitating the fabrication of some technically challenging features such as divergent/convergent surfaces, overhangs, hollow internal networks, and demonstrated the fabrication of a nose and thus satisfactorily meets criterion (2); however further experiments did not go on to further explore more challenging anatomical geometries. Whilst the properties of the bath was appropriate to allow for a high resolution 30 gauge nozzle (i.e. 160  $\mu\text{m}$  inner diameter) to permeate the gel, the resolution of printed structures was retrospectively not of the same standard as those fabricated with the agar fluid gel method due to the prevalence of a surface quality defect termed ‘fluff’ in this thesis, and thus criterion (3) was arguably met less satisfactorily. The gelatine baths however excel in criteria (4) and (5) due to being

prepared in the most simple manner with a straightforward and gentle thermal release mechanism. Other experiments with these baths sought to allow better rheological control and integrate a coaxial nozzle-based printing strategy, but were less successful on account of unfavourable interactions and unsuitable bath qualities respectively. A pictorial summary of quiescently gelled gelatine-based support baths is shown in figure 8.2.

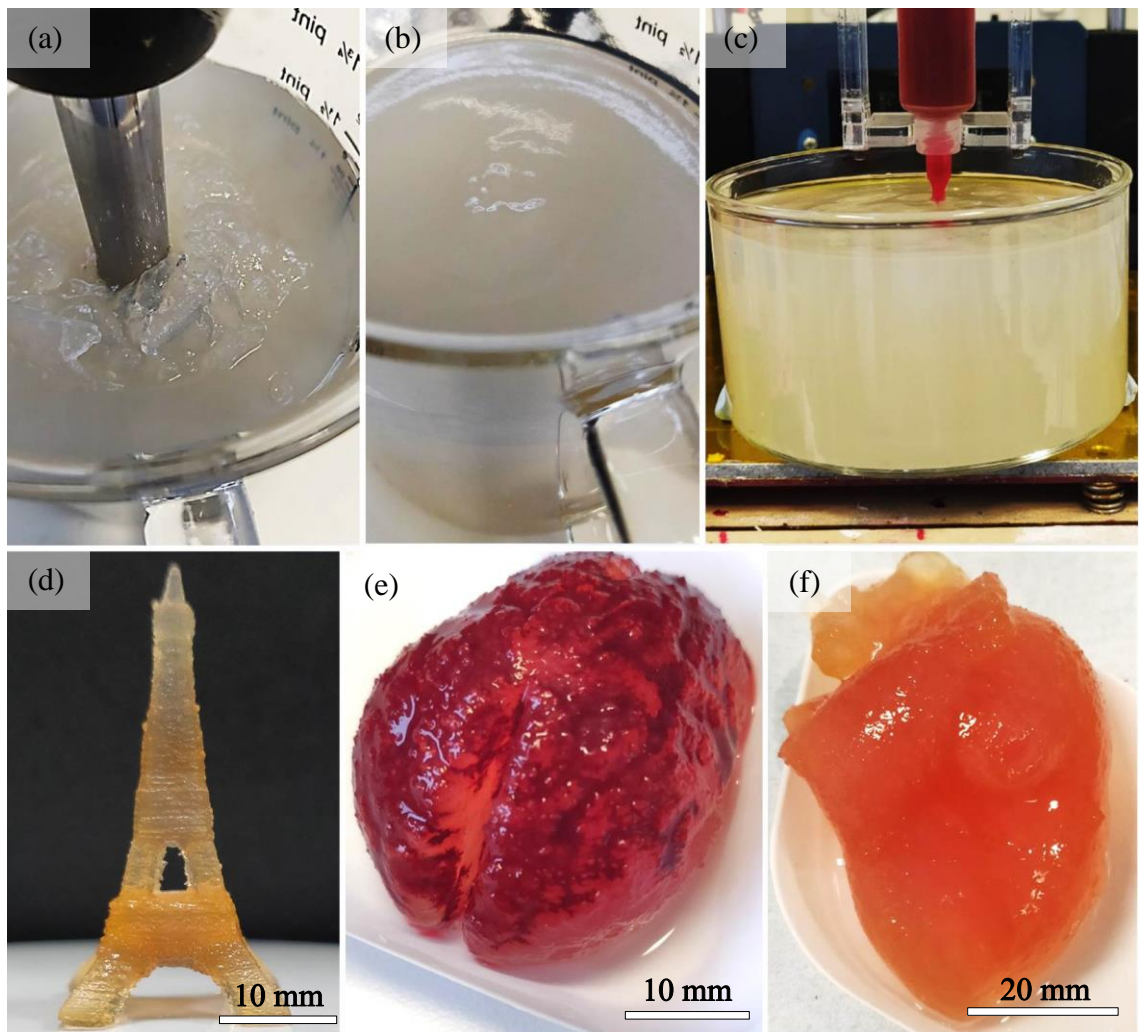


**Figure 8.2** – Overview of gelatine bath process: (a) gelatine solution is poured into a container and stored in a fridge, (b) once gelled, 0.8% w/v gelatine baths will be invertible and exhibit elastic-dominant behaviour, (c) printing into such baths can produce (d) thin tubes, (e) branched blood vessel-like structures, (f) and noses

The agar-based fluid gel support baths documented in Chapter 6 – Supported Fabrication of 3D Structures within an Agar-Agar Fluid Gel Medium are capable of suspending extruded inks within the medium; however the extrusion of cell-laden inks into such baths has not been shown in the work documented within this thesis and thus criterion (1) was not fully met. However the agar fluid gel baths have shown themselves to be exceedingly impressive in terms of the range of printable, geometrically complex structures, both anatomically and otherwise, and can do so with



the highest resolution nozzles available (30 gauge) without the development of surface quality defects, thus satisfying criteria (2) and (3). The preparation of agar fluid gels remains arguably as simple as it can be – the parameters for blending gelled agar pucks in this thesis may open to interpretation, but it remains simpler than the FRESH method. The user need not worry about blending too strongly or for too long as agar gels are thermally much more stable than gelatine, thus it is unlikely that the preparation process will fail and hence satisfies criterion (4). The retrieval of printed structures from agar fluid gels however is not as straightforward as simply liquefying the material like gelatine, and relies on the user's ability to delicately separate the fluid gel from the structure manually by jetting water around the structure. The difficulty or ease of doing this depends on the user's ability to do so and also on the mechanical properties of the fluid gel and crosslinked structure. Therefore criterion (5) is satisfied, but not to the same degree as the gelatine-based support baths. Other experiments with the agar fluid gels conducted in Chapter 7 – Agar Fluid Gels with Enhanced Tuneability for Further Engineering Control sought to provide further rheological control by means of controlling the volume fraction of gelled microparticles within the medium by means of diluting the fluid gel with a secondary solution. These experiments were successful and found that a low-viscosity secondary solution like water was better than highly-viscous or shear-thinning materials for rheological control with minimal compromise to other support bath success factors, the results of which has potential for future work. A pictorial summary of agar-based fluid gel support baths is shown in figure 8.3.



**Figure 8.3** – Overview of agar fluid gel support bath process: (a) gelled puck of agar is blended (b) until smooth and may be mixed with a secondary solution or used as is and (c) poured into a container for printing structures like (d) Eiffel towers, (e) human brains, (f) and human hearts

As both developed baths are capable of supporting the fabrication of structures using a low-viscosity, low concentration bioink, a comparison of the main qualities of each bath is surmised in table 8.1 and highlights various factors which a bioengineer may need to consider prior to choosing the most appropriate supportive strategy for bioprinting applications.

**Table 8.1** – Comparison of developed gelatine and agar support bath characteristics

	Gelatine Baths	Agar Fluid Gel Baths
Cell compatibility	Compatible with cells throughout print and release process	Bioprinting study not conducted
Print quality/ resolution	Using 30 gauge (160 µm) nozzles, structures have smooth bottom surfaces and rough top surfaces due to ‘fluff’ defects	Produces very high quality structures with 30 gauge (160 µm) nozzles
Preparation	Mix gelatine powder with water and heat (~60° Celsius) until dissolved, pour gelatine solution into container, store container in fridge for 12+ hours to gel	Mix agar powder with water and heat (>90° Celsius), leave to cool to initiate gelation, blend once gelled to fluidise the gel
Release Process	Thermally separated by melting the gel at 37° Celsius	Mechanically separated by washing away the fluid gel
Clarity	Clear/transparent	Slightly opaque
Options for rheological control	Small range of printable gelatine concentrations, poor stability with other biopolymers (GG, CMC)	Rheological control achievable via agar concentration, dilution ratio, and blending parameters, is stable with tested biopolymers (GG, CMC) but performed best when diluted with water

## 8.2 Future Perspectives

The work detailed in this thesis has successfully explored the potential of developing supportive strategies that are capable of fabricating highly complex anatomical structures from soft tissue-like materials. However there exists several opportunities for further development which could help project the technology further within the field of bioprinting, and perhaps even towards the fabrication of full-scale organs. Such opportunities include:

- The integration of multiple printing modalities with multi-material fabrication within the 3D bioprinting system. Whilst the printing of a single bioink into

supportive media was conducted in this work, the transition towards functional organs requires the fabrication of multi-cellular structures, the fabrication of which implies the use of additional printing nozzles. Extrusion-based bioprinting modalities can print large volumes reasonably quickly and attain print resolutions to around 100  $\mu\text{m}$ , but the fabrication of smaller cellular elements within larger constructs may benefit from the incorporation of, for example, droplet-based bioprinting technologies which can operate layer-by-layer alongside the extrusion-based approach.

- The integration of cell culture media within the preparation of agar fluid gel support baths. Based on the diluted agar fluid gel experimental data, the water used as the secondary solution could be replaced by cell culture media. This could create baths of a twofold supportive strategy: mechanical support and biological support. This could translate to longer printing times whilst retaining printed cell viability and potentially allow for technological scale up.
- The integration of a heating element/enclosure to retain physiological temperature during and after printing. Currently the bioprinter operates without a heated platform which inevitably means that there exists a time limitation before the cells begin to die. A heated platform may be an unfavourable solution as a temperature gradient between platform, the bath, and surrounding environment will exist and thus a uniform temperature may be difficult to maintain; however a heated platform would be beneficial for liquefying gelatine baths post-printing. An enclosure with a dedicated heating element to steadily control the temperature of the bioprinting environment could allow for technological scale up by maintaining physiological temperature for the cells before, during, and after printing.
- Increasing the bioprinter's fabrication scale - this accounts for both the extrudable material volume contained within the syringe barrel and also the available volume within the printer's bounds to create larger structures. A current restriction of the current bioprinter's design is the inability to use syringe barrels of sizes different from 10 cc. The largest structure printed with this syringe was the heart which was approximately 60 mm along its biggest axis,

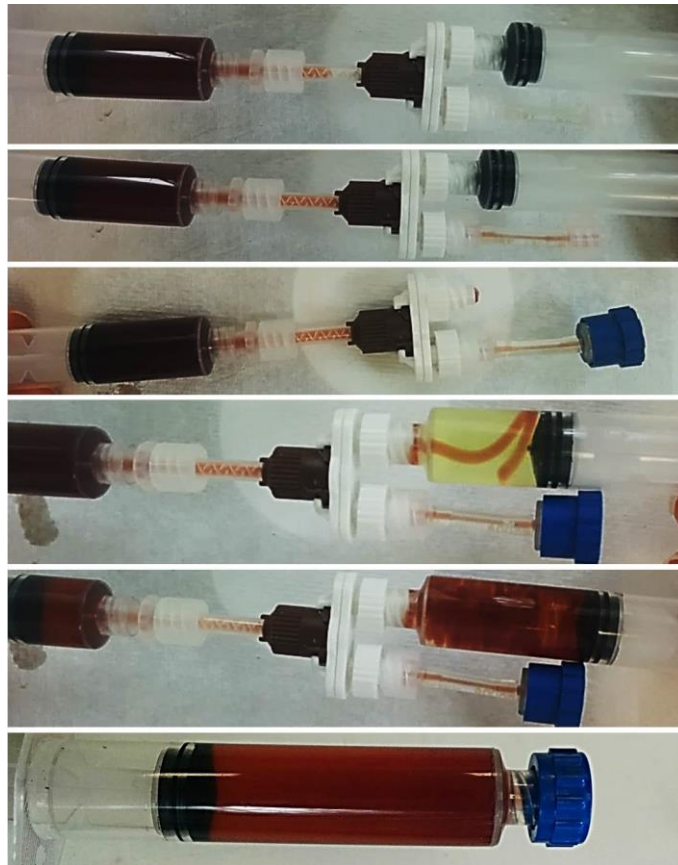


which is not large enough to resemble the scale of hearts found in human anatomy. Thus a larger capacity extrusion system would enable the fabrication of larger structures of more relevant anatomical scale. This would simultaneously require a proportional increase in the printer's size in order to fit a large enough support bath underneath the extruder.

- Co-culture printing by incorporating cells within the fluid gel network itself. As agar is biologically inert, its fluid gels could be mixed with cells to suspend them within the bath during printing. Although this would require an extortionate number of cells, there is an opportunity to bioprint cell-laden bioinks into a cell-laden support bath. By incorporating the macroporous printing strategy it has been shown that it is possible to trap fluid gel within such structures, thus it may be possible that the trapped fluid gel within the structure could contain cells. Hypothetically, endothelial cells could be incorporated within the fluid gel bath, which once trapped inside a structure could form vascular networks.

## Appendix A – Mixing Material with the Cellink Cellmixer Unit

The process of using the Cellink cellmixer as effectively as possible is shown in figure A.1 using partially crosslinked 2% protanal alginate and green dye solution to illustrate the method without cells. The unit is designed to help mix cells/media with bioink, but almost any two materials can be mixed together in this manner - materials not advised for mixing in this manner are those which crosslink together, such as alginate and  $\text{CaCl}_2$ , which could block the flow of material through the unit with no simple method of removing the blockage. This method is better suited for mixing greater volumes of bioink rather than small volumes due to the unit's dead volume of 0.5 ml. This limits the feasibility of preparing high cell-density, low-volume bioinks as the 0.5 ml dead volume becomes proportionally more significant.



**Figure A.1** – Process of effective hydrogel mixing with Cellmixer unit: (a) hydrogel is dispensed to force air out of unit, (b) one channel is blocked to allow hydrogel flow into other channel, (c) other channel is blocked to allow hydrogel flow into primary channel, (d) cell-laden syringe (green dye solution in figure) is fitted onto unit and filled with hydrogel, (e) material passed through unit multiple times (f) for homogeneous mixing

Firstly a half-filled alginate syringe is fitted onto the single outlet side of the unit. On the double outlet side, an empty syringe barrel and some microfluidic tubing with a male luer lock adaptor are fitted. With the empty syringe fully depressed to prevent material flow into that particular outlet, material is then transferred from the alginate syringe into the microfluidic tubing's outlet and forces out any air within that channel of the of mixing unit. With a cap now fitted onto the end of the microfluidic tubing, this channel is now blocked and restricts further material flow through this outlet; removing the empty syringe barrel opens up material flow through the other outlet, thus more alginate is pushed through the unit which displaces any remaining air within the unit out of the second outlet. With all air trapped internally within the mixing unit now displaced, a half-filled syringe filled with the second solution (lightly green dyed water, cells/media, etc.) is then fitted onto the open outlet whilst ensuring that as much air has been displaced out of the syringe as possible. The contents of the alginate syringe are then transferred across into the secondary material's syringe. Both syringes were only half-filled as to avoid accidental overfilling of either syringe, as the contents of one half-filled syringe when passed entirely into another half-filled syringe with the same capacity will completely fill the syringe. With the syringes at either side, the two materials can be passed back and forth which forces the materials to mix together homogeneously inside the spiralled mixing chamber. Multiple passes are needed to ensure complete homogeneity is achieved, of which the homogeneity can be deduced most easily by examining the mixture closely when dyes are used to add colour the materials; the colour of the mixed ink should be uniform throughout, else more mixing is required. Once all the material has been sufficiently mixed and loaded into a single syringe, the contents may then be transferred slowly into the bioprinter's syringe barrel using a female luer lock adaptor, after which the syringe barrel is loaded into the machine to begin printing.

## **Appendix B – Using Excel for Spiralling Structure G-code Generation**

In certain applications, it may be more desirable to have a 3D printer which operates with a continuously moving Z-axis instead of the traditional ‘start and stop’ characteristics exhibited by traditional layer-by-layer fabrication. Such an approach can be adopted by manually writing the g-code itself but can be a time-consuming process, particularly if an error related to the g-code is acknowledged during printing which then requires the user to read through the code to find the mistake. In an attempt to accelerate the g-code writing process, Excel was used for partial automation of the most tedious code-writing elements.

This g-code generating spreadsheet takes a series of input parameters and processes them through some equations to calculate positional data along the X, Y, and Z-axes. Afterwards, the generated data is manually copied and pasted over to another spreadsheet which takes that raw numerical data and combines it with machine/axis operators (such as G, X, Y, Z, E, F) in a particular order and recompiles everything together as a single unified list of code which can then be copied and pasted into a blank text document and saved with the extension “.gcode” using Microsoft Notepad. Changes to the g-code can be made quickly by editing the input parameters and repeating the two copy-and-paste processes, which can save a lot of time compared to manually writing several hundred lines of code.

The described spreadsheet is set up to generate data for a simple circle along the X/Y plane, which is projected as a spiral with the addition of Z-axis data. This spreadsheet however is only set up to create simple circular/spiralling geometries; data for other simple geometries cannot be readily created using this spreadsheet and would require setup on an individual basis.

### **B.1 Generating positional data for the x- and y-axis**

The Excel spreadsheet was set up to create data points in the X- and Y-axes for a single and simple geometric shape, the circle, which combining the obtained data points for the X- and Y-axes with some Z-axis data, the circle propagates into a 3D shape that resembles a spiral. The manner in which this spreadsheet was set up to generate custom g-code

To overcome the perceived restrictions of Slic3r in the context of extruding material through the coaxial nozzle’s core using the bioprinter, custom g-code was written with the use of Excel to formulate the data points necessary in the X, Y, Z, E (extruder) axes,

F to set the speed, and G to set the command. For testing the feasibility of coaxial printing into the gelatine support baths, a simple spiralling tubular construct was planned for fabrication. The idea was that the structure could be perfused at an inlet situated at the base of the structure and the pressure would drive the liquid up along the inside of the structure in a spiral path and leave at an outlet at the top. The g-code was generated in four steps: determining the X/Y points, determining the Z points, setting a reasonable F value and finally choosing reasonable E values.


Information about the desired circle radius and the number of data points per circle revolution is the required input parameters to generate the X- and Y-axis positional data. This data is used to apply Pythagorean trigonometric identities (equations (B.1) and (B.2)) to calculate the relative lengths of X and Y which corresponds with their respective coordinates for a circle centred around (0, 0) and for a given angle generated by the number of data points per circle. To ensure that the generated data points are correct and indeed lie on the circle's perimeter, the data may be checked by the equation of a circle centred around (0, 0) (equation (B.3)).

$$X_{Coordinate} = r \sin \theta \quad (B.1)$$

$$Y_{Coordinate} = r \cos \theta \quad (B.2)$$

$$(X - a)^2 + (Y - b)^2 = r^2 \quad (B.3)$$

In the spreadsheet (figure B.1), the formulae for calculating the X and Y coordinate data is dragged down manually to fill as many lines as necessary to complete a single revolution of the circle – in the case above the number of steps per revolution is set to 100 and means that a set of X/Y coordinates is generated every 3.6 degrees; therefore 100 lines of data is necessary to generate all the X and Y positional data for a full 360 degree circle.

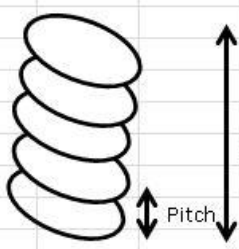
Centre of Circle @ Origin (0,0)			Circle Radius	
			10 mm	
			#Steps per Rev	
Top_Right Quadrant			100 Steps	
X=0, Y=max > @ X=Max, Y=0				
				
Angle Step Size				
(Radians)	(Degrees)	Angle Fraction	X_Value	Y_Value
0	0	0.00	0	10
0.062832	3.6	0.01	0.63	9.98
0.125664	7.2	0.02	1.25	9.92
0.188496	10.8	0.03	1.87	9.82
0.251327	14.4	0.04	2.49	9.69
0.314159	18	0.05	3.09	9.51
0.376991	21.6	0.06	3.68	9.3
0.439823	25.2	0.07	4.26	9.05
0.502655	28.8	0.08	4.82	8.76
0.565487	32.4	0.09	5.36	8.44
0.628319	36	0.10	5.88	8.09
0.69115	39.6	0.11	6.37	7.71
0.753982	43.2	0.12	6.85	7.29
0.816814	46.8	0.13	7.29	6.85
0.879646	50.4	0.14	7.71	6.37
0.942478	54	0.15	8.09	5.88
1.00531	57.6	0.16	8.44	5.36
1.068142	61.2	0.17	8.76	4.82
1.130973	64.8	0.18	9.05	4.26
1.193805	68.4	0.19	9.3	3.68
1.256637	72	0.20	9.51	3.09
1.319469	75.6	0.21	9.69	2.49

**Figure B.1** – Generation of X and Y positional data using the g-code generating Excel spreadsheet

### **B.2 Generating positional data for the z-axis**

Positional data for the Z-axis is based on the desired vertical distance covered per circle revolution (pitch), and the desired height of the structure. From the X and Y positional data generated prior, it is known that there are 100 steps per revolution – similarly, this also means that 100 data points is required in the Z-direction to travel a distance equal to one pitch. In figure B.2, the pitch is set to 1 millimetre; therefore a single Z-axis step covers a distance of 10 micrometres.

Desired Pitch	Desired Spiral Height	#Steps Per Revolution
1 mm	10 mm	100

Step Size	Line of code #ref	Z_Values
0.01	Line 1	0
	Line 2	0.01
	Line 3	0.02
	Line 4	0.03
	Line 5	0.04
	Line 6	0.05
	Line 7	0.06
	Line 8	0.07
	Line 9	0.08
	Line 10	0.09
	Line 11	0.1
	Line 12	0.11
	Line 13	0.12
	Line 14	0.13
	Line 15	0.14
	Line 16	0.15
	Line 17	0.16
	Line 18	0.17
	Line 19	0.18
	Line 20	0.19
	Line 21	0.2

**Figure B.2** – Generation of Z-axis positional data using the g-code generating Excel spreadsheet

The number of revolutions is determined by dividing the height parameter by the pitch. This provides information relating to the number of times the X and Y positional data needs to be repeated and the number of lines of g-code necessary to complete a print of the desired structure. A structure with a desired height of 10 millimetres and a pitch of 1 millimetre will comprise of 10 complete circle revolutions – this means that the X and Y positional data needs to be copied and pasted 10 times over, and at 100 steps per revolution corresponds with a total of 1000 lines of code.

### ***B.3 Generating start and end scripts***

The generation of a start script is useful as it helps to prime the nozzle with material and helps to ensure a steady material flow at the start of the spiral as it is being printed. An end script is also useful as it provides a clear visual indication of when the print is about to finish and can provide an easily accessible point of entry for perfusion. These scripts are considered best as simple straight lines – the start script is offset from the spiral structure and aims to project a straight line which meets the spiral tangentially along the X/Y plane, followed by the printing of the spiral, and ends with another straight line

which leaves the top of the spiral structure tangentially also. As these scripts are intended as straight lines, only a single coordinate needs varied (either X or Y) and the other coordinate retains a static value. In figure B.3 below the Y axis maintains the static value, 10, which corresponds with the circle radius established earlier. The X-axis value is the variable and is determined by the desired line length and tangentially meets the spiral when X is zero. The average step distance may be arbitrarily defined, but a reasonable value which approximates a similar distance of all other travel moves in the X/Y plane is derived by applying the Pythagorean theorem; the adjacent and opposing sides of the right angled triangle corresponds with the absolute difference between X and Y values between two lines of code, and calculating the hypotenuse results in the absolute distance travelled per step.

			Avg Step Distance	0.628 mm
Set line distance	15 mm		Circle Radius	10 mm
Start script			End Script	
X_Value	Y_Value	X_Value	Y_Value	
-15	10	0	10	
-14.372	10	0.628	10	
-13.744	10	1.256	10	
-13.116	10	1.884	10	
-12.488	10	2.512	10	
-11.86	10	3.14	10	
-11.232	10	3.768	10	
-10.604	10	4.396	10	
-9.976	10	5.024	10	
-9.348	10	5.652	10	
-8.72	10	6.28	10	
-8.092	10	6.908	10	
-7.464	10	7.536	10	
-6.836	10	8.164	10	
-6.208	10	8.792	10	
-5.58	10	9.42	10	
-4.952	10	10.048	10	
-4.324	10	10.676	10	
-3.696	10	11.304	10	
-3.068	10	11.932	10	
-2.44	10	12.56	10	
-1.812	10	13.188	10	
-1.184	10	13.816	10	
-0.556	10	14.444	10	
		15.072	10	

**Figure B.3** – Start and end scripts generated using the g-code generating Excel spreadsheet



### B.4 Compiling generated x, y, and z values into g-code

G-code functions with a letter operator, such as G, X, or E, followed by a numerical value. Hence the creation of g-code requires a method of adding such operators as a prefix to the X, Y, and Z positional data generated thus far.

With reference to figure B.4, the manner by which this is achieved is by first creating five columns which correspond with the following operators in the following order: G, X, Y, Z, and F (E is added later). The positional data for X, Y, and Z has already been generated and thus can be simply copied and pasted into their respective columns, remembering to replicate such coordinates as many times as necessary to create a structure of the desired height.

		Speed	8	mm/s			Iterative E_Step Value	0.003525								
		Paste Values from sheets					Basic Spiral G-code									
G_Value	X_Value	Y_Value	Z_Value	F_Value	Machine/Axis Operator											
1	0	10	0	480	G	X	Y	Z	E	F	G1	X0	Y10	Z0	E0.004	F480
1	0.63	9.98	0.01	480	G	X	Y	Z	E	F	G1	X0.63	Y9.98	Z0.01	E0.008	F480
1	1.25	9.92	0.02	480	G	X	Y	Z	E	F	G1	X1.25	Y9.92	Z0.02	E0.012	F480
1	1.87	9.82	0.03	480	G	X	Y	Z	E	F	G1	X1.87	Y9.82	Z0.03	E0.016	F480
1	2.49	9.69	0.04	480	G	X	Y	Z	E	F	G1	X2.49	Y9.69	Z0.04	E0.02	F480
1	3.09	9.51	0.05	480	G	X	Y	Z	E	F	G1	X3.09	Y9.51	Z0.05	E0.024	F480
1	3.68	9.3	0.06	480	G	X	Y	Z	E	F	G1	X3.68	Y9.3	Z0.06	E0.028	F480
1	4.26	9.05	0.07	480	G	X	Y	Z	E	F	G1	X4.26	Y9.05	Z0.07	E0.032	F480
1	4.82	8.76	0.08	480	G	X	Y	Z	E	F	G1	X4.82	Y8.76	Z0.08	E0.036	F480
1	5.36	8.44	0.09	480	G	X	Y	Z	E	F	G1	X5.36	Y8.44	Z0.09	E0.04	F480
1	5.88	8.09	0.1	480	G	X	Y	Z	E	F	G1	X5.88	Y8.09	Z0.1	E0.044	F480
1	6.37	7.71	0.11	480	G	X	Y	Z	E	F	G1	X6.37	Y7.71	Z0.11	E0.048	F480
1	6.85	7.29	0.12	480	G	X	Y	Z	E	F	G1	X6.85	Y7.29	Z0.12	E0.052	F480
1	7.29	6.85	0.13	480	G	X	Y	Z	E	F	G1	X7.29	Y6.85	Z0.13	E0.056	F480
1	7.71	6.37	0.14	480	G	X	Y	Z	E	F	G1	X7.71	Y6.37	Z0.14	E0.06	F480
1	8.09	5.88	0.15	480	G	X	Y	Z	E	F	G1	X8.09	Y5.88	Z0.15	E0.064	F480
1	8.44	5.36	0.16	480	G	X	Y	Z	E	F	G1	X8.44	Y5.36	Z0.16	E0.068	F480
1	8.76	4.82	0.17	480	G	X	Y	Z	E	F	G1	X8.76	Y4.82	Z0.17	E0.072	F480
1	9.05	4.26	0.18	480	G	X	Y	Z	E	F	G1	X9.05	Y4.26	Z0.18	E0.076	F480
1	9.3	3.68	0.19	480	G	X	Y	Z	E	F	G1	X9.3	Y3.68	Z0.19	E0.08	F480

**Figure B.4** – Compiling custom g-code with generated X/Y/Z data using the g-code generating Excel spreadsheet (excerpt taken after start script)

G values correspond with certain machine operations and depends on the firmware (see the RepRap website for details on g-codes compatible with Marlin [244]). In the G value column, a value of 1 is given which is the machine operator for ‘conduct a linear travel move’. Setting every value as 1 keeps the g-code generation as simple as possible; integrating multiple machine operators in an automated manner would likely rely on contextual information based on surrounding lines of code and thus considered difficult and unnecessary to implement for the generation of simple spiral structures.

F values represent the feedrate and are expressed as millimetres of travel per minute. A value of 480 was used for all operations and corresponds to a travel speed of 8 millimetres per second which seems reasonable when compared to standard 3D printing travel speeds and feasible given the large shell of the coaxial nozzle used. This value may be readily changed if the print speed is considered too fast or slow.

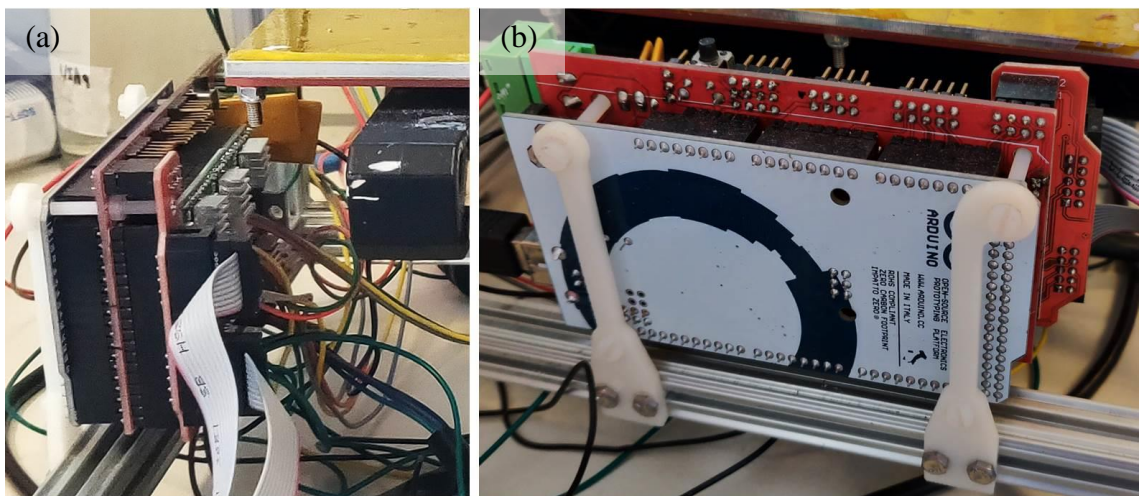
The E value is the displacement of the extruder's piston in the syringe barrel. The values of E are obtained iteratively but can be approximated initially by imagining the spiral structure being unwound and resembling a single straight line of cylindrical filament. In this calculation, the diameter of the filament is approximated to be close to that of the shell of the coaxial nozzle assembly; its volume being its cross-sectional area multiplied by its length. Dividing this volume by the cross-sectional area of the extruder's syringe barrel gives a value for the total piston displacement required to extrude the necessary volume of material and thus corresponds with the final value of E. This E value is divided by the total number of steps to obtain a value for how much material volume to be extruded for every print move. After conducting test prints, the E value may be increased or lowered proportionally to optimise the extrusion conditions.

With values obtained for the six letter operators found in simple g-code, their respective prefixes are added by using the concatenate function within Excel to combine strings of text and numbers together - and six terms are listed in order to the right of the spreadsheet. At this point, the concatenated text can simply be copied and pasted into a blank Notepad document and saved with the explicit file extension ".gcode" - this ensures that the file can be correctly interpreted as g-code by the 3D bioprinter and will function at a basic level. Any changes that need to be made to any of the processing parameters can be readily edited and the values will be automatically recalculated, so further revisions only need to be copied and pasted again and thus a significant amount of time is saved by not writing the g-code.

Creating g-code in this manner is only appropriate for simple geometries which follow a simple toolpath, but is useful as it allows for the Z-axis to be moving continuously like the X and Y axes which is of use in the context of coaxial bioprinting. The traditional layer-by-layer approach using Slic3r is perceived highly likely to encounter toolpath-related issues which may fail to produce structures with a single and continuous perfusable core.

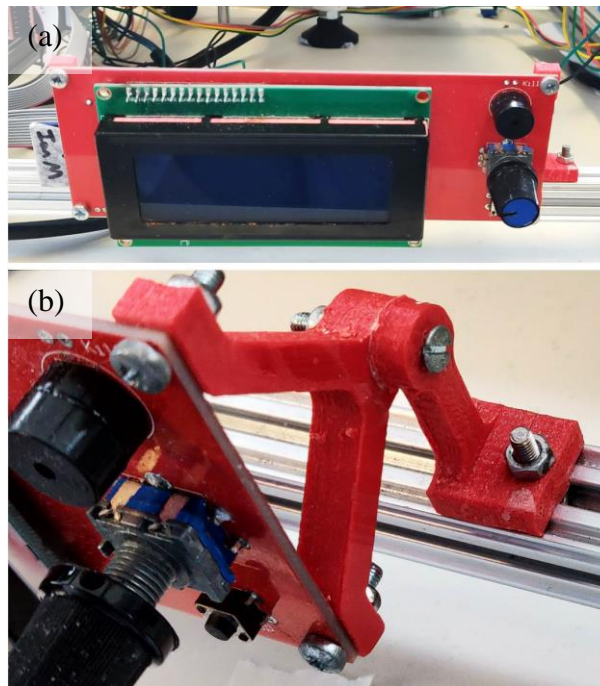
## Appendix C – Miscellaneous Hardware

Situated at the left hand side of the bioprinter are two 3D printed panels for mounting a RAMPS 1.4 microcontroller board to the side of the frame (figure C.1). This satisfies multiple ergonomic factors such as being located in a reasonably central position for all motor and endstop wires to reach without being in the way of the moving axes, keeps the electronics elevated from the workbench and is therefore safer should the workbench become wet due to any accidental spills, and also improves operation safety by keeping the board's reset button upright in an easy to access location should something go wrong during a print such as a nozzle crash.



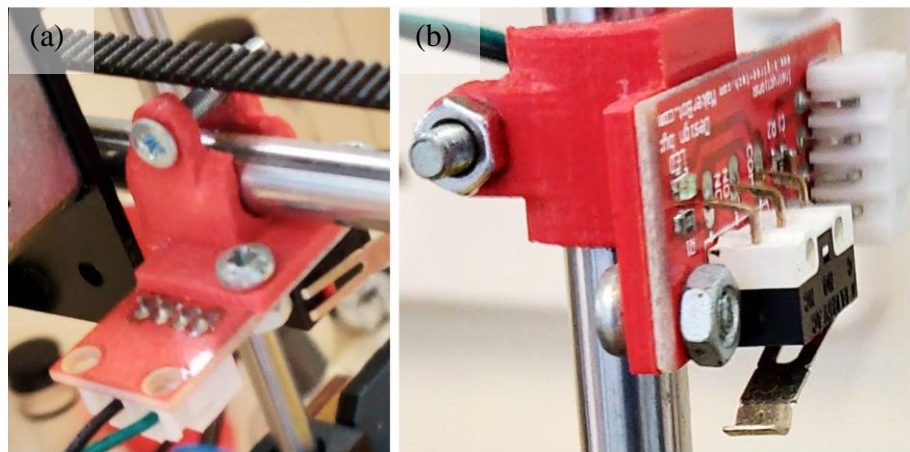
*Figure C.1 – (a) RAMPS 1.4 microcontroller board is installed onto the frame on the left-hand side of the printer, (b) using 3D printed mounts which matches the beam's and microcontroller's profiles*

Similarly to the microcontroller board, the LCD screen used for operating the bioprinter is affixed to 3D printed mounts which are situated at the front of the machine, facing the user (figure C.2). The 3D printed mounts are adjustable to vary the angle of the screen to suit the user. Again this ensures that the electronics are safely elevated from the workbench whilst being operable in a manner which is most comfortable for the user.



**Figure C.2** – (a) Front view of LCD2004 screen, (b) mounted to the front of the frame with rotatable 3D printed fittings which matches the beam's and screen's profiles

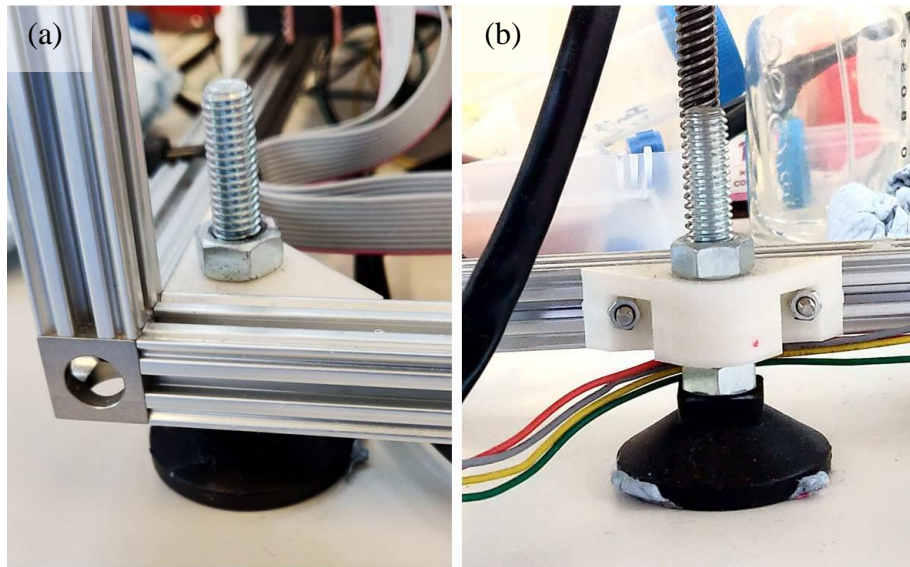
Designating an appropriate location for a mechanical endstop is trivial along the X-axis, whereby the secondary Y-axis carriage has a fitting specifically for this purpose and is engaged when contact with the X-axis carriage has been made. The Y and Z-axis endstops do not have access to such fittings, thus a custom 3D printed mount was used instead to locate the endstops in the most appropriate positions (figure C.3). An endstop may be affixed to the 3D printed mount with two M3 nuts and bolts. The 3D printed mount is then clamped around a linear rod of the corresponding axis and can be tightened with a nut and bolt to hold the endstop securely in position. This design also offers flexibility in regards to endstop position – the Z-axis endstop for example can be positioned low down or high up on one of the Z-axis linear rods and secured in position. This is particularly useful for bath printing whereby the lowest nozzle position can be set manually through careful positioning of the Z-axis endstop, and can ensure that the nozzle does not collide with the base of the bath and that the extruder housing does not collide with the bath's container.



*Figure C.3 – 3D printed endstop mounts which clamps around linear rods along the (a) Y-axis, (b) and Z-axis*

Lastly, the entire bioprinter is raised and balanced with three adjustable feet as shown in figure C.4. The feet are attached to the frame with 3D printed components and are affixed to the inside of the frame at the base. Two of these components are located at the front left and right inside corners and one is positioned centrally at the back of the frame, thus the feet are positioned triangularly relative to each other to keep the machine as balanced and level as possible. As discussed earlier in the chapter, the Z-axis stepper motor with integrated leadscrew is longer than the bioprinter; the incorporation of the adjustable feet ensure that there is enough height to accommodate the leadscrew without the tip making contact with the workbench. With the adjustable feet, the height of each foot on the frame of the bioprinter can be adjusted thus allowing the machine (not the printbed) to be levelled when placed on a multitude of work surfaces. Once appropriately levelled, the adjustable feet are locked in position by tightening the nut on the foot against its respective 3D printed component.





*Figure C.4 – 3D printed mounts for affixing stabilising feet onto the bioprinter’s frame; (a) there are two ‘corner’ pieces (b) and a single ‘flat’ piece to triangularly align the feet positions*

## **Appendix D – Firmware Configuration**

Note that most of the following firmware changes are made within the configuration.h file within the Marlin directory, unless otherwise specified. To access this file, or any other firmware file, to make changes to it the file must be opened within the Arduino IDE software, either by dragging and dropping the configuration.h file into a new Arduino sketch or by opening the Arduino software within the same directory as the configuration.h file.

### ***D.1 Basic settings***

Between lines 1 and 68 in the configuration.h file are the basic settings pertaining to the custom built 3D bioprinter (figure D.1). Several unimportant settings such as specifying the name of the printer can be set here, but the most important settings to configure are: baudrate, motherboard, number of extruders, and power supply.

The baudrate is a value given to specify the rate of communications with the printer. This setting is most relevant when control of the 3D printer is achieved with a computer using software such as Pronterface to directly send commands and g-code to the printer, whereby the commands are sent through the serial port to the printer. Within Pronterface, the port number and baudrate need to be correctly specified in order to communicate with the printer correctly, thus it makes sense to configure the baudrate in Marlin to match one of the selectable baudrates within the Pronterface software for compatible communications between computer and printer. The baudrate values in Pronterface are: 2400, 9600, 19200, 38400, 57600, 115200, and 250000. Configuring which baudrate works best with the 3D bioprinter is generally a trial and error process; with the highest setting of 250000 in Pronterface and specified within the firmware, the user should conduct some prints and look for any communication-related errors, such as strange characters/symbols appearing on the LCD screen or irregular motor movement. If the prints are okay, then the baudrate value should be okay to use. With the developed bioprinter, a baudrate of 250000 did not seem to contribute to any noticeable problems and thus was deemed an appropriate value to use in the firmware.

```

#define STRING_VERSION_CONFIG_H __DATE__ " " __TIME__ // build date and t
#define STRING_CONFIG_H_AUTHOR "(Ian MacKenzie, default config)" // Who m

// SERIAL_PORT selects which serial port should be used for communication
// This allows the connection of wireless adapters (for instance) to non-
// Serial port 0 is still used by the Arduino bootloader regardless of th
#define SERIAL_PORT 0

// This determines the communication speed of the printer
#define BAUDRATE 250000

// This enables the serial port associated to the Bluetooth interface
//#define BTENABLED // Enable BT interface on AT90USB device

// The following define selects which electronics board you have.
// Please choose the name from boards.h that matches your setup
#ifndef MOTHERBOARD
#define MOTHERBOARD BOARD_RAMPS_13_EFB
#endif

// Define this to set a custom name for your generic Mendel,
#define CUSTOM_MENDEL_NAME "Ian-1"

// Define this to set a unique identifier for this printer, (Used by some
// You can use an online service to generate a random UUID. (eg http://ww
// #define MACHINE_UUID "00000000-0000-0000-0000-000000000000"

// This defines the number of extruders
#define EXTRUDERS 1

//// The following define selects which power supply you have. Please cho
// 1 = ATX
// 2 = X-Box 360 203Watts (the blue wire connected to PS_ON and the red w
#define POWER_SUPPLY 2

```

**Figure D.1** – Configured basic settings in Marlin firmware

The motherboard setting is crucial to ensure proper working operation and cooperation of the microcontroller board and the printer. The importance of this setting is due to the differences in how various microcontroller boards are manufactured which do not share the same pin assignments. When stacking the RAMPS shield on top of the Arduino, the Arduino's outputs are mapped as specified pin numbers which, in conjunction with the firmware, is necessary for sending the correct digital output signals to control the 3D printer. The motherboard may be configured to the correct board by typing 'BOARD\_RAMPS\_13\_EFB' after '#define MOTHERBOARD' - for a full list of compatible microcontroller boards, and to see which numbers correspond to which type of board, the file 'pins.h' needs to be opened in Arduino. Whilst 'BOARD\_RAMPS\_13\_EFB' is the correct board to use, some settings within the pins.h file need to be changed to make the firmware work (figure D.2). At approximately line 545 in 'pins.h', the line '#define RAMPS\_V\_1\_3' needs to be uncommented, and can be achieved by deleting the two forward slashes that precede the code. Furthermore, only three endstops were inserted into the board's minimum on the bioprinter, thus the



pin assignments for the max pins in the firmware can be disabled. This allows the printer to move along both directions of each axis normally as otherwise the max pins would remain triggered by default. To stop each axis from instantly locking, the pin assignments for the RAMPS 1.4 board can be found under the ‘#else’ function (line 594) and changing the values of #define X\_MAX\_PIN, #define Y\_MAX\_PIN, and #define Z\_MAX\_PIN (lines 600, 606, and 612 respectively) to a value of ‘-1’ to disable them.

```

else

#define X_STEP_PIN      54
#define X_DIR_PIN      55
#define X_ENABLE_PIN   38
#define X_MIN_PIN      3  //++3
#define X_MAX_PIN      -1 //++2

#define Y_STEP_PIN      60
#define Y_DIR_PIN      61
#define Y_ENABLE_PIN   56
#define Y_MIN_PIN      14 //++14
#define Y_MAX_PIN      -1 //++15

#define Z_STEP_PIN      46
#define Z_DIR_PIN      48
#define Z_ENABLE_PIN   62
#define Z_MIN_PIN      18
#define Z_MAX_PIN      -1 //++19

#define Y2_STEP_PIN     36
#define Y2_DIR_PIN     34
#define Y2_ENABLE_PIN  30

#define Z2_STEP_PIN     36
#define Z2_DIR_PIN     34
#define Z2_ENABLE_PIN  30

#define E0_STEP_PIN     26
#define E0_DIR_PIN     28
#define E0_ENABLE_PIN  24

#define E1_STEP_PIN     36
#define E1_DIR_PIN     34
#define E1_ENABLE_PIN  30

```

*Figure D.2 – Configured pin definitions within the Marlin firmware*

Defining the number of extruders is as straightforward as inputting a single number. As the bioprinter only has a single extruder, a value of ‘1’ was input next to the line of code which read #define EXTRUDERS’, found on line 58.

Defining the power supply is somewhat ambiguous in the firmware. There are two settings which may be specified by inputting a digit: ‘1’ corresponds with an ATX style of power supply, ‘2’ corresponds and X-Box 360 power supply unit. The ATX style units refer to power supply units commonly found in computers, whereas the ‘X-Box 360’ setting refers specifically to those kinds of power supply units but may also correspond with other switch mode power supplies, such as the Meanwell 60W adaptor

used to power the bioprinter. For this reason, a value of '2' was specified for this setting after the line of code which read '#define POWER\_SUPPLY' (line 64).

## ***D.2 Thermal settings***

Whilst the developed bioprinter foregoes the use of a heated bed, there exist many thermal settings which need to be adjusted because the firmware is natively designed for incorporation in typical plastic extrusion-based 3D printers. The thermal settings are specified between lines 73 and 263 (figure D.3).

The bioprinter does not incorporate the use of any temperature sensing thermistors, thus a value of '0' is input when asked to define what types of sensors are used with the machine (#define TEMP\_SENSOR\_0, #define TEMP\_SENSOR\_1, #define TEMP\_SENSOR\_2, and #define TEMP\_SENSOR\_BED, found on lines 107 to 110).

The minimum and maximum temperatures need to be set to a low value in order for the printer to work without heating. Definitions for the minimum and maximum temperatures can be found in lines 124 to 127 and 132 to 136 respectively. Without changing the default values, the printer will stall indefinitely prior to printing because the machine will wait to reach the expected extruder and bed temperatures specified within the firmware, which can never happen because the printer was constructed without any thermistors or heating elements (except for the platform which is disconnected from any power). Thus the default values for all of these settings were changed to '1', which means that the minimum and maximum temperatures for the extruder and heated bed would be theoretically set to 1° Celsius. By setting the firmware as such and in conjunction with setting the temperature controls found within Slicer to zero (filament settings > filament), one can guarantee that all temperature-related logic is rendered disabled and will not interfere with printing.

```

#define TEMP_SENSOR_0 0
#define TEMP_SENSOR_1 0
#define TEMP_SENSOR_2 0
#define TEMP_SENSOR_BED 0

// This makes temp sensor 1 a redundant sensor for sensor 0
//#define TEMP_SENSOR_1_AS_REDUNDANT
/**#define MAX_REDUNDANT_TEMP_SENSOR_DIFF 10

// Actual temperature must be close to target for this long
#define TEMP_RESIDENCY_TIME 10 // (seconds)
#define TEMP_HYSTERESIS 3 // (degC) range of +/- temp
#define TEMP_WINDOW 1 // (degC) Window around tar

// The minimal temperature defines the temperature below wh
// to check that the wiring to the thermistor is not broken
// Otherwise this would lead to the heater being powered on
#define HEATER_0_MINTEMP 1 //5
#define HEATER_1_MINTEMP 1 //5
#define HEATER_2_MINTEMP 1 //5
#define BED_MINTEMP 1 //5

// When temperature exceeds max temp, your heater will be s
// This feature exists to protect your hotend from overheat
// You should use MINTEMP for thermistor short/failure prot
#define HEATER_0_MAXTEMP 1 //275
#define HEATER_1_MAXTEMP 1 //275
#define HEATER_2_MAXTEMP 1 //275
#define BED_MAXTEMP 1 //150

```

*Figure D.3 – Configured thermal settings within Marlin firmware*

### ***D.3 Mechanical settings***

Mechanical settings, as the name implies, relates to all the settings involving 3D printer motion. This includes setting the positive and negative directions of each axis, use of endstops, the length of each axis, and the steps per millimetre units for each axis. These settings are found between lines 264 and 508.

The positive direction of each axis can be defined between lines 320 and 325 (figure D.4). For most practical applications, the direction of each axis does not matter greatly save for the Z-axis and the E (extrusion)-axis – having an inverted direction for the E-axis means that the extruder motor would rotate in such a way that standard extrusion operations would retract instead. Similarly, ensuring that the direction of the Z-axis is correct ensures that the print platform is lowered for every printed layer; raising the platform erroneously would ultimately cause the nozzle to collide with the printed structure and result in print failure. Choosing the direction of the X and Y-axes is arbitrary – it may be desired to set the directions to correspond exactly with the plater in Slic3r so that a top-left position on the plater’s grid corresponds with the back-left hand

side of the printer’s platform, but is unnecessary for function. The definitions are set by typing ‘true’ or ‘false’ after the definition code, and should the direction of a specific axis need reversed then this may be achieved by changing ‘true’ to ‘false’ and vice-versa. The firmware settings for the developed bioprinter were set to true for ‘INVERT\_X\_DIR’ and ‘INVERT\_Y\_DIR’, and were set to false for ‘INVERT\_Z\_DIR’ and ‘INVERT\_E0-DIR’ – the directions of E1 and E2 (for a second and third extruder respectively) can be either true or false as secondary or tertiary extruders are not present in the bioprinter’s design.

```
// For Inverting Stepper Enable Pins (Active Low) use 0, Non Inverting (Activ
#define X_ENABLE_ON 0
#define Y_ENABLE_ON 0
#define Z_ENABLE_ON 0
#define E_ENABLE_ON 0 // For all extruders

// Disables axis when it's not being used.
#define DISABLE_X false
#define DISABLE_Y false
#define DISABLE_Z false
#define DISABLE_E false // For all extruders
#define DISABLE_INACTIVE_EXTRUDER true //disable only inactive extruders and

#define INVERT_X_DIR true // for Mendel set to false, for Orca set to true
#define INVERT_Y_DIR true // for Mendel set to true, for Orca set to false
#define INVERT_Z_DIR false // for Mendel set to false, for Orca set to tr
#define INVERT_E0_DIR false // for direct drive extruder v9 set to true, fo
#define INVERT_E1_DIR true // for direct drive extruder v9 set to true, fo
#define INVERT_E2_DIR true // for direct drive extruder v9 set to true, for

// ENDSTOP SETTINGS:
// Sets direction of endstops when homing; 1=MAX, -1=MIN
#define X_HOME_DIR -1
#define Y_HOME_DIR -1
#define Z_HOME_DIR -1

#define min_software_endstops false //true // If true, axis won't move to coo
#define max_software_endstops false //true // If true, axis won't move to co

// Travel limits after homing
#define X_MAX_POS 70
#define X_MIN_POS -70
#define Y_MAX_POS 60
#define Y_MIN_POS -60
#define Z_MAX_POS 60
#define Z_MIN_POS 0
```

**Figure D.4** – Configured positional/directional settings within Marlin firmware

Software endstops, as opposed to mechanical endstops, can be configured to be turned on or off within the firmware. As suggested by the name, software endstops will prevent any axis motion beyond a set distance defined by the travel limits set within the firmware. Definitions for the maximum and minimum software endstops (lines 333 and 334) are stated as either ‘true’ for active, or ‘false’ for disabled. For the bioprinter,

these were set to false, although whether they should be turned on or off is ultimately based on user discretion and particularly so if the homing command is used frequently and large structures are commonly printed. The travel limits (lines 337 to 342) are specified as a maximum value and a minimum value for each axis, and essentially defines a boundary volume which is safe to print within after homing. The values should relate to the printing space available in each direction after the extruder is homed, therefore minimum and maximum X-axis values of '-70' and '70' would mean that the X-axis is at least 140 millimetres wide. The dimensions of the bioprinter's platform were input into the travel limit settings in case the use of software endstops became desirable in future use. The input values, in the order of X-axis (max/min), Y-axis (max/min), and Z-axis (max/min) are 70, -70, 60, -60, 60, and 0.

The settings which must be configured to ensure positional accuracy of printing are the axis steps per millimetre (figure D.5). This setting describes the number of motor (micro) steps to linearly move a distance of one millimetre, and a value is set for each axis. The number of steps per millimetre for each axis is based on various parameters pertaining to the motors, pulleys, threaded rods/leadscrews used and is highly likely to require configuration on a per-printer basis. The steps per millimetre can be calculated by understanding the relationship between the total number of steps per motor revolution and the mechanism responsible for converting rotational motion into linear motion, such as the distance travelled per revolution of a belted pulley or leadscrew/threaded rod (equations (4.2) and (4.5), chapter 4.5 Theoretical Resolution). The X and Y axes have 80 steps per millimetre, the Z-axis has 400 steps per millimetre, and the extruder has 6400 steps per millimetre

```

//Manual homing switch locations:
// For deltabots this means top and center of the Cartesian print volume.
#define MANUAL_X_HOME_POS 0
#define MANUAL_Y_HOME_POS 0
#define MANUAL_Z_HOME_POS 0
//#define MANUAL_Z_HOME_POS 402 // For delta: Distance between nozzle and print

//// MOVEMENT SETTINGS
#define NUM_AXIS 4 // The axis order in all axis related arrays is X, Y, Z, E
#define HOMING_FEEDRATE {50*60, 50*60, 4*60, 0} // set the homing speeds (mm/m:

// default settings

#define DEFAULT_AXIS_STEPS_PER_UNIT {80,80,200*16/8,200*16/0.5} // default st
/// CORRECT steps per unit (XY belt) = (motor steps per rev * #ofmicrosteps)/(B
/// CORRECT steps per unit (ZE ThreadedRod/Leadscrew) = (motor steps per rev *
/// CORRECT resolution in mm per axis = (1mm)/(#Steps per unit mm)
/// 40.0 * 16/0.5 worked well with (green) nozzle of ID 0.838mm @ 0.4mm layer h
/// 40.0 * 16/0.5 worked well (enough) with (purple) nozzle of ID 0.514mm @ 0.1
/// 20.0*16/0.5 worked well with (purple) nozzle of ID 0.514 mm @ 0.05mm layer l
/// 3.75*16/0.5 worked good with (purple) nozzle with ID 0.514mm @ 0.025mm layer
#define DEFAULT_MAX_FEEDRATE {500, 500, 5, 25} // (mm/sec) E default
#define DEFAULT_MAX_ACCELERATION {9000,9000,100,10000} // X, Y, Z, E max

#define DEFAULT_ACCELERATION 3000 // X, Y, Z and E max acceleration
#define DEFAULT_RETRACT_ACCELERATION 3000 // X, Y, Z and E max acceleration :

```

**Figure D.5** - Configured axis steps per mm within the Marlin firmware

#### D.4 Additional settings

The section of code which denotes the additional settings begins from line 508. Settings within this section are generally related to the incorporation of extra features such as some sort of display for the 3D printer. The only setting here which needs to be configured for the developed 3D bioprinter is to uncomment line 559 (`#define REPRAP_DISCOUNT_SMART_CONTROLLER`) which enables the use of the LCD2004 display that was bundled as part of the RAMPS 1.4 kit (figure D.6).

```

// The RepRapDiscount Smart Controller (white PCB)
// http://reprap.org/wiki/RepRapDiscount\_Smart\_Controller
#define REPRAP_DISCOUNT_SMART_CONTROLLER

// The GADGETS3D G3D LCD/SD Controller (blue PCB)
// http://reprap.org/wiki/RAMPS\_1.3/1.4\_GADGETS3D\_Shield\_with\_Panel
//#define G3D_PANEL

// The RepRapDiscount FULL GRAPHIC Smart Controller (quadratic white PCB)
// http://reprap.org/wiki/RepRapDiscount\_Full\_Graphic\_Smart\_Controller
//
// ==> REMEMBER TO INSTALL U8glib to your ARDUINO library folder: http://co
//#define REPRAP_DISCOUNT_FULL_GRAPHIC_SMART_CONTROLLER

```

**Figure D.6** – Configured LCD2004 settings within Marlin firmware

## References

- [1] J. M. Tarr, K. Kaul, K. Wolanska, E. M. Kohner, and R. Chibber, “Retinopathy in diabetes,” 2013.
- [2] P. Bjornstad, D. Cherney, and D. M. Maahs, “Early diabetic nephropathy in type 1 diabetes: New insights,” *Curr. Opin. Endocrinol. Diabetes Obes.*, vol. 21, no. 4, pp. 279–286, 2014.
- [3] B. C. Spillman and J. Lubitz, “The effect of longevity on spending for acute and long-term care,” *N. Engl. J. Med.*, vol. 342, no. 19, pp. 1409–1415, 2000.
- [4] M. Caley and K. Sidhu, “Estimating the future healthcare costs of an aging population in the UK: Eexpansion of morbidity and the need for preventative care,” *J. Public Health (Bangkok)*, vol. 33, no. 1, pp. 117–122, 2011.
- [5] M. Mallappallil, E. A. Friedman, B. G. Delano, S. I. Mcfarlane, and M. O. Salifu, “Chronic kidney disease in the elderly: Evaluation and management,” *Clin. Pract.*, vol. 11, no. 5, pp. 525–535, 2014.
- [6] M. Kerr, B. Bray, J. Medcalf, D. J. O’Donoghue, and B. Matthews, “Estimating the financial cost of chronic kidney disease to the NHS in England,” *Nephrol. Dial. Transplant.*, vol. 27, no. SUPPL. 3, 2012.
- [7] Department of Health, “Organs for Transplants,” 2008.
- [8] M. J. Irving *et al.*, “Factors that influence the decision to be an organ donor: A systematic review of the qualitative literature,” *Nephrol. Dial. Transplant.*, vol. 27, no. 6, pp. 2526–2533, 2012.
- [9] NHS Blood and Transplant, “Taking Organ Transplantation to 2020: A detailed strategy,” 2013.
- [10] J. Neuberger and A. Keogh, “Organ donation in the UK: How general practice can help,” *Br. J. Gen. Pract.*, vol. 63, no. 615, pp. 513–514, 2013.
- [11] J. Donahue, “Obesity in the US and UK,” *J. Nutr. Food Sci.*, vol. 08, no. 04, 2018.
- [12] NHS Blood and Transplant, “Organ Donation and Transplantation Activity Report 2017/18,” 2018.

- [13] H. Liu, H. Zhou, H. Lan, and T. Liu, "Organ regeneration: integration application of cell encapsulation and 3D bioprinting," *Virtual Phys. Prototyp.*, vol. 12, no. 4, pp. 279–289, 2017.
- [14] J. J. Kim, L. Hou, and N. F. Huang, "Vascularization of three-dimensional engineered tissues for regenerative medicine applications," *Acta Biomater.*, vol. 41, pp. 17–26, 2016.
- [15] S. Breslin and L. O'Driscoll, "The relevance of using 3D cell cultures, in addition to 2D monolayer cultures, when evaluating breast cancer drug sensitivity and resistance," *Oncotarget*, vol. 7, no. 29, pp. 45745–45756, 2016.
- [16] M. P. Chae, F. Lin, R. T. Spychal, D. J. Hunter-Smith, and W. M. Rozenx, "3D-printed haptic 'reverse' models for preoperative planning in soft tissue reconstruction: A case report," *Microsurgery*, vol. 35, no. 2, pp. 148–153, 2015.
- [17] F. Rengier *et al.*, "3D printing based on imaging data: Review of medical applications," *Int. J. Comput. Assist. Radiol. Surg.*, vol. 5, no. 4, pp. 335–341, 2010.
- [18] J. Zuniga *et al.*, "Cyborg beast: A low-cost 3d-printed prosthetic hand for children with upper-limb differences," *BMC Res. Notes*, vol. 8, no. 1, 2015.
- [19] J. D. Prince, "3D Printing: An Industrial Revolution," *J. Electron. Resour. Med. Libr.*, vol. 11, no. 1, pp. 39–45, 2014.
- [20] A. Savini and G. G. Savini, "A short history of 3D printing, a technological revolution just started," in *Proceedings of the 2015 ICOHTEC/IEEE International History of High-Technologies and their Socio-Cultural Contexts Conference, HISTELCON 2015: The 4th IEEE Region 8 Conference on the History of Electrotechnologies*, 2015.
- [21] L. Vinet and A. Zhedanov, "A 'missing' family of classical orthogonal polynomials," 2011.
- [22] V. Bagaria, R. Bhansali, and P. Pawar, "3D printing- creating a blueprint for the future of orthopedics: Current concept review and the road ahead!," *J. Clin. Orthop. Trauma*, vol. 9, no. 3, pp. 207–212, 2018.
- [23] F. G. Arcella and G. G. Lessmann, "Casting Shapes," 1989.



- [24] H. Narasaki, K. Ogawa, and K. Tsujimoto, "Determination of trace phosphorus in organic materials by a combined low temperature ashing-spectrophotometry," 1979.
- [25] M. Feygin, "Apparatus and method for forming an integral object from laminations," 1988.
- [26] I. Gibson, D. Rosen, B. Stucker, I. Gibson, D. Rosen, and B. Stucker, "The Impact of Low-Cost AM Systems," in *Additive Manufacturing Technologies*, Springer New York, 2015, pp. 293–301.
- [27] C. W. Hull and C. Arcadia, "United States Patent (19) Hull (54) (75) (73) 21) 22 (51) 52) (58) (56) Apparatus for Production of Three-Dimensional Objects by Stereolithography."
- [28] E. Matias and B. Rao, "3D printing: On its historical evolution and the implications for business," New York, 2015.
- [29] R. Jones *et al.*, "Reprap - The replicating rapid prototyper," *Robotica*, vol. 29, no. 1 SPEC. ISSUE, pp. 177–191, 2011.
- [30] "RepRap.org." [Online]. Available: <https://reprap.org/wiki/RepRap>. [Accessed: 16-Sep-2019].
- [31] Wohlers Associate, "Wohlers Report 2015 – History of Additive Manufacturing," 2015.
- [32] J. M. Pearce, N. C. Anzalone, and C. L. Heldt, "Open-Source Wax RepRap 3-D Printer for Rapid Prototyping Paper-Based Microfluidics," *J. Lab. Autom.*, vol. 21, no. 4, pp. 510–516, 2016.
- [33] J. Sun, G. S. Hong, S. Vijayavenkataraman, and J. Tantra, "Development of a Desktop Food Printer for Dough Extrusion," *ETP Int. J. Food Eng.*, pp. 316–321, 2018.
- [34] M. Lanaro *et al.*, "3D printing complex chocolate objects: Platform design, optimization and evaluation," *J. Food Eng.*, vol. 215, pp. 13–22, Dec. 2017.

- [35] G. C. Anzalone, B. Wijnen, and J. M. Pearce, “Multi-material additive and subtractive prosumer digital fabrication with a free and open-source convertible delta RepRap 3-D printer,” *Rapid Prototyp. J.*, vol. 21, no. 5, pp. 506–519, 2015.
- [36] D. Fichou and G. E. Morlock, “Open-Source-Based 3D Printing of Thin Silica Gel Layers in Planar Chromatography,” *Anal. Chem.*, vol. 89, no. 3, pp. 2116–2122, 2017.
- [37] G. C. Anzalone, C. Zhang, B. Wijnen, P. G. Sanders, and J. M. Pearce, “A low-cost open-source metal 3-D printer,” *IEEE Access*, vol. 1, pp. 803–810, 2013.
- [38] V. Kostakis and M. Papachristou, “Commons-based peer production and digital fabrication: The case of a RepRap-based, Lego-built 3D printing-milling machine,” *Telemat. Informatics*, vol. 31, no. 3, pp. 434–443, Aug. 2014.
- [39] W. C. Wilson and T. Boland, “Cell and organ printing 1: Protein and cell printers,” *Anat. Rec. - Part A Discov. Mol. Cell. Evol. Biol.*, vol. 272, no. 2, pp. 491–496, Jun. 2003.
- [40] N. Cubo, M. Garcia, J. F. Del Cañizo, D. Velasco, and J. L. Jorcano, “3D bioprinting of functional human skin: Production and in vivo analysis,” *Biofabrication*, vol. 9, no. 1, 2017.
- [41] N. Bessler *et al.*, “NyduS One Syringe Extruder (NOSE): A Prusa i3 3D printer conversion for bioprinting applications utilizing the FRESH-method,” *HardwareX*, vol. 6, p. e00069, Oct. 2019.
- [42] R. Attalla, E. Puersten, N. Jain, and P. R. Selvaganapathy, “3D bioprinting of heterogeneous bi- and tri-layered hollow channels within gel scaffolds using scalable multi-axial microfluidic extrusion nozzle,” *Biofabrication*, vol. 11, no. 1, p. 15012, 2019.
- [43] A. Bandyopadhyay, V. K. Dewangan, K. Y. Vajanthri, S. Poddar, and S. K. Mahto, “Easy and affordable method for rapid prototyping of tissue models in vitro using three-dimensional bioprinting,” *Biocybern. Biomed. Eng.*, vol. 38, no. 1, pp. 158–169, 2018.
- [44] C. De Maria *et al.*, “Design and validation of an open-hardware print-head for bioprinting application,” *Procedia Eng.*, vol. 110, pp. 98–105, 2015.

- [45] N. Okubo, A. J. Qureshi, K. Dalgarno, K. L. Goh, and S. Derebail, “Cost-effective microvalve-assisted bioprinter for tissue engineering,” *Bioprinting*, vol. 13, p. e00043, Mar. 2019.
- [46] Y. Zhang, Y. Yu, and I. T. Ozbolat, “Direct bioprinting of vessel-like tubular microfluidic channels,” *J. Nanotechnol. Eng. Med.*, vol. 4, no. 2, pp. 1–7, May 2013.
- [47] B. Duan, L. A. Hockaday, K. H. Kang, and J. T. Butcher, “3D Bioprinting of heterogeneous aortic valve conduits with alginate/gelatin hydrogels,” *J. Biomed. Mater. Res. - Part A*, vol. 101 A, no. 5, pp. 1255–1264, May 2013.
- [48] A. Skardal, J. Zhang, L. McCoard, X. Xu, S. Oottamasathien, and G. D. Prestwich, “Photocrosslinkable hyaluronan-gelatin hydrogels for two-step bioprinting,” *Tissue Eng. - Part A*, vol. 16, no. 8, pp. 2675–2685, Aug. 2010.
- [49] A. Isaacson, S. Swioklo, and C. J. Connon, “3D bioprinting of a corneal stroma equivalent,” *Exp. Eye Res.*, vol. 173, pp. 188–193, Aug. 2018.
- [50] M. M. Laronda *et al.*, “A bioprosthetic ovary created using 3D printed microporous scaffolds restores ovarian function in sterilized mice,” *Nat. Commun.*, vol. 8, 2017.
- [51] J. H. Shim, J. S. Lee, J. Y. Kim, and D. W. Cho, “Bioprinting of a mechanically enhanced three-dimensional dual cell-laden construct for osteochondral tissue engineering using a multi-head tissue/organ building system,” *J. Micromechanics Microengineering*, vol. 22, no. 8, p. 11, 2012.
- [52] F. Pati, J. Jang, J. W. Lee, and D. W. Cho, “Extrusion Bioprinting,” in *Essentials of 3D Biofabrication and Translation*, no. 5, Elsevier Inc., 2015, pp. 123–152.
- [53] J. S. Lee, J. M. Hong, J. W. Jung, J. H. Shim, J. H. Oh, and D. W. Cho, “3D printing of composite tissue with complex shape applied to ear regeneration,” *Biofabrication*, 2014.
- [54] J. Malda *et al.*, “25th Anniversary Article: Engineering Hydrogels for Biofabrication,” *Adv. Mater.*, vol. 25, no. 36, pp. 5011–5028, 2013.

- [55] A. G. Tabriz, M. A. Hermida, and N. R. Leslie, “Three-dimensional Bioprinting of Complex Cell Laden Alginate Hydrogel Structures,” *Biofabrication*, vol. 7, no. 4, pp. 1–18, 2015.
- [56] A. L. Rutz, K. E. Hyland, A. E. Jakus, W. R. Burghardt, and R. N. Shah, “A multimaterial bioink method for 3D printing tunable, cell-compatible hydrogels,” *Adv. Mater.*, vol. 27, no. 9, pp. 1607–1614, Mar. 2015.
- [57] I. T. Ozbolat and M. Hospodiuk, “Current advances and future perspectives in extrusion-based bioprinting,” 2016.
- [58] X. Zhang and Y. Zhang, “Tissue Engineering Applications of Three-Dimensional Bioprinting,” *Cell Biochem. Biophys.*, vol. 72, no. 3, pp. 777–782, Jul. 2015.
- [59] S. V. Murphy and A. Atala, “3D bioprinting of tissues and organs,” *Nat. Biotechnol.*, vol. 32, no. 8, pp. 773–785, 2014.
- [60] “Blunt End Stainless Steel Dispensing Tips - Intertronics.” [Online]. Available: <https://www.intertronics.co.uk/product/blunt-end-stainless-steel-dispensing-tips/>. [Accessed: 19-Sep-2019].
- [61] K. Nair *et al.*, “Characterization of cell viability during bioprinting processes,” *Biotechnol. J.*, vol. 4, no. 8, pp. 1168–1177, 2009.
- [62] Ž. P. Kačarević *et al.*, “An introduction to 3D bioprinting: Possibilities, challenges and future aspects,” *Materials (Basel)*, vol. 11, no. 11, 2018.
- [63] T. Xu, J. Jin, C. Gregory, J. J. Hickman, and T. Boland, “Inkjet printing of viable mammalian cells,” *Biomaterials*, vol. 26, no. 1, pp. 93–99, 2005.
- [64] C. Colosi *et al.*, “Microfluidic Bioprinting of Heterogeneous 3D Tissue Constructs Using Low-Viscosity Bioink,” *Adv. Mater.*, vol. 28, no. 4, pp. 677–684, 2015.
- [65] P. Calvert, “Printing Cells,” *Science (80-. )*, vol. 318, no. 5848, pp. 207–208, 2007.
- [66] M. Nakamura, S. Iwanaga, C. Henmi, K. Arai, and Y. Nishiyama, “Biomatrices and biomaterials for future developments of bioprinting and biofabrication,” *Biofabrication*, vol. 2, no. 1, p. 6, 2010.

- [67] X. Cui, D. Dean, Z. M. Ruggeri, and T. Boland, "Cell damage evaluation of thermal inkjet printed chinese hamster ovary cells," *Biotechnol. Bioeng.*, vol. 106, no. 6, pp. 963–969, 2010.
- [68] R. Seetharam and S. K. Sharma, *Purification and analysis of recombinant proteins*. M. Dekker, 1991.
- [69] B. Derby, "Inkjet Printing of Functional and Structural Materials: Fluid Property Requirements, Feature Stability, and Resolution," *Annu. Rev. Mater. Res.*, vol. 40, no. 1, pp. 395–414, 2010.
- [70] X. Li, J. Chen, B. Liu, X. Wang, D. Ren, and T. Xu, "Inkjet Printing for Biofabrication," *3D Print. Biofabrication*, pp. 283–301, 2018.
- [71] Y. J. Seol, H. W. Kang, S. J. Lee, A. Atala, and J. J. Yoo, "Bioprinting technology and its applications," *Eur. J. Cardio-thoracic Surg.*, vol. 46, no. 3, pp. 342–348, Sep. 2014.
- [72] R. E. Saunders and B. Derby, "Inkjet printing biomaterials for tissue engineering: Bioprinting," *Int. Mater. Rev.*, vol. 59, no. 8, pp. 430–448, 2014.
- [73] B. Lorber, W. K. Hsiao, I. M. Hutchings, and K. R. Martin, "Adult rat retinal ganglion cells and glia can be printed by piezoelectric inkjet printing," *Biofabrication*, vol. 6, no. 1, p. 15001, 2014.
- [74] R. E. Saunders, J. E. Gough, and B. Derby, "Delivery of human fibroblast cells by piezoelectric drop-on-demand inkjet printing," *Biomaterials*, vol. 29, no. 2, pp. 193–203, Jan. 2008.
- [75] S. Parsa, M. Gupta, F. Loizeau, and K. C. Cheung, "Effects of surfactant and gentle agitation on inkjet dispensing of living cells," *Biofabrication*, vol. 2, no. 2, 2010.
- [76] M. E. Pepper, V. Seshadri, T. C. Burg, K. J. L. Burg, and R. E. Groff, "Characterizing the effects of cell settling on bioprinter output," *Biofabrication*, vol. 4, no. 1, 2012.
- [77] T. Xu, W. Zhao, J.-M. Zhu, M. Z. Albanna, J. J. Yoo, and A. Atala, "Complex heterogeneous tissue constructs containing multiple cell types prepared by inkjet printing technology," *Biomaterials*, vol. 34, no. 1, pp. 130–139, Jan. 2013.

- [78] X. Cui, K. Breitenkamp, M. G. Finn, M. Lotz, and D. D. D’Lima, “Direct human cartilage repair using three-dimensional bioprinting technology.,” *Tissue Eng. Part A*, vol. 18, no. 11–12, pp. 1304–12, Jun. 2012.
- [79] W. Lee *et al.*, “Multi-layered culture of human skin fibroblasts and keratinocytes through three-dimensional freeform fabrication,” *Biomaterials*, vol. 30, no. 8, pp. 1587–1595, Mar. 2009.
- [80] A. Faulkner-Jones, S. Greenhough, J. a King, J. Gardner, A. Courtney, and W. Shu, “Development of a valve-based cell printer for the formation of human embryonic stem cell spheroid aggregates.,” *Biofabrication*, vol. 5, no. 1, p. 015013, 2013.
- [81] A. Faulkner-Jones *et al.*, “Bioprinting of human pluripotent stem cells and their directed differentiation into hepatocyte-like cells for the generation of mini-livers in 3D,” *Biofabrication*, vol. 7, no. 4, 2015.
- [82] S. Tasoglu and U. Demirci, “Bioprinting for stem cell research.,” *Trends Biotechnol.*, vol. 31, no. 1, pp. 10–9, Jan. 2013.
- [83] H. Gudapati, M. Dey, and I. Ozbolat, “A comprehensive review on droplet-based bioprinting: Past, present and future,” *Biomaterials*, vol. 102, pp. 20–42, 2016.
- [84] V. Lee *et al.*, “Design and fabrication of human skin by three-dimensional bioprinting,” *Tissue Eng. - Part C Methods*, vol. 20, no. 6, pp. 473–484, Jun. 2014.
- [85] I. T. Ozbolat, *Laser-Based Bioprinting*. 2017.
- [86] A. Skardal and A. Atala, “Biomaterials for Integration with 3-D Bioprinting,” *Ann. Biomed. Eng.*, vol. 43, no. 3, pp. 730–746, Mar. 2015.
- [87] Z. Wang, R. Abdulla, B. Parker, R. Samanipour, S. Ghosh, and K. Kim, “A simple and high-resolution stereolithography-based 3D bioprinting system using visible light crosslinkable bioinks,” *Biofabrication*, vol. 7, p. 45009, 2015.
- [88] J. R. Tumbleston *et al.*, “Continuous liquid interface production of 3D objects,” *Science (80-. )*, vol. 347, no. 6228, pp. 1349–1352, 2015.

- [89] H. Lin *et al.*, “Application of Visible Light-based Projection Stereolithography for Live Cell-Scaffold Fabrication with Designed Architecture,” 2012.
- [90] H. Cui, M. Nowicki, J. P. Fisher, and L. G. Zhang, “3D Bioprinting for Organ Regeneration,” *Adv. Healthc. Mater.*, vol. 6, no. 1, 2017.
- [91] M. Guvendiren, J. Molde, R. M. D. Soares, and J. Kohn, “Designing Biomaterials for 3D Printing,” *ACS Biomater. Sci. Eng.*, vol. 2, no. 10, pp. 1679–1693, 2016.
- [92] J. B. Lewis, J. C. Wataha, R. L. W. Messer, G. B. Caughman, T. Yamamoto, and S. D. Hsu, “Blue Light Differentially Alters Cellular Redox Properties,” 2004.
- [93] A. Slominski, “Animals under the sun: effects of ultraviolet radiation on mammalian skin,” *Clin. Dermatol.*, vol. 16, no. 4, pp. 503–515, Jul. 1998.
- [94] V. Chan, P. Zorlutuna, J. H. Jeong, H. Kong, and R. Bashir, “Three-dimensional photopatterning of hydrogels using stereolithography for long-term cell encapsulation,” *Lab Chip*, vol. 10, no. 16, p. 2062, Jul. 2010.
- [95] L. Elomaa, S. Teixeira, R. Hakala, H. Korhonen, D. W. Grijpma, and J. V. Seppälä, “Preparation of poly( $\epsilon$ -caprolactone)-based tissue engineering scaffolds by stereolithography,” *Acta Biomater.*, vol. 7, no. 11, pp. 3850–3856, 2011.
- [96] F. P. W. Melchels, J. Feijen, and D. W. Grijpma, “A poly(d,l-lactide) resin for the preparation of tissue engineering scaffolds by stereolithography,” *Biomaterials*, vol. 30, no. 23–24, pp. 3801–3809, Aug. 2009.
- [97] J. A. S. Neiman *et al.*, “Photopatterning of hydrogel scaffolds coupled to filter materials using stereolithography for perfused 3D culture of hepatocytes,” *Biotechnol. Bioeng.*, vol. 112, no. 4, pp. 777–787, 2015.
- [98] D. Rana, T. S. S. Kumar, and M. Ramalingam, “Cell-laden hydrogels for tissue engineering,” *J. Biomater. Tissue Eng.*, vol. 4, no. 7, pp. 507–535, 2014.
- [99] R. Ben *et al.*, “Advances in bioprinted cell-laden hydrogels for skin tissue engineering.”
- [100] L. Tan, Y. Ren, and R. Kuijjer, “A 1-min Method for Homogenous Cell Seeding in Porous Scaffolds,” *J. Biomater. Appl.*, vol. 26, 2012.

- [101] T. Billiet, M. Vandenhaute, J. Schelfhout, S. Van Vlierberghe, and P. Dubruel, "A review of trends and limitations in hydrogel-rapid prototyping for tissue engineering," *Biomaterials*, vol. 33, no. 26, pp. 6020–6041, 2012.
- [102] S. Vijayavenkataraman, W.-C. Yan, W. F. Lu, C.-H. Wang, and J. Y. H. Fuh, "3D bioprinting of tissues and organs for regenerative medicine," *Adv. Drug Deliv. Rev.*, vol. 132, pp. 296–332, Jul. 2018.
- [103] R. D. Pedde *et al.*, "Emerging Biofabrication Strategies for Engineering Complex Tissue Constructs," *Adv. Mater.*, vol. 29, no. 19, 2017.
- [104] A. B. Dababneh and I. T. Ozbolat, "Bioprinting Technology: A Current State-of-the-Art Review," *J. Manuf. Sci. Eng. Trans. ASME*, vol. 136, no. 6, 2014.
- [105] L. Koch *et al.*, "Laser printing of skin cells and human stem cells," *Tissue Eng. - Part C Methods*, vol. 16, no. 5, pp. 847–854, 2010.
- [106] L. Koch *et al.*, "Laser bioprinting of human induced pluripotent stem cells - The effect of printing and biomaterials on cell survival, pluripotency, and differentiation," *Biofabrication*, vol. 10, no. 3, 2018.
- [107] B. Guillotin *et al.*, "Laser assisted bioprinting of engineered tissue with high cell density and microscale organization," *Biomaterials*, vol. 31, no. 28, pp. 7250–7256, Oct. 2010.
- [108] E. S. Bishop *et al.*, "3-D bioprinting technologies in tissue engineering and regenerative medicine: Current and future trends," *Genes Dis.*, vol. 4, no. 4, pp. 185–195, 2017.
- [109] S. Catros *et al.*, "Laser-assisted bioprinting for creating on-demand patterns of human osteoprogenitor cells and nano-hydroxyapatite.," *Biofabrication*, vol. 3, p. 025001, 2011.
- [110] X. Cui and T. Boland, "Human microvasculature fabrication using thermal inkjet printing technology," *Biomaterials*, vol. 30, no. 31, pp. 6221–6227, 2009.
- [111] J. Park *et al.*, "Cell-laden 3D bioprinting hydrogel matrix depending on different compositions for soft tissue engineering: Characterization and evaluation," *Mater. Sci. Eng. C*, vol. 71, pp. 678–684, Feb. 2017.



- [112] W. Lee *et al.*, “Multi-layered culture of human skin fibroblasts and keratinocytes through three-dimensional freeform fabrication,” *Biomaterials*, vol. 30, no. 8, pp. 1587–1595, 2009.
- [113] F. Pati *et al.*, “Printing three-dimensional tissue analogues with decellularized extracellular matrix bioink,” *Nat. Commun.*, vol. 5, p. 3935, 2014.
- [114] W. Schuurman, V. Khristov, M. W. Pot, P. R. Van Weeren, W. J. A. Dhert, and J. Malda, “Bioprinting of hybrid tissue constructs with tailorable mechanical properties,” *Biofabrication*, vol. 3, no. 2, 2011.
- [115] J. Visser *et al.*, “Biofabrication of multi-material anatomically shaped tissue constructs,” *Biofabrication*, vol. 5, no. 3, 2013.
- [116] J.-S. Lee, J. M. Hong, J. W. Jung, J.-H. Shim, J.-H. Oh, and D.-W. Cho, “3D printing of composite tissue with complex shape applied to ear regeneration,” *Biofabrication*, vol. 6, no. 2, p. 024103, 2014.
- [117] H. W. Kang, S. J. Lee, I. K. Ko, C. Kengla, J. J. Yoo, and A. Atala, “A 3D bioprinting system to produce human-scale tissue constructs with structural integrity,” *Nat. Biotechnol.*, vol. 34, no. 3, pp. 312–319, 2016.
- [118] S. Mohanty *et al.*, “Fabrication of scalable and structured tissue engineering scaffolds using water dissolvable sacrificial 3D printed moulds,” *Mater. Sci. Eng. C*, vol. 55, pp. 569–578, 2015.
- [119] J. S. Miller *et al.*, “Rapid casting of patterned vascular networks for perfusable engineered three-dimensional tissues,” *Nat. Mater.*, vol. 11, no. 9, pp. 768–74, Sep. 2012.
- [120] D. B. Kolesky, R. L. Truby, A. S. Gladman, T. A. Busbee, K. A. Homan, and J. A. Lewis, “3D bioprinting of vascularized, heterogeneous cell-laden tissue constructs,” *Adv. Mater.*, vol. 26, no. 19, pp. 3124–3130, 2014.
- [121] D. B. Kolesky, K. A. Homan, M. A. Skylar-Scott, and J. A. Lewis, “Three-dimensional bioprinting of thick vascularized tissues,” *Proc. Natl. Acad. Sci. U. S. A.*, vol. 113, no. 12, pp. 3179–3184, 2016.

- [122] Y. Nishiyama *et al.*, “Development of a three-dimensional bioprinter: construction of cell supporting structures using hydrogel and state-of-the-art inkjet technology,” *J. Biomech. Eng.*, vol. 131, no. 3, p. 035001, 2009.
- [123] C. Xu, W. Chai, Y. Huang, and R. R. Markwald, “Scaffold-free inkjet printing of three-dimensional zigzag cellular tubes,” *Biotechnol. Bioeng.*, vol. 109, no. 12, pp. 3152–3160, 2012.
- [124] K. Christensen, C. Xu, W. Chai, Z. Zhang, J. Fu, and Y. Huang, “Freeform inkjet printing of cellular structures with bifurcations,” *Biotechnol. Bioeng.*, vol. 112, no. 5, pp. 1047–1055, 2015.
- [125] R. Xiong, Z. Zhang, W. Chai, Y. Huang, and D. B. Chrisey, “Freeform drop-on-demand laser printing of 3D alginate and cellular constructs,” *Biofabrication*, vol. 7, no. 4, 2015.
- [126] Q. Gao, Y. He, J.-Z. Fu, A. Liu, and L. Ma, “Coaxial nozzle-assisted 3D bioprinting with built-in microchannels for nutrients delivery,” *Biomaterials*, vol. 61, pp. 203–15, 2015.
- [127] C. S. O’Bryan *et al.*, “Three-dimensional printing with sacrificial materials for soft matter manufacturing,” *MRS Bull.*, vol. 42, no. 8, pp. 571–577, 2017.
- [128] T. Bhattacharjee *et al.*, “Writing in the granular gel medium,” *Sci. Adv.*, vol. 1, no. 8, p. e1500655, Sep. 2015.
- [129] C. S. O’Bryan, T. Bhattacharjee, S. L. Marshall, W. Gregory Sawyer, and T. E. Angelini, “Commercially available microgels for 3D bioprinting,” *Bioprinting*, vol. 11, p. e00037, Sep. 2018.
- [130] T. Bhattacharjee *et al.*, “Liquid-like Solids Support Cells in 3D,” *ACS Biomater. Sci. Eng.*, vol. 2, no. 10, pp. 1787–1795, 2016.
- [131] Y. Jin, A. Compaan, T. Bhattacharjee, and Y. Huang, “Granular gel support-enabled extrusion of three-dimensional alginate and cellular structures,” 2016.
- [132] T. J. Hinton, A. Hudson, K. Pusch, A. Lee, and A. W. Feinberg, “3D Printing PDMS Elastomer in a Hydrophilic Support Bath via Freeform Reversible Embedding,” 2016.

- [133] S. R. Moxon *et al.*, “Suspended Manufacture of Biological Structures,” *Adv. Mater.*, vol. 29, no. 13, p. 1605594, Apr. 2017.
- [134] T. J. Hinton *et al.*, “Three-dimensional printing of complex biological structures by freeform reversible embedding of suspended hydrogels,” *Sci. Adv.*, vol. 1, no. 9, 2015.
- [135] G. Štumberger and B. Vihar, “Freeform perfusable microfluidics embedded in hydrogel matrices,” *Materials (Basel)*, vol. 11, no. 12, 2018.
- [136] A. Lee *et al.*, “3D bioprinting of collagen to rebuild components of the human heart,” *Science (80-. )*, vol. 365, no. 6452, pp. 482–487, 2019.
- [137] N. Noor, A. Shapira, R. Edri, I. Gal, L. Wertheim, and T. Dvir, “3D Printing of Personalized Thick and Perfusable Cardiac Patches and Hearts,” *Adv. Sci.*, vol. 6, no. 11, 2019.
- [138] Y. Jin, A. Compaan, W. Chai, and Y. Huang, “Functional Nanoclay Suspension for Printing-Then-Solidification of Liquid Materials,” *ACS Appl. Mater. Interfaces*, vol. 9, no. 23, pp. 20057–20066, 2017.
- [139] Y. Jin, W. Chai, and Y. Huang, “Printability study of hydrogel solution extrusion in nanoclay yield-stress bath during printing-then-gelation biofabrication,” *Mater. Sci. Eng. C*, vol. 80, pp. 313–325, 2017.
- [140] H. Ding and R. C. Chang, “Bioprinting of liquid hydrogel precursors in a support bath by analyzing two key features: Cell distribution and shape fidelity,” *ASME 2018 13th Int. Manuf. Sci. Eng. Conf. MSEC 2018*, vol. 1, pp. 1–12, 2018.
- [141] C. B. Highley, C. B. Rodell, and J. A. Burdick, “Direct 3D Printing of Shear-Thinning Hydrogels into Self-Healing Hydrogels,” *Adv. Mater.*, vol. 27, no. 34, pp. 5075–5079, 2015.
- [142] L. Shi *et al.*, “Dynamic Coordination Chemistry Enables Free Directional Printing of Biopolymer Hydrogel,” *Chem. Mater.*, vol. 29, no. 14, pp. 5816–5823, 2017.
- [143] C. S. O’Bryan *et al.*, “Self-assembled micro-organogels for 3D printing silicone structures,” *Sci. Adv.*, vol. 3, no. 5, 2017.

- [144] M. Rocca, A. Fragasso, W. Liu, M. A. Heinrich, and Y. S. Zhang, “Embedded Multimaterial Extrusion Bioprinting,” *SLAS Technol.*, vol. 23, no. 2, pp. 154–163, 2018.
- [145] W. Liu *et al.*, “Rapid Continuous Multimaterial Extrusion Bioprinting,” *Adv. Mater.*, vol. 29, no. 3, p. 1604630, Jan. 2017.
- [146] K. H. Bouhadir, E. Alsberg, and D. J. Mooney, “Hydrogels for combination delivery of antineoplastic agents,” *Biomaterials*, vol. 22, no. 19, pp. 2625–2633, Oct. 2001.
- [147] S. Dhivya, V. V. Padma, and E. Santhini, “Wound dressings - A review,” *Biomed.*, vol. 5, no. 4, pp. 24–28, 2015.
- [148] Vv. Nandini, Kv. Venkatesh, and Kc. Nair, “Alginate impressions: A practical perspective,” *J. Conserv. Dent.*, vol. 11, no. 1, p. 37, Jan. 2008.
- [149] L. Wang, R. M. Shelton, P. R. Cooper, M. Lawson, J. T. Triffitt, and J. E. Barralet, “Evaluation of sodium alginate for bone marrow cell tissue engineering,” *Biomaterials*, vol. 24, no. 20, pp. 3475–3481, Sep. 2003.
- [150] B. Balakrishnan, N. Joshi, A. Jayakrishnan, and R. Banerjee, “Self-crosslinked oxidized alginate/gelatin hydrogel as injectable, adhesive biomimetic scaffolds for cartilage regeneration,” *Acta Biomater.*, vol. 10, no. 8, pp. 3650–3663, Aug. 2014.
- [151] Y. Sapir, O. Kryukov, and S. Cohen, “Integration of multiple cell-matrix interactions into alginate scaffolds for promoting cardiac tissue regeneration,” *Biomaterials*, vol. 32, no. 7, pp. 1838–1847, Mar. 2011.
- [152] T. K. Merceron and S. V. Murphy, “Hydrogels for 3D Bioprinting Applications,” in *Essentials of 3D Biofabrication and Translation*, Elsevier Inc., 2015, pp. 249–270.
- [153] Ý. A. Mørch, I. Donati, B. L. Strand, and G. Skjåk-Bræk, “Effect of Ca<sup>2+</sup>, Ba<sup>2+</sup>, and Sr<sup>2+</sup> on alginate microbeads,” *Biomacromolecules*, vol. 7, no. 5, pp. 1471–1480, 2006.

- [154] S. H. Gwon, J. Yoon, H. K. Seok, K. H. Oh, and J.-Y. Sun, “Gelation Dynamics of Ionically Crosslinked Alginate Gel with Various Cations,” *Macromol. Res.*, vol. 23, no. 12, pp. 1112–1116, 2015.
- [155] H. H. Tønnesen and J. Karlsen, “Alginate in Drug Delivery Systems,” *Drug Dev. Ind. Pharm.*, vol. 28, no. 6, pp. 621–630, 2002.
- [156] J. N. BeMiller, *Food Polysaccharides and Their Applications*, vol. 7, no. 6. 1996.
- [157] I. T. Ozbolat, *Droplet-Based Bioprinting*. 2017.
- [158] G. A. Paredes Juárez, M. Spasojevic, M. M. Faas, and P. de Vos, “Immunological and technical considerations in application of alginate-based microencapsulation systems,” *Front. Bioeng. Biotechnol.*, vol. 2, no. AUG, 2014.
- [159] B. Aktar, M. S. Erdal, O. Sagirli, S. Güngör, and Y. Özsoy, “Optimization of biopolymer based transdermal films of metoclopramide as an alternative delivery approach,” *Polymers (Basel)*, vol. 6, no. 5, pp. 1350–1365, 2014.
- [160] J. Jia *et al.*, “Engineering alginate as bioink for bioprinting,” *Acta Biomater.*, vol. 10, no. 10, pp. 4323–4331, 2014.
- [161] Z. Wu, X. Su, Y. Xu, B. Kong, W. Sun, and S. Mi, “Bioprinting three-dimensional cell-laden tissue constructs with controllable degradation,” *Sci. Rep.*, vol. 6, no. April, p. 24474, 2016.
- [162] J. Cohen, K. L. Zaleski, G. Nourissat, T. P. Julien, M. A. Randolph, and M. J. Yaremchuk, “Survival of porcine mesenchymal stem cells over the alginate recovered cellular method,” *J. Biomed. Mater. Res. - Part A*, vol. 96 A, no. 1, pp. 93–99, 2011.
- [163] M. van der Rest and R. Garrone, “Collagen family of proteins,” *FASEB J.*, vol. 5, no. 13, pp. 2814–2823, 1991.
- [164] J. K. Carrow, P. Kerativitayanan, M. K. Jaiswal, G. Lokhande, and A. K. Gaharwar, “Polymers for Bioprinting,” in *Essentials of 3D Biofabrication and Translation*, 2015, pp. 229–248.
- [165] K. E. Kadler, D. F. Holmes, J. A. Trotter, and J. A. Chapman, “Collagen fibril formation,” *Biochem. J.*, vol. 11, pp. 1–11, 1996.

- [166] C. Mota and L. Moroni, *High Throughput Screening with Biofabrication Platforms*. Elsevier Inc., 2015.
- [167] K. Y. Lee and D. J. Mooney, “Hydrogels for Tissue Engineering,” *Chem. Rev.*, vol. 101, no. 7, pp. 1869–1879, 2001.
- [168] M. D. Shoulders and R. T. Raines, “Collagen Structure and Stability,” *Annu. Rev. Biochem.*, vol. 78, no. 1, pp. 929–958, 2009.
- [169] C. H. Lee, A. Singla, and Y. Lee, “Biomedical applications of collagen,” *Int. J. Pharm.*, vol. 221, no. 1–2, pp. 1–22, 2001.
- [170] N. Carolina, “Bioprinted Amniotic Fluid-Derived Stem Cells Accelerate Healing of Large Skin Wounds,” *Stem Cells Transl. Med.*, vol. 1, no. 11, pp. 792–802, 2012.
- [171] J. C. Reichert, a Heymer, a Berner, J. Eulert, and U. Nöth, “Fabrication of polycaprolactone collagen hydrogel constructs seeded with mesenchymal stem cells for bone regeneration.,” *Biomed. Mater.*, vol. 4, no. 6, p. 065001, 2009.
- [172] K. Pataky, T. Braschler, A. Negro, P. Renaud, M. P. Lutolf, and J. Brugger, “Microdrop printing of hydrogel bioinks into 3D tissue-like geometries,” *Adv. Mater.*, vol. 24, no. 3, pp. 391–396, 2012.
- [173] T. Boland, V. Mironov, A. Gutowska, E. a Roth, and R. R. Markwald, “Cell and Organ Printing 2: Fusion of Cell Aggregates in Three-Dimensional Gels,” *Anat. Rec. A. Discov. Mol. Cell. Evol. Biol.*, vol. 272, no. 2, pp. 497–502, 2003.
- [174] V. Beghetto, A. Zancanaro, A. Scrivanti, U. Matteoli, and G. Pozza, “The Leather Industry : A Chemistry Insight Part I : an Overview of the Industrial Process,” *Sci. Ca' Foscari*, vol. 1, no. May, pp. 12–22, 2013.
- [175] S. Baghapour, P. Parvin, A. Reyhani, S. Z. Mortazavi, S. Mokhtari, and A. Amjadi, “Chemo-physical properties of renal capsules under ultraviolet-c exposure,” *J. Appl. Phys.*, vol. 116, no. 5, pp. 1–12, 2014.
- [176] W. H. Nijhuis *et al.*, “Current concepts in osteogenesis imperfecta: Bone structure, biomechanics and medical management,” *J. Child. Orthop.*, vol. 13, no. 1, pp. 1–11, 2019.

- [177] G. Tomoaia and R. D. Pasca, "On the collagen mineralization. A review," *Clujul Med.*, vol. 88, no. 1, pp. 15–22, 2015.
- [178] J. Zhu and L. J. Kaufman, "Collagen i self-assembly: Revealing the developing structures that generate turbidity," *Biophys. J.*, vol. 106, no. 8, pp. 1822–1831, 2014.
- [179] D. L. Christiansen, E. K. Huang, and F. H. Silver, "Assembly of type I collagen: Fusion of fibril subunits and the influence of fibril diameter on mechanical properties," *Matrix Biol.*, vol. 19, no. 5, pp. 409–420, 2000.
- [180] Q. Zhang, C. Weber, U. S. Schubert, and R. Hoogenboom, "Thermoresponsive polymers with lower critical solution temperature: From fundamental aspects and measuring techniques to recommended turbidimetry conditions," *Mater. Horizons*, vol. 4, no. 2, pp. 109–116, 2017.
- [181] J. Parkinson, K. E. Kadler, and A. Brass, "Simple Physical Model of Collagen Fibrillogenesis Based on Diffusion Limited Aggregation," *Mol. Biol.*, pp. 823–831, 1995.
- [182] X. Yang, Z. Lu, H. Wu, W. Li, L. Zheng, and J. Zhao, "Collagen-alginate as bioink for three-dimensional (3D) cell printing based cartilage tissue engineering," *Mater. Sci. Eng. C*, vol. 83, no. September 2017, pp. 195–201, 2018.
- [183] GMIA, *Gelatin Handbook*. 2012.
- [184] I. J. Haug and K. I. Draget, "5 – Gelatin in Handbook of Food Proteins," *Handb. Food Proteins*, no. 1964, pp. 92–115, 2011.
- [185] A. A. Mariod and H. F. Adam, "Review: Gelatin, source, extraction and industrial applications," *Acta Sci. Pol. Technol. Aliment.*, vol. 12, no. 2, pp. 135–147, 2013.
- [186] Y. Meng and S. Cloutier, *Gelatin and Other Proteins for Microencapsulation*. Elsevier Inc., 2014.
- [187] X. Wang *et al.*, "Gelatin-based hydrogels for organ 3D bioprinting," *Polymers (Basel)*, vol. 9, no. 9, 2017.

- [188] L. Gasperini, A. P. Marques, and R. L. Reis, "Microfluidics for Processing of Biomaterials," in *Biomaterials- and Microfluidics-Based Tissue Engineered 3D Models*, J. Miguel Oliveira and R. L. Reis, Eds. Springer Nature, 2020, pp. 15–26.
- [189] M. Taylor, P. Tomlins, and T. Sahota, "Thermoresponsive Gels," *Gels*, vol. 3, no. 1, p. 4, 2017.
- [190] D. G. Dastidar and G. Chakrabarti, "Thermoresponsive Drug Delivery Systems, Characterization and Application," in *Applications of Targeted Nano-Drugs and Delivery Systems: Nanoscience and Nanotechnology in Drug Delivery*, S. Mohapatra, S. Ranjan, N. Dasgupta, R. Kumar, and S. Thomas, Eds. Elsevier, 2019, pp. 133–156.
- [191] S. Kommareddy, D. B. Shenoy, and M. M. Amiji, "Gelatin Nanoparticles and Their Biofunctionalization," *Nanotechnologies Life Sci.*, no. February 2018, 2007.
- [192] D. Achet and X. W. He, "Determination of the renaturation level in gelatin films," *Polymer (Guildf.)*, vol. 36, no. 4, pp. 787–791, 1995.
- [193] S. Gorgieva and V. Kokol, "Collagen- vs. Gelatine-Based Biomaterials and Their Biocompatibility: Review and Perspectives," *Biomater. Appl. Nanomedicine*, 2011.
- [194] S. Thakur, P. P. Govender, M. A. Mamo, S. Tamulevicius, and V. K. Thakur, "Recent progress in gelatin hydrogel nanocomposites for water purification and beyond," *Vacuum*, vol. 146, no. November, pp. 396–408, 2017.
- [195] J. K. Williams, J. J. Yoo, and A. Atala, *Regenerative Medicine Approaches for Tissue Engineered Heart Valves*. Elsevier Inc., 2019.
- [196] M. P. Chae, D. J. Hunter-Smith, S. V. Murphy, and M. W. Findlay, *3D bioprinting adipose tissue for breast reconstruction*. Elsevier Ltd., 2017.
- [197] J. W. Nichol, S. T. Koshy, H. Bae, C. M. Hwang, S. Yamanlar, and A. Khademhosseini, "Cell-laden microengineered gelatin methacrylate hydrogels," *Biomaterials*, vol. 31, no. 21, pp. 5536–5544, 2010.



- [198] K. Ulubayram, E. Aksu, S. I. D. Gurhan, K. Serbetci, and N. Hasirci, "Cytotoxicity evaluation of gelatin sponges prepared with different cross-linking agents," *J. Biomater. Sci. Polym. Ed.*, vol. 13, no. 11, pp. 1203–1219, 2002.
- [199] W. Lee *et al.*, "On-demand three-dimensional freeform fabrication of multi-layered hydrogel scaffold with fluidic channels," *Biotechnol. Bioeng.*, vol. 105, no. 6, pp. 1178–1186, 2010.
- [200] A. C. Guedes, H. M. Amaro, I. Sousa-Pinto, and F. X. Malcata, *Algal spent biomass—A pool of applications*, Second Edi. Elsevier B.V., 2019.
- [201] G. Hernández-Carmona, Y. Freile-Pelegrín, and E. Hernández-Garibay, *Conventional and alternative technologies for the extraction of algal polysaccharides*. 2013.
- [202] L. Rioux and S. L. Turgeon, *Chapter 7 - Seaweed carbohydrates*. Elsevier Inc., 2015.
- [203] Y. Zhang, X. Fu, D. Duan, J. Xu, and X. Gao, "Preparation and characterization of agar, agarose, and agarpectin from the red alga *Ahnfeltia plicata*," *J. Oceanol. Limnol.*, vol. 37, no. 3, pp. 815–824, 2019.
- [204] K. Izumi, "A new Method for Fractionation of Agar," *Agric. Biol. Chem.*, vol. 34, no. 11, pp. 1739–1740, 1970.
- [205] P. Zucca, R. Fernandez-Lafuente, and E. Sanjust, "Agarose and Its Derivatives as Supports for Enzyme Immobilization," *Molecules*, vol. 21, no. 11, p. 1577, Nov. 2016.
- [206] H. Suzuki, Y. Sawai, and M. Takada, "The Effect of Apparent Molecular Weight and Components of Agar on Gel Formation," *Food Sci. Technol. Res.*, vol. 7, no. 4, pp. 280–284, 2001.
- [207] P. Y. Lee, J. Costumbrado, C. Y. Hsu, and Y. H. Kim, "Agarose gel electrophoresis for the separation of DNA fragments," *J. Vis. Exp.*, no. 62, pp. 1–5, 2012.
- [208] S. Ven and A. Rani, "Discriminatory Power of Agarose Gel Electrophoresis in DNA Fragments Analysis," *Gel Electrophor. - Princ. Basics*, no. May, 2012.

- [209] S. Bhatia, A. G. Namdeo, and S. Nanda, "Factors effecting the gelling and emulsifying properties of a natural polymer," *Syst. Rev. Pharm.*, vol. 1, no. 1, pp. 86–92, 2010.
- [210] W. Zhang, "Encapsulation of Transgenic Cells for Gene Therapy," *Gene Ther. - Princ. Challenges*, no. December, 2015.
- [211] J. Y. Xiong, J. Narayanan, X. Y. Liu, T. K. Chong, S. B. Chen, and T. S. Chung, "Topology evolution and gelation mechanism of agarose gel," *J. Phys. Chem. B*, vol. 109, no. 12, pp. 5638–5643, 2005.
- [212] A. Hayashi, K. Kinoshita, and S. Yasueda, "Studies of the agarose gelling system by the fluorescence polarization method. III," *Polym. J.*, vol. 12, no. 7, pp. 447–453, 1980.
- [213] B. Dai and S. Matsukawa, "NMR studies of the gelation mechanism and molecular dynamics in agar solutions," *Food Hydrocoll.*, vol. 26, no. 1, pp. 181–186, 2012.
- [214] A. Pegg, *The application of natural hydrocolloids to foods and beverages*. Woodhead Publishing Limited, 2012.
- [215] S. W. Cui, Y. Wu, and H. Ding, "The range of dietary fibre ingredients and a comparison of their technical functionality," *Fibre-Rich Wholegrain Foods Improv. Qual.*, pp. 96–119, 2013.
- [216] Z. M. Jessop, N. Gao, S. Manivannan, A. Al-Sabah, and I. S. Whitaker, "3D bioprinting cartilage," *3D Bioprinting Reconstr. Surg.*, pp. 277–304, Jan. 2018.
- [217] H. A. Awad, M. Q. Wickham, H. A. Leddy, J. M. Gimble, and F. Guilak, "Chondrogenic differentiation of adipose-derived adult stem cells in agarose, alginate, and gelatin scaffolds," *Biomaterials*, vol. 25, no. 16, pp. 3211–3222, 2004.
- [218] S. M. O'Connor, D. A. Stenger, K. M. Shaffer, and W. Ma, "Survival and neurite outgrowth of rat cortical neurons in three-dimensional agarose and collagen gel matrices," *Neurosci. Lett.*, vol. 304, no. 3, pp. 189–193, 2001.

- [219] G. R. López-Marcial, A. Y. Zeng, C. Osuna, J. Dennis, J. M. García, and G. D. O'Connell, "Agarose-Based Hydrogels as Suitable Bioprinting Materials for Tissue Engineering," *ACS Biomater. Sci. Eng.*, vol. 4, no. 10, pp. 3610–3616, 2018.
- [220] R. Fan, M. Piou, E. Darling, D. Cormier, J. Sun, and J. Wan, "Bio-printing cell-laden Matrigel-agarose constructs," *J. Biomater. Appl.*, vol. 31, no. 5, pp. 684–692, 2016.
- [221] L. E. Bertassoni *et al.*, "Direct-write bioprinting of cell-laden methacrylated gelatin hydrogels," *Biofabrication*, vol. 6, no. 2, p. 024105 (11pp), 2014.
- [222] E. Mirdamadi, N. Muselimyan, P. Koti, H. Asfour, and N. Sarvazyan, "Agarose slurry as a support medium for bioprinting and culturing freestanding cell-laden hydrogel constructs," *3D Print. Addit. Manuf.*, vol. 6, no. 3, pp. 158–164, 2019.
- [223] M. H. Mahdi, B. R. Conway, and A. M. Smith, "Evaluation of gellan gum fluid gels as modified release oral liquids," *Int. J. Pharm.*, vol. 475, no. 1, pp. 335–343, 2014.
- [224] H. Kiani, M. E. Mousavi, and Z. E. Mousavi, "Particle stability in dilute fermented dairy drinks: Formation of fluid gel and impact on rheological properties," *Food Sci. Technol. Int.*, vol. 16, no. 6, pp. 543–551, 2010.
- [225] I. T. Norton, D. A. Jarvis, and T. J. Foster, "A molecular model for the formation and properties of fluid gels," *Int. J. Biol. Macromol.*, vol. 26, no. 4, pp. 255–261, 1999.
- [226] I. Fernández Farrés, R. J. A. Moakes, and I. T. Norton, "Designing biopolymer fluid gels: A microstructural approach," *Food Hydrocoll.*, vol. 42, no. P3, pp. 362–372, 2014.
- [227] S. H. Ching, N. Bansal, and B. Bhandari, "Alginate gel particles—A review of production techniques and physical properties," *Crit. Rev. Food Sci. Nutr.*, vol. 57, no. 6, pp. 1133–1152, 2017.
- [228] D. A. Garrec and I. T. Norton, "Understanding fluid gel formation and properties," *J. Food Eng.*, vol. 112, no. 3, pp. 175–182, 2012.

- [229] T. Mills, A. Koay, and I. T. Norton, “Fluid gel lubrication as a function of solvent quality,” *Food Hydrocoll.*, vol. 32, no. 1, pp. 172–177, 2013.
- [230] C. J. Ferris, K. J. Gilmore, S. Beirne, D. McCallum, G. G. Wallace, and M. in het Panhuis, “Bio-ink for on-demand printing of living cells,” *Biomater. Sci.*, vol. 1, no. 2, p. 224, 2013.
- [231] S. Holland, C. Tuck, and T. Foster, “Fluid Gels: a New Feedstock for High Viscosity Jetting,” *Food Biophys.*, vol. 13, no. 2, pp. 175–185, 2018.
- [232] A. Gabriele, F. Spyropoulos, and I. T. Norton, “Kinetic study of fluid gel formation and viscoelastic response with kappa-carrageenan,” *Food Hydrocoll.*, vol. 23, no. 8, pp. 2054–2061, 2009.
- [233] I. Fernández Farrés, M. Douaire, and I. T. Norton, “Rheology and tribological properties of Ca-alginate fluid gels produced by diffusion-controlled method,” *Food Hydrocoll.*, vol. 32, no. 1, pp. 115–122, 2013.
- [234] A. Gabriele, F. Spyropoulos, and I. T. Norton, “A conceptual model for fluid gel lubrication,” *Soft Matter*, vol. 6, no. 17, pp. 4205–4213, 2010.
- [235] “Speedy Laser Engraving Machines.” [Online]. Available: <https://www.troteclaser.com/en-gb/trotec-laser-machines/laser-engravers-speedy-series/>. [Accessed: 25-Oct-2019].
- [236] “MakerBot Replicator 2X.” [Online]. Available: <https://pages.makerbot.com/ap-replicator-2x.html>. [Accessed: 25-Oct-2019].
- [237] Cellink, “Application Note.” pp. 1–2, 2017.
- [238] “Eclipse TE300 Inverted Microscope | MicroscopyU.” [Online]. Available: <https://www.microscopyu.com/museum/eclipse-te300-inverted-microscope>. [Accessed: 25-Oct-2019].
- [239] E. Malone and H. Lipson, “Fab@Home: the personal desktop fabricator kit,” *Rapid Prototyp. J.*, vol. 13, no. 4, pp. 245–255, 2007.
- [240] Fab@Home, “Tools : Model 2 Syringe tools,” [http://www.fabathome.org/wiki/index.php?title=Tools:\\_Model\\_2\\_Syringe\\_tools](http://www.fabathome.org/wiki/index.php?title=Tools:_Model_2_Syringe_tools), 2013. .

- [241] “Allegro A4988 Stepper Motor Driver Datasheet.” [Online]. Available: <https://www.pololu.com/file/0J450/A4988.pdf>. [Accessed: 25-Oct-2019].
- [242] “17HS3001-20B Datasheet.” [Online]. Available: <http://www.robotdigg.com/upload/pdf/17HS3001-20B.pdf>. [Accessed: 25-Oct-2019].
- [243] “17HS3001-350N Datasheet.” [Online]. Available: <https://datasheetspdf.com/pdf-file/1038752/ROBOTDIGG/17HS3001-350N/1>. [Accessed: 25-Oct-2019].
- [244] “G-code - RepRap.” [Online]. Available: <https://reprap.org/wiki/G-code>. [Accessed: 25-Oct-2019].
- [245] “GitHub - MarlinFirmware/Marlin: Optimized firmware for RepRap 3D printers based on the Arduino platform.” [Online]. Available: <https://github.com/MarlinFirmware/Marlin>. [Accessed: 04-Nov-2019].
- [246] “RepRap Calculator - Prusa Printers.” [Online]. Available: <https://blog.prusaprinters.org/calculator/>. [Accessed: 26-Oct-2019].
- [247] J. A. Reid, P. A. Mollica, G. D. Johnson, R. C. Ogle, R. D. Bruno, and P. C. Sachs, “Accessible bioprinting: Adaptation of a low-cost 3D-printer for precise cell placement and stem cell differentiation,” *Biofabrication*, vol. 8, no. 2, 2016.
- [248] I. T. Ozbolat, K. K. Moncal, and H. Gudapati, “Evaluation of bioprinter technologies,” *Addit. Manuf.*, vol. 13, pp. 179–200, 2017.
- [249] J. A. Reid, P. A. Mollica, G. D. Johnson, R. C. Ogle, R. D. Bruno, and P. C. Sachs, “Accessible bioprinting: Adaptation of a low-cost 3D-printer for precise cell placement and stem cell differentiation,” *Biofabrication*, vol. 8, no. 2, 2016.
- [250] M. Kahl, M. Gertig, P. Hoyer, O. Friedrich, and D. F. Gilbert, “Ultra-low-cost 3D bioprinting: Modification and application of an off-the-shelf desktop 3D-printer for biofabrication,” *Front. Bioeng. Biotechnol.*, vol. 7, no. JUL, pp. 1–12, 2019.
- [251] “The Top 10 Bioprinters - 3D Printing Industry.” [Online]. Available: <https://3dprintingindustry.com/news/top-10-bioprinters-55699/>. [Accessed: 23-May-2020].

- [252] “RegenHU 3DDiscovery review - 3D bioprinter for labs.” [Online]. Available: <https://www.aniwaa.com/product/3d-printers/regenhu-3ddiscovery/>. [Accessed: 23-May-2020].
- [253] “Allevi 2 - Allevi.” [Online]. Available: <https://www.allevi3d.com/allevi-2/>. [Accessed: 23-May-2020].
- [254] “3D bioprinters.” [Online]. Available: <https://www.regenhu.com/3d-bioprinters>. [Accessed: 23-May-2020].
- [255] MakerBot, “Replicator 2X Experimental 3D Printer User Manual.”
- [256] “A8 — anet3d.com.” [Online]. Available: <https://anet3d.com/pages/a8>. [Accessed: 23-May-2020].
- [257] Y. Jin, A. Compaan, T. Bhattacharjee, and Y. Huang, “Granular gel support-enabled extrusion of three-dimensional alginate and cellular structures,” *Biofabrication*, vol. 8, no. 2, p. 025016, Jun. 2016.
- [258] S. B. Ross-Murphy, “Structure and rheology of gelatin gels,” *Imaging Sci. J.*, vol. 45, no. 3–4, pp. 205–209, 1997.
- [259] S. R. Derkach, N. G. Voron’ko, L. Kuranova, and N. I. Sokolan, “The rheology of food hydrogels based on the marine polysaccharide/gelatin polyelectrolyte complexes,” *Annu. Trans. Nord. Rheol. Soc.*, vol. 25, pp. 305–308, 2017.
- [260] N. Ohkubo, Y. Otsubo, and S. Aoyagi, “Viscoelastic properties of gelatin solutions near the gel point,” *Imaging Sci. J.*, vol. 47, no. 3, pp. 147–153, 1999.
- [261] A. Andersen, C. J. S. Ibsen, and H. Birkedal, “Influence of Metal Ions on the Melting Temperature, Modulus, and Gelation Time of Gelatin Gels: Specific Ion Effects on Hydrogel Properties,” *J. Phys. Chem. B*, vol. 122, no. 43, pp. 10062–10067, 2018.
- [262] M. Davidovich-Pinhas and H. Bianco-Peled, “A quantitative analysis of alginate swelling,” *Carbohydr. Polym.*, vol. 79, no. 4, pp. 1020–1027, 2010.

- [263] S. Li, K. Wang, X. Jiang, Q. Hu, C. Zhang, and B. Wang, "Rapid Fabrication of Ready-to-Use Gelatin Scaffolds with Prevascular Networks Using Alginate Hollow Fibers as Sacrificial Templates," *ACS Biomater. Sci. Eng.*, vol. 6, no. 4, pp. 2297–2311, 2020.
- [264] Y. Tsuchiya and K. C. Hong, "Agarose and Agarpectin in Gelidium and Gracilaria Agar," in *Proceedings of the Fifth International Seaweed Symposium, Halifax, August 25–28, 1965*, Elsevier, 1966, pp. 315–321.
- [265] A. Nussinovitch, "Hydrocolloid Applications: Gum technology in the food and other industries," in *Hydrocolloid Applications: Gum technology in the food and Three-dimensional printing of complex biological structures by freeform reversible embedding of suspended other industries*, 1st ed., Chapman & Hall, 1997, p. 6.
- [266] F. Y. De Boer, R. J. A. Van Dijk-Moes, A. Imhof, and K. P. Velikov, "Characterization of the Scattering and Absorption of Colored Zein Colloids in Optically Dense Dispersions," *Langmuir*, vol. 35, no. 37, pp. 12091–12099, 2019.
- [267] D. S. Richardson and J. W. Lichtman, "Clarifying Tissue Clearing," *Cell*, vol. 162, no. 2, pp. 246–257, 2015.
- [268] P. Burey, B. R. Bhandari, T. Howes, and M. J. Gidley, "Hydrocolloid gel particles: Formation, characterization, and application," *Crit. Rev. Food Sci. Nutr.*, vol. 48, no. 5, pp. 361–377, 2008.
- [269] A. J. Crowle, "Immunodiffusion," in *Methods of Protein Separation*, N. Catsimpoilas, Ed. Springer, 1975, pp. 69–92.
- [270] J. A. Casas, A. F. Mohedano, and F. García-Ochoa, "Viscosity of guar gum and xanthan/guar gum mixture solutions," *J. Sci. Food Agric.*, vol. 80, no. 12, pp. 1722–1727, Sep. 2000.